Correlating Electronic and Nuclear Motions in Ultrafast Photoinduced Charge Transfer Reactions with Femtosecond Multidimensional Spectroscopies

Michael Stanley Lynch

A dissertation
submitted in partial fulfillment of the
requirements for the degree of

Doctor of Philosophy

University of Washington

2013

Reading Committee:

Munira Khalil, Chair

Philip J. Reid

Daniel R. Gamelin

Program Authorized to Offer Degree:
Chemistry

University of Washington

Abstract

Correlating Electronic and Nuclear Motions in Ultrafast Photoinduced Charge Transfer Reactions with Femtosecond Multidimensional Spectroscopies

Michael Stanley Lynch

Chair of the Supervisory Committee:
Assistant Professor Munira Khalil
Chemistry Department

Photochemical reactions in solution are probed using femtosecond multidimensional infrared spectroscopies to elucidate the role high-frequency vibrations play in condensed phase charge transfer processes. In all cases presented in this thesis, electronically excited molecules adjust the position of nuclei in unique ways to accommodate excess electronic energy. In the case of sodium nitroprusside, $Na_2[Fe(CN)_5NO]$, we observe a competition between isomerism (bond rotation) and photodissociation (bond breakage) of the nitrosyl ligand on the sub-picosecond time scale.

Photoinduced electron transfer in mixed-valence (MV) systems is explored using four vibrations of the cyano-bridged MV complex $[(NC)_5Fe^{II}-CN-Pt^{IV}(NH_3)_4-NC-Fe^{II}(CN)_5]^{4-}$ ($Fe^{II}Pt^{IV}Fe^{II}$) in D_2O. Third-order nonlinear infrared (IR) spectroscopies are used to determine the molecular nature of the four high-frequency CN stretching (ν_{CN}) modes in the ground electronic state (GS), including vibrational energy relaxation time, anharmonic vibrational couplings, relative magnitudes and orientations of the permanent dipole moments, and solvent relaxation time scales. These data, which effectively describe the shape of the $Fe^{II}Pt^{IV}Fe^{II}$ GS potential energy surface (PES), are crucial in subsequent chapters when the metal-to-metal charge transfer (MMCT) transition is initiated with a $\lambda = 400$ nm pulse and subsequent non-equilibrium vibrational energy relaxation dynamics are observed. We find that back-electron transfer occurs in 110 ± 10 fs, during which greater than six vibrational

quanta of the bridging ν_{CN} mode are excited. This excess energy quickly transfers into the other ν_{CN} modes until it eventually is deposited into the solvent. We delved further into the electronic spectroscopy of $Fe^{II}Pt^{IV}Fe^{II}$ by developing a coherent fifth-order visible−infrared spectroscopy in order to obtain a more detailed picture of the complex PES governing the MMCT reaction in solution. The goal is to collect third-order nonlinear IR spectroscopic information from an electronically excited state. Fifth order data of this nature allows for the measurement of time-dependent anharmonic couplings, non-equilibrium frequency correlation functions, incoherent and coherent vibrational relaxation and transfer dynamics, and coherent vibrational and electronic coupling as a function of a photochemical reaction. Results on $Fe^{II}Pt^{IV}Fe^{II}$ provide experimental evidence that the nuclear motions of the molecule are both coherently and incoherently coupled to the electronic charge transfer process.

This thesis concludes with the development of a novel coherent IR−Raman spectroscopic technique that combines direct IR excitation with a femtosecond stimulated Raman probe. This technique enables anharmonic couplings between low- and high-frequency modes to be obtained directly. Preliminary results suggest that the high-frequency CN stretching mode of acetonitrile is coupled to the low-frequency CCN bending vibration. It is proposed that this IR−FSRS technique will unravel couplings between localized high-frequency motions and global motions in biological systems such as proteins.

TABLE OF CONTENTS

LIST OF FIGURES

LIST OF TABLES

GLOSSARY

1D: One-dimensional.

2D: Two-dimensional.

IR: Infrared.

VIS: Visible.

UV: Ultraviolet.

MS: Metastable.

BET: Back-electron transfer.

FET: Forward-electron transfer.

SNP: Sodium nitroprusside.

OD: Optical density.

FTIR: Fourier transform infrared.

MLCT: Metal-to-ligand charge transfer.

MMCT: Metal-to-metal charge transfer.

CTS: Charge transfer state.

PES: Potential energy surface.

GS: Ground state.

ES: Excited state.

NIR: Near infrared.

MIR: Middle infrared.

OPA: Optical parametric amplifier.

DFG: Difference frequency generation.

FWHM: Full-width at half-maximum.

T: Tracer.

LO: Local oscillator.

MCT: Mercury cadmium telluride (HgCdTe).

R: Rephasing.

NR: Nonrephasing.

VEPS: Vibrational echo peak shift.

DPP: Dispersed pump−probe.

DVE: Dispersed vibrational echo.

MA: Magic angle.

IVR: Intramolecular vibrational relaxation.

VER: Vibrational energy relaxation.

VR: Vibrational relaxation.

NMR: Nuclear magnetic resonance.

NLS: Nodal line slope.

CLS: Center line slope.

FFCF: Frequency-frequency correlation function.

HDPP: Heterodyne-detected dispersed pump−probe.

HDVE: Heterodyne-detected dispersed vibrational echo.

T-HDVE: Transient heterodyne-detected dispersed vibrational echo.

FSRS: Femtosecond stimulated Raman spectroscopy.

ACN: Acetonitrile.

FRIKES: Femtosecond Raman-induced Kerr effect spectroscopy.

QWP: Quarter-wave plate.

HWP: Half-wave plate.

P: Polarizer.

A: Analyzer.

S/N: Signal-to-noise.

DPDA: Dual photodiode array.

EMCCD: Electron multiplication charge-coupled device.

β-BBO: β-Barium borate.

FF: Fundamental frequency.

SH: Second harmonic.

GDM: Group-delay mismatch.

OAP: Off-axis parabolic.

TDG: Timing delay generator.

NI: National Instruments.

ACKNOWLEDGMENTS

I would first like to thank Munira Khalil for trusting me with the responsibilities of the first graduate student. I had no experience in an ultrafast spectroscopy lab, but I think we both knew that we were going to work well together. Our lab wasn't even finished when both Munira and I arrived in September 2007. We didn't receive the first laser until the middle of January 2008. Of course, Dennis couldn't make it back to install it until January 29$^{\text{th}}$... so it wasn't until then that we could think about generating mid-IR. From that point on, Munira set up the optics while I learned, helped, and eventually took over the day-to-day lab work (the rate of phone calls to her office regarding decisions in the lab slowly decreased over time). I vividly remember the first signal I found. It was a SPIDER signal used to characterize our shiny new laser: "I just thought I'd let you know that I found the SPIDER signal today!" Pumping your arms and shouting "yes!" when seeing an extremely faint blue light on a business card in absolute darkness is really an experience that only a spectroscopist would find spectacular. The next time that happened was when I found my first vibrational echo signal from $W(CO)_6$, which is still a signal I can't believe I had faith in given the S/N was < 1. From day 1, Munira let me follow the path of the independent scientist and for that I am very grateful.

The group! Thank you Ben for being honest and admitting that you hated working in the laser lab! Thanks for being my go to theory guy and helping with (doing...) all of the electronic structure calculations, 2D IR simulations, C++ programming, the hard theory literature reviews, and talk about baseball. Thank you Mark for sticking with me in the early days in lab. It's never easy to walk into someone else's experiment, but you always kept it together. Not to mention you're the only one that ever talks to me about hockey, eh? The next group to come in 2009 was a big one: Jen, Karla, and Anthony. Anthony quickly started to work with Mark, but Jen and Karla were the next to step into "Lab 1"

and get some data. Thanks for keeping me honest in the lab and trusting my sometimes odd alignment methods. I also really need to thank the excellent undergraduates that have helped me immensely with chemical synthesis and steady-state spectra collection. Thanks to Hyung Sup, Kristin, Josiah, Jake, Stephanie, and Caitlin!

I was also very lucky to be able to do time-resolved X-ray absorption work with Ben at the ALS. I want to thank Munira for the opportunity and our collaborators Robert Schoenlein, Nils Huse, and Hana Cho for teaching me how things work at the ALS. I will never forgot the multiple middle-of-the-night trips Ben and I took to the honor-system snack room. Peppermint patties are forever correlated with transient XAS.

I want to take a moment to also thank the many scientists that got me to graduate school. My first research advisors, Drs. Erik Krogh and Chris Gill at Malaspina University-College (now Vancouver Island University), opened my eyes to research. It was Erik's general chemistry class that awoke my love for chemistry. The "aha!" moment we had while fitting the MIMS rise time signals is the first time I can remember feeling elated about research. I want to thank Drs. Edward Grant and Michael Blades for helping me become a more independent scientist during my years at UBC. Finally, I want to thank the amazing Dr. Bruce Todd who recently passed away unexpectedly. Bruce was a great man. He taught me everything from machining to lasers to LabVIEW to electronics to E&M. What I remember most, however, is how he taught me about balance. He is the only scientist even today that let me in behind the scenes to show me the importance of balance. Thank you.

My true support system is my family. They are and always have been behind me 100%. Thanks to my brother Brian for normalization and keeping me up with the "real world." Our shared loved for sports made my time in Seattle that much better. Thank you, Mom, for everything you have done. Not only did you make me the man I am today, you single-handedly put me through university. I would finally like to thank my one and true love, Emily. I would not have made it through graduate school without you. You put a smile on my face every day and I love you more than anything.

DEDICATION

to my mom Beth and my fiancé Emily

Chapter 1

INTRODUCTION

1.1 Correlating Electron and Nuclear Motion

The correlation of electronic and nuclear motion may appear to be an esoteric subject to some; however, this molecular "dance" is occurring all around us every day. Consider two cases: (i) an ultraviolet (UV) photon hitting your skin, and (ii) a chemist attempting to synthesize an efficient solar cell dye molecule. In case (i), the UV photon may be absorbed by the DNA molecule which results in the DNA containing an excess of energy. The fastest and most efficient way for that energy to be released is for the DNA molecule to "shake" the energy off via molecular vibrations.[1–4] In case (ii) the question is how energy from sunlight can be efficiently absorbed and subsequently transferred from a dye molecule into a metal contact. Does vibrational energy mediate charge separation or recombination in photovoltaic materials? A molecular understanding of charge transfer, separation, and recombination is critical for the development of chemical, electrical, and mechanical devices.[5–9] Both of these cases highlight the importance of a molecular-level understanding of how electrons couple to nuclei in solution at room temperature. In order to get a molecular picture of these processes, it is necessary to build experimental tools that can unravel coupled electronic, vibrational, spin, and solvent degrees of freedom for both reactants and products. The efficiency of a specific photochemical reaction, such as photosynthesis, is dependent on specific pathways leading the reaction from an initially excited state into product species. The goal of this thesis is to discover these relevant photochemical pathways, and the time-evolving molecular and electronic structure of the solute/solvent complexes.

The influence of an electron on an atom is generally ignored since the velocity of an electron is so much faster than a much heavier atom. This is the very well-known Born-Oppenheimer (BO) approximation, where it is assumed that nuclei are fixed with respect to electron motion (i.e., the motion of electrons and nuclei is separable).[10] Mathematically,

it is assumed that the molecular wavefunction can be written as a product of electronic (Ψ) and nuclear (χ) terms so that the total wavefunction can be separated as $\Psi(\mathbf{r};\mathbf{R})\chi(\mathbf{R})$ where $\mathbf{r}$ is the position of the electron the $\mathbf{R}$ is the position of the nucleus. In a lot of cases it is a good approximation, but what happens after an electron has been excited by a photon? An entirely new electronic structure around each atom in the molecule has been created and the atoms must adjust accordingly. This so-called non-equilibrium relaxation is a reoccurring theme in this thesis, where the correlation of electron and nuclear motion is observed by monitoring the nuclei with vibrational spectroscopy. Coupling between vibrational and electronic degrees of freedom, or vibronic coupling, represents a breakdown of the BO approximation.

Obtaining a deeper understanding of the correlation between electron and nuclear motion is imperative to the development of energy-harvesting materials. However, experimentally measuring these effects requires many sophisticated spectroscopies with the ability to separate electronic, vibrational, and solvent motion. Techniques used in this thesis follow a general principle of inducing a perturbation and probing the vibrations of the molecule (i.e., probing the nuclei). In this manner, the effect of the perturbation (e.g., photoinduced charge transfer) on the nuclei can be measured directly.

1.2 Photoinduced Charge Transfer Chemistry in Solution

Photochemistry has been an active area of research for over 150 years.[11,12] It aims to change the chemical structure of a molecule with only electromagnetic radiation. The ability to change the molecular structure of a molecule with light is extremely powerful; however, accurately predicting the outcome of a photochemical reaction is more difficult than a "traditional" chemical reaction in a beaker. Imagine placing a small ball onto the top edge of a large misshapen bowl, letting it go, and trying to predict where the ball will stop. That is essentially what one is doing when irradiating a molecule with light, except instead of being defined by position $\{x, y, z\}$ the potential energy surface is defined by bond lengths (r) and angles $\{r_{\mathrm{a}}, r_{\mathrm{b}}, r_{\mathrm{c}}, \theta_{\mathrm{ab}}, \phi_{\mathrm{ac}}\}$. Molecules have many more dimensions than three, so therefore a multidimensional surface defines the surface by which a photochemical reaction can proceed. It is the job of the spectroscopist to determine what the important

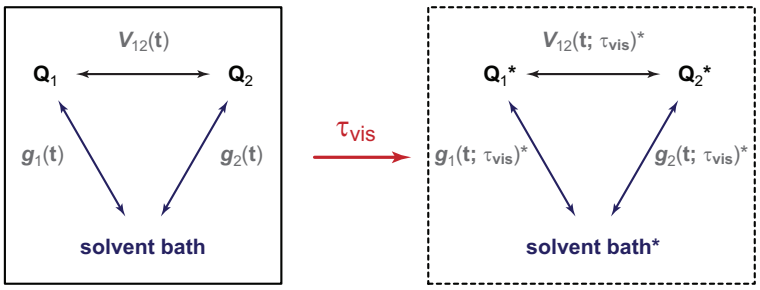

Figure 1.1: Photoinduced charge transfer chemistry in solution. (Left) "Equilibrium dynamics." (Right) "Non-equilibrium dynamics." The two high-frequency modes ($\mathbf{Q}_{1,2}$) are coupled by V_{12} and interact with the solvent bath through $g_{1,2}$. All parameters can change after photoexcitation, which is highlighted by the * in the photoexcited state.

dimensions are (generally known as the reaction coordinate) and how they change during a photochemical reaction.

Figure 1.1 gives a "spectroscopist's perspective" of the photochemistry of a molecule in solution that has two coupled high-frequency vibrational modes ($\mathbf{Q}_{1,2}$). In a beaker at room temperature and pressure, the modes couple to each other through V_{12} and to the solvent bath through $g_{1,2}$. This represents an equilibrium state with respect to any external perturbations. By shining a laser into the solution, heating the beaker, or adding another chemical to the mix, the parameters in the system can (but do not have to) change. The system is no longer at equilibrium as defined previously. In the case of photoexcitation by a laser, the parameters dependent on the time delay between the visible pump and the time of observation (i.e., the probe) denoted as τ_{vis}. For example, imagine a molecule of the form $[\text{N}{\equiv}\text{C}{-}\text{FeL}_4{-}\text{N}{\equiv}\text{O}]^{n-}$ in aqueous solution (L is any ligand) with a metal-to-ligand charge transfer (MLCT) absorption at $\lambda_{\text{max}} = 400$ nm. An infrared spectroscopist would define the CN stretching (ν_{CN}) mode as $\mathbf{Q}_1$ and the NO stretching (ν_{NO}) mode as $\mathbf{Q}_2$. The ν_{CN} and ν_{NO} modes are coupled via V_{12}. Hydrogen bonding dynamics between CN^- and H_2O would be governed by g_1 and between NO^+ and H_2O by g_2. A $\lambda = 400$ nm photon then excites the MLCT band, which shifts a large amount of electron density into the π^* orbitals of the NO^+ ligand; thus, $\mathbf{Q}_2$ turns into $\mathbf{Q}_2^*$. This causes $\mathbf{Q}_1$ to change into $\mathbf{Q}_1^*$ through V_{12}^*, which is essentially the interaction of the π orbitals of the ligands through the d orbitals of the

iron atom. Of course, the new electronic configurations around $\mathbf{Q}^*_{1,2}$ lead to a significantly different hydrogen bonding interaction with each of the ligands via $g^*_{1,2}$. Eventually the non-equilibrium system will relax back to the initial equilibrium system, assuming that nothing has happened to the parent molecule (photodissociation, for example).

This simple example in fact forms the basis for all of the experiments presented in this thesis. The main difficulty lies in converting measured experimental data into the fundamental parameters that govern the molecular dynamics, as one must consider these parameters when designing real-world devices. Experiments in this thesis aim to obtain as many of the parameters highlighted in Figure 1.1 as possible. Again, throughout this thesis, dynamics in the solid box (the electronic ground state of the system) will be called "equilibrium dynamics" whereas dynamics in the dotted box (an electronic excited state) will be denoted "non-equilibrium dynamics" all with respect to electronic excitation.

1.3 Model Systems

Two model systems will be featured in this thesis, both of which have applications and implications towards biological, material, and energy transfer research. The first is a metal−nitrosyl-containing coordination compound called sodium nitroprusside (SNP), which (by design) matches the form of the hypothetical molecule discussed in Section 1.2 with L = CN^- and $n = 2$. The second is a cyano-bridged MV complex containing two iron(II) (Fe^{II}) atoms and a central platinum(IV) (Pt^{IV}) atom.

1.3.1 Metal−nitrosyl chemistry: sodium nitroprusside

Sodium nitroprusside, $Na_2[Fe^{II}(CN)_5NO]\cdot 2H_2O$, is an excellent model system for nitrosyl (NO) photochemistry in solution. Interest in the photochemistry of SNP began with the presence of two metastable linkage isomers of SNP that are accessible with UV light: $[Fe^{II}(CN)_5(\eta^1\text{-ON})]^{2-}$ (MS1) and $[Fe^{II}(CN)_5(\eta^2\text{-NO})]^{2-}$ (MS2).[13] That is to say, shifting electron density from the iron atom to the nitrosyl ligand induces a rotation of the NO ligand. This phenomenon had been seen in solids at low temperatures ($T < 77$ K) but both MS1 and MS2 had never been observed in solution simultaneously.[14,15] A cartoon of the potential energy surface (PES) governing photochemistry in SNP is presented in Figure

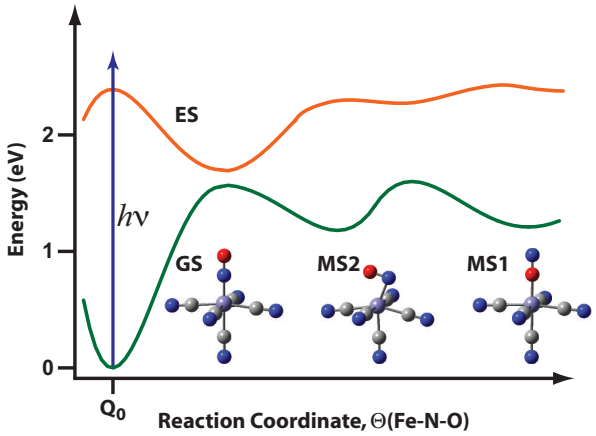

Figure 1.2: Ground (GS) and excited (ES) state potential energy surfaces of SNP adapted from Delley et al.[16] Photoexcitation in the UV/vis region leads to linkage isomerism.

1.2. This figure represents a two-dimensional (2D) slice of a multidimensional PES along the most important reaction coordinate, the Fe−N−O angle (Θ). If we look at the ground state PES (GS), we can see one deep global minimum corresponding to the initial position of the nitrosyl ligand ($\mathbf{Q}_0$), which we call $\Theta = 0$. Upon rotation of the NO ligand, two local minima are present at $\Theta = 90°$ (MS2) and $\Theta = 180°$ (MS1). When we excite the GS with a high-energy photon ($\lambda = 400$ nm $= 3.1$ eV) to the excited state (ES), the nuclei do not move right away (i.e., a vertical transition). Then, progress along $\mathbf{Q}$ begins and proceeds until a so-called conical intersection (CI) is reached at $\mathbf{Q} = \mathbf{Q}_{\mathrm{CI}}$ where the ES is at a minimum in energy. The excited species continues either back to $\mathbf{Q}_0$ or into a local minimum of MS2 (or MS1) where it can live for hundreds of nanoseconds (ns).

The photochemistry of SNP in solution is investigated in Chapter 2, where both MS1 and MS2 are identified in solution at room temperature by their unique NO stretching (ν_{NO}) frequencies.

1.3.2 Mixed-valence chemistry: $Fe^{II}Pt^{IV}Fe^{II}$

The majority of this thesis is focused on a trinuclear mixed-valence (MV) complex of the form $Na_4[(NC)_5Fe^{II}-CN-Pt^{IV}(NH_3)_4-NC-Fe^{II}(CN)_5]$ (denoted as $Fe^{II}Pt^{IV}Fe^{II}$) first synthesized by Bocarsly and coworkers in 1990.[17] By definition this is a mixed-valence complex,

given that it contains metal atoms with different oxidation states. The term "valence" is seldom used to describe the oxidation state of an atom currently, though for historic reasons the term mixed-valence is still used today. The origin of the term dates back to 1915 when the phenomenon was first called "oscillating valency".[18,19] The history of MV complexes is extremely rich.[20,21] The first and probably most famous MV complex is Prussian Blue, which is formally ferric hexacyanoferrate(II) or $Fe^{III}[Fe^{II}(CN_6)]^-$.[22,23] The synthesis of Prussian Blue goes all the way back to 1724, though it was first discovered in 1710.[24–26] More recently (with respect to the 1700s), the chemistry of MV complexes was brought to the forefront in 1969 by Creutz and Taube, who created the so-called Creutz-Taube ion. This molecular ion has the form $[(NH_3)_5Ru(\mu\text{-}C_4H_4N_2)Ru(NH_3)_5]^{5+}$.[22,27] The goal was to learn what fundamental molecular properties govern the rate of inner-sphere electron transfer (ISET) in solution. Taube was quite successful with this endeavor, as he was rewarded the Nobel Prize in Chemistry in 1983 for his efforts.[28] Theoretical aspects of electron transfer were explored by Marcus and Hush, who developed theories to help understand the fundamental properties driving electron transfer in solution.[29,30] The complexity of ISET is brought to the forefront again by this thesis, as still today hundreds of scientists aim to discover what governs ISET in solution.

One of the fundamental questions about mixed-valence systems dating back almost 50 years is what the "actual" oxidation state of the metal is.[19] Using $Fe^{II}Pt^{IV}Fe^{II}$ as an example, is it correct to think of it as $Fe^{2.0}Pt^{4.0}Fe^{2.0}$, $Fe^{2.66}Pt^{2.66}Fe^{2.66}$, $Fe^{2.1}Pt^{3.8}Fe^{2.1}$, or something in between? In 1967, Robin and Day came up with a classification scheme to identify these three limiting cases.[31] Class I is the limiting case where the valences are trapped (i.e., localized) on the metal atoms, which is the assumption made when writing $Fe^{II}Pt^{IV}Fe^{II}$ (for example). An example of such a compound is Pb_3O_4.[19] Class II is an intermediate case where the charge is mostly localized but there is some mixing (e.g., $Fe^{2.1}Pt^{3.8}Fe^{2.1}$). A good example of a molecule in Class II is Prussian Blue. Class III is the other limiting case where the valences are completely delocalized. The famous Creutz-Taube ion falls into this Class of mixed-valence compounds, as it has been shown that the average oxidation state of each of the ruthenium (Ru) atoms is $Ru^{2.5+}$. A natural first question when studying a mixed-valence complex is what class the molecule is in, as this is crucial

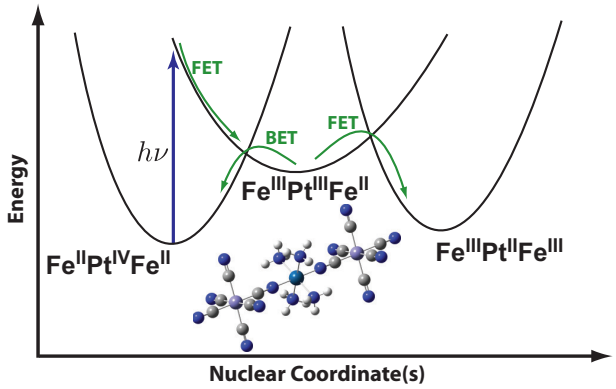

Figure 1.3: $Fe^{II}Pt^{IV}Fe^{II}$ PES illustrating forward-electron transfer (FET) and back-electron transfer (BET) adapted from Pfennig and Bocarsly.[32]

for understanding the electronic absorption spectrum of the molecule.

The mixed-valence complex $Fe^{II}Pt^{IV}Fe^{II}$ studied in this thesis has been shown to fall under the Robin and Day Class II classification by Pfennig et al. who determined this using Marcus-Hush theory.[30,32] This molecule was initially chosen as a model system for one-photon two-electron transfer chemistry, whereby one incident photon leads to a net two electron transfer reaction. A cartoon of the PES governing $Fe^{II}Pt^{IV}Fe^{II}$ is shown in Figure 1.3. When a $\lambda = 424$ nm photon is incident on $Fe^{II}Pt^{IV}Fe^{II}$, vertical excitation puts the system into a highly excited charge-transfer state (CTS) given by $Fe^{III}Pt^{III}Fe^{II}$ or $Fe^{II}Pt^{III}Fe^{III}$ (they are equivalent). From the CTS, 99% of the population undergoes back-electron transfer (BET) to form a "hot" electronic ground state. The remaining 1% undergoes a second, thermally induced forward-electron transfer (FET) reaction to form $Fe^{III}Pt^{II}Fe^{III}$. This molecule is highly unstable and immediately dissociates into two equivalents of $[Fe(CN)_6]^{3-}$ and $[Pt(NH_3)_4]^{2+}$.[17,32] The very low yield of the second FET step makes it difficult to measure experimentally; however, it turns out that the BET step and subsequent vibrational relaxation is extremely interesting and complicated, as will be discussed in great detail in Chapter 4. In brief, relaxation down to the bottom of the $Fe^{II}Pt^{IV}Fe^{II}$ well proceeds along a 4-dimensional (at least) PES defined by four high-frequency ν_{CN} modes.

1.3.3 The effect of high-frequecy vibrational modes on electron transfer

The role high-frequency vibrational modes have on electron transfer reactions was a very hot topic in the late 1970s and early 1980s.[33–37] At the time, the fundamental idea behind the rate of outer-sphere electron transfer (OSET) reactions between separate donor and acceptor molecules was Marcus theory, whereby the reaction coordinate was simplified to a one-dimensional classical solvent mode. In this manner, the activation energy for the reaction is related to the driving force of the reaction (ΔG°) and the outer-sphere solvent reorganization energy (λ_o) by[29]

$$\Delta G_o^\ddagger = \frac{(\lambda_o + \Delta G^\circ)^2}{4\lambda_o}, \tag{1.1}$$

where $\Delta G_o^\ddagger$ is the activation energy. By varying ΔG° from large positive to negative values, three regions can be achieved: the normal region ($\Delta G^\circ > -\lambda_o$), $\Delta G_o^\ddagger = 0$ ($\Delta G^\circ = -\lambda_o$), and the inverted region ($\Delta G^\circ < -\lambda_o$). The rate of activation is calculated by

$$k_{act} = A \exp\left(-\frac{\Delta G_o^\ddagger}{RT}\right), \tag{1.2}$$

where the exponential term represents the probability of forming the transition state and A contains the probability of forming the product species.

Studies have shown that high-frequency vibrational modes are especially important in predicting k_{act} in the so-called Marcus inverted region. In other words, ISET reaction dynamics must be considered to correctly predict the rate of the electron transfer. Thus the reorganization energy is broken up into two components (outer- and inner-sphere) such that $\lambda_{total} = \lambda_o + \lambda_i$. These reorganization energies can be separated into the role of the solvent (λ_o) and intramolecular vibrational modes (λ_i). A detailed review of electron transfer dynamics in the condensed phase is out of the scope of this thesis; however, the concept of ISET and OSET is quite relevant. The role that high-frequency vibrations play in charge transfer reactions in solution is a common theme in this thesis. In addition,

the role of the solvent will be addressed at every step along the way. In that sense, this thesis aims to directly measure the important coordinates in both λ_{i} and λ_{o}. A central question is can one combine electronic and vibrational spectroscopy to unearth specific reaction coordinates that activate (or deactivate) a charge transfer reaction pathway? Can outer- and inner-sphere reorganization energies then be written as $\lambda_{\mathrm{o}}(\mathbf{Q}_1, \mathbf{Q}_2, \ldots, \mathbf{Q}_N)$ and $\lambda_{\mathrm{i}}(\mathbf{Q}'_1, \mathbf{Q}'_2, \ldots, \mathbf{Q}'_N)$? Such "multidimensional reaction coordinates" represent the "holy grail" to many spectroscopists alike.

1.4 Femtosecond Multidimensional Spectroscopy

Photochemical reactions in solution at room temperature are very fast and can occur in less than 100 millionth-of-a-billionth seconds (s), or 100 femtoseconds (fs) where 1 fs $= 10^{-15}$ s. This is on the order of the time scale of a molecular vibration, as the frequency range of vibrations in solution is generally $50-3500$ cm^{-1} ($1.5-105$ THz) which corresponds to a vibrational period (T) of $10-680$ fs. Throughout this thesis the terms "high-frequency vibration" and "low-frequency vibration" will be used, where a high-frequency vibration is considered >1500 cm^{-1} and a low-frequency vibration is less than 1000 cm^{-1}. Vibrational energy relaxation also occurs on the femtosecond to picosecond time scale (1 ps $= 1000$ fs $= 10^{-12}$ s). There back-of-the-envelope calculations show why vibrations are an excellent probe of photochemical reactions, as they occur on roughly the same time scale. In addition, many high-frequency vibrations are localized in space such that spatial information (i.e., the flow of energy from point A to point B) can be inferred from the probed vibrations.

At first glance, the phrase "femtosecond multidimensional spectroscopy" may appear to be one technique; however, it is more accurate to consider it as a tool box from which many different tools can be selected. Tools used in this thesis include dispersed visible$-$infrared and infrared$-$infrared pump$-$probe, vibrational echo peak shift, and two-dimensional infrared spectroscopies. Non-equilibrium (i.e., transient) analogs of these tools are used as well, including transient dispersed pump$-$probe and transient dispersed vibrational echo spectroscopies, in order to obtain information gained from these techniques of electronic excited state. In all cases, analysis of the experimental data consists of correlating variables, such as a time delay to a vibrational frequency or an excited frequency to a probed

frequency. These correlations are important for obtaining a molecular-level description of ultrafast photoinduced charge transfer in solution and will aid in the development of energy-harvesting materials.

1.5 Thesis Outline

The body of work presented in this thesis describes how many novel femtosecond multi-dimensional spectroscopies can be used to correlate electron and nuclear motion. These spectroscopies rely on the effect an external perturbation has on molecular vibrations in solution. Chapter 2 looks at the case of sodium nitroprusside where a UV pulse induces linkage isomerization of a nitrosyl ligand, which is essentially a rotation of nuclei with respect to a metal center. From there we move into mixed-valence chemistry, where in Chapter 3 the perturbation is an infrared pulse exciting four CN stretching vibrations that are subsequently probed a given time later. We are able to use the molecular insight gained in Chapter 3 to assign optically induced states in Chapter 4. Chapter 5 describes the development of a new spectroscopy that combines the techniques used in Chapters 2 and 4 with 2D IR described in Chapter 3, creating a fifth-order visible−infrared spectroscopy that we call transient heterodyne-detected dispersed vibrational echo spectroscopy (t-HDVE). This technique is then applied to $Fe^{II}Pt^{IV}Fe^{II}$ in Chapter 6, where detailed information about vibrational relaxation on electronic excited states is gained. Finally, a novel infrared−Raman technique is developed in Chapter 7, where Raman modes are detected by probing with a UV/visible pulse. The goal of this experiment is to measure the Raman spectrum of a molecule after it has been coherently excited by IR light in order obtain detailed information about the coupling of IR and Raman vibrational modes.

REFERENCES

[1] Schreier, W. J.; Schrader, T. E.; Koller, F. O.; Gilch, P.; Crespo-Hernández, C. E.; Swaminathan, V. N.; Carell, T.; Zinth, W.; Kohler, B. *Science* **2007**, *315*, 625–629.

[2] Middleton, C. T.; de La Harpe, K.; Su, C.; Law, Y. K.; Crespo-Hernández, C. E.; Kohler, B. *Annu. Rev. Phys. Chem.* **2009**, *60*, 217–239.

[3] Kohler, B. *J. Phys. Chem. Lett.* **2010**, *1*, 2047–2053.

[4] de La Harpe, K.; Kohler, B. *J. Phys. Chem. Lett.* **2011**, *2*, 133–138.

[5] Xiong, W.; Laaser, J. E.; Paoprasert, P.; Franking, R. A.; Hamers, R. J.; Gopalan, P.; Zanni, M. T. *J. Am. Chem. Soc.* **2009**, *131*, 18040–18041.

[6] Pensack, R. D.; Banyas, K. M.; Asbury, J. B. *IEEE J. Select. Topics Quantum Electron.* **2010**, *16*, 1776–1783.

[7] Tang, J.; Kemp, K. W.; Hoogland, S.; Jeong, K. S.; Liu, H.; Levina, L.; Furukawa, M.; Wang, X.; Debnath, R.; Cha, D.; Chou, K. W.; Fischer, A.; Amassian, A.; Asbury, J. B.; Sargent, E. H. *Nat. Mater.* **2011**, *10*, 765–771.

[8] Jeong, K. S.; Tang, J.; Liu, H.; Kim, J.; Schaefer, A. W.; Kemp, K.; Levina, L.; Wang, X.; Hoogland, S.; Debnath, R.; Brzozowski, L.; Sargent, E. H.; Asbury, J. B. *ACS Nano* **2012**, *6*, 89–99.

[9] Pensack, R. D.; Guo, C.; Vakhshouri, K.; Gomez, E. D.; Asbury, J. B. *J. Phys. Chem. C* **2012**, *116*, 4824–4831.

[10] Born, M.; Oppenheimer, J. R. *Ann. Phys.* **1927**, *84*, 457.

[11] Trommsdorf, J. B. *Ann. Chem. Pharm.* **1834**, 11.

[12] Natarajan, A.; Tsai, C. K.; Khan, S. I.; McCarren, P.; Houk, K. N.; Garcia-Garibay, M. A. *J. Am. Chem. Soc.* **2007**, *129*, 9846–9847.

[13] Coppens, P.; Fomitchev, D.; Carducci, M.; Culp, K. *J. Chem. Soc., Dalton Trans.* **1998**, 865–872.

[14] Güida, J. A.; Aymonino, P. J.; Piro, O.; Castellano, E. *Spectrochim. Acta A* **1993**, *49*, 535–542.

[15] Chacón Villalba, M. E.; Güida, J. A.; Varetti, E. L.; Aymonino, P. J. *Inorg. Chem.* **2003**, *42*, 2622–2627.

[16] Delley, B.; Schefer, J.; Woike, T. *J. Chem. Phys.* **1997**, *107*, 10067–10074.

[17] Zhou, M.; Pfennig, B. W.; Steiger, J.; Vanengen, D.; Bocarsly, A. B. *Inorg. Chem.* **1990**, *29*, 2456–2460.

[18] Hofmann, K. A.; Hschele, K. *Ber. Deut. Chem. Ges.* **1915**, *48*, 20–28.

[19] Day, P.; Hush, N. S.; Clark, R. J. *Phil. Trans. R. Soc. A* **2008**, *366*, 5–14.

[20] Allen, G. C.; Hush, N. S. *Prog. Inorg. Chem.* **1967**, *8*, 357–390.

[21] Hush, N. S. *Prog. Inorg. Chem.* **1967**, *8*, 391–444.

[22] Creutz, C.; Taube, H. *J. Am. Chem. Soc.* **1969**, *91*, 3988–3989.

[23] Robin, M. B. *Inorg. Chem.* **1962**, *1*, 337–342.

[24] Woodward, J. *Philos. Trans. R. Soc.* **1724**, *33*, 15–17.

[25] Brown, J. *Philos. Trans. R. Soc.* **1724**, *33*, 17–24.

[26] Kraft, A. *Bull. Hist. Chem.* **2008**, *33*, 61–67.

[27] Creutz, C.; Taube, H. *J. Am. Chem. Soc.* **1969**, *91*, 3988–3989.

[28] Taube, H.; Myers, H.; Rich, R. L. *J. Am. Chem. Soc.* **1953**, *75*, 4118–4119.

[29] Marcus, R. A. *J. Chem. Phys.* **1956**, *24*, 966–978.

[30] Hush, N. S. *Trans. Faraday Soc.* **1961**, *57*, 557–580.

[31] Robin, M. B.; Day, P. *Adv. Inorg. Chem. Radiochem.* **1967**, *10*, 247–422.

[32] Pfennig, B. W.; Bocarsly, A. B. *J. Phys. Chem.* **1992**, *96*, 226–233.

[33] Bixon, M.; Jortner, J. *Faraday Discuss. Chem. Soc.* **1982**, *74*, 17.

[34] Newton, M. D.; Sutin, N. *Annu. Rev. Phys. Chem.* **1984**, *35*, 437–480.

[35] Marcus, R. A.; Sutin, N. *Biochim. Biophys. Acta* **1985**, *811*, 265–322.

[36] Jortner, J.; Bixon, M. *J. Chem. Phys.* **1988**, *88*, 167–170.

[37] Barbara, P. F.; Walker, G. C.; Smith, T. *Science* **1992**, *256*, 975–981.

Chapter 2

PROBING THE PHOTOINDUCED METAL−NITROSYL LINKAGE ISOMERISM OF SODIUM NITROPRUSSIDE IN SOLUTION USING TRANSIENT INFRARED SPECTROSCOPY

The work presented in this chapter has been published in the following article:
Lynch, M.S.; Cheng, M.; Van Kuiken, B.E.; Khalil, M. "Probing the Photoinduced Metal−Nitrosyl Linkage Isomerism of Sodium Nitroprusside in Solution Using Transient Infrared Spectroscopy," *J. Am. Chem. Soc.* **2011**, *133*, 5255.

We study photoinduced metal−nitrosyl linkage isomerism in sodium nitroprusside (SNP, $Na_2[Fe^{II}(CN)_5NO]\cdot 2H_2O$) dissolved in methanol using picosecond transient infrared (IR) spectroscopy. The high sensitivity of this technique allows the simultaneous observation of two known metastable (MS) iron−nitrosyl linkage isomers of SNP, $[Fe^{II}(CN)_5(\eta^1\text{-ON})]^{2-}$ (MS1) and $[Fe^{II}(CN)_5(\eta^2\text{-NO})]^{2-}$ (MS2) at room temperature. The transient population of free nitrosyl radicals (NO·) is also measured in the sample solution. These three transient species are detected using their distinct nitrosyl stretching frequencies at 1794 cm^{-1} (MS1), 1652 cm^{-1} (MS2) and 1851 cm^{-1} (NO·). The metastable isomers and NO· are formed on a sub-picosecond timescale and have lifetimes greater than 100 ns. A UV (400 nm)−pump power dependence study reveals that MS1 can be formed with one photon, while MS2 requires two photons to be populated at room temperature in solution. Other photodissociation products including cyanide ion, Prussian Blue and $[Fe^{III}(CN)_5(CH_3OH)]^{2-}$ are observed. We develop a photochemical kinetic scheme to model our data and the analysis reveals that photoisomerization and photodissociation of the metal−NO moiety are competing photochemical pathways in SNP dissolved in methanol at room temperature. Based on the analysis, the solvent-associated Fe(III) species and Prussian Blue form on a 130 ps and 320 ps timescale respectively. The simultaneous detection and characterization of photoinduced linkage isomerism (MS1 and MS2) and photodissociation of the metal−NO bond

in SNP highlights the importance of understanding the role played by metastable metal-nitrosyl linkage isomers in the photochemistry of metal−nitrosyl compounds in chemistry and biology.

2.1 Introduction

Photoinduced linkage isomerism in metal−nitrosyl compounds is a rich field of study in which irradiation of the sample by light causes the nitrosyl ligand to bond to the metal center in multiple ways.[1–5] There are three limiting binding forms of the metal−nitrosyl moiety. The metal−NO species with the nitrogen atom bound to the metal is observed in the electronic ground state (GS). Upon photoexcitation, the nitrosyl ligand can rotate by 180° to form the metal−ON (isonitrosyl) species or by 90° to form the η^2-NO ligand bound to the metal in a side-on geometry as illustrated in Figure 2.1. To date, photoinduced linkage isomerism has been documented in several transition metal−nitrosyl species, and there is great interest in understanding how the metal−NO coordination of these species relates to the overall photochemistry of the compound including NO release pathways.[6–9] Studies on nitrosyl porphyrins and nitrosyl heme proteins have also discovered metastable linkage isomers, underlining the importance of understanding the role played by metal−nitrosyl isomers in nitric oxide signaling pathways in biological systems.[10–15]

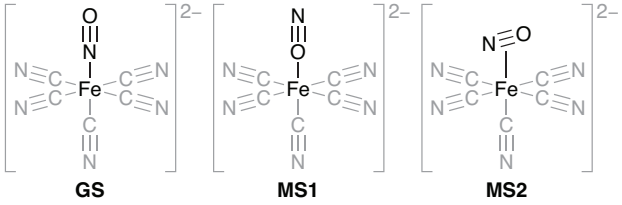

Figure 2.1: Structure of the GS, MS1 and MS2 of the nitroprusside ion highlighting Fe−NO linkage isomerism.

Sodium nitroprusside (SNP, $Na_2[Fe^{II}(CN)_5NO]\cdot 2H_2O$) is a prototypical system for studying photoinduced metal−nitrosyl linkage isomerism. Approximately thirty years ago, SNP was found to exhibit at least two long-lived electronic excited states following photoexcitation with 350−580 nm radiation.[16,17] The exact nature of these photoinduced metastable

states (MS) remained unknown until Coppens and co-workers identified and characterized two unique MS linkage isomers formed upon photoexcitation of a single crystal of SNP using low-temperature X-ray crystallography.[18–20] One of the linkage isomers contained an isonitrosyl group (MS1) while the other involved an η^2-NO ligand (MS2) bound to the iron core (Figure 2.1). The discovery of photoinduced linkage isomerism occurring in crystalline SNP generated significant interest for its use in high capacity optical storage devices due to the large change of refractive index upon irradiation with light.[5,21–27] Along with creating metastable linkage isomers, the photoexcitation of SNP can result in the dissociation of the nitrosyl ligand. This property is utilized in the medical community where aqueous SNP is used as an NO delivery agent in extreme hypertensive emergencies.[28–31]

Given its possible uses, photoinduced linkage isomerism in SNP has garnered intense experimental and theoretical attention over the past decades as summarized in several recent reviews.[1,5,32] The experimental study of photoinduced linkage isomerism has mainly focused on the solid state where the metastable species can be trapped at low temperatures and subsequently characterized with steady-state spectroscopic and structural probes.[20,33–43] An exception to this is work by Schaniel et al. where nanosecond transient absorption experiments on SNP in aqueous solutions detected the formation of MS2 with a lifetime of ∼110 ns.[44] Experiments photoexciting aqueous solutions of SNP with continuous wave radiation have shown the formation of several dissociation products including NO·, CN^-, $[Fe^{II}(CN)_5(H_2O)]^{2-}$ and Prussian Blue.[45–48] Theoretical works have calculated the electronic absorption spectra of the GS, MS1 and MS2 species and have considered the energetics of photoinduced linkage isomerism occurring on a multidimensional potential energy surface.[43,49–55] The theoretical studies along with the trapping of the linkage isomers using light of different wavelengths have suggested that the formation of MS1 and MS2 requires more than one photon depending on the experimental temperature.[20,54]

Despite the rich history of studying SNP, important questions remain unanswered regarding the formation of photoinduced metastable states in solution. Can both MS1 and MS2 be populated at room temperature in solution? What are their lifetimes? What role do the linkage isomers play in the photogeneration of NO radical and other photodissociation products? The goal of this study is to answer the questions listed above and provide

a detailed understanding of the photochemistry of SNP in solution at room temperature, which is currently lacking.

In this Chapter, we use picosecond transient infrared (IR) spectroscopy to probe the photoinduced linkage isomers and related photoproducts of SNP generated at room temperature with a 400 nm pump pulse. The photoinduced MS1 and MS2 species have nitrosyl stretching frequencies distinct from the ground state of SNP allowing us to probe their structural dynamics on a picosecond timescale. We directly observe the formation of both MS1 and MS2 linkage isomers of SNP at room temperature in a methanol solution and find that their lifetimes are greater than 100 ns. The 400 nm pump power dependence reveals that MS1 is formed via a one-photon process while the formation of MS2 requires two photons. In addition to Fe−NO linkage isomers, photodissociation products including free nitrosyl radical (NO·), cyanide ion (CN^-), Prussian Blue (PB) and $[Fe^{III}(CN)_5(CH_3OH)]^{2-}$ are observed and their picosecond dynamics are measured. We construct a photochemical model based on our data which reveals that photoinduced linkage isomerism and photodissociation of the nitrosyl ligand are competing photochemical pathways when SNP is dissolved in methanol at room temperature.

2.2 Materials and Methods

2.2.1 Materials

All chemical samples were purchased from Sigma-Aldrich Co. and used without further purification. Solutions of SNP dissolved in methanol were prepared under ambient conditions (295 K) to concentrations of 120 mM or 60 mM for experiments in the NO (1600−2000 cm^{-1}) or CN (2000−2200 cm^{-1}) stretching regions, respectively. Figure 2.2 shows the UV/vis and FTIR spectra of SNP in methanol. The optical absorption spectrum of SNP displays two resonances at 393 nm and 520 nm assigned as the $7e \leftarrow 6e$ [$\pi^*(NO) \leftarrow 3d_{xz,yz}$] and $7e \leftarrow 2b_2$ [$\pi^*(NO) \leftarrow 3d_{xy}$] transitions, respectively.[43,49] The UV/vis spectrum was obtained using a JASCO V-630 spectrometer with 1 nm resolution. The solvent-subtracted FTIR spectrum of SNP in methanol shows peaks corresponding to the nitrosyl stretch (ν_{NO}) and the cyanide stretches (ν_{CN}) centered at 1909 cm^{-1} ($\epsilon = \int \epsilon_\nu d\nu = 3.3 \times 10^4$ M^{-1} cm^{-2})

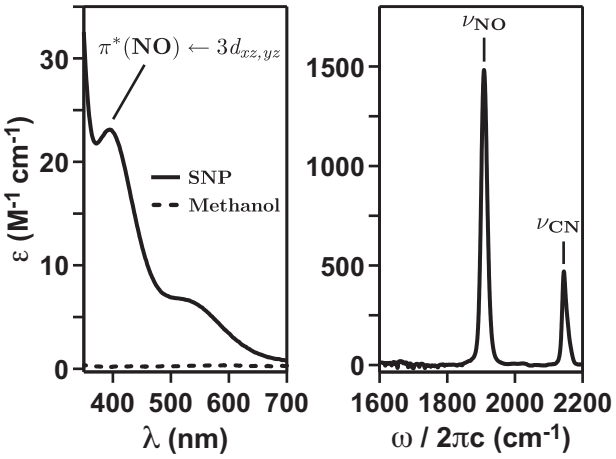

Figure 2.2: (Left) UV/Vis spectra of SNP in methanol (solid line) and neat methanol (dashed line) at T = 295 K. (Right) Solvent-subtracted FTIR spectrum of SNP dissolved in methanol. The center frequencies for ν_{NO} and ν_{CN} are respectively 1909 cm^{-1} and 2145 cm^{-1}.

and 2145 cm^{-1}. The asymmetric ν_{CN} band contains contributions from multiple IR active modes corresponding to the C_{4v} symmetry of the molecule,[56] with an E mode centered at 2144 cm^{-1} ($\epsilon = 4.8 \times 10^3$ M^{-1} cm^{-2}) and A_1 modes centered at 2155 cm^{-1} ($\epsilon = 3.7 \times 10^3$ M^{-1} cm^{-2}). The IR spectrum was obtained using a JASCO FT/IR-4100 spectrometer with 2 cm^{-1} resolution.

2.2.2 Transient infrared spectroscopy

The experiment is performed in a pump−probe geometry. The optical pump and the IR probe pulses are derived from the output of a commercial Spectra Physics regenerative amplifier ($\lambda = 800$ nm, $\Delta t = 35$ fs, $P = 3$ W).

The 400 nm pump pulse is generated by frequency doubling ∼1 W of the 800 nm pulse in a 0.5 mm BBO crystal. To minimize multiphoton effects in the solvent and nonlinear processes on the sample windows, the pulse is stretched to ∼850 fs by passage through 5.5 cm of fused silica. The pump pulse energy at the sample is ∼40 μJ (80 μJ) over a focal spot-size of ∼430 μm (500 μm) resulting in a pump fluence of ∼28 $\mathrm{mJ/cm}^2$ (∼41 $\mathrm{mJ/cm}^2$) for experiments probing the NO (CN) regions. The polarization and input energy

of the pump pulse is controlled using a half-waveplate and a calcite polarizer. The mid-IR probe pulse is obtained by sending ∼1 W of the 800 nm light to pump a two-pass optical parametric amplifier. The signal and idler fields are then difference-frequency mixed in a 0.5 mm $AgGaS_2$ crystal to produce ∼60 fs mid-IR pulses with spectral bandwidths greater than 250 cm^{-1} at center wavelengths of 4.6 μm and 5.6 μm. The IR probe is focused to a spot size of 190 μm at the sample with an energy of ∼0.5 μJ per pulse. The pump and probe pulses spatially and temporally overlap at the sample that is held between two 1 mm thick CaF_2 windows with a 50 μm Teflon spacer in a home-built flow cell. A sample volume of 60 mL is mechanically pumped through the cell at rate of ∼1 m/s, and the sample cell is translated in the sample plane at 0.125 mm/s. A computer-controlled translation stage in the pump arm controls the relative time delay between the UV-pump and IR-probe with a maximum time delay of 500 ps. The polarization of the pump pulse is set to magic angle (54.7°) with respect to the probe pulse to selectively sample the isotropic vibrational dynamics. Transient IR difference spectra are collected with a mechanical chopper operating at 500 Hz in the pump arm. A portion of the probe field is split to create a reference field used for performing shot-to-shot normalization of the IR intensity fluctuations. After the sample, the pump is blocked and the vertically displaced probe and reference fields are sent through a 190 mm spectrometer. The signal is detected at the focal plane of a 2×64 element HgCdTe array IR detector with a spectral resolution of ∼4 cm^{-1} (3 cm^{-1}) across the NO (CN) spectral regions. Our instrument response time is ∼1 ps. The signals are averaged over 2500 laser shots and each kinetic trace is averaged $7-30$ times depending on the signal level. This apparatus detects differences in optical density as low as 40 μOD. Error in the data is shown at the 95% confidence level unless otherwise stated. The kinetic traces shown in Figures 2.3b and 2.4b are obtained by summing over the full-width at half-maximum (fwhm) of the transient spectral lineshapes.

2.3 Results

2.3.1 NO stretching region ($1600 - 2000$ cm^{-1})

Figure 2.3a shows time-resolved difference spectra of 120 mM SNP in methanol on a picosecond timescale in the NO stretching region at various pump−probe time delays. The spectra consist of several positive spectral features corresponding to transient photoproducts formed upon photoexcitation at 400 nm. We observe the transient infrared absorbance of the nitrosyl stretch (ν_{NO}) for the MS1 and MS2 photoinduced linkage isomers at 1794 cm^{-1} and 1652 cm^{-1} respectively. The assignments are based on previously reported ν_{NO} downshifts of approximately 100 cm^{-1} and 250 cm^{-1} with respect to the GS for MS1 and MS2 respectively, in SNP and other metal−nitrosyl species at low temperatures.[4,40,41]

Along with the metastable linkage isomers, we observe nitrosyl radical (NO·) generation with the presence of a transient absorption at 1851 cm^{-1}. This frequency corresponds to the stretching frequency of NO· and has a Gaussian line width of 23 cm^{-1}. We assign this frequency based on previous work of NO· in aqueous solutions.[57] The transient absorption from the ν_{NO} overtone ($v = 2 \leftarrow v = 1$) of the GS of SNP peaks at 1881 cm^{-1}, as it is downshifted by the vibrational anharmonicity of 28 cm^{-1} for the NO stretch.[58] A negative spectral feature at 1909 cm^{-1} corresponding to the bleach of the GS species is shown in Figure 2A.1 in the appendix.

Figure 2.3b displays the measured dynamics of the photochemically generated transient species MS1, MS2 and NO·. The black solid lines are fits to the data with a sum of three exponential functions. The complete results from the fits are tabulated in Table 2A.1 in the appendix. All transient species exhibit an initial biexponential decay with ∼3 ps and ∼12 ps time constants. We attribute these timescales to the decay of the resonant solvent (see Figure 2A.2) and the non-resonant CaF_2 window response following photoexcitation of the sample at 400 nm. We measure the same time constants (grey triangles in Figure 2.3b at $\omega = 1909$ cm^{-1}) when we excite a sample containing only methanol with all other experimental conditions remaining the same.

The lifetimes of the photoinduced metastable states and NO· at room temperature in solution are found to be greater than 100 ns as given by the third time constant extracted

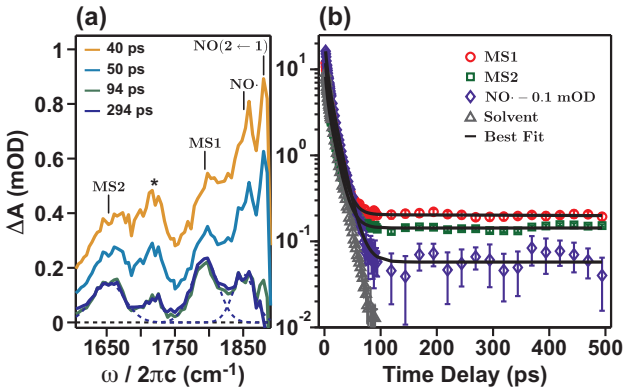

Figure 2.3: (a) Picosecond transient IR spectra of SNP in methanol in the NO stretching region at four pump-probe time delays. The peak labeled NO($2 \leftarrow 1$) refers to the transient absorption of the NO overtone in the GS. Dotted lines are Gaussian fits of MS1 ($\omega_c = 1794$ cm^{-1}), MS2 ($\omega_c = 1652$ cm^{-1}) and NO· ($\omega_c = 1851$ cm^{-1}) IR lineshapes at a time delay of 294 ps. Here ω_c refers to the central frequency of the Gaussian lineshapes. The feature marked with an asterisk is due to solvent background. (b) Kinetics in the NO stretching region with best fit. The NO radical has been shifted by -0.1 mOD for clarity.

from the fits.[59] This long time constant is consistent with the work of Schaniel et al. who found that MS2 decays on a 110 ± 10 ns timescale when an aqueous SNP solution is pumped at 532 nm.[44] However, they were not able to detect the presence of MS1 species in their experiment. The ν_{NO} bleach of the GS shows no recovery on the timescale of the experiment, while the ν_{NO} overtone of the GS relaxes back to the vibrational ground state on a 32 ± 7 ps timescale (see Figure 2A.1).

2.3.2 CN stretching region ($2000 - 2200$ cm^{-1})

Figure 2.4a displays transient IR spectra following the photoexcitation of 60 mM SNP dissolved in methanol in the CN stretching region at various pump− probe time delays. The transient spectra show four positive features at 2083 cm^{-1}, 2100 cm^{-1}, 2123 cm^{-1}, and 2133 cm^{-1} corresponding to various photoproducts that absorb in the CN region. The largest transient feature in Figure 2.4a at 2123 cm^{-1} grows as a function of the pump−probe time delay. This is the CN stretch frequency (ν_{CN}) of $[Fe^{III}(CN)_5(CH_3OH)]^{2-}$, which is generated as a result of NO dissociation and subsequent solvent association at the vacant site.[47] The

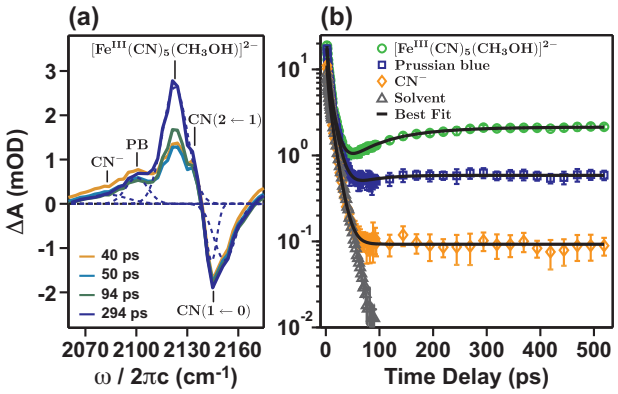

Figure 2.4: (a) Time-resolved IR absorption spectra of SNP in methanol in the CN stretching region at four time delays. Dotted lines are Gaussian fits of CN^- (ω_c = 2083 cm^{-1}), PB (ω_c = 2100 cm^{-1}) and $[Fe^{III}(CN)_5(CH_3OH)]^{2-}$ (ω_c = 2123 cm^{-1}) at a time delay of 294 ps. The CN bleach [CN(1 ← 0)] has been fit using the FTIR spectrum of SNP in methanol (Fig. 2.2). The peak labeled CN(2 ← 1) refers to the transient absorption of the CN overtone of the GS. (b) Kinetics in the CN stretching region with best fit.

transient feature at 2100 cm^{-1} corresponds to the ν_{CN} of the mixed valence compound Prussian Blue.[60] The transient spectral feature at 2083 cm^{-1} is the CN stretching frequency of the free cyanide ion (CN^-).[61]

The dynamics of the transient species in the CN stretching region are shown in Figure 2.4b. The solid lines are fits to a sum of two decaying and one rising exponential function. For the detailed list of kinetic parameters see Table 2A.3. As in the NO stretching region, there is an initial biexponential decay of ∼3 ps and ∼12 ps time scale resulting from resonant solvent and non-resonant CaF_2 window response (grey triangles in Figure 2.4b at ω = 2145 cm^{-1}). It is clear from Figure 2.4b that the transient populations of both $[Fe^{III}(CN)_5(CH_3OH)]^{2-}$ and PB are increasing with time. In the case of the cyanide ion, any rise is within the error of the experiment. The data for the solvent-associated species $[Fe^{III}(CN)_5(CH_3OH)]^{2-}$ is fit with a rise time of 95 ± 9 ps, which represents the time scale of a diffusion-limited solvent association process.[62] The transient population of all species remains constant on the timescale of our measurement as seen by the long-time offset.

Note that we do not see signatures of the photoinduced linkage isomers in the CN stretching region. This is because the ν_{CN} in MS1 and MS2 is expected to downshift by

only ∼10 cm^{-1} with respect to the ground state.[39–41] Given the spectral congestion of other photoproducts in that region and the very small concentration of MS1 and MS2, we do not expect to observe the peaks corresponding to MS1 and MS2 in the CN stretching region.

2.3.3 UV-pump power dependence

To determine whether the formation of the photoinduced linkage isomers is a result of one- or two-photon processes, we perform a UV-pump power dependence in the NO stretching region over a 400 nm pump fluence range of 14−52 mJ/cm^2. The results are shown in Figure 2.5 where the area of the transient peaks is graphed versus the excitation fluence on a log−log scale plot. Here the slope (m) of the best-fit line indicates whether the species is formed by a one- ($m = 1$) or two- ($m = 2$) photon process. A slope between 1 and 2 represents a combination of both processes.[63] The data reveals that MS1 is formed via a one-photon mechanism ($m = 0.9 \pm 0.1$), whereas MS2 is formed via a two-photon process ($m = 1.9 \pm 0.2$). Free nitrosyl radical is formed from a combination of both one- and two-photon processes ($m = 1.4 \pm 0.2$).

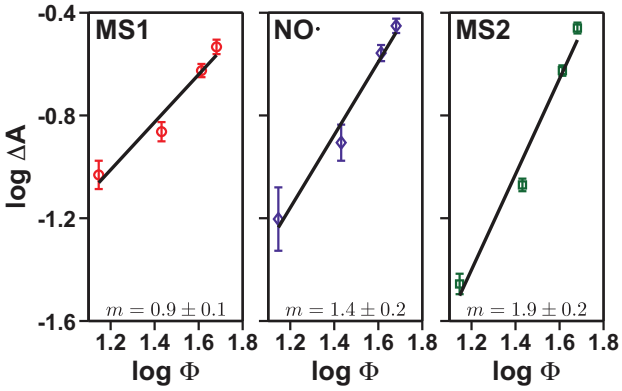

Figure 2.5: UV-pump power dependence of transients in the NO stretching region (MS1, MS2, NO·) at a time delay of 500 ps presented on a log−log scale plot of transient IR absorption signal (ΔA) vs. fluence (Φ, mJ/cm^2). Slope (m) error is shown as the standard error of the linear fit.

2.3.4 Extracting the integrated molar absorption coefficient for the nitrosyl stretch of MS1, MS2, and NO radical

Given the low oscillator strength of the $7e \leftarrow 6e$ [π^*(NO) $\leftarrow 3d_{xz,yz}$] metal-to-ligand charge transfer (MLCT) transition at 400 nm ($\epsilon_{400\text{ nm}} \approx 23$ M^{-1} cm^{-1}), the total photoexcitation yield of SNP is ~2% even at the relatively high fluence used in this experiment. The population of the metastable states accounts for less than 0.1% of the total quantum yield. The photodissociation of SNP leading to nitrosyl radical generation is the dominant photochemical pathway which is consistent with previous studies.[45,47,48]

The molar absorption coefficients of the NO stretches for the MS linkage isomers are estimated by taking the ratio of oscillator strengths of GS, MS1 and MS2 calculated using Gaussian 03 and normalizing them with the experimentally obtained value for the GS.[64,65] Based on these estimates, we calculate the transient concentrations of MS1, MS2 and NO· at long delay times to be 0.047 mM, 0.040 mM and 1.2 mM, respectively. The integrated molar absorption coefficients for MS1 and MS2 are found to be $\epsilon_{\text{MS1}} = 4.4 \pm 0.3 \times 10^4$ M^{-1} cm^{-2} and $\epsilon_{\text{MS2}} = 2.0 \pm 0.1 \times 10^4$ M^{-1} cm^{-2}, respectively. See the appendix for more computational details. The infrared spectrum of the free NO radical is difficult to isolate in solution at room temperature because of its propensity to dimerize at low concentrations.[66] Therefore, the characterization of the vibrational spectrum of NO radical in solution has eluded researchers. A recent study has predicted the integrated absorption coefficient for ν_{NO} of the NO radical to be 200 M^{-1} cm^{-2} in solution.[67] The data collected in this experiment allows a direct estimate of the integrated absorption coefficient of ν_{NO} of NO· in methanol to be $\nu_{\text{NO}\cdot} = 170 \pm 20$ M^{-1} cm^{-2}.

2.4 Discussion

Most experiments probing metal−nitrosyl linkage isomerism in SNP have been done at very low temperatures to trap the photoinduced metastable states for characterization with X-ray crystallography and various spectroscopies. On the other hand, the generation of NO radical and CN^- following the irradiation of aqueous SNP with continuous-wave light has been studied at room temperature. This work brings these two disparate experimental

camps together by performing a detailed time-resolved investigation of the photochemistry of SNP dissolved in methanol at room temperature using picosecond transient infrared spectroscopy.

2.4.1 Transient IR spectra of the ν_{NO} of MS1, MS2 and NO radical

For the first time, both metal−nitrosyl linkage isomerism and nitrosyl radical generation has been simultaneously observed at room temperature in solution. Table 2.1 lists a comparison of the nitrosyl stretching frequencies of the linkage isomers of SNP and the photogenerated NO radical under different experimental conditions.

Table 2.1: Nitrosyl stretching frequencies in cm^{-1} for SNP under different experimental conditions and integrated molar absorptivities ($\epsilon \times 10^{-2}$, M^{-1} cm^{-2}) from this work.

T (K)	GS	MS1	MS2	NO·	Reference
295[1]	1909 (330)	1794 (440)	1652 (200)	1851 (1.7)	This work
77[2]	1960	1835	1664	–	41
20[3]	1953	1835	1663	–	39

[1] In methanol solution with $\lambda_{\text{pump}} = 400$ nm. [2] Suspended solid (Nujol) with $\lambda_{\text{pump}} = 488$ nm to obtain GS + MS1 and $\lambda_{\text{pump}} = 1064$ nm to obtain GS + MS2. [3] Single crystal ($E||c$) with $\lambda_{\text{pump}} = 488$ nm.

The significant frequency shift of the ν_{NO} for the two metastable species with respect to the ground state arises from the changes in π backbonding as a result of the rotation of the NO ligand. There are strong π backbonding interactions through the π^* orbital of NO^+ in MS1, though orbital overlap is less efficient than in the GS due to the smaller contribution of the oxygen atom to the π^*(NO) orbital. On the other hand, the symmetry of MS2 (C_s) only allows for π backbonding through one of the Fe $3d$ orbitals.[54] A reduction in π backbonding results in a lower NO stretching frequency,[68] which is apparent from the trend in the observed stretching frequencies of the GS, MS1 and MS2 listed in all three rows of Table 2.1.

Table 2.1 shows that the relative downshifts in the ν_{NO} for MS1 and MS2 from the ν_{NO} of the GS measured in this experiment are similar to what has been reported for solid-

state samples at low temperatures. The Gaussian line widths of the nitrosyl stretches for MS1, MS2 and the GS in methanol are 40 cm^{-1}, 45 cm^{-1} and 21 cm^{-1}, respectively. The NO stretching frequencies of GS, MS1 and MS2 listed in Table 2.1 clearly illustrate the influence of the solvent. The primary hydrogen bonding interactions between the solvent and SNP occur through the more negatively charged cyano ligands, which modulates the NO π backbonding through the metal center.[56,69] It is this shift in electron density resulting in reduced Fe−NO π backbonding that changes the ν_{NO} frequency in the GS, MS1 and MS2 when solvated by methanol molecules. As expected from the coordination geometry of the metal−NO moiety, the solvent-induced frequency shifts are seen most strongly in the GS and MS1 species.

2.4.2 Role of MS1 and MS2 in the photochemistry of SNP

Using the results from the UV-pump power dependence as described in the previous section, we have built a kinetic model (see the scheme in Figure 2.6) to understand the photochemistry of SNP in methanol at room temperature. The absorption of a 400 nm photon by the GS puts the system in an excited state manifold labeled GS*. From this state(s), the molecule can undergo an intramolecular rearrangement to form MS1 or dissociate to form $[Fe^{III}(CN)_5]^{2-}$ and NO radical. On absorbing another 400 nm photon from GS*, the molecule can reach a second excited state manifold labeled X. From this state(s), the molecule can rotate around the metal−nitrosyl bond to form MS2 or dissociate into $[Fe^{III}(CN)_5]^{2-}$ and NO radical. The solvent associated species, $[Fe^{III}(CN)_5(CH_3OH)]^{2-}$, Prussian Blue and CN^- are assumed to form after NO radical photodissociation. The metastable linkage isomers, MS1 and MS2, eventually relax back to the GS. We do not include inter-conversion between MS1 and MS2 and geminate recombination of NO because we do not observe these processes in our experiment. We view the excited states GS* and X representing multidimensional potential energy surfaces, from which many crossings or seams can be accessed. We note that our experimental time-resolution of ∼1 ps does not allow us to uniquely identify GS* and X through their IR signatures. The photochemical scheme described above accounts for the fact that MS1 is formed via a one-photon interac-

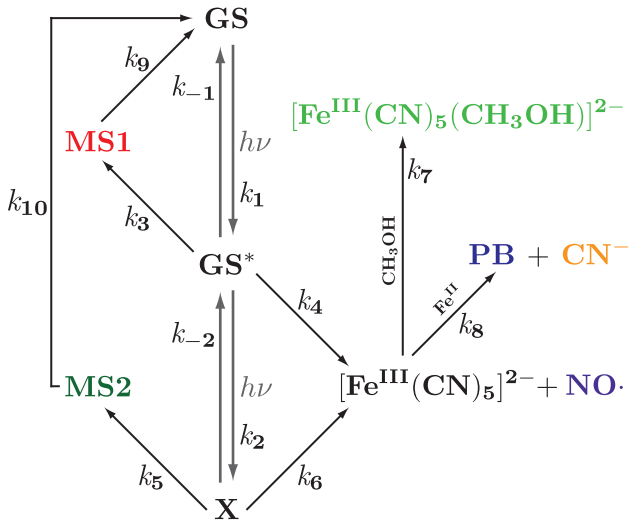

Figure 2.6: Proposed kinetic model for the simultaneous photochemical formation of the observed linkage isomerism products (MS1, MS2) and dissociation products (NO·, $[Fe^{III}(CN)_5(CH_3OH)]^{2-}$, CN^- and Prussian Blue). Rates (k_i) are shown beside each corresponding kinetic step and single photon interactions are written as $h\nu$. The Fe^{II} species needed to generate PB over k_8 is meant to represent any iron(II) species in solution, such as an SNP molecule that has not undergone photoexcitation.

tion, MS2 is formed via a two-photon process and NO radical is formed via a combination of one and two-photon pathways.

Using the scheme in Figure 2.6 and the aforementioned assumptions, we generate a set of ten coupled differential equations that are solved numerically. We iteratively fit this model to our solvent-subtracted dataset using a nonlinear least-squares algorithm with the assumption that only the GS is populated before the 400 nm pump pulse arrives. A more detailed discussion on the model, the fitting procedure and the fit results can be found in the appendix.

Figure 2.7 presents the fit results of the model (solid lines) with the solvent-subtracted data (points). Figure 2.7a displays the concentration of MS1, MS2 and NO radical obtained using the data from the NO stretching region. The inset shows the formation of the three species on a ~300 fs timescale. This is consistent with a recent study which found that MS2 was formed on a 300 fs timescale in single crystals of SNP at 296 K.[70] We stress that since

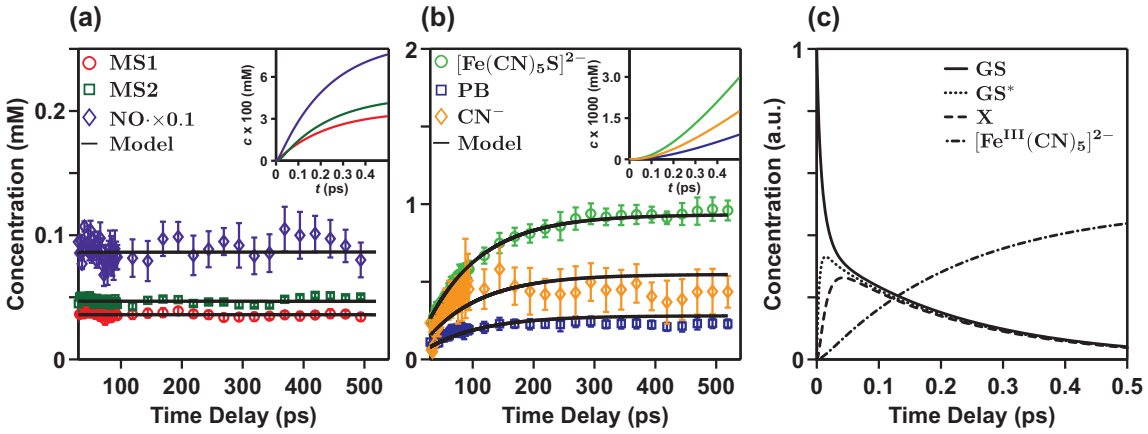

Figure 2.7: Results of fitting the photochemical kinetic model presented in Figure 2.6 to the solvent-subtracted experimental data. (a) Transient concentrations of photochemical species observed in the NO stretching region. Early-time dynamics (model only) are shown in the inset, (b) Transient concentrations of the photodissociated products observed in the CN stretching region. Early-time dynamics (model only) are shown in the inset. Here, S is short for solvent (methanol) (c) Early-time dynamics of the intermediate species as predicted by the model in Figure 2.6.

the solvent background response dominates the early time data, the ultrafast rate constants (k_{1-6}) cannot be assigned uniquely. We see that MS1, MS2 and NO· reach their maximum concentration by ∼1.5 ps and remain constant over the timescale of the experiment. Figure 2.7b shows the concentration of the dissociation products $[Fe^{III}(CN)_5(CH_3OH)]^{2-}$, PB and CN^- increasing as a function of the experimental time delay. From the model, we extract the methanol association rate of $k_7 = (130\ \text{ps})^{-1}$, which is consistent with diffusion-limited association of a methanol molecule into the vacant site of $[Fe^{III}(CN)_5]^{2-}$. The rate of formation of Prussian Blue is slower, with $k_8 = (320\ \text{ps})^{-1}$, due to the lower concentration of the iron(II) species in solution. Figure 2.7c shows model predictions for the early-time dynamics of the GS and the three chemical intermediates (GS*, X and $[Fe^{III}(CN)_5]^{2-}$) not observed in the experiment. The model predicts that the GS decays on 10 fs and 220 fs timescales and recovers on a timescale much longer than the experimental time delay. X and GS* form in <20 fs and decay on a ∼230 fs timescale. The intermediate $[Fe^{III}(CN)_5]^{2-}$ species grows on a slower timescale (∼240 fs) and decays on a similar timescale (∼76 ps) as the

formation of $[Fe^{III}(CN)_5(CH_3OH)]^{2-}$ (the decay is not shown in 2.7c). Since IR signatures and accurate absorbance cross-sections for the three intermediates are not available, Figure 2.7c is in relative units taken directly from the results of the model (i.e., $c_{GS}(t = 0) = 1$).

The role of the metastable linkage isomers in NO photodissociation is often discussed in the literature. Our data analysis shows that the photorelease of NO· competes with photoinduced metastable linkage isomerism in SNP. As shown in Fig. 2.6 these two pathways share common excited state(s) labeled as GS* and X. After absorbing one-photon and reaching state(s) GS*, the NO ligand in SNP can undergo a 180° rotation to form the MS1 isomer or photodissociate to form NO radical. Alternatively, SNP can absorb another photon to reach an intermediate state X. These intermediate states are viewed to be highly delocalized multidimensional potential energy surfaces with many surface crossings. From this X state, the primary pathway is NO release with a small portion of the population relaxing into MS2 by rotation of the NO ligand by 90°. This agrees with our experimental data and takes into account that MS1 is formed via a one-photon process, MS2 is formed via a two-photon process and NO· is generated from a combination of one- and two-photon pathways.

2.4.3 Comparison with previous studies

As noted earlier, most studies of photoinduced linkage isomerism in SNP and other related metal−nitrosyl compounds have been done at low temperature in the solid state. We expect that the hydrogen bonding interactions of methanol and SNP will significantly impact the photochemistry of SNP at room temperature by stabilizing/destabilizing highly excited intermediate states and/or the metastable product states. Keeping this in mind we compare the major findings of our experiment with previous photochemical studies of SNP.

The role of MS1 and MS2 in the photorelease of NO· in metal−nitrosyl photochemistry has been studied by various groups and there are two main mechanisms that have been suggested in the literature − one of which involves competing processes leading to either linkage isomerism or photorelease of NO· and the other involves nitrosyl ligand dissociation following linkage isomerism in a two-step consecutive mechanism. In a recent review on

photoactive ruthenium nitrosyls, the authors suggest that NO· may be generated through a consecutive mechanism where the nitrosyl ligand is dissociated from either MS1 or MS2.[6] In this scenario, MS1 and MS2 are transient species that are depleted to generate NO·. This consecutive mechanism has been considered by Dieckmann et al. who observed phototriggered ($\lambda_{\text{pump}} = 532$ nm) nitric oxide and cyanide release from SNP molecules deposited on thin films at 294 K.[71] Though they were not able to detect either MS1 or MS2, they modeled their data using a two-step NO· release process suggesting the linkage isomers as intermediate species. Einarsdottir and coworkers measured a transient state from which they observed NO· photorelease in flash photolysis experiments ($\lambda_{\text{pump}} = 355$ nm) on a Ru nitrosyl compound in aqueous solution at 298 K.[72] They attributed the transient intermediate state formed within $\leq$100 ns to either MS1 or MS2. Giglmeier et al. observed the production of MS1, MS2 and NO photorelease using FTIR spectroscopy after photoexciting single crystals of a Ru nitrosyl porphyrin.[9] The authors were not able to conclusively determine whether photoisomerization and photodissociation were occurring in a consecutive manner (i.e., formation of NO from a metastable state), if the processes were competing or if there was no relation between the photochemical processes at all. On the basis of the studies mentioned above and others, the role of MS1 and MS2 in the overall photochemistry of SNP remains unclear, though it is possible that different experimental conditions lead to different photochemical outcomes.

Our experiment is able to measure the formation and dynamics of MS1, MS2 and NO· in solution at room temperature and our results demonstrate that photoinduced linkage isomerism and photodissociation are in fact competing processes, as shown in Figures 2.6 and 2.7. Note that our data does not support the idea that MS1 and MS2 are intermediate species in NO photodissociation. If this were the case, we would observe a depletion of the population of MS1 and MS2 over the course of our experiment, which we do not. In our model, GS* and X represent complex potential energy surfaces from where the molecule can undergo linkage isomerism (minor pathway) or photodissociation (major pathway).

It is important to point out that the UV pump power dependence we observed in this experiment is different from what is currently in the literature.[1,54,55] Most previous experiments have employed excitation light in the range of 450−530 nm followed by longer

wavelength irradiation to efficiently trap one or more linkage isomers at low temperatures. In the present experiment utilizing 400 nm pump pulses, we have observed that we can form MS1 with one photon, and that it takes two photons to form MS2 at room temperature in solution. Our results demonstrate that given the right excitation conditions and high detection sensitivity, it is possible to observe both MS1 and MS2 linkage isomers at room temperature.

Previous steady-state photochemical studies of SNP in solution at room temperature have measured the primary photoproduct to be $[Fe^{III}(CN)_5(solvent)]^{2-}$ (solvent = CH_3OH, H_2O).[45,47,48] Other dissociation products such as NO, CN and Prussian Blue are also observed by infrared spectroscopy and mass spectrometry. Due to the steady-state nature of these experiments, the metastable states MS1 and MS2 were not observed. In this study, we are able to observe all the photochemical products listed above in a time-resolved manner. This allows us to measure the solvent association timescale of $[Fe^{III}(CN)_5(CH_3OH)]^{2-}$ to be 130 ps and the formation time of Prussian Blue to be 320 ps. Our model suggests that MS1, MS2 and NO· are formed within ∼300 fs and decay on a ∼100 ns timescale.

2.5 Concluding Remarks

The high structural sensitivity of transient infrared spectroscopy has allowed the simultaneous detection of the photoinduced linkage isomers MS1 ($[Fe^{II}(CN)_5(\eta^1\text{-ON})]^{2-}$) and MS2 ($[Fe^{II}(CN)_5(\eta^2\text{-NO})]^{2-}$) of SNP and the photodissociated free nitrosyl radical at room temperature in a methanol solution. These three transient species are detected using their distinct nitrosyl stretching frequencies at 1794 cm^{-1} (MS1), 1652 cm^{-1} (MS2) and 1851 cm^{-1} (NO·). Additional photodissociation products including $[Fe^{III}(CN)_5(CH_3OH)]^{2-}$, the cyanide ion, and Prussian Blue are measured. The UV-pump power dependence enabled the development of a kinetic model involving a one-photon absorption pathway to MS1, a two-photon absorption pathway to MS2 and a combination of both one- and two-photon absorption processes leading to the photodissociation products including free NO radical. Our results suggest that photoisomerization of MS1 and MS2 and photodissociation of NO are competing pathways in the photochemistry of SNP at room temperature.

The results from our experiments demonstrate that the photochemistry of metal−nitrosyl

complexes in solution at room temperature (most relevant to chemistry and biology) needs further attention from theorists and experimentalists alike. The above findings have implications for the photochemistry of transition metal−nitrosyl compounds, the design of optical devices based on the metastable isomers, the photodelivery of NO in medicine and the understanding of M−NO bonding in metalloproteins.

REFERENCES

[1] Coppens, P.; Novozhilova, I.; Kovalevsky, A. *Chem. Rev.* **2002**, *102*, 861–884.

[2] Fomitchev, D. V.; Novozhilova, I.; Coppens, P. *Tetrahedron* **2000**, *56*, 6813–6820.

[3] Coppens, P.; Fomitchev, D.; Carducci, M.; Culp, K. *J. Chem. Soc., Dalton Trans.* **1998**, 865–872.

[4] Bitterwolf, T. E. *Coord. Chem. Rev.* **2006**, *250*, 1196–1207.

[5] Gutlich, P.; Garcia, Y.; Woike, T. *Coord. Chem. Rev.* **2001**, *219-221*, 839–879.

[6] Rose, M. J.; Mascharak, P. K. *Coord. Chem. Rev.* **2008**, *252*, 2093–2114.

[7] Hayton, T. W.; Legzdins, P.; Sharp, W. B. *Chem. Rev.* **2002**, *102*, 935–992.

[8] Bitterwolf, T. E. *Inorg. Chem. Communications* **2008**, *11*, 772–773.

[9] Giglmeier, H.; Kerscher, T.; Klüfers, P.; Schaniel, D.; Woike, T. *Dalton Trans.* **2009**, 9113–9116.

[10] Xu, N.; Yi, J.; Richter-Addo, G. B. *Inorg. Chem.* **2010**, *49*, 6253–6266.

[11] Cheng, L.; Novozhilova, I.; Kovalevsky, A.; Bagley, K.; Coppens, P.; Richter-Addo, G. *J. Am. Chem. Soc.* **2000**, *122*, 7142–7143.

[12] Fomitchev, D. V.; Coppens, P.; Li, T. S.; Bagley, K. A.; Chen, L.; Richter-Addo, G. *Chem. Comm.* **1999**, *128*, 2013–2014.

[13] Novozhilova, I.; Coppens, P.; Lee, J.; Richter-Addo, G.; Bagley, K. *J. Am. Chem. Soc.* **2006**, *128*, 2093–2104.

[14] Nutt, D.; Karplus, M.; Meuwly, M. *J. Phys. Chem. B* **2005**, *109*, 21118–21125.

[15] Nutt, D. R.; Meuwly, M. *ChemPhysChem* **2007**, *8*, 527–536.

[16] Hauser, U.; Oestreich, V.; Rohrweck, H. D. *Z. Phys. A* **1977**, *280*, 17–25.

[17] Zöllner, H.; Krasser, W.; Woike, T.; Haussüehl, S. *Chem. Phys. Lett.* **1989**, *161*, 497–501.

[18] Pressprich, M. R.; White, M.; Coppens, P. *J. Am. Chem. Soc.* **1993**, *115*, 6444–6445.

[19] Pressprich, M. R.; White, M.; Vekhter, Y.; Coppens, P. *J. Am. Chem. Soc.* **1994**, *116*, 5233–5238.

[20] Carducci, M.; Pressprich, M. R.; Coppens, P. *J. Am. Chem. Soc.* **1997**, *119*, 2669–2678.

[21] Morioka, Y.; Saitoh, H.; Machida, H. *J. Phys. Chem. A* **2002**, *106*, 3517–3523.

[22] Schaniel, D.; Imlau, M.; Weisemoeller, T.; Woike, T.; Kraemer, K. W.; Guedel, H.-U. *Adv. Mater.* **2007**, *19*, 723–726.

[23] Imlau, M.; Woike, T.; Schaniel, D.; Schefer, J.; Fally, M.; Rupp, R. A. *Opt. Lett.* **2002**, *27*, 2185–2187.

[24] Imlau, M.; Woike, T.; Schieder, R.; Rupp, R. A. *Phys. Rev. Lett.* **1999**, *82*, 2860–2863.

[25] Imlau, M.; Haussüehl, S.; Woike, T.; Schieder, R.; Angelov, V.; Rupp, R.; Schwarz, K. *App. Phys. B* **1999**, *68*, 877–885.

[26] Woike, T.; Haussüehl, S.; Sugg, B.; Rupp, R.; Beckers, J.; Imlau, M.; Schieder, R. *App. Phys. B* **1996**, *63*, 243–248.

[27] Schuy, A.; Woike, T.; Schaniel, D. *J. Sol-Gel Sci. Technol.* **2009**, *50*, 403–408.

[28] Butler, A.; Glidewell, C. *Chem. Soc. Rev.* **1987**, *16*, 361–380.

[29] Hollenberg, S. M. *Heart Fail. Rev.* **2007**, *12*, 143–147.

[30] Shin David, D.; Brandimarte, F.; De Luca, L.; Sabbah Hani, N.; Fonarow Gregg, C.; Filippatos, G.; Komajda, M.; Gheorghiade, M. *Am. J. Cardiol.* **2007**, *99*, 4A–23A.

[31] Ford, P. C.; Wecksler, S. *Coord. Chem. Rev.* **2005**, *249*, 1382–1395.

[32] Schaniel, D.; Woike, T. *Phys. Chem. Chem. Phys.* **2009**, *11*, 4391–4395.

[33] Woike, T.; Krasser, W.; Bechthold, P.; Haussüehl, S. *Solid State Commun.* **1983**, *45*, 503–506.

[34] Woike, T.; Krasser, W.; Bechthold, P.; Haussüehl, S. *Solid State Commun.* **1983**, *45*, 499–502.

[35] Krasser, W.; Woike, T.; Bechthold, P.; Haussüehl, S. *J. Mol. Struc.: Theochem* **1984**, *114*, 57–60.

[36] Zöllner, H.; Woike, T.; Krasser, W.; Haussüehl, S. *Z. Kristallogr.* **1989**, *188*, 139–153.

[37] Schaniel, D.; Woike, T.; Schefer, J.; Petříček, V.; Krämer, K.; Güdel, H. *Phys. Rev. B* **2006**, *73*, 174108.

[38] Schaniel, D.; Woike, T.; Schefer, J.; Petříček, V. *Phys. Rev. B* **2005**, *71*, 174112.

[39] Güida, J. A.; Aymonino, P. J.; Piro, O.; Castellano, E. *Spectrochim. Acta A* **1993**, *49*, 535–542.

[40] Chacón Villalba, M. E.; Güida, J. A.; Varetti, E. L.; Aymonino, P. J. *Spectrochim. Acta A* **2001**, *57*, 367–373.

[41] Chacón Villalba, M. E.; Güida, J. A.; Varetti, E. L.; Aymonino, P. J. *Inorg. Chem.* **2003**, *42*, 2622–2627.

[42] Schefer, J.; Woike, T.; Imlau, M.; Delley, B. *Euro. Phys. J. B* **1998**, *3*, 349–352.

[43] Schaniel, D.; Schefer, J.; Delley, B.; Imlau, M.; Woike, T. *Phys. Rev. B* **2002**, *66*, 085103.

[44] Schaniel, D.; Woike, T.; Merschjann, C.; Imlau, M. *Phys. Rev. B* **2005**, *72*, 195119.

[45] Wolfe, S.; Swinehart, J. *Inorg. Chem.* **1975**, *14*, 1049–1053.

[46] Kudo, S.; Bourassa, J.; Boggs, S.; Sato, Y.; Ford, P. *Anal. Biochem.* **1997**, *247*, 193–202.

[47] Deoliveira, M.; Langley, G.; Rest, A. *J. Chem. Soc., Dalton Trans.* **1995**, 2013–2019.

[48] Stochel, G.; Stasicka, Z. *Polyhedron* **1985**, *4*, 1887–1890.

[49] Manoharan, P. T.; Gray, H. B. *J. Am. Chem. Soc.* **1965**, *87*, 3340–3348.

[50] Ishikawa, T.; Tanaka, K. *J. Chem. Phys.* **2005**, *122*, 074314.

[51] Ishikawa, T.; Tanaka, K. *Z. Kristallogr.* **2008**, *223*, 334–342.

[52] Boulet, P.; Buchs, M.; Chermette, H.; Daul, C.; Furet, E.; Gilardoni, F.; Rogemond, F.; Schläpfer, C. W.; Weber, J. *J. Phys. Chem. A* **2001**, *105*, 8999–9003.

[53] Boulet, P.; Buchs, M.; Chermette, H.; Daul, C.; Gilardoni, F.; Rogemond, F.; Schläpfer, C. W.; Weber, J. *J. Phys. Chem. A* **2001**, *105*, 8991–8998.

[54] Buchs, M.; Daul, C. A.; Manoharan, P. T.; Schläpfer, C. W. *Int. J. Quant. Chem.* **2002**, *91*, 418–431.

[55] Delley, B.; Schefer, J.; Woike, T. *J. Chem. Phys.* **1997**, *107*, 10067–10074.

[56] Sando, G. M.; Zhong, Q.; Owrutsky, J. C. *J. Chem. Phys.* **2004**, *121*, 2158–2168.

[57] Stamler, J. S.; Singel, D. J.; Loscalzo, J. *Science* **1992**, *258*, 1898–1902.

[58] Experimentally determined from the 2D IR spectrum of SNP in methanol.

[59] This value cannot be determined accurately due to the maximum time delay of 0.5 ns.

[60] Upon prolonged excitation at 400 nm, a bleach appears at 2100 cm^{-1} corresponding to formation of Prussian blue.

[61] Independently determined from the FTIR spectrum of KCN in methanol.

[62] Shanoski, J.; Glascoe, E.; Harris, C. *J. Phys. Chem. B* **2006**, *110*, 996–1005.

[63] Fisher, J. A. N.; Susumu, K.; Therien, M. J.; Yodh, A. G. *J. Chem. Phys.* **2009**, *130*, 134506.

[64] Calculated at the BP86 level of theory with 6-31G(d) for iron atoms and 6-311+G(3df) for all other atoms. All calculations were performed using the polarizability continuum model with a methanol dielectric.

[65] Frisch, M. J.; et al.; *Gaussian 03, Revision C.02*; Gaussian, Inc., Wallingford, CT, 2004.

[66] Smith, A.; Keller, W.; Johnston, H. *J. Chem. Phys.* **1951**, *19*, 189–192.

[67] Kim, S.; Heo, J.; Lim, M. *Bull. Korean Chem. Soc.* **2005**, *26*, 151–156.

[68] Nakamoto, K. *Infrared and Raman Spectra of Inorganic and Coordination Compounds*, 4th ed.; John Wiley and Sons: New York, 1986.

[69] Estrin, D. A.; Baraldo, L. M.; Slep, L. D.; Barja, B. C.; Olabe, J. A.; Paglieri, L.; Corongiu, G. *Inorg. Chem.* **1996**, *35*, 3897–3903.

[70] Schaniel, D.; Nicoul, M.; Woike, T. *Phys. Chem. Chem. Phys.* **2010**, *12*, 9029–9033.

[71] Dieckmann, V.; Imlau, M.; Taffa, D. H.; Walder, L.; Lepski, R.; Schaniel, D.; Woike, T. *Phys. Chem. Chem. Phys.* **2010**, *12*, 3283–3288.

[72] Szundi, I.; Rose, M. J.; Sen, I.; Eroy-Reveles, A. A.; Mascharak, P. K.; Einarsdottir, O. *Photochem. Photobiol.* **2006**, *82*, 1377–1384.

2.A Chapter 2 Supporting Information

2.A.1 Bleach Dynamics

The metastable nature of the transient species is clear from the bleach recovery dynamics, shown in Figure 2A.1, as there is no recovery evident through 0.5 ns. Fig. 2A.1a shows the NO bleach, where self-absorption (positive dip) is present due to the high sample concentration (120 mM). Note that since the NO stretching frequencies of the transient species are well separated from the NO bleach, the high sample concentration does not have an effect on the dynamics of the transient species. The 32 ± 7 ps vibrational relaxation timescale of $\nu_{\mathrm{NO}}(2 \leftarrow 1)$ is shown in Figure 2A.1b. This timescale is consistent with the population relaxation time (T_1) of $\nu_{\mathrm{NO}}(1 \leftarrow 0)$ in SNP dissolved in methanol reported by Owrutsky and co-workers of 29 ± 2 ps.[1]

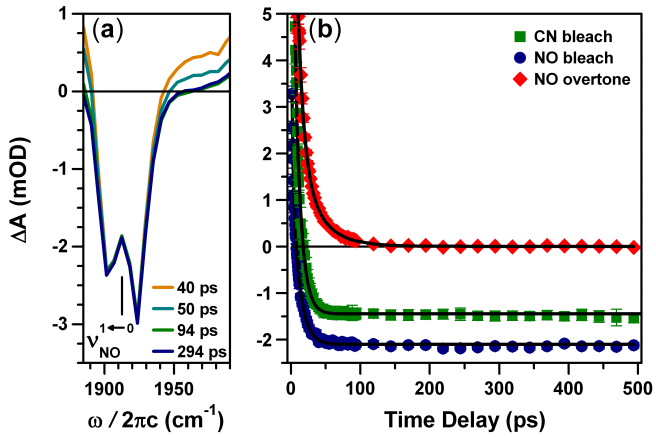

Figure 2A.1: (a) Time-resolved infrared absorption spectra of SNP in methanol at 295 K showing the ν_{NO} bleach at 1909 cm^{-1}. (b) Bleach dynamics of the ν_{NO} (blue circles, 1909 cm^{-1}), ν_{CN} (green squares, 2145 cm^{-1}) and ν_{NO} overtone (red diamonds, 1881 cm^{-1}). Best fits to the data are shown as black solid lines.

2.A.2 Kinetic Parameteres Extracted from Best Fit

NO stretching region

Table 2A.1 presents the fitting parameters extracted from the NO stretching region of the transient IR spectrum fit to Equation 2A.1. The data for neat methanol is given in Table 2A.2. The neat methanol data illustrates that solvent and/or CaF_2 relaxation dominates the first two decay channels. Each of the kinetic traces was obtained by integrating the spectral resonance over the full-width at half-maximum (fwhm) of the peak to ensure accurate kinetic parameters.

$$\Delta A(t) = \sum_{i=1}^{3} A_i \exp(-t/\tau_i) \tag{2A.1}$$

Table 2A.1: Best-fit parameters for transients in the NO stretching region. Center frequencies are given in cm^{-1}.

Assign.	ω_c	τ_1 (ps)	τ_2 (ps)	τ_3 (ns)	A_1[4]	A_2	A_3[5]
MS1	1794	2.6 ± 0.5	11.6 ± 0.5	83[6]	0.56 ± 0.06	0.47 ± 0.04	0.011 ± 0.003
MS2	1652	2.6 ± 0.5	12.2 ± 0.3	200[3]	0.52 ± 0.06	0.47 ± 0.03	0.011 ± 0.002
NO·	1851	3.3 ± 0.6	13.1 ± 0.3	200[3]	0.52 ± 0.04	0.47 ± 0.05	0.007 ± 0.002
NO bl.	1909	2.3 ± 0.6	11 ± 1	–	0.44 ± 0.06	0.56 ± 0.05	–
NO ov.	1881	1.8 ± 0.5	9 ± 1	32 ± 7	0.37 ± 0.05	0.52 ± 0.04	0.11 ± 0.05

[1] Amplitudes normalized such that $\sum_i A_i = 1$. [2] A constant offset (-2.11 ± 0.02 mOD) replaced A_3 for the bleach since it goes negative. [3] Approximate values due to the maximum time delay of 0.5 ns in this experiment. The bounds of the fit were held between 80−200 ps.

There is a lot of discussion in the chapter regarding the early-time solvent response (the solvent refers to both methanol and the sample cell windows) as it is this response that hinders the observation of the early photochemical events occurring in this experiment. Figure 2A.2 shows the FTIR spectrum of SNP in methanol (solvent subtracted) and neat methanol to illustrate the non-zero absorbance of the solvent over the entire spectral region of this experiment. This leads to resonant solvent response at early time delays.

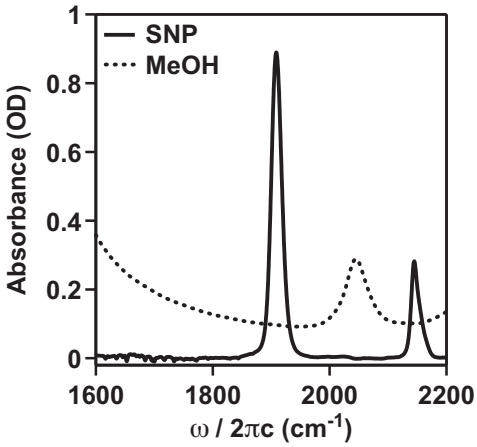

Figure 2A.2: FTIR spectra of 120 mM SNP in methanol (solid line, solvent subtracted) and neat methanol (dotted line) at room temperature with $l = 50$ μm. The resonance at 2045 cm^{-1} in the neat methanol spectrum is the $2\nu_{CO}$ mode.[2]

Table 2A.2: Best-fit parameters for neat methanol in the NO stretching region.

Assign.	ω_c (cm^{-1})	τ_1 (ps)	τ_2 (ps)	A_1[1]	A_2
MS1	1794	2.3 ± 0.3	11.7 ± 0.5	0.49 ± 0.03	0.51 ± 0.03
MS2	1652	2.4 ± 0.3	11.7 ± 0.5	0.49 ± 0.03	0.51 ± 0.03
NO·	1851	2.2 ± 0.3	11.4 ± 0.5	0.49 ± 0.04	0.51 ± 0.03
NO bleach	1909	2.3 ± 0.2	9.2 ± 0.7	0.68 ± 0.03	0.31 ± 0.03
NO overtone	1881	2.4 ± 0.2	9.4 ± 0.7	0.69 ± 0.03	0.31 ± 0.04

[1] Amplitudes normalized such that $\sum_i A_i = 1$.

CN stretching region

Table 2A.3 shows the extracted fitting parameters (using Eqn. 2A.2) obtained from the CN stretching region along with assignments consistent with the work of Rest and coworkers.[3] Recall that the stretching frequency of CN^- in methanol was confirmed by taking an FTIR spectrum of 0.25 M KCN in methanol, whereas the Prussian Blue stretching frequency was measured in our laboratory using transient IR absorption spectroscopy (i.e. allowing a high concentration of PB to form such that a bleach appears in the transient IR spectrum).

$$\Delta A(t) = \sum_{i=1}^{2} A_i \exp(-t/\tau_i) + A_3(1 - \exp(-t/\tau_3)) \tag{2A.2}$$

Table 2A.3: Best-fit parameters for transients in the CN stretching region. Center frequencies are given in cm^{-1}.

Assignment	ω_c	τ_1 (ps)	τ_2 (ps)	τ_3 (ns)	A_1[1]	A_2	A_3[2]
$[Fe^{III}(CN)_5(CH_3OH)]^{2-}$	2123	3.5 ± 0.8	13 ± 1	95 ± 9	0.66 ± 0.07	0.27 ± 0.09	0.070 ± 0.008
Prussian Blue	2100	3.1 ± 0.8	12 ± 1	40 ± 4	0.65 ± 0.07	0.33 ± 0.08	0.021 ± 0.003
CN^-	2083	2.5 ± 0.4	10 ± 1	–	0.59 ± 0.04	0.41 ± 0.06	–
CN bleach	2145	2.5 ± 0.5	10 ± 1	–	0.58 ± 0.06	0.42 ± 0.08	–

[1] Amplitudes normalized such that $\sum_i A_i = 1$. [2] A constant offset replaced A_3 for CN^- (0.10 ± 0.03 mOD) and the CN bleach (-1.46 ± 0.04 mOD).

2.A.3 Kinetic Model

As discussed in the chapter, the model consists of ten coupled differential equations each of which describes the time-evolution of the concentration of one of the ten species in the photochemical scheme (Figure 2A.3). Both stimulated absorption and emission during the

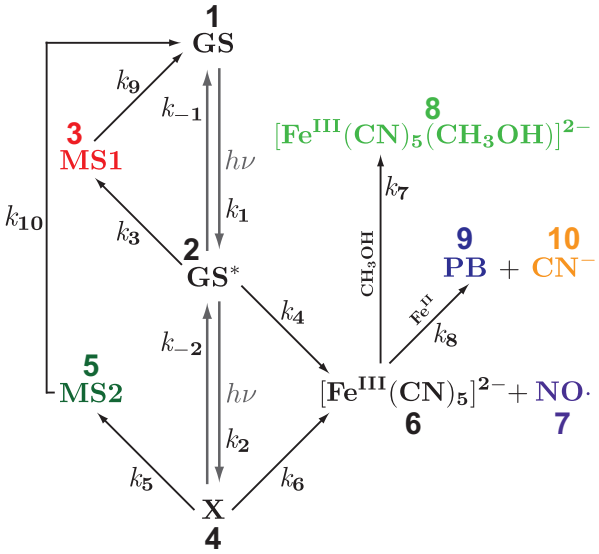

Figure 2A.3: The scheme from Figure 2.6, as presented in the chapter, including numbered labels on each of the species.

duration of the pump pulse are accounted for with forward- (k_i) and back- (k_{-i}) electron transfer rates. It is assumed that $k_i = k_{-i}$ and that each kinetic step is a first-order process.

The set of differential equations in shown in Eqns. 2A.3, where each species has been labeled with a number from 1−10. In the equations below, $k_{-1} = k_1$ and $k_{-2} = k_2$.

$$\begin{aligned}
\dot{c}_1 &= k_1c_2(t) - k_1c_1(t) + k_9c_3(t) + k_{10}c_5(t) \\
\dot{c}_2 &= k_1c_1(t) - k_1c_2(t) - k_2c_2(t) + k_2c_4(t) - k_3c_2(t) - k_4c_2(t) \\
\dot{c}_3 &= k_3c_2(t) - k_9c_3(t) \\
\dot{c}_4 &= k_2c_2(t) - k_2c_4(t) - k_5c_4(t) - k_6c_4(t) \\
\dot{c}_5 &= k_5c_4(t) - k_{10}c_5(t) \\
\dot{c}_6 &= k_4c_2(t) + k_6c_4(t) - k_7c_6(t) - k_8c_6(t) \\
\dot{c}_7 &= k_4c_2(t) + k_6c_4(t) \\
\dot{c}_8 &= k_7c_6(t) \\
\dot{c}_9 &= k_8c_6(t) \\
\dot{c}_{10} &= k_8c_6(t)
\end{aligned} \tag{2A.3}$$

The solution of the model is obtained by the following procedure. First, Equation 2A.3 is solved numerically with an initial guess of the rate constants ($k_9 = k_{10} = 1/110$ ns^{-1}) and the initial conditions at $t = 2$ ps (Table 2A.4). This time is used to avoid pulse overlap effects in the experimental data. This solution is evaluated at the experimental time points and then subtracted from the solvent-subtracted experimental data (in units of mM). The eight rate constants are iteratively changed within their selected bounds (Tab. 2A.4) using a nonlinear least-squares fitting routine to minimize the difference between experiment and model. Once the solution is found, Equation 2A.3 is solved from $t = 0 - 520$ ps with the initial condition that $c_1(0) = 1$ (i.e. only the GS is populated before the pump pulse arrives at the sample).

Table 2A.4: Model fitting parameters. The fit bounds for species 3−6 are based on the 300 fs time scale found for the formation of MS2 in the solid state.[4] The concentration at 2 ps is normalized to a sum of 1.

Species, i	τ_i (ps)	Fit Bounds (ps)	$c_i(t = 2$ ps) (Norm.)
1	0.010	$[0.010, 0.020]$	0.002
2	0.015	$[0.010, 0.020]$	0.008
3	0.30	$[0.28, 0.32]$	0.05
4	0.30	$[0.28, 0.32]$	0.01
5	0.30	$[0.28, 0.32]$	0.05
6	0.30	$[0.28, 0.32]$	0.44
7	130	$[20, 500]$	0.44
8	320	$[20, 1000]$	0
9	110000	–	0
10	110000	–	0

2.A.4 Molar Absorptivity Calculations

Quantum yield

The total photoexcitation yield was calculated by taking a ratio of the total integrated bleach area (Figs. 2.4a and 2A.1) to the integrated area of the FTIR spectrum (Fig. 2.2) where self-absorption of the NO bleach was not included in the Gaussian fit.

Quantum yields of transient photoproducts were calculated using a ratio of the transient integrated area to that of the total bleach area. This was then multiplied by the total photoexcitation yield to give the final quantum yield. For transients that have molar absorptivities close to that of the parent species ($[Fe^{III}(CN)_5(CH_3OH)]^{2-}$, Prussian Blue), transient concentrations can be obtained by multiplying the total quantum yield by the initial concentration (120 mM). For the other transient species (MS1, MS2, $NO\cdot$, CN^-), molar absorptivities need to be calculated. Transient concentrations of all species (at $t = 294$ ps) can be calculated. Finally, transient quantum yields relative to $[Fe^{III}(CN)_5(CH_3OH)]^{2-}$ were calculated and factored into the total photoexcitation yield. The sum of the transient quantum yields is $1.93 \pm 0.06\%$.

Integrated molar absorptivity

We report integrated molar absorptivities ($\epsilon = \int \epsilon_\nu d\nu$) of the NO stretch for the NO radical, MS1 and MS2. Since it is very difficult to obtain accurate cross-section information for these species, this information may prove to be useful in a variety of fields. The values were calculated by integrating the area under each of the transient species and dividing that area by the total bleach area where differences in sample concentrations for the CN region and NO region data were accounted for.

Simply taking the ratio of areas assumes that the molar absorptivity of the transient is the same as that of the parent species, which is accurate for $[Fe^{III}(CN)_5(CH_3OH)]^{2-}$ but not for NO$\cdot$ and CN^-. The concentration (at $t = 294$ ps) of $[Fe^{III}(CN)_5(CH_3OH)]^{2-}$ generated was $\sim$1.2 mM. If we make the assumption that every NO photodissociation event leads to one solvent-associated species, then $c_{Fe^{III}} = c_{NO\cdot}$. This gives enough information to calculate $\epsilon_{NO}(NO\cdot) = 1.7 \times 10^2$ M^{-1} cm^{-2}.

We estimate the molar absorptivities of the linkage isomers by taking the ratio of oscillator strengths of GS, MS1 and MS2 calculated using Gaussian 03[5] at the BP86 level of theory[6,7] with 6-31G(d)[8] for iron and 6-311+G(3df)[9] for all other atoms. All calculations were performed using the polarizability continuum model with a methanol dielectric.[10] This allows the calculation of the transient concentration of the linkage isomers. The spectrum at $t = 294$ ps (y-axis converted to concentration) can then be fit to Gaussians to afford the area under the curve. The FTIR spectrum of SNP in methanol reveals $\epsilon_{NO}(GS) = 3.3 \times 10^4$ M^{-1} cm^{-2}, from which we calculate $\epsilon_{NO}(MS1) = 4.4 \times 10^4$ M^{-1} cm^{-2} and $\epsilon_{NO}(MS2) = 2.0 \times 10^4$ M^{-1} cm^{-2}. Note that the error bars reported in the chapter are derived from the error in the Gaussian fit of the experimental spectra.

REFERENCES

[1] Sando, G. M.; Zhong, Q.; Owrutsky, J. C. *J. Chem. Phys.* **2004**, *121*, 2158–2168.

[2] Krasser, W.; Woike, T.; Bechthold, P.; Haussüehl, S. *J. Mol. Struc.: Theochem* **1984**, *114*, 57–60.

[3] Deoliveira, M.; Langley, G.; Rest, A. *J. Chem. Soc., Dalton Trans.* **1995**, 2013–2019.

[4] Schaniel, D.; Nicoul, M.; Woike, T. *Phys. Chem. Chem. Phys.* **2010**, *12*, 9029–9033.

[5] Frisch, M. J.; et al.; *Gaussian 03, Revision C.02*; Gaussian, Inc., Wallingford, CT, 2004.

[6] Becke, A. D. *Phys. Rev. A* **1988**, *38*, 3098.

[7] Perdew, J. P. *Phys. Rev. B* **1986**, *33*, 8822.

[8] Rassolov, V.; Pople, J. A.; Ratner, M. A.; Windus, T. L. *J. Chem. Phys.* **1998**, *109*, 1223.

[9] Krishnan, R.; Binkley, J. S.; Seeger, R.; Pople, J. A. *J. Chem. Phys.* **1980**, *72*, 650.

[10] Tomasi, J.; Mennucci, B.; Cammi, R. *Chem. Rev.* **2005**, *105*, 2999.

Chapter 3

ANHARMONIC VIBRATIONAL COUPLINGS AND RELAXATION IN A CYANO-BRIDGED TRINUCLEAR MIXED-VALENCE COMPLEX

The work presented in this chapter is in preparation for publication:

Lynch, M. S.; Van Kuiken, B. E.; Daifuku, S. L.; Khalil, M. *J. Chem. Phys.* **2013**, *in prep.*

3.1 Vibrational Spectroscopy of Cyano-Bridged Mixed-Valence Complexes

The vibrational spectroscopy of cyano-bridged mixed-valence (MV) complexes in solution is a topic that has not received much attention in the past. Perhaps the most studied cyano-bridged mixed-valence complex is Prussian Blue (PB); however, the complexities in the chemical structure of PB make it very difficult to study in solution. Dating back to the late 1980s to early 1990s, Barbara, Hupp, Walker, and Woodruff starting studying the vibrational spectroscopy of mixed-valence complexes.[1–11] The former two generally took the Raman spectroscopy approach, whereas Walker and Woodruff independently investigated the picosecond-resolved infrared spectroscopy of cyano-bridged homo- and heteronuclear dimers (in this context, "dimer" means a two-metal-atom-containing molecule). Spears and coworkers were also very interested in extracting electron transfer rates with vibrational state resolution. They were looking at donor-acceptor ion pairs of the form $[A^+|D^-] = [Co(Cp)_2^+|V(CO)_6^-]$ (Cp = cyclopentadienyl), where it was determined that electron transfer rates depend on the vibrational quantum number of the ν_{CO} mode.[12–14] Also in the 1990s, Endicott and coworkers performed experiments on a series of cyano-bridged transition metal complexes where they suggested a simple vibronic coupling model to explain the frequency of ν_{CN} in the series.[15–17] Naturally, all of these studies focused on the effect the vibrational modes had on the electron transfer rates. A detailed investigation of the electronic ground state of each of the complexes was always missing, as ultrafast mid-IR spectroscopy was in its early stages of development. In fact, 21 years ago Woodruff was one of the first to

propose the use of ultrafast IR spectroscopy for studying complex chemical reactions with his work on $[(CN)_5Ru^{II}-CN-Ru^{III}(NH_3)_5]^-$ (RuRu).[18]

Examples of complexes that Walker studied by optical−IR pump−probe spectroscopy are $[(CN)_5Os^{II}-CN-Ru^{III}(NH_3)_5]^-$ (OsRu) and $[(CN)_5Fe^{II}-CN-Ru^{III}(NH_3)_5]^-$ (FeRu) in D_2O, formamide, and *N*-methylformamide (NMF).[7,8] They labelled the CN stretching (ν_{CN}) modes as $\nu_{\text{bridge-CN}}$ (2096 cm^{-1}), $\nu_{cis\text{-CN}}$ (2048 cm^{-1}), and $\nu_{trans\text{-CN}}$ (2018 cm^{-1}), where the frequencies shown here are the reported frequencies for FeRu in D_2O. The main conclusions from this work are that back-electron transfer rates are faster than 3×10^{12} s^{-1} (i.e., $\tau_{BET} < 333$ fs) and that the majority of the excess electronic excitation energy is *not* deposited into ν_{CN} modes. They attributed the dynamics to solvent heating. These results are in stark contrast to the conclusions that Woodruff drew on the RuRu dimer, where it was said that "upon return to the ground state, large amounts of energy (up to 7 quanta, 14 000 cm^{-1}) are placed into the terminal MC≡N stretching mode." They also measured the decay of this vibrational energy to range from less than 0.5 to 6 ps.[5,6] It is worth noting that in the latter case ν_{CN} modes were not separated into ν_{bridge}, etc.; rather, all of the ν_{CN} modes were grouped into the aforementioned $\nu_{\text{terminal-CN}}$ mode.

It was therefore clear from the beginning that the role of the ν_{CN} modes in charge transfer in mixed-valence species was a somewhat controversial subject. It is surprising, however, that more groups did not first focus on dynamics taking place in the electronic ground state before trying to elucidate the role of the ν_{CN} mode in charge transfer. One of the first questions to consider is why the ν_{bridge} mode is the highest energy transition?[19] Walker assigned the ν_{CN} modes in OsRu and FeRu by comparison with previous work, where in the previous work the ν_{CN} frequencies of $[Fe(CN)_6]^{3-}$ (2132 cm^{-1}) and $[Fe(CN)_6]^{4-}$ (2094 cm^{-1}) were compared to MV complexes and it was concluded that the ν_{bridge} was at the highest frequency due to electron withdrawal from the lowest antibonding orbital (σ^*) of the ν_{bridge} mode.[20–22] Why is the ν_{bridge} mode so much weaker? What is the structure of the molecule in solution? How many separate ν_{CN} modes are there within the IR absorption band? Once those questions are addressed one might ask why are charge transfer dynamics in these systems so very fast? Back-electron transfer occurring in <300 fs must have a highly energetically-favorable pathway in order to occur so rapidly.

Worked on cyano-bridged MV compounds is not the only work done on the ultrafast vibrational spectroscopy of the ν_{CN} mode. The free cyanide ion (CN^-) in solution behaves much differently than when it is ligated to a metal center, as in the latter case the π^* orbitals of the ligand interact very strongly with the d orbitals of the metal. Vibrational energy phase and relaxation dynamics of CN^- in aqueous solution have been investigated both experimentally and theoretically.[23–29] The frequency of CN^- in D_2O is 2079 cm^{-1} and the vibrational relaxation time (T_1) is 71 ± 3 ps.

More recent work on metal−CN vibrational dynamics has come out of the Owrutsky group, where they have characterized vibrational relaxation dynamics for mononuclear systems including $Au(CN)_2^-$, $Pt(CN)_4^{2-}$, $Mn(CN)_6^{3-}$, and $Ru(CN)_6^{4-}$.[30,31] They have also attempted a study on soluble Prussian Blue nanoparticles.[32] Their work alone shows how much the electronic structure adjacent to the π orbitals of a CN ligand changes the nature of the vibration itself. Finally, this group has also measured the vibrational relaxation times of ferro- and ferricyanide in solution. These results are tabulated in Table 3.1 with D_2O as the solvent, where T_1 times vary from 8 to 170 ps depending on the structure and charge of the molecule in solution.

Table 3.1: Intramolecular vibrational relaxation (T_{IVR}) and vibrational population relaxation (T_1) in metal cyanides in D_2O.[31] PB refers to a Prussian Blue nanoparticle.[32]

Molecule	T_{IVR} (ps)	T_1 (ps)
$Au(CN)_2^-$	–	170 ± 24
$Pt(CN)_4^{2-}$	1.6 ± 0.6	100 ± 30
$Mn(CN)_6^{3-}$	1.1 ± 0.4	28 ± 2
$Ru(CN)_6^{4-}$	1.4 ± 0.6	34 ± 4
$Fe(CN)_6^{4-}$	–	24 ± 3
$Fe(CN)_6^{3-}$	–	8.0 ± 1.5
PB	–	32 ± 4

We chose to study a novel trinuclear mixed-valence species first synthesized by Bocarsly and coworkers in 1990.[33] The assignment of the modes in the FTIR spectrum of $Fe^{II}Pt^{IV}Fe^{II}$ is loosely based ob previous work that separated the two bands into "terminal" and "bridging" ν_{CN} modes.[19] The starting point for the work on $Fe^{II}Pt^{IV}Fe^{II}$ in D_2O in this chapter

is to assign specific modes in the FTIR spectrum in order to understand vibrational energy flow in the complex system and the role that energy flow plays in chemical reactivity.[34]

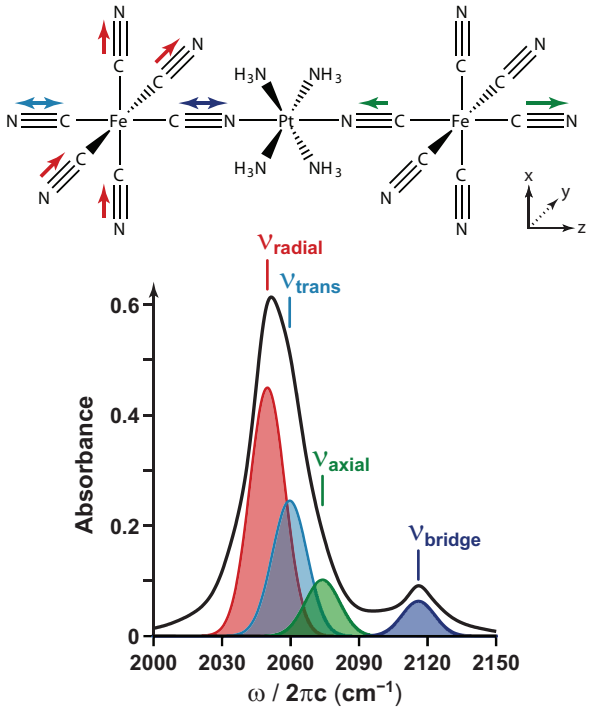

Figure 3.1: (Top) Cartoon of the molecular structure of $[Fe^{II}Pt^{IV}Fe^{II}]^{4-}$ with D_{4h} symmetry. Colored arrows correspond to simplified depictions of four ν_{CN} modes. The transition moments of the ν_{trans} (cyan), ν_{axial} (green), and ν_{bridge} (blue) modes lie along the MMCT axis and are perpendicular to the ν_{radial} (red) mode. Detailed descriptions of each normal mode are presented in Figure 4A.2 on page 103. (Bottom) Solvent-subtracted FTIR spectrum of $Fe^{II}Pt^{IV}Fe^{II}$ in D_2O fitted to four Gaussian peaks centered at 2050, 2060, 2074, and 2116 cm^{-1} corresponding to the center frequencies of the ν_{CN} modes defined above.

The molecular structure and Fourier transform infrared (FTIR) spectrum of $Fe^{II}Pt^{IV}Fe^{II}$ are shown in Figure 3.1. The FTIR spectrum contains contributions from four ν_{CN} modes labeled as ν_{radial} (2050 cm^{-1}), ν_{trans} (2060 cm^{-1}), ν_{axial} (2074 cm^{-1}), and ν_{bridge} (2116 cm^{-1}).[35,36] These assignments are consistent with previous resonance Raman studies on $Fe^{II}Pt^{IV}Fe^{II}$ in solution, previous IR studies of dinuclear cyano bridged mixed-valence complexes, as well as pump−probe anisotropy measurements shown later in this chapter.[37–40]

Bocarsly and coworkers have applied Hush-Mulliken analysis on $Fe^{II}Pt^{IV}Fe^{II}$ in order to

extract the energetics involved in the three-parabola system as shown in Chapter 1.[41] They have also done some nice work to prove that the best way to think of $Fe^{II}Pt^{IV}Fe^{II}$ is as two dimers with a shared acceptor.[40] They also showed that there is no electronic coupling between the equivalent electronic excited state defined by $Fe^{III}Pt^{III}Fe^{II}$ and $Fe^{II}Pt^{III}Fe^{III}$. Hush theory can be applied to $Fe^{II}Pt^{IV}Fe^{II}$ since it falls under Class II of the Robin and Day classification. The crystal structure of $Fe^{II}Pt^{IV}Fe^{II}$ revealed that the distance between the Fe and Pt atoms is 4.99 Å.[33] The results are as follows, where the ground state (GS) is state 1 and the charge-transfer state (CTS) is state 2. Consider the following parameters: E_{op} is the energy of the optical pump, E_{th12} is the thermal energy required to induce the $Fe^{II}Pt^{IV}Fe^{II} \rightarrow Fe^{III}Pt^{III}Fe^{II}$ reaction, λ_{12} is the solvent reorganization energy, and ΔE_{12} is the free energy of the redox couple between $Fe^{II}Pt^{IV}Fe^{II}$ and $Fe^{III}Pt^{III}Fe^{II}$. When pumping the MMCT band at 424 nm, $E_{\mathrm{op}} = 23585\ \mathrm{cm}^{-1}$. ΔE_{12} has been calculated by Pfennig and Bocarsly by the difference in reduction potential $E_{\mathrm{red}}(Fe^{\mathrm{III/II}}) - E_{\mathrm{red}}(Pt^{\mathrm{IV/III}}) = 1.1\ \mathrm{eV} = 8900\ \mathrm{cm}^{-1}$. Then, $\lambda_{12} = E_{\mathrm{op}} - \Delta E_{12} = 14650\ \mathrm{cm}^{-1}$ and $E_{\mathrm{th12}} = E_{\mathrm{op}}^2/4\lambda_{12} = 9500\ \mathrm{cm}^{-1}$. Finally, the activation energy required to move from state 2 (the CTS) to state 1 (the GS) is $E_{\mathrm{a21}} = E_{\mathrm{th12}} - \Delta E_{12} = 600\ \mathrm{cm}^{-1}$. This analysis reveals that optical excitation into the MMCT band deposits a huge amount of excess energy that must reorganize and that the barrier to back-electron transfer is very small ($\sim 3k_{\mathrm{B}}T$). Moreover, the CTS is separated from the GS by >4 quanta of a ν_{CN} mode.

The goal of this chapter is to learn as much as possible about the electronic ground state of $Fe^{II}Pt^{IV}Fe^{II}$ in D_2O, as this information will be crucial in later chapters when electronic excitation brings the system far from equilibrium and non-equilibrium relaxation dynamics back to the electronic ground state are probed. The measurement of the anharmonic vibrational couplings between each of the four ν_{CN} modes in solution is relied upon for assignments. Here, the challenge of understanding the electronic ground state of a trinuclear mixed-valence complex in solution with many ν_{CN} modes is explored. This chapter begins with a brief description of the experimental apparatus used to collect and subsequently analyze third-order nonlinear infrared signals in Section 3.2. The main body of this chapter is in the results and discussion section that makes up Section 3.3. This section looks to extract structural (§3.3.1), dynamical (§3.3.2), solvation (§3.3.3), and anharmonic coupling

(§3.3.4−3.3.5) information for $Fe^{II}Pt^{IV}Fe^{II}$ in D_2O. A brief summary and outlook follows in Section 3.4.

3.2 Experimental

The experimental procedure used to collect 2D IR spectra in the boxcar phase-matching geometry has been explained in detail elsewhere.[42] In brief, approximately 30% of a 35 fs, 2.8 mJ, 800 nm beam originating in a titanium sapphire regenerative amplifier (Newport, Spitfire Pro 35F-XP) is directed into a commercial dual-pass optical parametric amplifier (Newport, OPA-800C) to produce near-IR (NIR) signal and idler beams. These beams are focused softly into a 0.5 mm $AgGaS_2$ crystal for difference frequency mixing to afford a mid-IR (MIR) pulse centered at $\omega_{\mathrm{MIR}} = 2030$ cm^{-1} ($\lambda_{\mathrm{MIR}} = 4.9$ μm) with a spectral bandwidth of $\Delta\omega_{\mathrm{MIR}} = 270$ cm^{-1}. Any residual NIR is filtered out with a germanium long-pass filter and then the MIR is overlapped with a tracing HeNe beam on an antireflection-coated Ge window at normal incidence. Finally, the MIR beam is temporally compressed to ∼80 fs via material compensation with 3 mm of bare CaF_2.[43] An example mid-IR spectrum and corresponding autocorrelation is shown in Figure 3.2.

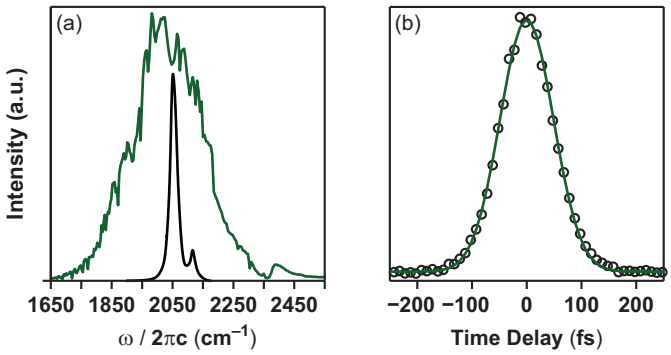

Figure 3.2: (a) Mid-IR spectrum (green) and FTIR spectrum of $Fe^{II}Pt^{IV}Fe^{II}$ in D_2O. The spetrum is centered at 2030 cm^{-1} ($\lambda = 4.9$ μm) and has a bandwidth of 270 cm^{-1}. (b) Autocorrelation (ac) of two IR pulses in $AgGaS_2$ (∘) fit to a Gaussian line shape (−) with $\Delta t_{\mathrm{pulse}} = 80$ fs ($\Delta t^{\mathrm{ac}}_{\mathrm{fwhm}} = \sqrt{2}\Delta t_{\mathrm{pulse}} = 113$ fs).

The MIR beam (∼3 μJ) is split into five beams using a 5-beam Michelson interferometer involving a combination of 4 mm ZnSe 50:50 beamsplitters and compensation plates (Rocky

Mountain Instrument Co.) Each reflective optic is gold coated. Each arm has a half-wave plate (company) and wire-grid polarizer (Thorlabs) combination for polarization control. The beams are labeled as follows: beams 1−3 are incident on the sample to generate a third-order signal, beam 4 is the tracer (T) beam for alignment and pump−probe experiments, and beam 5 is the local oscillator (LO) for heterodyne detection. Relative timing of the beams is controlled with three computer-controlled delay stages (Newport, XMS50) in the 1, 2, and T arms. Beam 3 is fixed and is used to define a time delay of zero ($t = 0$). Beams 1−3 are aligned in the boxcar geometry (1-inch box) and focused onto the sample with a $f = 127$ mm 90° off-axis parabolic mirror to a spot-size of ∼150 μm ($1/e^2$). Time zero between each of the pulse pairs was found by correlation of the pulses in a 0.5 mm $AgGaS_2$ crystal. All MIR signal fields are focused into a monochromator (Horiba Jobin Yvon, Triax 190) for spectral dispersion and detected with a 2×64 HgCdTe (MCT) array detector (Infrared Systems Development, IR0144).

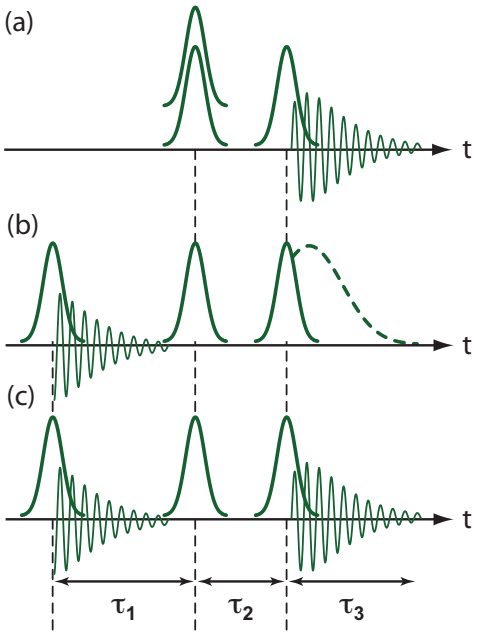

Figure 3.3: Pulse sequences for third-order IR spectroscopies, including (a) DPP, (b) VEPS, and (c) 2D IR. $\tau_1 \equiv$ coherence, $\tau_2 \equiv$ population ("waiting"), and $\tau_3 \equiv$ detection time.

Fourier transform third-order IR spectroscopies involve the interaction of three IR elec-

tric fields with the system of interest. The experiment is defined by three time delays as illustrated in the pulse sequences shown in Figure 3.3. These time delays are referred to as the evolution (τ_1), population (τ_2), and detection (τ_3) periods. The most general pulse sequence for 2D IR is shown in Figure 3.3c. The first pulse prepares a vibrational coherence that oscillates and decays during τ_1. This is better known as a free-induction decay (FID). The second pulse can do many things, including (i) create a vibrational population in the ground or vibrationally-excited state, (ii) further excite the same vibrational mode, or (iii) excite another vibration. The final pulse creates another vibrational coherence that evolves along the detection period (τ_3). There are many third-order nonlinear IR spectroscopies that differ by the number of field/matter interactions and the time delays between the fields. These variations are useful for extracting unique information. Dispersed pump−probe (DPP, Fig. 3.3a) spectroscopy measured vibrational energy relaxation along τ_2, whereby the probe field mixes with the signal and is then detected. Vibrational echo peak shift (VEPS, Fig. 3.3b) involves scanning both τ_1 and τ_2, though the signal is background free and not mixed with a probe field. 2D IR (Fig. 3.3c) is similar to VEPS; however, the signal is mixed with a reference field so that the coherence along τ_3 can be measured. Each of these pulse sequences will be used and explored throughout this chapter. It will be shown when each sequence is appropriate and what information can be gained from each technique.

3.2.1 Dispersed pump−probe

IR−IR pump−probe experiments were performed using beam 1 as the pump, the tracer (T) as the probe, and a local oscillator (LO) as a reference. The probe was directed towards the top stripe of the array detector, while the LO was incident on the bottom stripe. In this manner, shot-to-shot normalization of the probe fluctuations were divided out to afford high signal-to-noise (S/N). Pump−probe data shown in this paper correspond to 25 scans from 0 to 100 ps at 2000 shots per data point (∼4.5 hour collection time).

3.2.2 Vibrational echo peak shift and 2D IR

Time delays between IR pulses follow labeling schemes used in third-order nonlinear IR spectroscopies where τ_1 is the vibrational coherence period, τ_2 is the vibrational population period (i.e., waiting time), and τ_3 is the detection period. There are two important phase matching conditions that lead to third-order signals, which are (i) rephasing (R) where $\mathbf{k}_{\text{sig}} = -\mathbf{k}_1 + \mathbf{k}_2 + \mathbf{k}_3$, and (ii) non-rephasing (NR) where $\mathbf{k}_{\text{sig}} = +\mathbf{k}_1 - \mathbf{k}_2 + \mathbf{k}_3$. Rephasing signals are known as vibrational echoes. All third-order IR signals are collected in the time-frequency arrangement, such that spectra are collected as τ_1 is scanned for fixed values of τ_2. In this manner the detected frequency axis is generated automatically since the grating effectively performs a cosine Fourier transform along τ_3. Homodyne-detected vibrational echo peak shift signals were sent directly to the array detector, as no shot-to-shot normalized of a probe is necessary. VEPS data shown in this paper correspond to 25 scans from $\tau_1 = -500$ to 1000 fs in 10 fs steps and $\tau_2 = 0$ to 30 ps in unequal time steps with 4000 shots per data point ($\sim$4.5 hour collection time). The maximum OD of the sample was 0.75 when $c \approx 13$ mM and $l = 50$ μm.

Heterodyne detection is more involved, as the third-order signal field is mixed with the LO on a ZnSe 50:50 beamsplitter. Balanced detection is achieved by measuring both the reflected and transmitted portions of the signal/LO combinations on each of the stripes of the MCT array and subtracting the two signals.[44,45] This effectively eliminates the noise and doubles the signal, which of course greatly improves the overall S/N of the data. 2D IR data shown in this paper correspond to 2 total scans from $\tau_1^{\text{R}} = 0$ to 2200 fs in 4 fs steps, $\tau_1^{\text{NR}} = 0$ to 1500 fs in 4 fs steps, and $\tau_2 = 0.150$, 0.340, 0.680, 1.34, 2.04, 5.00, 7.50, 10.0, and 15.0 ps with 2000 shots per data point ($\sim$4.5 hour collection time). The maximum OD of the sample was 0.75 when $c \approx 13$ mM and $l = 50$ μm.

3.2.3 Data analysis: generating a 2D IR spectrum

All 2D IR data in this chapter was taken in the so-called time-frequency arrangement, where the signal/LO combination is spectrally dispersed onto an array detector to measure the ω_3 axis. τ_1 is then scanned in small steps to build up a 2D signal matrix parameterized

by the value of τ_2: $S_{2D}(\tau_1, \omega_3; \tau_2)$. This section outlines how to turn $S_{2D}(\tau_1, \omega_3; \tau_2)$ into $S_{2D}(\omega_1, \omega_3; \tau_2)$ via Fourier transformation.

This section assumes the following has been collected in lab: (i) $S^{R}_{2D}(\tau_1^{R}, \omega_3; \tau_2)$ and $S^{NR}_{2D}(\tau_1^{NR}, \omega_3; \tau_2)$, (ii) the dispersed IR pump−probe spectra for all collected τ_2 points: $S_{DPP}(\omega_3; \tau_2)$, (iii) the tracer spectrum: $I_{TR}(\omega_3)$, (iv) the local oscillator spectrum: $I_{LO}(\omega_3)$, and (v) a calibrated ω_3 axis. It is also assumed that balanced detection (subtraction of oppositely-signed oscillating signals) was used in lab the the data matrices loaded are balanced (e.g., CN_mat_avg111R.dat).

The first step is to divide the DPP spectrum by the tracer to normalize out any responsivity differences along the array: $\tilde{S}_{DPP}(\omega_3; \tau_2) = S_{DPP}(\omega_3; \tau_2)/\sqrt{(I_{TR}(\omega_3))}$. One then finds an accurate value for $\tau_1 = 0$ by interpolating both $S^{R}_{2D}(\tau_1^{R}, \omega_3; \tau_2)$ and $S^{NR}_{2D}(\tau_1^{NR}, \omega_3; \tau_2)$ around $\tau_1 = 0$ and adding a small shift in $\tau_1^{R,NR}$ for best fit against $\tilde{S}_{DPP}(\omega_3; \tau_2)$. That shift is then added to correct for inaccuracies in $\tau_1 = 0$ and data for $\tau_1 < 0$ is deleted from the matrix. R and NR matrices are then zero padded to the appropriate Fourier transform length ($2^n; n = 13$ here). The matrices are then subtracted by their mean and multiplied by an apodization function to ensure that they decay smoothly to zero. Three examples of apodization functions are shown in Equation 3.1:

$$\begin{aligned}
\tilde{A}_{\text{triangle}} &= 1 - \frac{\tau_1}{\max(\tau_1)} \\
\tilde{A}_{\text{cosine}} &= \cos\left(\frac{\pi\tau_1}{2\max(\tau_1)}\right) \\
\tilde{A}_{\text{nuttal}} &= 0.355768 + 0.487396\cos\left(\frac{\pi\tau_1}{\max(\tau_1)}\right)\cdots \\
&\quad + 0.144232\cos\left(\frac{2\pi\tau_1}{\max(\tau_1)}\right) + 0.012604\cos\left(\frac{3\pi\tau_1}{\max(\tau_1)}\right)
\end{aligned} \tag{3.1}$$

Finally, both the R and NR matrices are Fourier transformed along τ_1 for each value of ω_3 and shifted for symmetry. Each spectrum is divided by $\sqrt{(I_{LO}(\omega_3))}$ for every ω_1 slice to normalize spectral response across the array. The so-called "correlation" spectrum is generated by adding the R and NR responses:

$$S_{2D}^{corr}(\omega_1, \omega_3; \tau_2) = S_{2D}^{R}(\omega_1, \omega_3; \tau_2) + S_{2D}^{NR}(\omega_1, \omega_3; \tau_2) \tag{3.2}$$

The final step is the most difficult step, as one has to "phase" the spectrum according to the projection-slice theorem. In essence, the projection of the correlation spectrum must be identical to the DPP spectrum.

$$S_{phased}^{corr}(\omega_1, \omega_3; \tau_2) = S_{2D}^{corr}(\omega_1, \omega_3; \tau_2) \exp\left[-i(\omega_3 \Delta\tau_3 + \Delta\phi_3)\right] \tag{3.3}$$

where $\Delta\tau_3$ corrects for inaccuracies in the signal/LO temporal overlap and $\Delta\phi_3$ is a constant phase factor. In some cases it helps to separate the ω_3 axis into two pieces, especially if the signal levels between the two regions are significantly different (as is the case for $Fe^{II}Pt^{IV}Fe^{II}$ in D_2O).

3.3 Results and Discussion

In theory, all of the information available from DPP and VEPS experiments is encoded in a collection of 2D IR spectra taken along the vibrational waiting time. However, due to the length of time it takes to collect one high fidelity 2D IR spectrum (in the traditional 3-beam geometry), it is more practical to use the DPP data to obtain the vibrational energy relaxation dynamics, the VEPS data for correlation time scales (i.e., the line shape function), and the 2D IR spectra to learn about the anharmonic vibrational couplings. No additional experimental effort is required to collect this set of data on the same day (or days). An added bonus of this approach is the ability to fix certain parameters obtained from the DPP and VEPS data when simulating 2D IR spectra. This reduces the number of variables in the fit, which is significant with a system of 4+ vibrational modes, such as $Fe^{II}Pt^{IV}Fe^{II}$ in D_2O.

3.3.1 Polarization-selective 2D IR spectroscopy

Two-dimensional infrared spectroscopy is a tool that can, in principle, determine all of the information contained in DPP and VEPS spectroscopy; however, the length of time it takes

to acquire a 2D IR spectrum generally makes it a better approach to combine all of the spectroscopies. Similar to 2D NMR, 2D IR spectroscopy spreads vibrational information onto two frequency axes (ω_1 and ω_3).[46] Each resonant vibrational modes will give a pair of "diagonal" peaks ($\omega_1 = \omega_3$) that are separated along the ω_3 axis by the vibrational mode anharmonicity, Δ. Thus, one can immediately obtain molecular information when looking at a spectrum, as the anharmonicity of a mode is related to the curvature of the potential energy surface of that mode. One of the real strengths of 2D IR spectroscopy is the ability to measure cross peaks. That is, if two resonant vibrational modes in the same molecule are both within the bandwidth of the mid-IR laser pulse a cross peak will appear (if the two modes are in fact coupled) on the anti-diagonal of the spectrum. A cross-peak will again appear as a double peak such that the mixed-mode anharmonicity can be pulled off of the spectrum. This helps create a multidimensional view of the molecule. Analysis of a 2D IR spectrum comes down to three things: peak position, amplitude, and line shape.

Experimental determination of anharmonicities

The anharmonic coupling of vibrational modes in solution can be obtained through analysis of peak positions in a 2D IR spectrum.[47–50] This is a relatively easy task with a system involving few modes that are separated in frequency and narrow.[42] With a system such as $Fe^{II}Pt^{IV}Fe^{II}$ in D_2O, peaks are broad and overlapping, which creates some confusion with assignment. The best way to determine parameters is by fitting the experiment to simulation, as will be discussed in Section 3.3.4. A 2D IR spectrum of $Fe^{II}Pt^{IV}Fe^{II}$ at $\tau_2 = 150$ fs in the YYZZ polarization geometry (to highlight cross peaks) is presented in Figure 3.4 with a grid to help understand the vibrational assignments. The FTIR spectrum in Fig. 3.1 on page 49 at first glance shows two main peaks corresponding to terminal ν_{CN} modes and ν_{bridge}, which is why there are two positive peaks along the diagonal of the 2D IR spectrum. The peak on the top left of the spectrum corresponds to many overlapping cross peaks between the ν_{bridge} mode and the terminal ν_{CN} modes. It's important to note that in a 2D IR spectrum, diagonal features of mode a (for example) are proportional to $|\mu_a|^4$ whereas the cross peak intensity between mode a and b is proportional to $|\mu_a|^2|\mu_b|^2$.[51]

Thus, one cannot associate the "strength of coupling" to just the cross-peak intensity. Rather, the mixed-mode anharmonicity is the ultimate determination of the strength of coupling between two modes. Anharmonicities for each of the modes and their mixed-mode anharmonicities are displayed in matrix form in Table 3.2. Diagonal anharmonicities range from approximately 21−24 cm^{-1} whereas mixed mode anharmonicities are all ∼8 cm^{-1}. The mixed-mode anharmonicity is very apparent in the slice along $\omega_3 = 2106$ cm^{-1} where there is a large negative peak at the $\omega_1 = \omega_{terminal}$ frequencies as well as $\omega_1 = \omega_{bridge}$. It is important to keep track of the multiplication factors used throughout the 2D IR spectrum in Fig. 3.4 since the amplitudes are quite different.

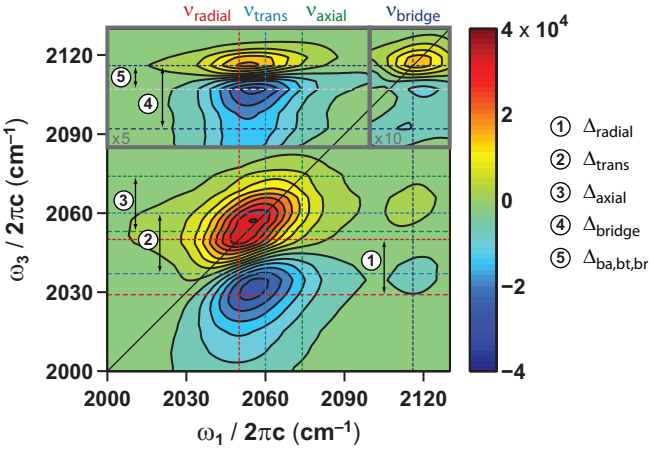

Figure 3.4: 2D IR spectrum of $Fe^{II}Pt^{IV}Fe^{II}$ in D_2O at $\tau_2 = 680$ fs in the YYZZ polarization geometry. The z-axis (intensity axis) is plotted on a linear scale according the color bar on the right with twenty equally-spaced contour lines. One solid black line is plotted along the diagonal. Dahsed lines are color-coded to the modes such that ν_{radial} is red, ν_{trans} is cyan, ν_{axial} is green, and ν_{bridge} is blue. The two same-colored lines in the ω_3 dimension correspond to the fundamental and the overtone transition with the separation labelled with a number from 1−5, as described in the legend to the right. Note that 5 is a combination band. The three boxes are scaled as follows $(\times n : \omega_1, \omega_3)$: $(\times 1 : 2000 - 2130\ cm^{-1}, 2000 - 2085\ cm^{-1}), (\times 5 : 2000 - 2085\ cm^{-1}, 2085 - 2130\ cm^{-1}), (\times 10 : 2085 - 2130\ cm^{-1}, 2085 - 2130\ cm^{-1})$.

While the peak amplitudes in one 2D IR spectrum do obtain information, such as the magnitude of the transition dipole moments of the vibrational modes, the best use of amplitude information is to follow the amplitude of a particular peak as a function of τ_2. In

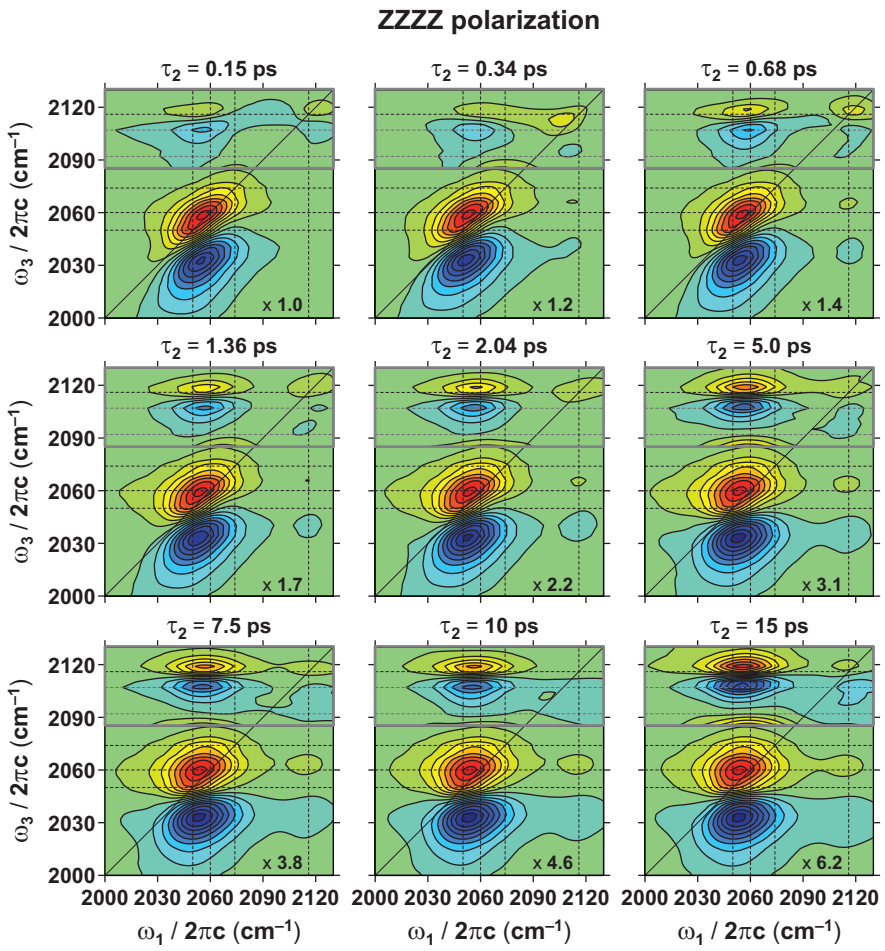

Figure 3.5: A series of 2D IR spectra as a function of τ_2 in the ZZZZ polarization geometry. The z-axis is given as twenty equally-spaced contour lines ranging from -1.2 to 1.2×10^5. Spectra have been normzlied to the positive terminal-region peak in the $\tau_2 = 150$ fs spectrum according to the multipication factors shown in the bottom right of each spectrum. In this manner, contour lines can be compared directly. The low-intensity ν_{bridge} region in the gray box has been multiplied by 5. Dashed lines are shown at the fundamental frequencies. In addition, lines have been added at $\omega_3 = 2106, 2092$ cm^{-1} to aid the eye.

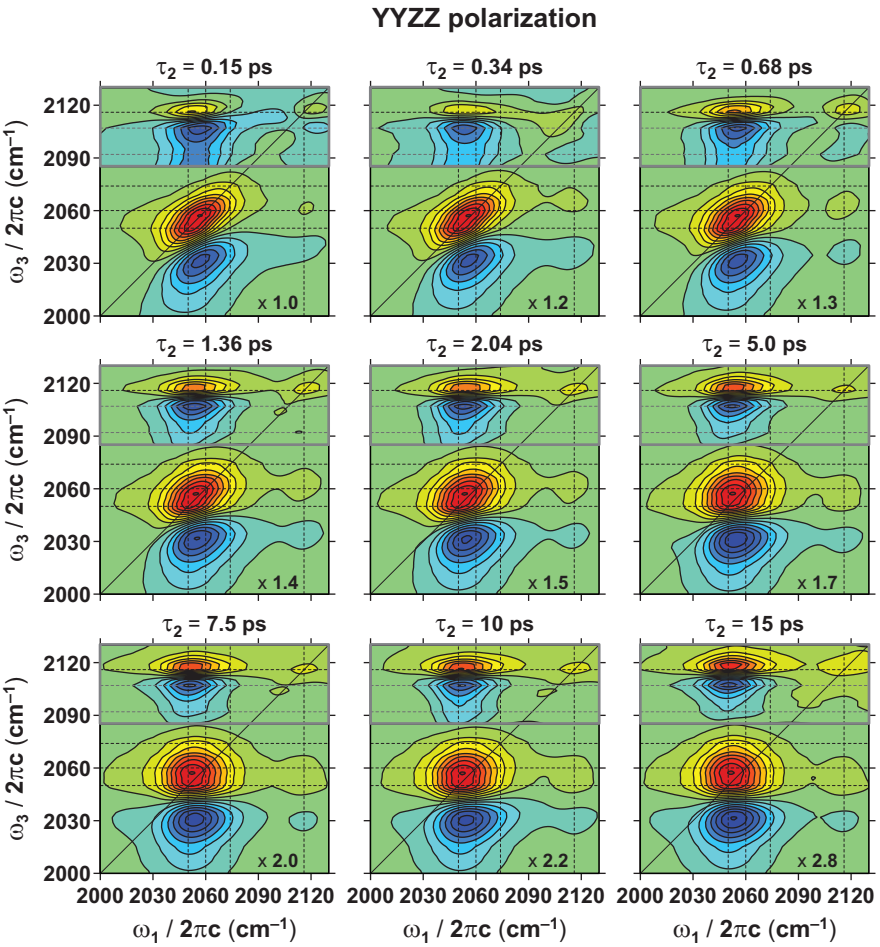

Figure 3.6: A series of 2D IR spectra as a function of τ_2 in the YYZZ polarization geometry. The z-axis is given as twenty equally-spaced contour lines ranging from -0.4 to 0.4×10^5. Spectra have been normzlied to the positive terminal-region peak in the $\tau_2 = 150$ fs spectrum according to the multipication factors shown in the bottom right of each spectrum. In this manner, contour lines can be compared directly. The low-intensity ν_{bridge} region in the gray box has been multiplied by 5. Dashed lines are shown at the fundamental frequencies. In addition, lines have been added at $\omega_3 = 2106, 2092$ cm^{-1} to aid the eye.

Table 3.2: Vibrational mode anharmonicity matrix for the four fundamental modes in $Fe^{II}Pt^{IV}Fe^{II}$. Values are given in cm^{-1}. Error in the values is estimated to be 2 cm^{-1}.

Mode	ν_{radial}	ν_{trans}	ν_{axial}	ν_{bridge}
ν_{radial}	21	8	8	8
ν_{trans}	–	23	8	8
ν_{axial}	–	–	21	8
ν_{bridge}	–	–	–	24

addition to the structural information one can obtain from 2D IR, Fayer and coworkers have pioneered a method called chemical exchange that can measure equilibrium constants of rapidly exchanging species in solution at room temperature.[52] 2D IR spectroscopy does not suffer from the overlap effects of DPP, meaning that specific "start" and "end" points of energy flow can be monitored. The amplitude of a peak is also dependent on the polarization of each of the input mid-IR beams. The two most common polarization geometries are "all-parallel" and "crossed" which will be written as ZZZZ and YYZZ. The convention is to write polarization in the lab-frame in capital letters and molecular-frame in small letters. The two series of 2D IR spectra at 9 values of τ_2 are shown in Figs. 3.5 (ZZZZ) and 3.6 (YYZZ).

Each of the series of spectra contains a lot of information. In this section, where we are considering the information available from peak amplitudes, it is best to monitor how the various signal intensities change as a function of τ_2. The general shape change of the peaks will be discussed in a later section. The figures have been presented such that contour levels on each spectrum can be compared directly (see caption). The region near the top in the grey box has been multiplied by 5 for clarity. Thus, perhaps the first thing to notice is that the cross peak intensity increases as a function of τ_2.

Angular information from 2D IR

Angular information can be obtained with 2D IR.[53–57] That is, the angle between transition dipole derivative vectors of two vibrational modes can be calculated using the ratio of the intensity of a cross-peak taken in the crossed and parallel polarization geometry. This

calculation has to be done as close to $\tau_2 = 0$ as possible since energy transfer between modes of differing polarization will change the calculated angle. Naturally, peak overlap also complicates the measurement. Phasing procedures using to obtain correlation spectra can also change the amplitude of features in a 2D spectrum. Therefore, sometimes it is better to use an absolute value rephasing or nonrephasing spectrum to determine the angles.[58]

$$\begin{aligned} \Theta_{\mathrm{ab}}(R) &= \frac{180}{\pi} \cos^{-1} \sqrt{\frac{2-R}{2R+1}} \\ R &= \frac{S_{\mathrm{NR}}(\omega_a, \omega_b; \mathrm{YYZZ})}{S_{\mathrm{NR}}(\omega_a, \omega_b; \mathrm{ZZZZ})} \end{aligned} \tag{3.4}$$

Equation 3.4 outlines the procedure for determining the angle between two vibrational modes, where $S_{\mathrm{NR}}(\mathrm{YYZZ})$ is the a,b cross peak amplitude in the crossed polarization geometry. Note that in some cases it is necessary to subtract a baseline. The results of the analysis are given in Table 3.3. The results suggest a slight deviation from D_{4h} symmetry.

Table 3.3: Calculated angles extracted from the ZZZZ and YYZZ 2D IR spectra at $\tau_2 = 150$ fs according to Equation 3.4. Absolute-value non-rephasing spectra were used.

Mode	Θ (deg)
ν_{radial}	70 ± 2
ν_{trans}	29 ± 4
ν_{axial}	31 ± 3
ν_{bridge}	0

For comparison, the relationship between absolute-value rephasing signals and Θ is[53]

$$\frac{S_{\mathrm{R}}(\omega_a, \omega_b; \mathrm{YYZZ})}{S_{\mathrm{R}}(\omega_a, \omega_b; \mathrm{ZZZZ})} = \frac{3 + \cos^2 \Theta_{\mathrm{ab}}}{4 + 8\cos^2 \Theta_{\mathrm{ab}}}. \tag{3.5}$$

3.3.2 Vibrational dynamics

Polarization-selective pump−probe

The dispersed pump−probe spectrum is shown in Figure 3.7a. Here, we use one of the 2D IR conventions where the signal bleach is positive ($\Delta A > 0$) and transient absorption is negative ($\Delta A < 0$).[42,59,60] Pump and probe polarizations were set at magic angle (54.7°)

to eliminate rotational alignment artifacts.[61] Dashed lines at the center frequencies for each of the modes (see Fig. 3.1) are overlaid. The kinetics of the pump−probe data are shown in Fig. 3.7b with the population time axis (τ_2) on a log-scale to highlight the early-time dynamics. Kinetic data were fit to a form shown in Equation 3.6, which includes two decaying exponentials and an exponentially decaying cosine term for the beat.[35] These fits are shown with gray solid lines.

$$\Delta A(\tau_2) = \sum_{i=0}^{1} A_i \exp(-\tau_2/T_i) + A_{\text{osc}} \exp(-\tau_2/T_{\text{osc}}) \cos(2\pi c\omega_{\text{osc}}\tau_2 + \phi_{\text{osc}}) + \Delta A_\infty \quad (3.6)$$

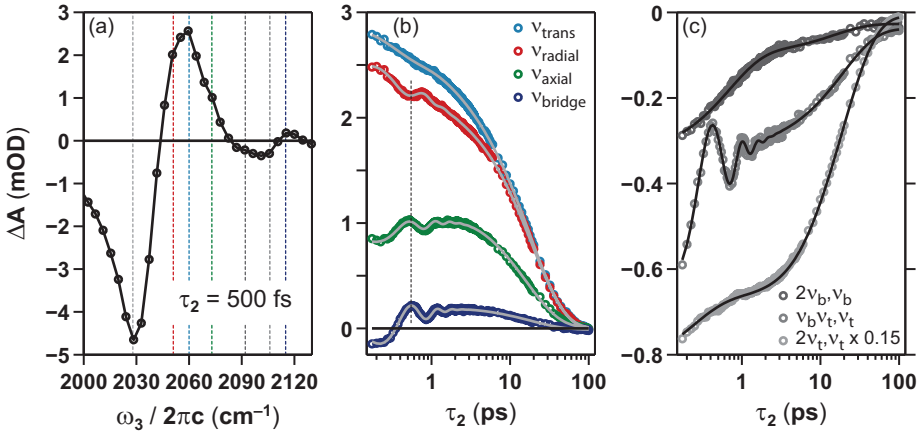

Figure 3.7: (a) Dispersed pump−probe spectrum of $Fe^{II}Pt^{IV}Fe^{II}$ in D_2O at $\tau_2 = 500$ fs. Keeping with one convention of 2D IR, positive signals ($\Delta A > 0$) correspond to a bleach and positive signals represent transient absorption. Dahsed vertical lines are color-coded according to frequencies monitored as a function of τ_2 in the next panels. (b) Bleach recovery dynamics representing vibraiotnal population relaxation of the four fundamental modes if $Fe^{II}Pt^{IV}Fe^{II}$. Fits are shown as solid gray lines (see Tables 3.4−3.5 starting on page 64). The dotted veritcal line aids helps see the difference in the phase of the beat. (c) VER dynamics of the ν_{bridge} overtone ($2\nu_b, \nu_b = 2092$ cm^{-1}), ν_{trans} overtone ($2\nu_t, \nu_t = 2037$ cm^{-1}), and the $\nu_{\text{bridge}} + \nu_{\text{trans}}$ combination band ($\nu_b\nu_t, \nu_t = 2106$ cm^{-1}).

The results from the fit have been broken up into two sets as displayed in Tables 3.4−3.5. Table 3.4 highlights the time scales of vibrational relaxation, where there is one relatively fast time scale (< 2 ps) corresponding to intramolecular vibrational energy relaxation (IVR)

and one longer time scale (15−20 ps) corresponding to vibrational population relaxation (sometimes called T_1 relaxation in correspondence with NMR). It is important to note the sign of the amplitude of the decay component, as here positive amplitude corresponds to a decay whereas negative amplitude corresponds to a rise. Therefore, the fitting results reveal that the ν_{radial} and ν_{trans} amplitudes only decay whereas population in the ν_{axial} and ν_{bridge} modes increases at early τ_2 and subsequently decays on a long time scale. Overtones of the ν_{trans} and ν_{bridge} modes also greatly differ when it comes to VER, as the $2\nu_{\text{trans}}$, ν_{trans} trace decays ∼17% on a 2.5 ps time scale and the majority (∼75%) on a 19 ps time scale. However, the majority of the $2\nu_{\text{bridge}}$, ν_{bridge} trace (∼77%) decays on a 680 fs time scale and a minority (∼23%) decays on a 15 ps time scale. This can be explained by a simple energy-level diagram, as the $2\nu_{\text{bridge}}$, ν_{bridge} mode at ($2\nu_b - \Delta_b = 4208$ cm^{-1}) is the highest energy level in the system ($2\nu_t - \Delta_t = 4097$ cm^{-1}).

Table 3.4: Population relaxation component of the DPP fitting results (Eq. 3.6) presented in Figs. 3.7b and 3.7c. Error is given as a 95% confidence interval.

Mode	T_0 (ps)	T_1 (ps)	A_0[1]	A_1	ΔA_∞ (mOD)
ν_{radial}	0.95 ± 0.05	19 ± 1	0.09 ± 0.02	0.84 ± 0.07	-0.01 ± 0.01
ν_{trans}	1.8 ± 0.1	18 ± 1	0.10 ± 0.01	0.79 ± 0.06	0.00 ± 0.01
ν_{axial}	1.2 ± 0.1	16 ± 1	-0.19 ± 0.02	0.73 ± 0.06	0.01 ± 0.01
ν_{bridge}	0.76 ± 0.03	19 ± 2	-0.26 ± 0.03	0.29 ± 0.03	-0.01 ± 0.01
$2\nu_{\text{trans}}, \nu_{\text{trans}}$	2.5 ± 0.1	19 ± 2	-0.17 ± 0.02	-0.75 ± 0.02	-0.06 ± 0.01
$2\nu_{\text{bridge}}, \nu_{\text{bridge}}$	0.68 ± 0.03	15 ± 1	-0.77 ± 0.06	-0.23 ± 0.03	-0.03 ± 0.02
$\nu_{\text{bridge}}\nu_{\text{trans}}, \nu_{\text{trans}}$	0.69 ± 0.03	19 ± 2	-0.16 ± 0.03	-0.41 ± 0.02	-0.01 ± 0.01

[1] Amplitudes normalized such that $\sum_i |A_i| = 1$ including A_{osc} in Tab. 3.5.

Table 3.5 separates the oscillatory component of the fit. This oscillation arises from the coherent coupling of two modes that have been excited by the same broad IR pump pulse. Therefore, T_0 is a measure of the time it takes for coherently coupled modes to dephase (400−600 fs in this case), and ω_{osc} represents the beat frequency (i.e., the difference between the frequency of the two modes.) For example, the ν_{bridge} trace oscillates with a beat frequency of ∼52 cm^{-1} implying that a mode at or near 2116 cm^{-1} − 52 cm^{-1} = 2064 cm^{-1} is strongly coupled to ν_{bridge}. The phase of the oscillation changes depending on what

Table 3.5: Oscillatory component of the DPP kinetics (Eq. 3.6) presented in Figs. 3.7b and 3.7c. Error is given as a 95% confidence interval.

Mode	T_{osc} (ps)	A_{osc}[1]	ω_{osc} (cm^{-1})	ϕ_{osc} (rad)
ν_{radial}	0.42 ± 0.03	0.07 ± 0.02	52 ± 2	-1.9 ± 0.3
ν_{trans}	...	...	...	...
ν_{axial}	0.62 ± 0.05	0.08 ± 0.02	55 ± 2	0.9 ± 0.2
ν_{bridge}	0.46 ± 0.04	0.45 ± 0.04	52 ± 1	0.6 ± 0.1
$2\nu_{\text{trans}}, \nu_{\text{trans}}$	...	...	...	...
$2\nu_{\text{bridge}}, \nu_{\text{bridge}}$	...	...	...	...
$\nu_{\text{bridge}}\nu_{\text{trans}}, \nu_{\text{trans}}$	0.43 ± 0.02	0.43 ± 0.02	57 ± 2	-4.7 ± 0.4

[1] Amplitudes normalized such that $\sum_i |A_i| = 1$ including amplitudes in Table 3.4.

frequency is plotted. This is a signature of coherent coupling, as the phase of the beat should change as a function of ω_3. That is why the ν_{trans} modes does not appear to beat, as the oscillations cancel out. It is clear to see that the ν_{bridge} mode has the strongest beat ($\sim$45%). This is because this frequency is highly overlapped with cross peaks as will be discussed in when the 2D IR results are presented in Section 3.3.1. It is important to note that the lack of beat in the overtones is not due to phase cancellation; rather, these frequencies should not beat at all. The fact that they do not beat is a large factor in assigning the peaks as they are currently assigned. For example, the $\nu_{\text{bridge}} + \nu_{\text{trans}}$ combination band oscillates as expected, which helped assign the feature as such.

Pump−probe anisotropy

Dispersed pump−probe anisotropy, which is a measure of the difference in signal as a function of polarization as defined in Equation 3.7, is a powerful piece of information. In this case of IR pump−probe anisotropy, $r(0)$ can be related to the angle between the transition dipole moment of an initially-excited vibrational mode i and the vibrational mode to which energy has been transferred j as shown in Equation 3.8.[62,63] Also, the decay of $r(\tau_2)$ is related to the orientation diffusion rate (D_{or}). Anisotropy decays for $Fe^{II}Pt^{IV}Fe^{II}$ in D_2O are presented in Figure 3.8.

$$r = \frac{I_{\parallel} - I_{\perp}}{I_{\parallel} + 2I_{\perp}} \tag{3.7}$$

$$r(\theta_{ij}) = \frac{1}{5}\left(\cos^2\theta_{ij} - 1\right) \tag{3.8}$$

DPP anisotropy fittings results are presented in Table 3.6. One of the major difficulties in understanding anisotropy data in a system like $Fe^{II}Pt^{IV}Fe^{II}$ in D_2O is the amount of spectral overlap present. This can create confusion since overlap with a parallel ($r(0) = 0.4$) and perpendicular ($r(0) = -0.2$) mode can give any range of values for $r(0)$. In addition, this overlap can change as a function of τ_2 depending on the difference in VER time scales of the two modes. However, it is still worth investigating to find trends.

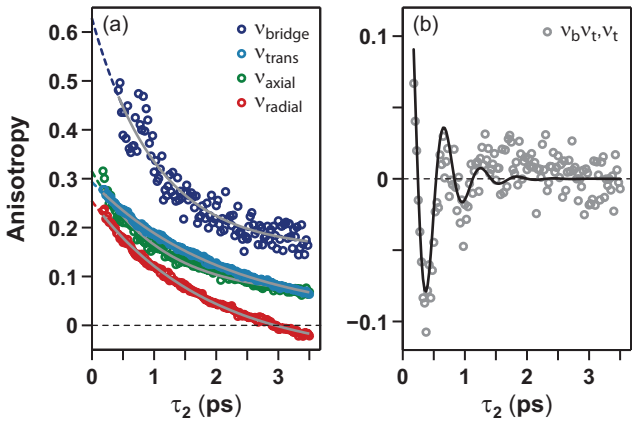

Figure 3.8: (a) IR pump−probe anisotropy dynamics for the four fundamental modes. Fitting results are given in Table 3.6 on page 67. Dashed lines correspond to an extrapolation of fit to $\tau_2 = 0$. (b) The pump−probe anisotropy of the $\nu_{\text{bridge}} + \nu_{\text{trans}}$ combination band oscillates as a function of τ_2 with a frequency of $\sim$57 cm^{-1}, as shown in Equation 3.10 (see pg. 67). The data has been shifted by a constant offset of 0.036 to highlight the beat decay of $\sim$0.4 ps.

$$\begin{aligned} r(\tau_2;\omega_3) &= r_0 \exp(-\tau_2/T_r) + r_\infty \\ D_{or}^{-1} &= 6 \cdot T_r \end{aligned} \tag{3.9}$$

Fundamental frequencies were fit to Eq. 3.9 in order to determine the orientation dif-

Table 3.6: DPP anisotropy fitting results (Eqns. 3.9−3.10) for the data presented in Fig. 3.8, where $r_{\mathrm{extrap}}(0) = r_0 + r_\infty$. Error is reported as a 95% confidence interval.

Mode	r_0	T_{r} (ps)	D_{or}^{-1} (ps)	r_∞	$r_{\mathrm{extrap}}(0)$
ν_{radial}	0.320 ± 0.005	1.9 ± 0.1	11.4 ± 0.6	-0.067 ± 0.007	0.25 ± 0.01
ν_{trans}	0.280 ± 0.005	2.2 ± 0.1	13.2 ± 0.6	0.013 ± 0.007	0.29 ± 0.01
ν_{axial}	0.253 ± 0.007	1.12 ± 0.09	6.7 ± 0.5	0.061 ± 0.005	0.31 ± 0.01
ν_{bridge}	0.47 ± 0.05	1.0 ± 0.2	6 ± 1	0.16 ± 0.02	0.63 ± 0.07

fusion rates and $r(0)$ values. The trend in D_{or} is interesting, as it seems that vibrational modes with more access to the solvent reorient slower than modes with less access to solvent molecules. Note that these values of D_{or} assume a spherical diffuser, which is a large assumption in the case of $Fe^{II}Pt^{IV}Fe^{II}$. This is logical, as more surrounding solvent molecules generally means more orientations available. The trend in $r(0)$ is also consistent with our current picture of the structure of $Fe^{II}Pt^{IV}Fe^{II}$ in solution, as ν_{bridge} and ν_{axial} are closer to parallel and ν_{radial} is closer to 0.2 which is expected for a degenerate mode.

$$\begin{aligned} r_{2106}(\tau_2) = 0.22 \pm 0.07 \exp\left(-\frac{\tau_2}{0.4 \pm 0.1 \text{ ps}}\right) \cdots \\ \times \cos\left(2\pi c(57 \pm 3 \text{ cm}^{-1})\tau_2 - 1.0 \pm 0.2 \text{ rad}\right) + 0.036 \pm 0.003 \end{aligned} \tag{3.10}$$

One very interesting observation is that the pump−probe anisotropy of the combination band at $\omega_3 = 2106$ cm^{-1} ($\nu_b\nu_t, \nu_t$) oscillates as a function of τ_2 with a beat frequency of $\sim$57 cm^{-1} and lives for $\sim$400 fs (see Eq. 3.10). This would indicate coherent transfer of population between two modes with a different angular relationship. Recall that this frequency is unique since there are many overlapping signal contributions from both parallel and perpendicular modes.

Mode-specific vibrational relaxation dynamics

The ability of 2D IR to spread spectral information into two dimensions allows a much more detailed study of intra- and intermolecular vibrational energy relaxation. By integrating a small area in 2D frequency space, one can attempt to correlate vibrational population

initially excited to a population probed at a later waiting time (τ_2). This is what is meant by "mode-specific" intramolecular vibrational relaxation dynamics. For example, if the ν_{bridge} mode is initially excited, how long does it take for vibrational population to flow into the ν_{trans} mode (assuming that energy does flow from ν_{bridge} to ν_{trans})? In addition, coherent beats can be observed in the cross peak region just as they were observed in the DPP results. Another big advantage of 2D IR spectroscopy is that combination bands (e.g., $\nu_{\text{bridge}} + \nu_{\text{trans}}$) appear in the spectrum and grow with τ_2. This occurs as vibrational energy distributes throughout all of the ν_{CN} energy levels, which opens up new transitions that were not previously available. The clearest region in the spectrum to observe these modes in $Fe^{II}Pt^{IV}Fe^{II}$ is right "below" the diagonal ν_{bridge} mode at $\omega_1 = \omega_3 = 2116$ cm^{-1}, as combination modes of the bridge and all other ν_{CN} modes excited will appear there.

Vibrational energy relaxation as measured from 2D IR is illustrated for five different integrated areas is presented in Figure 3.9. Note that Figure 3.9a is the same as Figure 3.4 on page 58 (YYZZ polarization) with a different grid and numbers corresponding to what area is integrated in Figures 3.9b−3.9f. In addition to the YYZZ polarization geometry, Figures 3.9b−3.9f also show the integrated area as a function of τ_2 for the ZZZZ and calculated magic angle (MA) geometries. The MA kinetics were fit to a sum of exponentials and in some cases a decaying cosine in order to extract IVR and VER rates. The five peak positions (1−5) are positioned as follows: ① $\nu_{\text{trans}} \rightarrow \nu_{\text{trans}}$, ② $\nu_{\text{bridge}} \rightarrow \nu_{\text{bridge}}$, ③ $\nu_{\text{trans}} \rightarrow \nu_{\text{bridge}}$, ④ $\nu_{\text{bridge}} \rightarrow \nu_{\text{trans}}$, and ⑤ $\nu_{\text{bridge}} \rightarrow \nu_{\text{bridge}} + \nu_{\text{trans}}$.

Peak 1, representing diagonal population relaxation of the ν_{trans} mode, decays on 0.41 ps and 12.3 ps time scales. Diagonal relaxation of the ν_{bridge} mode is given by peak 2, where overlapping peaks cause a oscillation of the integrated area of the peak. The 54 cm^{-1} oscillation lives for 0.4 ps, at which point a 2.2 ps decay representing IVR is followed by a 22 ps T_1 relaxation process. Peak 3 represents the ν_{trans} pump ν_{bridge} probe area. This peak illustrates a 0.72 ps rise occurring due to IVR, a 55 cm^{-1} beat that lives for 0.6 ps, and a 22 ps vibrational relaxation time scale. In contrast, the MA trace of the ν_{bridge} pump ν_{trans} probe peak (peak 4) does not rise. Rather, it beats at 55 cm^{-1} for 0.6 ps, decays on a 0.48 ps time scale, and subsequently decays on the a long 21 ps time scale. Finally, peak 5 corresponds to pumping the ν_{bridge} mode and probing multiple combination bands. This

feature has a strong 56 cm^{-1} beat decaying on a 0.6 ps time scale. It then decays with two time constants of 0.42 and 22 ps. Note that error in the fits has been omitted for ease of reading and that fitting the nine τ_2 points is somewhat uncertain with the overall number of parameters.

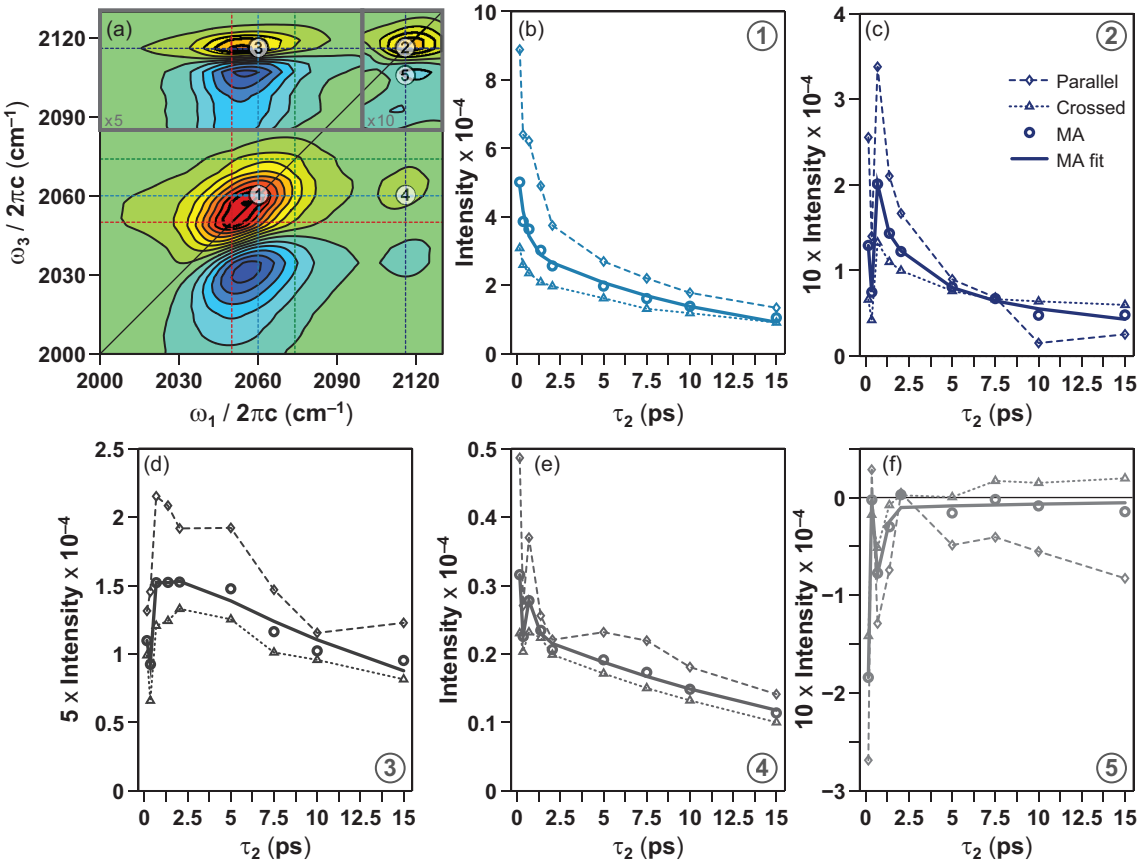

Figure 3.9: Vibrational energy relaxation dynamics from 2D IR. Kinetic traces in b−e show parallel ($\Diamond - -$), crossed ($\triangle \cdots$), magic angle ($\circ$), and the best fit of the magic angle data ($-$) for comparison. (a) 2D IR spectrum at $\tau_2 = 150$ fs in the YYZZ polarization geometry. Circles with numbers from 1−5 indicate regions that are integrated and plotted as a function of τ_2 in b−e. (b) ν_{trans} diagonal peak area with $\omega_1, \omega_3 = 2058.9 - 2061.5$ cm^{-1}. (c) ν_{bridge} diagonal peak area with $\omega_1, \omega_3 = 2114.5 - 2118.5$ cm^{-1}. (d) ν_{trans},ν_{bridge} cross peak over the previously quoted regions. (e) ν_{bridge},ν_{trans} cross peak over the previously quoted regions. (f) ν_{bridge},ν_{overtone} cross peak over $\omega_1 = 2114.5 - 2118.5$ cm^{-1}, $\omega_3 = 2105 - 2108$ cm^{-1}.

The picture that arises from analyzing the mode-specific VER dynamics in $Fe^{II}Pt^{IV}Fe^{II}$

available from 2D IR is rather complicated. In principle, all of the vibrational relaxation processes taking place in this system, including population relaxation, dephasing, and coherence transfer, can be modeled using the density matrix theory developed by Redfield.[64–66] However, this is extremely difficult in practice due to peak overlap and the total number of parameters needed to simulate the relatively sparse data set. The reduced density matrix for $Fe^{II}Pt^{IV}Fe^{II}$ contains 41 elements, which means that a 41×41 Redfield tensor is needed to fully describe population relaxation, cross relaxation, dephasing, and coherent transfer. Of these 1681 elements, 133 of them have to be assigned variables used to fit the data. However, it is clear from basic kinetic fitting that the vibrational modes are coherently coupled, energy is transferred between them on a sub-2 ps time scale, and that population relaxation occurs in $15-20$ ps.

3.3.3 Spectral diffusion in the ν_{CN} modes of $Fe^{II}Pt^{IV}Fe^{II}$

Vibrational echo peak shift (VEPS)

Homodyne peak shift data of $Fe^{II}Pt^{IV}Fe^{II}$ in D_2O are shown in Figure 3.10. The dispersed vibrational echo spectrum is related to the magnitude-squared of the third-order rephasing signal field and is therefore not a phase-sensitive measurement. The peak shift (generally written as τ_1^*) is related to the "memory" of a system.[67–69] In other words, how long does it take a molecule to "forget" a particular solvent geometry? That said, an inhomogeneous system with a much larger number of available solvent coordination geometries will have a larger initial $\tau_1^*(0)$. Since a particular solvent shell leads to a specific line shape in vibrational spectroscopy, monitoring $\tau_1^*(\tau_2)$ is proportional to the frequency-frequency correlation function (FFCF) of the system[70–72]

$$\tau_1^*(\tau_2) \propto \langle \delta\omega(\tau_2)\delta\omega(0)\rangle \tag{3.11}$$

where $\delta\omega(\tau_2) = \omega(\tau_2) - \langle\omega\rangle$. The FFCF holds molecular insight into what is leading a particular vibrational line shape to have the width that it does.

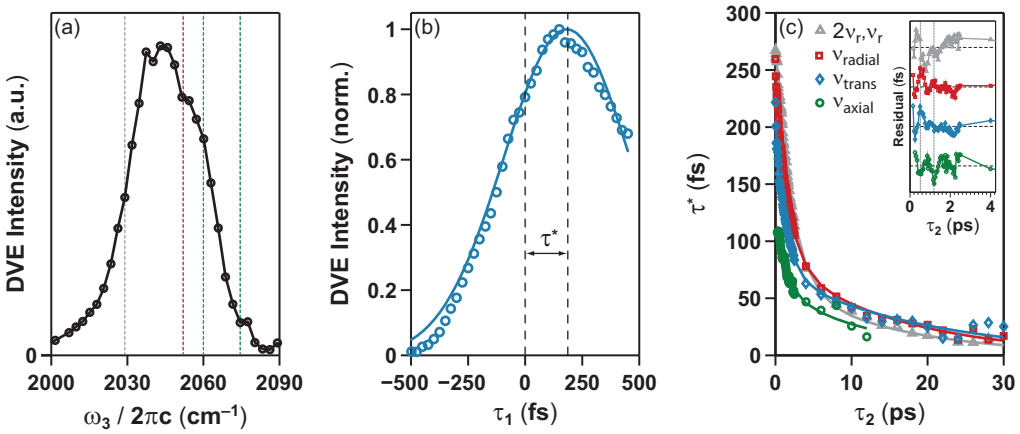

Figure 3.10: (a) Dispersed vibrational echo spectrum at $\tau_1 = \tau_2 = 500$ fs. Vertical lines highlight the three fundamental modes in the terminal region and one overtone for comparison. (b) An experimental example of the peak shift (τ_1^*), where the DVE intensity has been normalized and plotted as a function of τ_1 at fixed $\omega_3 = 2060$ cm^{-1} and $\tau_2 = 500$ fs. The signal was fit to a Gaussian such that $\tau_1^* = \tau_1^{\max}$. (c) Plot of $\tau_1^*(\tau_2)$ shows how the peak shift is proportional to a correlation function. Biexponential fitting results are given in Table 3.7 on page 72. The inset shows the residual of fit at early τ_2, suggesting that the peak shift coherently beats as well. Vertical dotted lines aid the eye in determining the phase of the oscillation. Data for ν_{axial} ends at $\tau_2 = 12$ ps due to poor S/N.

Figure 3.10a illustrates a homodyne DVE spectrum at $\tau_1 = \tau_2 = 500$ fs. As mentioned above, DVE signals are not phase sensitive and are therefore positive; however, the lack of heterodyne detection means that the signals are quite small. It is clear to see the signal at the ν_{axial} frequency is very small. Not shown is the ν_{bridge} region where no signal was found within the S/N of the measurement. The rephasing nature of the signal is demonstrated in Fig. 3.10b for $\omega_3 = 2060$ cm^{-1} (ν_{trans}) and $\tau_2 = 500$ fs where the signal is clearly increasing at $\tau_1 = 0$ to a maximum at $\tau_1 > 0$. The peak of the signal along τ_1 was determined by fitting a Gaussian function to the data. We tried other methods, such as the first moment of the signal, but found that this was the most reproducible method for the broad overlapping features of $Fe^{II}Pt^{IV}Fe^{II}$ in water. Finally, by fitting all signals $S(\tau_1;\tau_2,\omega_3)$ to a Gaussian, we can plot the peak shift as a function of the vibrational waiting time, $\tau_1^*(\tau_2)$, as presented in Fig. 3.10c for the three fundamental terminal frequencies and the ν_{radial} overtone. Three things to notice about this Figure are (i) the initial peak shift value $\tau_1^*(0)$, (ii) the decay of

the traces, and (iii) the early-time dynamics as shown in the inset. Fitting results presented in Table 3.7 summarize the trends for the first two points. Within error, time scales of the FFCF can be broken down into two groups: fast and slow. The fast time scale of $1-2$ ps is consistent with hydrogen bonding dynamics, where the slow time scale of $10-20$ ps most likely corresponds to orientational relaxation dynamics occurring on that time scale.

Table 3.7: Biexponential fitting results of the peak shift data shown in Figure 3.10c. The starting peak shift value, $\tau^*(0)$, is also tabulated for comparison.

Mode	T_{fast} (ps)	T_{slow} (ps)	A_{fast}[1]	A_{slow}	$\tau^*(0)$ (fs)
ν_{radial}	1.6 ± 0.1	16 ± 2	0.66 ± 0.04	0.34 ± 0.04	248
ν_{trans}	1.4 ± 0.2	20 ± 4	0.65 ± 0.04	0.35 ± 0.05	203
ν_{axial}	1.3 ± 0.5	14 ± 7	0.5 ± 0.1	0.5 ± 0.1	126[2]
$2\nu_{\text{radial}}, \nu_{\text{radial}}$	2.0 ± 0.2	15 ± 5	0.77 ± 0.07	0.23 ± 0.07	274

[1] Amplitudes normalized such that $\sum_i |A_i| = 1$. [2] Calculated by extrapolation of the fit to $\tau_1 = 0$ from the starting point of 0.25 ps.

The inset of Fig. 3.10c is very interesting, as it suggests that the frequency correlation function coherently oscillates at early times. That is to say, a low-frequency ($\sim$50 cm^{-1}) mode of the solvent (where here the "solvent" is considered as anything that is not the high-frequency ν_{CN} modes, such as D_2O itself or a low-frequency mode of the solute molecule) is coherently coupled to the high-frequency ν_{CN} modes. This low-frequency mode is most likely the best channel for the high-frequency modes to use for energy transfer (i.e., vibrational energy relaxation).

2D IR line shape analysis: nodal line slope

One of the most natural upgrades when moving from 1D to 2D spectroscopy is that the line shape is spread onto two axes. It is therefore much more informative. Over the past decade and a half, the 2D IR community has shown the difference between inhomogeneous and homogeneous line shapes and how one can easily differentiate the two scenarios with 2D IR. In brief, an inhomogeneous line shape leads to a peak elongated along the diagonal as if a grain of rice had been laid upon the diagonal axis. In this manner both the inhomogeneous

and homogeneous widths can be determined from the long and short axis of the grain, respectively. On the other hand, a homogeneous line shape is characterized by a diamond-shaped peak. Aside from determining both the inhomogeneous and homogeneous widths, one can monitor the line shape as a function of τ_2 to see how it evolves as the vibrational waiting time increases.

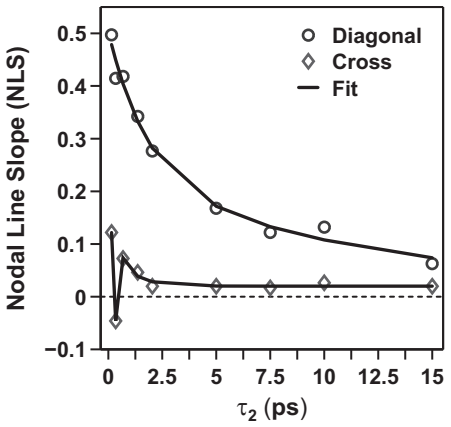

Figure 3.11: 2D IR line shape analysis via the NLS. The two regions correspond to the diagonal terminal peak (∘, peak 1) and the ν_{bridge} / ν_{trans} cross peak (◊, peak 3). The diagonal trace decays with two time constants: 1.8 ps and 14 ps. The NLS of the cross peak rapidly decays in 0.8 ps, oscillates at ∼56 cm^{-1}, and maintains a constant offset of 0.02.

This is a measure of spectral diffusion, as one can see what happens when you excite a vibration at one frequency and measure at another (i.e., a 2D probability distribution). Many metrics have been used to measure spectral diffusion and subsequently relate the rate of spectral diffusion to the FFCF. These metrics include the slope of the nodal line (NLS), inhomogeneity index, center line slope (CLS), and the ellipticity of the peak.[72,73] A real strength of the technique is that both auto- and cross-correlation functions can be measured and therefore the entire PES can be mapped. Here, line shape analysis is demonstrated using the NLS method, where a slices along ω_3 are taken between the maxima of the $n = 0 \rightarrow 1$ (positive) and $n = 1 \rightarrow 2$ (negative) peaks and the zero-crossing is found. This procedure is done for a small range of ω_1 values in order to generate a line of the form $\omega_3 = m_{\text{NLS}} \cdot \omega_1 + b$ where the slope of the line (m_{NLS}) is the definition of the NLS. Figure 3.11 shows how the

NLS changes as a function of τ_2 for the large diagonal "terminal" peak centered around $\omega_1 = \omega_3 = 2060$ cm^{-1} (auto-correlation function) and the smaller ν_{bridge} /ν_{trans} cross peak at $\omega_1 = 2060$ cm^{-1} and $\omega_3 = 2116$ cm^{-1} (cross-correlation function). The auto-correlation function decays with one fast (1.8 ps) and one slow (14 ps) time constant just as was observed in the peak shift measurement. In contrast, the cross-correlation function decays extremely rapidly with a time constant of 800 fs and also shows evidence of a coherent oscillation with a beat frequency of ∼56 cm^{-1}. Therefore, frequency fluctuations of the ν_{bridge} mode are positively correlated with the frequency fluctuations of the ν_{trans} mode for approximately 1 ps.

3.3.4 Simulations of 2D IR spectra

Theoretical simulations of 2D IR spectra are generally approached with a response function formalism.[42,51] Spectra can be simulated with knowledge of the quantum mechanical material Hamiltonian (H_{M}), that is: transition dipole strength (μ), vibrational frequency (ω), and line shape function (F). The total material Hamiltonian is written as

$$H_{\text{M}} = H_{\text{S}} + H_{\text{B}} + H_{\text{SB}}, \tag{3.12}$$

where H_{S}, H_{B}, and H_{SB} are the system, bath, and system-bath Hamiltonians, respectively. Here, H_{S} contains coupled vibrational coordinates $\mathbf{Q}$, whereas H_{B} and H_{SB} lead to fluctuations in the vibrational frequencies and vibrational relaxation processes. The system Hamiltonian is generally represented in a local-mode picture.

Signals emitted from the sample are electric fields that are proportional to the polarization of the sample, $\mathbf{P}$. Many descriptions of nonlinear spectroscopy require the polarization to be expanded perturbatively in powers of the incoming electric fields such that $\mathbf{P} = \mathbf{P}^{(0)} + \mathbf{P}^{(1)} + \mathbf{P}^{(2)} + \mathbf{P}^{(3)} + \cdots$. The third-order polarization, $\mathbf{P}^{(3)}$, is proportional to the third-order material response function of the system, which contains all of the molecular and dynamics information.[51] In the interaction picture $\mathbf{P}^{(3)}$ can be expressed as,

$$\mathbf{P}^{(3)}(\mathbf{k}_s, t, \tau_2, \tau_1) = \iiint_0^\infty \overleftrightarrow{\mathbf{R}}^3(\tau_3', \tau_2', \tau_1') \vdots \mathbf{E}_3(\mathbf{k}_3, \nu_3, t - \tau_3') \mathbf{E}_2(\mathbf{k}_2, \nu_2, t + \tau_2 - \tau_3' - \tau_2') \cdots \\ \times \mathbf{E}_1(\mathbf{k}_1, \nu_1, t + \tau_2 + \tau_1 - \tau_3' - \tau_2' - \tau_1') \mathrm{d}\tau_1' \mathrm{d}\tau_2' \mathrm{d}\tau_3', \tag{3.13}$$

where $\overleftrightarrow{\mathbf{R}}^3$ is the material response function and $\mathbf{E}(\mathbf{k}, \nu, t)$ is an input electric field moving in the $\mathbf{k}$ direction with frequency ν. The response function is then expressed as

$$\overleftrightarrow{\mathbf{R}}^3(\tau_3, \tau_2, \tau_1) = (i/\hbar)^3 \langle [[[\mathbf{M}(\tau_3 + \tau_2 + \tau_1), \mathbf{M}(\tau_2 + \tau_1)] \mathbf{M}(\tau_1)], \mathbf{M}(0)] \boldsymbol{\rho}_{\mathrm{eq}} \rangle, \tag{3.14}$$

where $\mathbf{M}$ is the vibrational dipole operator with vibrational transition dipole matrix elements $\mu^{n,n'} = \langle n | \mathbf{M}(\mathbf{Q}) | n' \rangle$ over the local system vibrational coordinates $\mathbf{Q}$, $\boldsymbol{\rho}_{\mathrm{eq}}$ is the initial equilibrium reduced density matrix, and the trace denoted as $\langle \cdots \rangle$ is over the vibrational state manifold. This nested commutator can be expanded into eight terms containing both vibrational and orientation response. One example of a term in the response function describing the nonlinear vibrational response is given by,

$$R_3^{a,b,c,d}(\tau_3, \tau_2, \tau_1) = P_a \mu^{c,b} \mu^{b,a} \mu^{d,c} \mu^{a,d} \exp(-i\omega_{b,c}^0 \tau_3 + i\omega_{c,a}^0 \tau_2 + i\omega_{d,a}^0 \tau_1) F_3^{a,b,c,d}(\tau_3, \tau_2, \tau_1), \tag{3.15}$$

where P_a is the probability of occupying state a, and F_3 is the dephasing function for this particular component of the response function. Within the dephasing function are the time-dependent fluctuations of the vibrational transition frequency that are generally written as bath-induced frequency shifts about an ensemble average frequency,[42]

$$\omega_{p,q}(t) = \omega_{p,q}^0 + \delta\omega_{p,q}(t). \tag{3.16}$$

Time scales and amplitudes of these fluctuations are then expressed as auto- and cross-correlation functions by $\zeta_{pq}(t) = \langle \delta\omega_{p,a}(t)\delta\omega_{q,a}(0)\rangle$, where the $\omega_{p,a}$ fluctuations are correlated to the $\omega_{q,a}$ fluctuations over a time t. Components of the line shape function F are related to the frequency-frequency correlation function (FFCF). In practice, the FFCFs are represented by the stochastic model of frequency fluctuations introduced by Kubo.[74] In this model, frequency fluctuations are assumed to be Gaussian with a variance Δ^2 and that the two-point time correlation decays with a time constant τ. In this limit, when the absorption line shape is Gaussian when $\Delta\tau \gg 1$ and Lorentzian when $\Delta\tau \ll 1$. These two limits are respectively known as the inhomogeneous and homogeneous limits.[74] It is common for FFCFs to decay on two time scales in solution, as different broadening processes occurring at room temperature can fall within either the inhomogeneous (slow) or homogeneous (fast) limit.[75,76] Thus, for the case of $Fe^{II}Pt^{IV}Fe^{II}$ in D_2O the FFCF is written as

$$C(\tau_2) = \langle \omega(\tau_2)\omega(0)\rangle = \Delta_1^2 \exp(-\tau_2/t_1) + \Delta_2^2 \exp(-\tau_2/t_2), \tag{3.17}$$

where the FFCF has relaxation time t_1 and t_2. The line shape $g(\tau_2)$ is related to $C(\tau_2)$ by

$$\begin{aligned} g(\tau_2) &= \int_0^{\tau_2} \mathrm{d}\tau_2'(\tau_2 - \tau_2')C(\tau_2') \\ &= \rho_{12}\left[\Delta_1^2 t_1\tau_2 + \Delta_1^2 t_1^2(\exp(-\tau_2/t_1) - 1) + \Delta_2^2 t_2\tau_2 + \Delta_2^2 t_2^2(\exp(-\tau_2/t_2) - 1)\right], \end{aligned} \tag{3.18}$$

where the correlation coefficient ρ_{12} is an empirical term that has been added to define positive ($\rho_{12} = +1$) and negative ($\rho_{12} = -1$) correlation.[42] Simulation results using the parameters given in Table 3.8 are shown in Figure 3.12. Time scales of the frequency correlation were obtained from the VEPS results in Section 3.3.3, where as dipole strengths were obtained by fitting the experimental FTIR spectrum to the linear absorption spectrum generated in the simulation. The correlation coefficient was estimated based on the NLS analysis in Section 3.3.3. In addition, the ν_{radial} mode was treated as degenerate, the

anharmonicies were taken from Table 3.2 on page 61, and the relative angles were those in Table 3.3 on page 62.

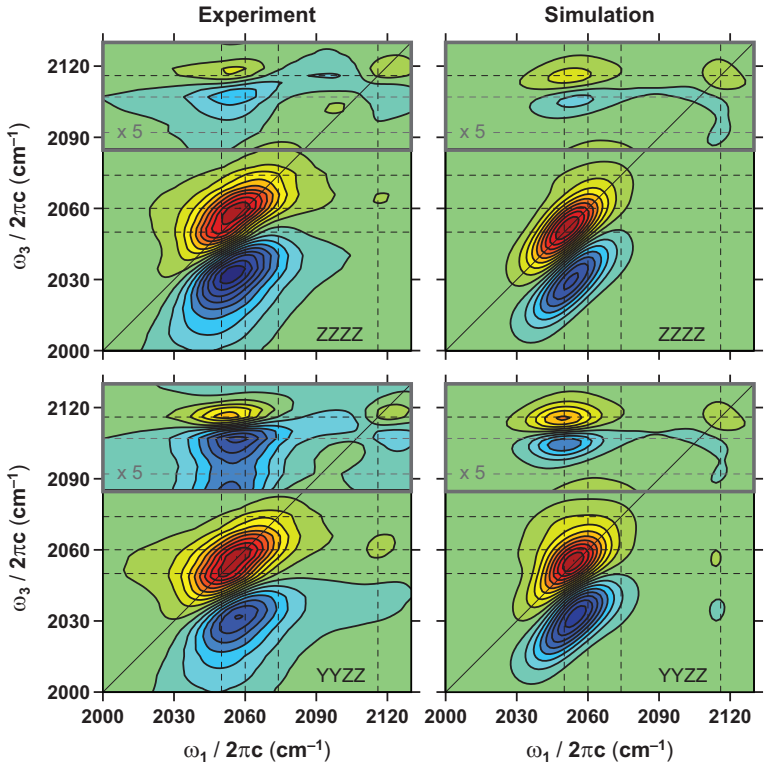

Figure 3.12: Simulation results at $\tau_2 = 150$ fs. The z-axis has been normalized for each polarization pair and is displayed with twenty equally-spaced contour lines. See text for detailed discussion on simulation parameters.

Table 3.8: Simulation parameters (see eq 3.18). All cross-correlation functions had a correlation time of 800 fs where an average of the amplitudes between each of the modes was used. Harmonic scaling was assumed.

Mode	μ	Δ_1 (ps^{-1})	t_1 (ps)	Δ_2 (ps^{-1})	t_2 (ps)	ρ_{12}
ν_{radial}	0.67	1.7	1.7	0.84	12	1
ν_{trans}	0.66	1.6	1.3	10	7	1
ν_{axial}	0.20	1.2	2.2	–	–	1
ν_{bridge}	0.20	1.1	1.5	–	–	0.3

These results are preliminary, as the best way to match experimental results with simulation is to create a fitting routine that iteratively changes the parameters until a best fit to the experiment is achieved.

3.3.5 Extracting vibrational couplings assuming linearly coupled anharmonic oscillators

An increasingly popular way to model 2D IR spectra is based on the picture of vibrational excitonic states (vibrons) that are used to describe the vibrational response of the system. This model separates each vibrational degree of freedom of interest and describes the coupling between them using the Frenkel-exciton Hamiltonian,[77]

$$H_{\mathrm{S}} = \sum_i \epsilon_i b_i^\dagger b_i + \sum_{i<j} \beta_{ij}(b_i^\dagger b_j + b_j^\dagger b_i), \tag{3.19}$$

where $b_i^\dagger$ and b_i are respectively the creation and annihilation operators of each of the harmonic vibrational modes. This model is equivalent to the normal mode picture in certain limits. Here, the ν_{CN} modes are treated as coupled, weakly anharmonic oscillators. These are quite valid assumptions, as it has already been observed above that the modes are anharmonically coupled. The largest $\Delta = 24$ cm^{-1} is still only $\sim$1% of the fundamental vibrational frequency of 2116 cm^{-1} for the case of ν_{bridge}.

Given that the number of excitations is conserved, the Hamiltonian separates into blocks representing the ground state, the one-excitonic state, and the two-excitonic state. For a system of four coupled vibrational modes, here defined as $|r, t, a, b\rangle$ corresponding to ν_{radial}, ν_{trans}, ν_{axial}, and ν_{bridge}, one can order the site-basis as

$$
\begin{aligned}
\{&|0,0,0,0\rangle,\\
&|1,0,0,0\rangle,\\
&|0,1,0,0\rangle,\\
&|0,0,1,0\rangle,\\
&|0,0,0,1\rangle,\\
&|2,0,0,0\rangle,\\
&|0,2,0,0\rangle,\\
&|0,0,2,0\rangle,\\
&|0,0,0,2\rangle,\\
&|1,1,0,0\rangle,\\
&|1,0,1,0\rangle,\\
&|1,0,0,1\rangle,\\
&|0,1,1,0\rangle,\\
&|0,1,0,1\rangle,\\
&|0,0,1,1\rangle\},
\end{aligned}
\tag{3.20}
$$

where the integer ($n = 0, 1, 2$) represents the number of vibrational quanta in a given mode. The vibrational mode anharmonicity is included directly by lowering the site-energies of the two-quantum states by Δ. In the weak coupling limit, two-quantum states can be calculated as a product of one-quantum states lowered by diagonal and off-diagonal anharmonicity. The full Hamiltonian can be expanded as follows:

$$
H_{\mathrm{S}} = \begin{bmatrix}
0 & & & & & & & & & & & & & & \\
 & \epsilon_r & \beta_{rt} & \beta_{ra} & \beta_{rb} & & & & & & & & & & \\
 & \beta_{rt} & \epsilon_t & \beta_{ta} & \beta_{tb} & & & & & & & & & & \\
 & \beta_{ra} & \beta_{ta} & \epsilon_a & \beta_{ab} & & & & & & & & & & \\
 & \beta_{rb} & \beta_{tb} & \beta_{ab} & \epsilon_b & & & & & & & & & & \\
 & & & & & 2\epsilon_r - \Delta_r & & & & \sqrt{2}\beta_{rt} & \sqrt{2}\beta_{ra} & \sqrt{2}\beta_{rb} & & & \\
 & & & & & & 2\epsilon_t - \Delta_t & & & \sqrt{2}\beta_{rt} & & & \sqrt{2}\beta_{ta} & \sqrt{2}\beta_{tb} & \\
 & & & & & & & 2\epsilon_a - \Delta_a & & & \sqrt{2}\beta_{ra} & & \sqrt{2}\beta_{ta} & & \sqrt{2}\beta_{ab} \\
 & & & & & & & & 2\epsilon_b - \Delta_b & & & \sqrt{2}\beta_{rb} & & \sqrt{2}\beta_{tb} & \sqrt{2}\beta_{ab} \\
 & & & & & \sqrt{2}\beta_{rt} & \sqrt{2}\beta_{rt} & & & \epsilon_r + \epsilon_t & & & & & \\
 & & & & & \sqrt{2}\beta_{ra} & & \sqrt{2}\beta_{ra} & & & \epsilon_r + \epsilon_a & & & & \\
 & & & & & \sqrt{2}\beta_{rb} & & & \sqrt{2}\beta_{rb} & & & \epsilon_r + \epsilon_b & & & \\
 & & & & & & \sqrt{2}\beta_{ta} & \sqrt{2}\beta_{ta} & & & & & \epsilon_t + \epsilon_a & & \\
 & & & & & & \sqrt{2}\beta_{tb} & & \sqrt{2}\beta_{tb} & & & & & \epsilon_t + \epsilon_b & \\
 & & & & & & & \sqrt{2}\beta_{ab} & \sqrt{2}\beta_{ab} & & & & & & \epsilon_a + \epsilon_b
\end{bmatrix} \tag{3.21}
$$

In the normal mode picture, the harmonic nuclear potential (V_{harm}) is described as

$$\begin{aligned} V_{\text{harm}}(q_r, q_t, q_a, q_b) = \tfrac{1}{2}\epsilon_r q_r^2 + \tfrac{1}{2}\epsilon_t q_t^2 + \tfrac{1}{2}\epsilon_a q_a^2 + \tfrac{1}{2}\epsilon_b q_b^2 \cdots \\ + \beta_{rt} q_r q_t + \beta_{ra} q_r q_a + \beta_{rb} q_r q_b + \beta_{ta} q_t q_a + \beta_{tb} q_t q_b + \beta_{ab} q_a q_b, \end{aligned} \tag{3.22}$$

where the bilinear coupling terms are given as $\beta_{ij} q_i q_j$.

Diagonalization of the site-basis Hamiltonian shown in Equation 3.21 ($\tilde{H}_{\text{S}} = T^{-1} H_{\text{S}} T$ where T is a transformation matrix) leads to absolute energies of the bilinearly coupled anharmonic oscillators in the excitonic basis. The lowest 15 levels in the resulting Hamiltonian in the eigenbasis correspond to the zero, one, and two quantum states:

$$y = \text{diag}[\tilde{H}_{\text{S}}(1:15)] = \begin{bmatrix} 0 \\ \epsilon_r \\ \epsilon_t \\ \epsilon_a \\ \epsilon_b \\ 2\epsilon_r - \Delta_r \\ 2\epsilon_t - \Delta_t \\ \epsilon_t + \epsilon_r - \Delta_{tr} \\ \epsilon_r + \epsilon_a - \Delta_{ra} \\ \epsilon_t + \epsilon_a - \Delta_{ta} \\ 2\epsilon_a - \Delta_a \\ \epsilon_r + \epsilon_b - \Delta_{rb} \\ \epsilon_t + \epsilon_b - \Delta_{tb} \\ \epsilon_a + \epsilon_b - \Delta_{ab} \\ 2\epsilon_b - \Delta_b \end{bmatrix} = \begin{bmatrix} 0 \\ 2050\ \text{cm}^{-1} \\ 2060\ \text{cm}^{-1} \\ 2074\ \text{cm}^{-1} \\ 2116\ \text{cm}^{-1} \\ 4079\ \text{cm}^{-1} \\ 4097\ \text{cm}^{-1} \\ 4101\ \text{cm}^{-1} \\ 4115\ \text{cm}^{-1} \\ 4125\ \text{cm}^{-1} \\ 4127\ \text{cm}^{-1} \\ 4157\ \text{cm}^{-1} \\ 4167\ \text{cm}^{-1} \\ 4181\ \text{cm}^{-1} \\ 4208\ \text{cm}^{-1} \end{bmatrix} \tag{3.23}$$

where the values of β_{ij} are determined by iteratively performing the transformation to mini-

mize the difference between experimentally determined anharmonicities and frequencies and calculated anharmonicies and frequencies. This is achieved by calculating $\Delta'_{\mathrm{r}} = 2y(2) - y(6)$, $\Delta'_{\mathrm{t}} = 2y(3) - y(7)$, $\Delta'_{\mathrm{a}} = 2y(4) - y(11)$, and $\Delta'_{\mathrm{b}} = 2y(5) - y(15)$. This ordering is defined by increasing energy, as that is how the vector is output after diagonalization. Results of the fitting routine provide each of the site energies and the bilinear coupling constants. Preliminary fitting results are: $\epsilon_r = 2054$ cm^{-1}, $\epsilon_t = 2062$ cm^{-1}, $\epsilon_a = 2071$ cm^{-1}, $\epsilon_b = 2114$ cm^{-1}, $\beta_{rt} = 0$ cm^{-1}, $\beta_{ra} = 8$ cm^{-1}, $\beta_{rb} = 7$ cm^{-1}, $\beta_{ta} = 5$ cm^{-1}, $\beta_{tb} = 6$ cm^{-1}, and $\beta_{ab} = 5$ cm^{-1}. The basic model used here struggles to accurately reproduce all of the experimental anharmonicities; however, it represents a good starting point for the extraction of anharmonic couplings in 4-dimensional systems. Additional terms in the system Hamiltonian, such as cubic coupling constants of the form $V_{\mathrm{cubic}} = \gamma_{\mathrm{ijk}} q_{\mathrm{i}} q_{\mathrm{j}} q_{\mathrm{k}}$, are required to fully reproduce the experimental data.

3.4 Summary

This chapter has illustrated how complex the electronic ground state of a charge transfer system can be and how third-order nonlinear IR spectroscopy is a useful tool that can be used to address the role of high-frequency vibrations and of the solvent. We found with 2D IR spectroscopy that the four ν_{CN} modes are coherently coupled; that is, the vibration of one influences the other. Coupling constants were estimated using a relatively basic excitonic coupling model where moderate couplings were found. In addition, 2D line shape analysis revealed that even the frequency fluctuations of different modes are coupled at least for 1 ps. The polarization selectivity of 2D IR allowed the relative angles between the dipole moments to be estimated. Dispersed IR pump−probe spectroscopy enabled an accurate measurement of IVR and T_1 time scales. The vibrational echo peak shift technique provided additional insight into the role of the solvent, where two time scales for solvation dynamics were observed via the frequency-frequency correlation function.

The chapter concludes with a look back at charge transfer in mixed-valence complexes. Figure 3.13 illustrates a cartoon of two potential energy surfaces corresponding to the GS and the CTS of $Fe^{II}Pt^{IV}Fe^{II}$ along a generalized "charge transfer coordinate," which as we have found out in this chapter is a high dimensional surface consisting of (at least) four high-

frequency ν_{CN} modes. The PESs have been drawn to scale according to the calculations provided in Section 3.1. Inset into the GS PES is the progression of the ν_{bridge} mode with a frequency of 2116 cm^{-1} and an anharmonicity of 24 cm^{-1}. The shaded grey rectangle represents $\Delta\lambda_{fwhm}$ of the metal-to-metal charge transfer band of $Fe^{II}Pt^{IV}Fe^{II}$ in D_2O (also to scale) with the darkest horizontal slice of the gradient corresponding to $\lambda_{max} = 424$ nm.

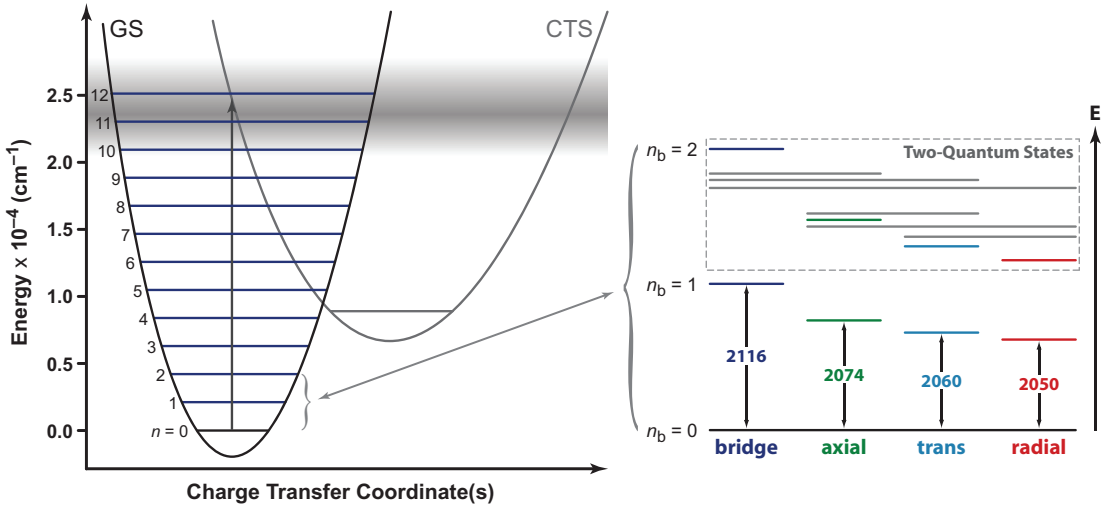

Figure 3.13: An energy-scaled cartoon of the ground state (GS) and charge-transfer state (CTS) of $Fe^{II}Pt^{IV}Fe^{II}$ in D_2O. Vibrational quanta of the ν_{bridge} mode have been drawn into the GS. The CTS($n' = 0$)−GS($n = 0$) separation corresponds to $\Delta E_{12} = 8900$ cm^{-1}. The shaded grey rectangle corresponds to the MMCT band with a maximum of 23585 cm^{-1} and a width (fwhm) of 7300 cm^{-1}. The zoom-in on the right illustrates the amount of vibrational levels within the $n = 0$−2 manifold determined with 2D IR spectroscopy.

The zoom-in on the right-hand side of the figure highlights the number of vibrational states only within the $n = 0$−2 manifold of vibrational states as determined by 2D IR spectroscopy in this chapter. As we will see starting in Chapter 4, excitation of the MMCT transition with a $\lambda = 400$ nm pump pulse (vertical arrow) leads to very rapid back-electron transfer (BET) in the GS within ∼110 fs. It seems quite plausible that this rapid BET is enabled due to the extremely high density of vibrational states available in the GS PES. We will see that greater than 6 quanta of the ν_{bridge} mode are excited upon BET at which point the excess vibrational energy is dissipated among the other ν_{CN} mode via IVR.

REFERENCES

[1] Doorn, S. K.; Hupp, J. T. *J. Am. Chem. Soc.* **1989**, *111*, 1142–1144.

[2] Barbara, P. F.; Walker, G. C.; Smith, T. P. *Science* **1992**, *256*, 975–981.

[3] Wang, C.; Mohney, B.; Williams, R.; Petrov, V.; Hupp, J.; Walker, G. *J. Am. Chem. Soc.* **1998**, *120*, 5848–5849.

[4] Kliner, D. A. V.; Tominaga, K.; Walker, G.; Barbara, P. *J. Am. Chem. Soc.* **1992**, *114*, 8323–8325.

[5] Doorn, S. K.; Stoutland, P. O.; Dyer, R. B.; Woodruff, W. H. *J. Am. Chem. Soc.* **1992**, *114*, 3133–3134.

[6] Doorn, S. K.; Dyer, R. B.; Stoutland, P. O.; Woodruff, W. H. *J. Am. Chem. Soc.* **1993**, *115*, 6398–6405.

[7] Wang, C.; Mohney, B.; Akhremitchev, B.; Walker, G. *J. Phys. Chem. A* **2000**, *104*, 4314–4320.

[8] Tivansky, A.; Wang, C.; Walker, G. *J. Phys. Chem. A* **2003**, *107*, 9051–9058.

[9] Reid, P. J.; Silva, C.; Barbara, P.; Karki, L.; Hupp, J. *J. Phys. Chem.* **1995**, *99*, 2609–2616.

[10] Vance, F. W.; Karki, L.; Reigle, J. K.; Hupp, J. T.; Ratner, M. A. *J. Phys. Chem. A* **1998**, *102*, 8320–8324.

[11] Hupp, J. T.; Williams, R. D. *Acc. Chem. Res.* **2001**, *34*, 808–817.

[12] Spears, K.; Wen, X.; Arrivo, S. *J. Phys. Chem.* **1994**, *98*, 9693–9696.

[13] Spears, K. G. *J. Phys. Chem.* **1995**, *99*, 2469–2476.

[14] Spears, K. G.; Wen, X.; Zhang, R. *J. Phys. Chem.* **1996**, *100*, 10206–10209.

[15] Watzky, M.; Endicott, J.; Song, X.; Lei, Y.; Macatangay, A. *Inorg. Chem.* **1996**, *35*, 3463–3473.

[16] Watzky, M.; Macatangay, A.; VanCamp, R.; Mazzetto, S.; Song, X.; Endicott, J.; Buranda, T. *J. Phys. Chem. A* **1997**, *101*, 8441–8459.

[17] Macatangay, A.; Mazzetto, S.; Endicott, J. *Inorg. Chem.* **1999**, *38*, 5091–5101.

[18] Stoutland, P. O.; Dyer, R. B.; Woodruff, W. H. *Science* **1992**, *257*, 1913–1917.

[19] Dows, D. A.; Haim, A.; Wilmarth, W. *J. Inorg. Nucl. Chem.* **1961**, *21*, 33–37.

[20] Hester, R. E.; Nour, E. M. *J. Chem. Soc., Dalton Trans.* **1981**, 939.

[21] Swanson, B. *Inorg. Chem.* **1976**, *15*, 253–259.

[22] Swanson, B. I.; Rafalko, J. J. *Inorg. Chem.* **1976**, *15*, 249–253.

[23] Heilweil, E. J.; Doany, F. E.; Moore, R.; Hochstrasser, R. M. *J. Chem. Phys.* **1982**, *76*, 5632–5634.

[24] Hamm, P.; Lim, M.; Hochstrasser, R. M. *J. Chem. Phys.* **1997**, *107*, 10523–10531.

[25] Lee, M. W.; Meuwly, M. *J. Phys. Chem. A* **2011**, *115*, 5053–5061.

[26] Kuo, C.-H.; Hochstrasser, R. M. *Chem. Phys.* **2007**, *341*, 21–28.

[27] Rey, R.; Hynes, J. T. *J. Chem. Phys.* **1998**, *108*, 142–153.

[28] Bastida, A.; Zúñiga, J.; Requena, A.; Miguel, B. *J. Chem. Phys.* **2008**, *129*, 154501.

[29] Shiga, M.; Okazaki, S. *Chem. Phys. Lett.* **1998**, *292*, 431–436.

[30] Sando, G. M.; Zhong, Q.; Owrutsky, J. C. *J. Chem. Phys.* **2004**, *121*, 2158–2168.

[31] Weidinger, D.; Sando, G. M.; Owrutsky, J. C. *Chem. Phys. Lett.* **2010**, *489*, 169–174.

[32] Weidinger, D.; Brown, D. J.; Owrutsky, J. C. *J. Chem. Phys.* **2011**, *134*, 124510.

[33] Zhou, M.; Pfennig, B. W.; Steiger, J.; Vanengen, D.; Bocarsly, A. B. *Inorg. Chem.* **1990**, *29*, 2456–2460.

[34] Gruebele, M.; Wolynes, P. G. *Acc. Chem. Res.* **2004**, *37*, 261–267.

[35] Lynch, M. S.; Van Kuiken, B. E.; Cheng, M.; Daifuku, S.; Khalil, M. In *Ultrafast Phenomena XVII*; Chergui, M.; Jonas, D. M.; Riedle, E.; Schoenlein, R. W.; Taylor, A. J., Eds.; Oxford University Press: New York, 2011; pp 346–348.

[36] Lynch, M. S.; Van Kuiken, B. E.; Daifuku, S. L.; Khalil, M. *J. Phys. Chem. Lett.* **2011**, *2*, 2252–2257.

[37] Pfennig, B. W.; Wu, Y.; Kumble, R.; Spiro, T.; Bocarsly, A. B. *J. Phys. Chem.* **1996**, *100*, 5745–5750.

[38] Hennessy, M.; Wu, Y.; Bocarsly, A. B.; Soos, Z. *J. Phys. Chem. A* **1998**, *102*, 8312–8319.

[39] Hennessy, M.; Soos, Z.; Watson, D.; Bocarsly, A. B. *J. Phys. Chem. B* **2000**, *104*, 10909–10914.

[40] Watson, D.; Bocarsly, A. B. *Coord. Chem. Rev.* **2001**, *211*, 177–194.

[41] Pfennig, B. W.; Bocarsly, A. B. *J. Phys. Chem.* **1992**, *96*, 226–233.

[42] Khalil, M.; Demirdöven, N.; Tokmakoff, A. *J. Phys. Chem. A* **2003**, *107*, 5258–5279.

[43] Demirdöven, N.; Khalil, M.; Golonzka, O.; Tokmakoff, A. *Opt. Lett.* **2002**, *27*, 433–435.

[44] Chung, H. S.; Khalil, M.; Smith, A. W.; Tokmakoff, A. *Rev. Sci. Instrum.* **2007**, *78*, 063101.

[45] Lynch, M. S.; Slenkamp, K. M.; Cheng, M.; Khalil, M. *J. Phys. Chem. A* **2012**, *116*, 7023–7032.

[46] Ernst, R. R.; Bodenhausen, G.; Wokaun, A. *Principles of Nuclear Magnetic Resonance in One and Two Dimensions*; Oxford University Press: New York, 1990.

[47] Heyne, K.; Huse, N.; Nibbering, E. T. J.; Elsaesser, T. *Chem. Phys. Lett.* **2003**, *382*, 19–25.

[48] Zheng, J.; Kwak, K.; Fayer, M. D. *Acc. Chem. Res.* **2007**, *40*, 75–83.

[49] Szyc, Ł.; Yang, M.; Nibbering, E. T. J.; Elsaesser, T. *Angew. Chem. Int. Ed.* **2010**, *49*, 3598–3610.

[50] Yang, M.; Szyc, Ł.; Röttger, K.; Fidder, H.; Nibbering, E. T. J.; Elsaesser, T.; Temps, F. *J. Phys. Chem. B* **2011**, *115*, 5484–5492.

[51] Sung, J.; Silbey, R. J. *J. Chem. Phys.* **2001**, *115*, 9266–9287.

[52] Fayer, M. D. *Annu. Rev. Phys. Chem.* **2009**, *60*, 21–38.

[53] Golonzka, O.; Tokmakoff, A. *J. Chem. Phys.* **2001**, *115*, 297–309.

[54] Choi, J.-H.; Cho, M. *J. Chem. Phys.* **2010**, *133*, 241102.

[55] Choi, J.-H.; Cho, M. *J. Phys. Chem. A* **2011**, *115*, 3766–3777.

[56] Lee, K.-K.; Park, K.-H.; Park, S.; Jeon, S.-J.; Cho, M. *J. Phys. Chem. B* **2011**, *115*, 5456–5464.

[57] Messmer, A. T.; Lippert, K. M.; Steinwand, S.; Lerch, E.-B. W.; Hof, K.; Ley, D.; Gerbig, D.; Hausmann, H.; Schreiner, P. R.; Bredenbeck, J. *Chem. Eur. J.* **2012**, *18*, 14989–14995.

[58] Demirdöven, N.; Cheatum, C. M.; Chung, H. S.; Khalil, M.; Knoester, J.; Tokmakoff, A. *J. Am. Chem. Soc.* **2004**, *126*, 7981–7990.

[59] Roberts, S. T.; Loparo, J. J.; Ramasesha, K.; Tokmakoff, A. *Opt. Commun.* **2011**, *284*, 1062–1066.

[60] Thielges, M. C.; Fayer, M. D. *Acc. Chem. Res.* **2012**, *45*, 1866–1874.

[61] Bredenbeck, J.; Helbing, J.; Hamm, P. *J. Chem. Phys.* **2004**, *121*, 5943–5957.

[62] Baskin, J. S.; Zewail, A. H. *J. Phys. Chem.* **1994**, *98*, 3337–3351.

[63] Baskin, J.; Banares, L.; Pedersen, S.; Zewail, A. *J. Phys. Chem.* **1996**, *100*, 11920–11933.

[64] Redfield, A. G. *Adv. Mag. Res.* **1965**, *1*, 1.

[65] Khalil, M.; Demirdöven, N.; Tokmakoff, A. *J. Chem. Phys.* **2004**, *121*, 362–373.

[66] Ishizaki, A.; Fleming, G. R. *J. Chem. Phys.* **2009**, *130*, 234110.

[67] de Boeij, W. P.; Pshenichnikov, M. S.; Wiersma, D. A. *Annu. Rev. Phys. Chem.* **1998**, *49*, 99–123.

[68] Stenger, J.; Madsen, D.; Hamm, P.; Nibbering, E. T. J.; Elsaesser, T. *J. Phys. Chem. A* **2002**, *106*, 2341–2350.

[69] Cowan, M. L.; Bruner, B. D.; Huse, N.; Dwyer, J. R.; Chugh, B.; Nibbering, E. T. J.; Elsaesser, T.; Miller, R. J. D. *Nature* **2005**, *434*, 199–202.

[70] Cho, M.; Yu, J.; Joo, T.; Nagasawa, Y.; Passino, S.; Fleming, G. R. *J. Phys. Chem.* **1996**, *100*, 11944–11953.

[71] Cho, M.; Fleming, G. R. *J. Chem. Phys.* **2005**, *123*, 114506.

[72] Roberts, S. T.; Loparo, J. J.; Tokmakoff, A. *J. Chem. Phys.* **2006**, *125*, 084502.

[73] Park, S.; Kwak, K.; Fayer, M. D. *Laser Phys. Lett.* **2007**, *4*, 704–718.

[74] Kubo, R. *Adv. Chem. Phys.* **1969**, *15*, 101.

[75] Schmidt, J. R.; Sundlass, N.; Skinner, J. L. *Chem. Phys. Lett.* **2003**, *378*, 559–566.

[76] Ohta, K.; Tayama, J.; Saito, S.; Tominaga, K. *Acc. Chem. Res.* **2012**, *45*, 1982–1991.

[77] Woutersen, S.; Hamm, P. *J. Phys.: Condens. Matter* **2002**, *14*, R1035–R1062.

Chapter 4

ON THE ROLE OF HIGH-FREQUENCY INTRAMOLECULAR VIBRATIONS IN ULTRAFAST BACK-ELECTRON TRANSFER REACTIONS

The work presented in this chapter has been published in the following article:
Lynch, M.S.; Van Kuiken, B.E.; Daifuku, S.L.; Khalil, M. "On the Role of High-Frequency Intramolecular Vibrations in Ultrafast Back-Electron Transfer Reactions," *J. Phys. Chem. Lett.* **2012**, *2*, 2252.

Femtosecond infrared spectroscopy is used to study photoinduced metal-to-metal charge transfer in the mixed-valence complex $[(NC)_5Fe^{II}-CN-Pt^{IV}(NH_3)_4-NC-Fe^{II}(CN)_5]^{4-}$ dissolved in D_2O. Four intramolecular cyanide stretching (ν_{CN}) vibrations create a multidimensional probe of vibrational excitation, redistribution, and relaxation dynamics following ultrafast back-electron transfer (BET). We find that BET to the electronic ground state occurs in 110 ± 10 fs, during which greater than 6 quanta ($n > 6$) of vibrational energy are directed into the bridging ν_{CN} mode (ν_{bridge}). Intramolecular vibrational energy redistribution from the ν_{bridge} mode excites a solvent-accessible ν_{CN} mode on a 630 ± 50 fs time scale. Vibrational cooling to $n = 1$ and vibrational relaxation ensue on timescales of 1.3 ± 0.1 ps and 15−20 ps, respectively. These results highlight the important role played by a coupled network of high-frequency vibrations in ultrafast charge transfer processes in solution.

4.1 Introduction

Ultrafast photoinduced electron transfer is central to understanding fundamental chemical reaction dynamics and natural and artificial light harvesting. A molecular level understanding of the coupled electron and nuclear dynamics following the absorption of a photon is crucial for our ability to control charge transfer, charge separation, and charge recombination for efficient energy conversion applications. From a fundamental perspective, studies of

charge transfer processes are essential for developing a microscopic understanding of chemical reactions in solution. In the condensed phase, multiple solute and solvent degrees of freedom intertwine to determine the efficacy of the electron transfer process making this a multidimensional problem spanning various length and time scales. Among those degrees of freedom are high-frequency vibrations of the solute and there is considerable experimental and theoretical interest in elucidating their role in charge transfer processes in solution.[1–19]

In this chapter, we use sub-100 fs transient infrared (IR) spectroscopy to investigate the role of high-frequency vibrations in metal-to-metal charge transfer (MMCT) and subsequent back-electron transfer (BET) in the trinuclear cyano-bridged mixed-valence complex $[(NC)_5Fe^{II}-CN-Pt^{IV}(NH_3)_4-NC-Fe^{II}(CN)_5]^{4-}$ (here after referred to as $Fe^{II}Pt^{IV}Fe^{II}$, see Fig. 4.1) dissolved in D_2O. The MMCT band ($\lambda_{max} = 424$ nm) is pumped with a 400 nm photon transferring charge from Fe (d_{xy}) to Pt ($d_{x^2-y^2}$) to afford the charge transfer state (CTS) $Fe^{III}Pt^{III}Fe^{II}$ (or $Fe^{II}Pt^{III}Fe^{III}$). The majority of the CTS species undergo BET to regenerate $Fe^{II}Pt^{IV}Fe^{II}$ in the electronic ground state (GS), while a small amount ($\sim$1%) undergo forward-electron transfer (FET) creating $Fe^{III}Pt^{II}Fe^{III}$, which chemically dissociates into $[Fe(CN)_6]^{3-}$ and $[Pt(NH_3)_4]^{2+}$. The trinuclear mixed valence compound was first synthesized and characterized by Bocarsly and co-workers who concluded that $Fe^{II}Pt^{IV}Fe^{II}$ is well described by a three-well potential, and that the multi-electron transfer processes fall in the normal Marcus regime of electron transfer.[20] The same group has performed transient optical absorption experiments on the trinuclear mixed valence compounds $Fe^{II}Pt^{IV}Fe^{II}$ and $Ru^{II}Pt^{IV}Ru^{II}$.[21] In the case of the Fe-containing complex, which is the subject of this study, it was determined that the dynamics of FET, BET and vibrational relaxation (VR) all occur within 3.5 ps. Time-dependent resonance Raman analysis of $Fe^{II}Pt^{IV}Fe^{II}$ revealed relatively large reorganization energies associated with high-frequency CN stretching (ν_{CN}) modes along the MMCT axis, indicating that those modes (such as the bridging mode) are strongly coupled to the charge transfer process.[22–25] The lack of sub-100 fs time resolution in these experiments and the inability to directly obtain vibrational dynamics of each of the high-frequency ν_{CN} modes hindered a fully molecular-level description of the ultrafast charge transfer process in $Fe^{II}Pt^{IV}Fe^{II}$.

The molecular structure and Fourier transform infrared (FTIR) spectrum of $Fe^{II}Pt^{IV}Fe^{II}$

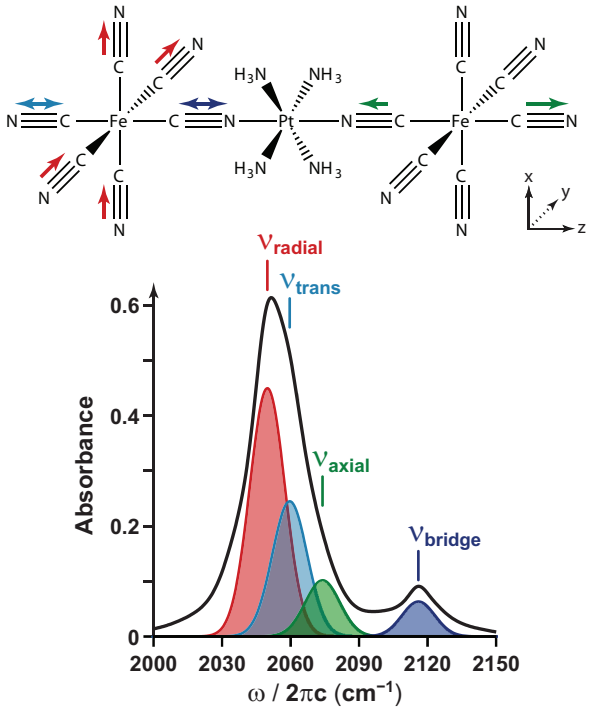

Figure 4.1: (Top) Cartoon of the molecular structure of $[Fe^{II}Pt^{IV}Fe^{II}]^{4-}$ with D_{4h} symmetry. Colored arrows correspond to simplified depictions of four ν_{CN} modes. The transition moments of the ν_{trans} (cyan), ν_{axial} (green), and ν_{bridge} (blue) modes lie along the MMCT axis and are perpendicular to the ν_{radial} (red) mode. Detailed descriptions of each normal mode are given in the appendix (Figure 4A.2 on page 103). (Bottom) Solvent-subtracted FTIR spectrum of $Fe^{II}Pt^{IV}Fe^{II}$ in D_2O fitted to four Gaussian peaks centered at 2050, 2060, 2074, and 2116 cm^{-1} corresponding to the center frequencies of the ν_{CN} modes defined above.

are shown in Figure 4.1. The FTIR spectrum contains contributions from four ν_{CN} modes labeled as ν_{radial} (2050 cm^{-1}), ν_{trans} (2060 cm^{-1}), ν_{axial} (2074 cm^{-1}), and ν_{bridge} (2116 cm^{-1}). These assignments are consistent with previous resonance Raman studies on $Fe^{II}Pt^{IV}Fe^{II}$ in solution, previous IR studies of dinuclear cyano bridged mixed valence complexes, as well as pump−probe anisotropy measurements collected in this work (see appendix).[11,12,22] We have used 2D IR spectroscopy to characterize the anharmonic vibrational couplings of these four modes in the electronic ground state of $Fe^{II}Pt^{IV}Fe^{II}$. The individual anharmonicities of the radial, trans, axial, and bridging ν_{CN} modes are 24, 23, 21, and 24 cm^{-1} respectively, whereas the mixed-mode anharmonicities range from 10−20 cm^{-1} (unpublished results).

The determination of these anharmonicities is crucial for assigning the frequencies of the higher lying vibrational states of the various ν_{CN} modes in the femtosecond transient IR spectra and their analysis shown in Figures 4.2a and 4.3b−4.3e. Based on previous studies of similar photoinduced intermediate species and the ν_{CN} frequency of $[Fe^{III}(CN)_6]^{3-}$ in solution, we expect the ν_{CN} frequencies of the terminal modes in the CTS to upshift by 70−100 cm^{-1}.[11] It should be noted that since the CTS is expected to be very short-lived, its transient IR resonances would be broad and overlapping.

The goal of this study is to measure the rate of back-electron transfer following optical MMCT excitation. We then aim to understand the role of high-frequency ν_{CN} vibrations coupled to the ultrafast back-electron transfer process. In particular, are one or more ν_{CN} modes excited upon back-electron transfer? If so, to what degree is each of the ν_{CN} modes excited? How does vibrational energy flow from one high-frequency mode to another and how is it coupled to the solvent bath?

4.2 Results and Discussion

Our results show that all four high-frequency ν_{CN} modes are involved in the ultrafast BET occurring on a 110 ± 10 fs time scale. Global and target analysis of the data reveal that greater than 6 vibrational quanta (n) of the intramolecular ν_{bridge} mode are excited (i.e., $n_{bridge} > 6$) upon BET. The vibrational energy is redistributed into coupled ν_{trans} and ν_{axial} modes, which are also aligned along the MMCT axis, at a rate of $\sim(630\text{ fs})^{-1}$. Intramolecular vibrational redistribution (IVR) is followed by vibrational cooling ($\tau_{VC} \sim 1.3$ ps) to the $n = 1$ vibrational states and finally VR to the solvent ($\tau_{VR} = 15 - 20$ ps) is given by the vibrational lifetime of the ν_{CN} modes. This study provides experimental evidence of multidimensional vibrational energy relaxation and redistribution along the four coupled vibrational coordinates coupled to ultrafast non-equilibrium back-electron transfer and has implications for the treatment of high-frequency intramolecular vibrations in current electron transfer theories.

Figure 4.2a shows time-resolved difference IR absorption spectra of $Fe^{II}Pt^{IV}Fe^{II}$ in D_2O on a femtosecond time scale at various pump−probe time delays (t_d). GS bleach peaks for the ν_{CN} terminal (ν_{radial}, ν_{trans} and ν_{axial}) and bridging (ν_{bridge}) modes are peaked at

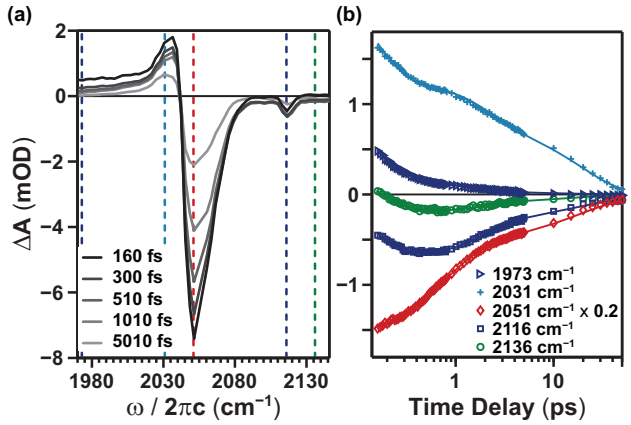

Figure 4.2: (a) Time-resolved IR absorption spectra of $Fe^{II}Pt^{IV}Fe^{II}$ in D_2O in the ν_{CN} region at five time delays (t_d) with pump and probe polarizations set to magic angle. The spectra consist of positive spectral features corresponding to transient photoproducts formed upon photoexcitation and negative features corresponding to bleaching of the electronic ground state. (b) Kinetics in the ν_{CN} region at five IR energies (dashed lines in (a)) from $t_d = 0.16 - 50$ ps on a logarithmic time axis. The solid lines are a global fit of the data to a target model. The timescales from the global fit are listed in the text and in Figure 4.3a. Complete fit parameters are listed in Table 4A.1.

2051 and 2116 cm^{-1}, respectively, as expected from the FTIR spectrum. The positive transient absorption peak centered at ~2031 cm^{-1} is due to hot transitions ($n = 2 \leftarrow 1$) of the GS terminal ν_{CN} modes, which have been assigned based on the measured vibrational anharmonicities of each of the modes. Transitions between high-lying vibrational states of the four ν_{CN} modes encompass the relatively featureless transient absorption spanning 1970−2045 cm^{-1} in the $t_d = 160$ fs spectral trace. The same trace also contains a broad, low-amplitude transient absorption at ~2136 cm^{-1}, which is in line with the expected $\nu_{terminal}$ frequencies of the intermediate $Fe^{III}Pt^{III}Fe^{II}$ (or equivalently $Fe^{II}Pt^{III}Fe^{III}$) species. Fig. 4.2a shows that as the pump−probe time delay increases, the amplitudes of the transient absorption features decrease, corresponding to population returning to the ground electronic state.

Figure 4.2b displays the measured photochemical kinetics at five IR frequencies. The data reveal complex non-exponential dynamics at each frequency indicating that various vibrational relaxation processes are coupled to the MMCT process. The time scales measured

in the kinetic traces includes an ultrafast (< 200 fs) decay in all traces, a rising component peaking at $t_d = 1$ ps (in the 2031 cm^{-1} trace), and a long decay component involving one (e.g., 1973 cm^{-1} trace) or more (e.g., 2051 cm^{-1} trace) time constants. We note that the bleach traces show an offset, indicating the formation of the two-electron photoproducts $[Fe(CN)_6]^{3-}$ and $[Pt(NH_3)_4]^{2+}$. From the data, we estimate that ~99% of the photoexcited molecules undergoing MMCT return to the ground electronic state, consistent with previous studies.[20]

With many broad, overlapping features congesting the transient IR spectra, it is beneficial to globally fit the spectrotemporal data to a target model to uncover the underlying photochemistry.[26,27] The target model used to fit the data is shown in Figure 4.3a. Here we have assumed that within the instrument response function (IRF, $\Delta t_{\mathrm{IRF}} = 94$ fs), the FET from Fe^{II} to Pt^{IV} has taken place such that the CTS, $Fe^{III}Pt^{III}Fe^{II}$, is the dominant species at $t_d = \Delta t_{\mathrm{IRF}}$. It is also assumed that the minor pathway ($\Phi \sim 1\%$) involving FET from the CTS to the chemically unstable product species, $Fe^{III}Pt^{II}Fe^{III}$, has taken place within the IRF resulting in a constant (i.e., non-decaying) concentration of $[Fe(CN)_6]^{3-}$ and $[Pt(NH_3)_4]^{2+}$ ("product"). Thus, the major pathway from the CTS is BET to the electronic GS. Upon returning to the electronic GS, the majority of the excess energy is directed into the ν_{bridge} mode (box labeled "bridge"), which then transfers vibrational energy to the ν_{trans} mode (box labeled "trans"). Vibrational cooling to the first vibrational state (box labeled "$n_i = 1$") follows, from which intermolecular VR to the electronic GS ($n_i = 0$) can occur. It is important to note that each label corresponds to the primary species and/or pathway contributing to the signal (as opposed to one unique species). Combining a target model with global analysis allows species-associated difference spectra (SADS) to be extracted from the fitting results, which in turn allow the composition of each transient species/box to be determined.[26] A SADS can be viewed as the transient spectrum of the non-equilibrium product species in the target model minus the spectrum of the GS. The assignments (i.e., labels) in the boxes (Fig. 4.3a) were generated by analyzing each of the SADS as described below. As seen from the solid lines representing the fit to the kinetic data in Fig. 4.2b, the global fit to the target model is in excellent agreement with the transient IR data.

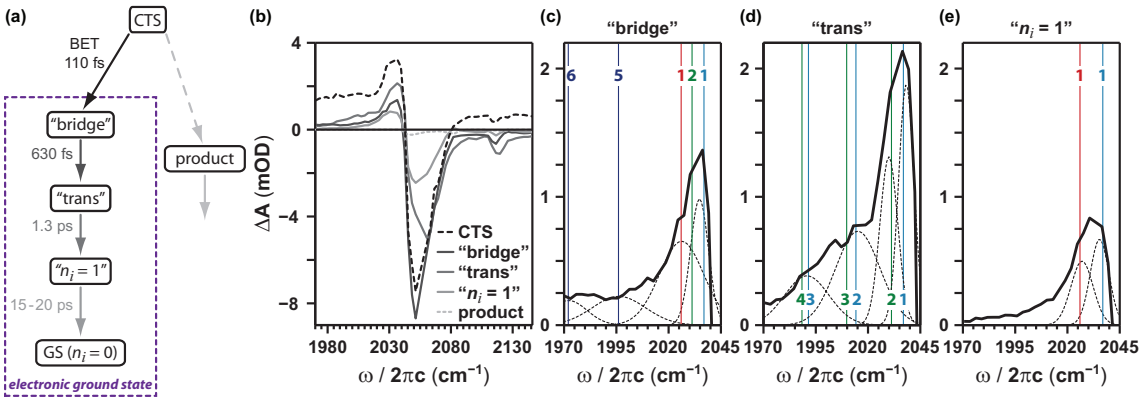

Figure 4.3: (a) Target model with corresponding time constants extracted from the global fit. The dashed gray arrow represents FET (∼1%) to the non-decaying product species occurring within the instrument response. The purple dashed box encompasses the electronic GS. (b) SADS of each species in the target model. (c−e) A closer look at the SADS associated with "bridge," "trans," and "$n_i = 1$" species. The spectra have been fit to a sum of Gaussian line shapes to serve as a visual aid for the spectral assignments discussed in the text. Vertical lines with numbers (i) correspond to integer quanta (ni) of ν_{radial} (red), ν_{trans} (cyan), ν_{axial} (green), and ν_{bridge} (blue) modes and represent the major contributions to each SADS.

The SADS generated from globally fitting the $Fe^{II}Pt^{IV}Fe^{II}$ data to the target model in Fig. 4.3a are shown in Fig. 4.3b. The spectrum of the CTS consists of two broad positive features spanning 1970−2045 cm^{-1} corresponding to highly excited CN stretching modes in the CTS. We cannot assign the degree of vibrational excitation of each of these modes because we have not measured the vibrational anharmonicities in the extremely short lived CTS. There is also a very broad transient absorption on the high-energy side (2080−2145 cm^{-1}) of the spectrum. This is consistent with the ν_{terminal} modes of the CTS being blue shifted relative to their frequencies in the GS, as was previously predicted.[11]

The SADS of the "bridge" species (see also Fig. 4.3c) can be broken down into two broad resonances centered at 1972 and 1996 cm^{-1} plus two more peaks at 2026 and 2035 cm^{-1}. We assign the former broad resonances as $n_{\text{bridge}} = 5-6$, while the latter are attributed to a combination of the $n_{\text{axial}} = 2$ and $n_{\text{trans}} = n_{\text{radial}} = 1$ states. Based on the position of the bridging CN ligands and the resonance Raman studies described in Reference 22, we would expect the ν_{bridge} mode to be the most strongly coupled to the back electron

transfer process, resulting in a high degree of vibrational excitation in the bridging mode as described by the SADS of the "bridge" species. We expect that greater than six quanta of the bridging vibrational mode are excited because the SADS of the "bridge" species clearly extends below 1970 cm^{-1} as seen in Figure 4.3c.

The non-equilibrium vibrational population of ν_{CN} modes contributing to the "trans" species SADS (Fig. 4.3d) can be fit to Gaussian line shapes centered at 1991, 2015, 2030, and 2038 cm^{-1} corresponding to $n_{axial} = 4$ and $n_{trans} = 3$, $n_{axial} = 3$ and $n_{trans} = 2$, $n_{axial} = 2$, and $n_{trans} = 1$, respectively. We note that the "trans" SADS has significantly more amplitude than the "bridge" SADS in the 1980−2140 cm^{-1} region, corresponding to the growth of population in $n_{trans} = 1-3$ and $n_{axial} = 2-4$ from the highly excited bridging mode. These IVR processes manifest themselves as a rising component in the kinetic traces observed clearly in the 2031 cm^{-1} trace in Fig. 4.2b which has a maximum at $t_d = 1$ ps. Notice in Fig. 4.3b that the large terminal CN bleach feature is centered near 2060 cm^{-1}, highlighting that this SADS contains predominantly a non-equilibrium distribution of the ν_{trans} mode. The positive portion of the "$n_i = 1$" SADS in Fig. 4.3e contains a peak centered at 2033 cm^{-1}, which corresponds to a vibrational population of $n = 1$ for the ν_{radial} and ν_{axial} modes.

The above spectral assignments in the SADS have been aided by polarization anisotropy work described in the appendix. In brief, transient IR absorption data were taken with the polarization of the pump pulse both parallel and perpendicular to the probe. The resulting data were fit to the target model in Figure 4.3a such that polarization-dependent SADS could be generated. These spectra prove to be very useful, as they reveal whether or not the transient IR features are aligned along the MMCT axis. For example, it is shown (see Figure 4A.7) that the features in the "trans" SADS between 1970−2045 cm^{-1} are approximately parallel to the charge transfer axis, consistent with both ν_{trans} and ν_{axial} modes accepting vibrational energy from the ν_{bridge} mode.

The target analysis reveals that on ultrafast BET in 110 fs, greater than 6 vibrational quanta of the bridging CN stretching mode are excited along with 1−2 quanta of ν_{trans}, ν_{axial}, and ν_{radial} in the electronic GS of $Fe^{II}Pt^{IV}Fe^{II}$. Excess energy from $n_{bridge} = 5-6$ is transferred via IVR into the ν_{trans} ($n_{trans} = 1-3$) and ν_{axial} ($n_{axial} = 2-4$) modes on a

630 ± 50 fs time scale, which is believed to occur in order to direct excess energy to the highly solvent-accessible ν_{trans} mode. Each of the ν_{CN} modes vibrationally cools to $n_i = 1$ on a 1.3 ± 0.1 ps time scale and subsequently relaxes to $n_i = 0$ by VR on a 15−20 ps time scale. Thus, not only do the anharmonically coupled high-frequency ν_{CN} modes provide a large density of states for rapid back-electron transfer, they also provide the necessary means for the non-equilibrium electronic GS to relax towards equilibrium.

Numerous studies by Bocarsly and coworkers have revealed that $Fe^{II}Pt^{IV}Fe^{II}$ can be viewed as two dimers, where each of the donating iron atoms shares the platinum acceptor and upon photoexcitation there is equal probability of generating either $Fe^{III}Pt^{III}Fe^{II}$ or $Fe^{II}Pt^{III}Fe^{III}$ as the CTS.[25] This allows us to compare our results with transient IR studies performed on mixed-valence dimers of the form $[(CN)_5M^{II}-CN-M^{III}(NH_3)_5]^-$ where M = Fe, Ru, Os. Woodruff and coworkers investigated back-electron transfer in the transition metal dimers using picosecond IR spectroscopy.[13,14] They reported that back-electron transfer occurs in less than 500 fs with vibrational excitation of $n_{\text{terminal}} = 7$ (each of the ν_{CN} modes were designated as one ν_{terminal} mode). They observed subsequent VR on time scales ranging from 0.5−18 ps for both the $Ru^{II}Ru^{III}$ and $Os^{II}Os^{III}$ analogs. Walker and coworkers investigated back-electron transfer in the transition metal dimers $Fe^{II}Ru^{III}$ and $Os^{II}Ru^{III}$ using 300-fs resolved IR spectroscopy.[11,12] The ability to spectrally resolve the transient data and the clear presence of multiple IR-active modes ($\nu_{\text{CN-trans}}$, $\nu_{\text{CN-cis}}$, and $\nu_{\text{CN-bridge}}$) in the FTIR spectrum allowed the role of multiple high-frequency vibrations to be addressed. The time resolution of these experiments allowed a lower limit of the BET rate of 3×10^{12} s^{-1} (i.e., $\tau_{\text{BET}} < 330$ fs) to be imposed. It was found that relatively minor excitation into the cis and trans vibrational modes ($n < 4$) accompanies back-electron transfer. In both the above-mentioned studies, a detailed mode-specific description of intramolecular vibrational energy relaxation following MMCT and the role of the bridging vibration was not addressed.

We note that this study has focused solely on the role of coupled high-frequency CN stretching vibrations in ultrafast charge transfer processes in transition metal mixed-valence complexes. Recent studies have shown that high frequency NH stretching modes play a significant role in the charge transfer emission spectra of binuclear mixed valence species.[28]

We imagine that the CN and NH stretching modes are anharmonically coupled to some degree and future studies probing the NH stretching vibrations will be able to elucidate their role in the MMCT excitation of $Fe^{II}Pt^{IV}Fe^{II}$. Several previous time-resolved studies have probed the role of coupled low-frequency intramolecular vibrations in the BET process in mixed valence dimers.[8,9,29] We anticipate that low-frequency vibrational modes of $Fe^{II}Pt^{IV}Fe^{II}$ are coupled to the high-frequency vibrational modes and are also involved in the ultrafast BET process. Our characterization of the anharmonic vibrational couplings of the ν_{CN} modes in the electronic GS of $Fe^{II}Pt^{IV}Fe^{II}$ has revealed coupled low-frequency modes in the $\sim$50 cm^{-1} spectral region, and we are currently investigating their role in the ultrafast BET process.

4.3 Summary

The results presented in this study allow for a multidimensional description of non-adiabatic BET following MMCT in a trinuclear cyano-bridged mixed-valence compound. Figure 4.4 visually summarizes our results with two cartoons. The top panel displays a 2D vibrational energy landscape as a function of the vibrational quantum numbers of the bridge and trans CN stretching modes in the GS. Excitation at 400 nm creates the intermediate $Fe^{III}Pt^{III}Fe^{II}$ species which decays via back-electron transfer to the electronic GS in 110 fs. Upon BET, greater than 6 quanta of vibrational energy is deposited into the cyanide bridging stretch. Instead of direct vibrational cooling to $n_{bridge} = 1$, energy from the bridge is transferred via IVR into the anharmonically coupled and solvent accessible trans vibrational coordinate. Each mode subsequently vibrationally cools to $n_i = 1$ and finally relaxes to $n_i = 0$.

The bottom panel is an attempt to convert the spectrotemporal data measured in the femtosecond transient IR experiment into a spatiotemporal description of charge and energy migration. We show a one-dimensional (1D) description of the on-axis vibrational energy flow from the Pt atom to the solvent, where the majority of the excess vibrational energy is directed along the charge transfer axis. Let us assume that the ν_{bridge} and ν_{trans} modes are completely localized on the CN bonds lying along the MMCT axis. Upon thermal BET, excess vibrational energy is dissipated to the solvent from the bridging to the terminal axial ligand separated by $\sim$0.5 nm in $\sim$0.8 ps.

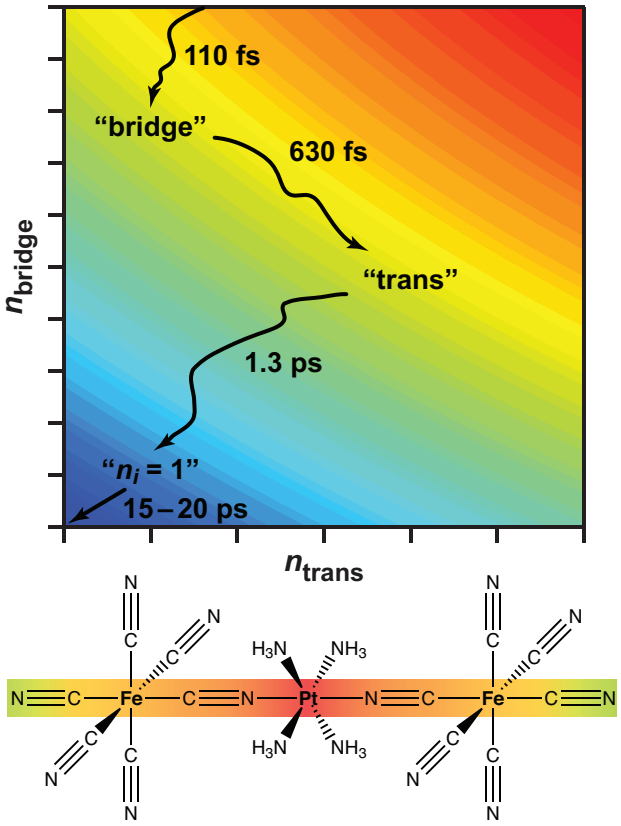

Figure 4.4: (Top) Cartoon of a 2D vibrational energy landscape of the electronic GS describing IVR, VC, and VR along two coordinates defined by vibrational quanta (n) of ν_{bridge} and ν_{trans} vibrational modes for fixed $n_{\text{radial}} = 1$ and $n_{\text{axial}} = 3$ following BET from the CTS. (Bottom) A cartoon representing the major component of vibrational energy (i.e., heat) flow occurring in $Fe^{II}Pt^{IV}Fe^{II}$ upon back-electron transfer from $Fe^{III}Pt^{III}Fe^{II}$ illustrating vibrational relaxation occurring along the MMCT axis to the solvent.

Our ability to design molecules and materials for energy capture and conversion relies on a microscopic map of the time-evolving multidimensional energy landscape following a photoinduced charge transfer event. This Letter provides a multidimensional spatiotemporal view of non-adiabatic charge and vibrational energy transfer in a trinuclear mixed valence compound in solution by probing the high-frequency cyanide stretching vibrations with sub-100 fs transient IR spectroscopy. The directionality of the MMCT transition and the subsequent on-axis vibrational energy excitation and relaxation has implications for materials relying on pseudo-1D energy transfer, such as molecular wires and organic pho-

tovoltaic materials. These data provide a testing ground for coupled electronic and nuclear motions in electron transfer theories and state-of-the-art electronic structure calculations of ultrafast charge transfer processes in solution.

4.4 Experimental Section

4.4.1 Sample preparation

$Na_4[(NC)_5Fe^{II}-CN-Pt^{IV}(NH_3)_4-NC-Fe^{II}(CN)_5]$ was synthesized according to literature procedures.[21] In brief, aqueous $K_3[Fe(CN)_6]$ and $[Pt(NH_3)_4](NO_3)_2$ were mixed at room temperature and the resulting solution was filtered using gravity filtration and purified by ion-exchange and size-exclusion chromatography. All chemicals were purchased from Sigma-Aldrich and used without further purification. Sample purity was verified with FTIR and UV/vis spectroscopy. Data were collected at room temperature ($T = 295$ K) with a sample concentration of ∼19 mM.

4.4.2 Transient infrared spectrometer

The basic visible−infrared pump−probe layout has been published elsewhere.[30] For this experiment, temporal compression of the pump pulse (400 nm, 35 fs, 1 μJ) was achieved with an acousto-optic programmable dispersive filter (Fastlite, DazzlerTM UV-250−400). A 400 nm pump-power dependence study revealed a linear dependence of the integrated signal area on the pump energy across an energy range of 0.05−1.0 μJ confirming a one-photon absorption process. The spectrum of the mid-IR probe (∼85 fs, 0.3 μJ) was centered at ∼2100 cm^{-1} ($\Delta\omega_{\mathrm{fwhm}} \sim 200$ cm^{-1}). Pump and probe beams were focused down to approximately 250 and 140 μm spots ($1/e^2$), respectively. Time-zero between the pump and probe was found by cross-correlating the two beams in a polished 250 μm Si wafer, which also revealed $\Delta t_{\mathrm{IRF}} = 94 \pm 8$ fs. The IR probe was spectrally dispersed and detected with a 2×64 element HgCdTe array detector such that differences in optical density as low as 30 μOD could be measured.

REFERENCES

[1] Sumi, H.; Marcus, R. *J. Chem. Phys.* **1986**, *84*, 4894–4914.

[2] Jortner, J.; Bixon, M. *J. Chem. Phys.* **1988**, *88*, 167–170.

[3] Bagchi, B.; Gayathri, N. *Adv. Chem. Phys.* **1999**, *107*, 1–80.

[4] Barbara, P.; Meyer, T.; Ratner, M. *J. Phys. Chem.* **1996**, *100*, 13148–13168.

[5] Jean, J. M.; Friesner, R. A.; Fleming, G. R. *J. Chem. Phys.* **1992**, *96*, 5827–5842.

[6] Barbara, P. F.; Walker, G. C.; Smith, T. P. *Science* **1992**, *256*, 975–981.

[7] Walker, G. C.; Aakesson, E.; Johnson, A. E.; Levinger, N. E.; Barbara, P. F. *J. Phys. Chem.* **1992**, *96*, 3728–3736.

[8] Reid, P. J.; Silva, C.; Barbara, P. F.; Karki, L.; Hupp, J. T. *J. Phys. Chem.* **1995**, *99*, 2609–2616.

[9] Kambhampati, P.; Son, D. H.; Kee, T. W.; Barbara, P. F. *J. Phys. Chem. A* **2000**, *104*, 10637–10644.

[10] Lockwood, D. M.; Ratner, M. A.; Kosloff, R. *J. Chem. Phys.* **2002**, *117*, 10125.

[11] Wang, C. F.; Mohney, B. K.; Akhremitchev, B. B.; Walker, G. C. *J. Phys. Chem. A* **2000**, *104*, 4314–4320.

[12] Tivansky, A.; Wang, C.; Walker, G. *J. Phys. Chem. A* **2003**, *107*, 9051–9058.

[13] Doorn, S. K.; Stoutland, P. O.; Dyer, R. B.; Woodruff, W. H. *J. Am. Chem. Soc.* **1992**, *114*, 3133–3134.

[14] Doorn, S. K.; Dyer, R. B.; Stoutland, P. O.; Woodruff, W. H. *J. Am. Chem. Soc.* **1993**, *115*, 6398–6405.

[15] Feskov, S. V.; Kichigina, A. O.; Ivanov, A. I. *J. Phys. Chem. A* **2011**, *115*, 1462–1471.

[16] Endicott, J. F.; Chen, Y. J. *Coord. Chem. Rev.* **2007**, *251*, 328–350.

[17] Endicott, J. F.; Chen, Y. J.; P, X. *Coord. Chem. Rev.* **2005**, *249*, 343–373.

[18] Demadis, K. D.; Hartshorn, C. M.; Meyer, T. J. *Chem. Rev.* **2001**, *101*, 2655–2686.

[19] Hupp, J. T.; Williams, R. D. *Acc. Chem. Res.* **2001**, *34*, 808–817.

[20] Zhou, M.; Pfennig, B. W.; Steiger, J.; Vanengen, D.; Bocarsly, A. B. *Inorg. Chem.* **1990**, *29*, 2456–2460.

[21] Watson, D. F.; Tan, H.-S.; Schreiber, E.; Mordas, C.; Bocarsly, A. B. *J. Phys. Chem. A* **2004**, *108*, 3261–3267.

[22] Pfennig, B. W.; Wu, Y.; Kumble, R.; Spiro, T.; Bocarsly, A. B. *J. Phys. Chem.* **1996**, *100*, 5745–5750.

[23] Hennessy, M.; Wu, Y.; Bocarsly, A. B.; Soos, Z. *J. Phys. Chem. A* **1998**, *102*, 8312–8319.

[24] Hennessy, M. H.; Soos, Z. G.; Watson, D. F.; Bocarsly, A. B. *J. Phys. Chem. B* **2000**, *104*, 10909–10914.

[25] Watson, D.; Bocarsly, A. B. *Coord. Chem. Rev.* **2001**, *211*, 177–194.

[26] van Stokkum, I. H. M.; Larsen, D. S.; van Grondelle, R. *Biochim. Biophys. Acta - Bioenergetics* **2004**, *1657*, 82–104.

[27] van der Veen, R. M.; Cannizzo, A.; van Mourik, F.; Vlček, A.; Chergui, M. *J. Am. Chem. Soc.* **2011**, *133*, 305–315.

[28] Chen, Y.-J.; Xie, P.; Endicott, J. F. *J. Phys. Chem. A* **2004**, *108*, 5041–5049.

[29] Son, D. H.; Kambhampati, P.; Kee, T. W.; Barbara, P. F. *J. Phys. Chem. A* **2002**, *106*, 4591–4597.

[30] Lynch, M. S.; Cheng, M.; Van Kuiken, B. E.; Khalil, M. *J. Am. Chem. Soc.* **2011**, *133*, 5255–5262.

4.A Chapter 4 Supporting Information

4.A.1 UV/visible Spectrum of $Fe^{II}Pt^{IV}Fe^{II}$ in D_2O

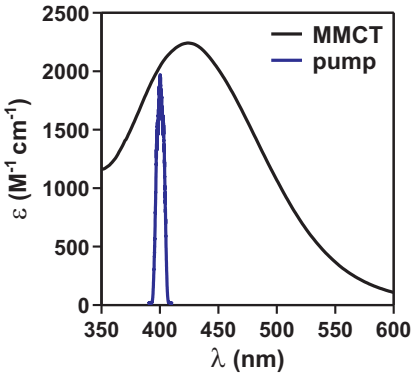

Figure 4A.1: UV/vis spectrum of $Fe^{II}Pt^{IV}Fe^{II}$ ($c \sim 0.7$ mM; $l = 0.1$ cm) in D_2O at $T = 295$ K and the spectrum of the 400 nm pump pulse. The MMCT band peaks at $\lambda = 424$ nm.

4.A.2 CN Stretching Modes of $Fe^{II}Pt^{IV}Fe^{II}$

The four ν_{CN} modes of $Fe^{II}Pt^{IV}Fe^{II}$ are shown in Figure 4A.2.

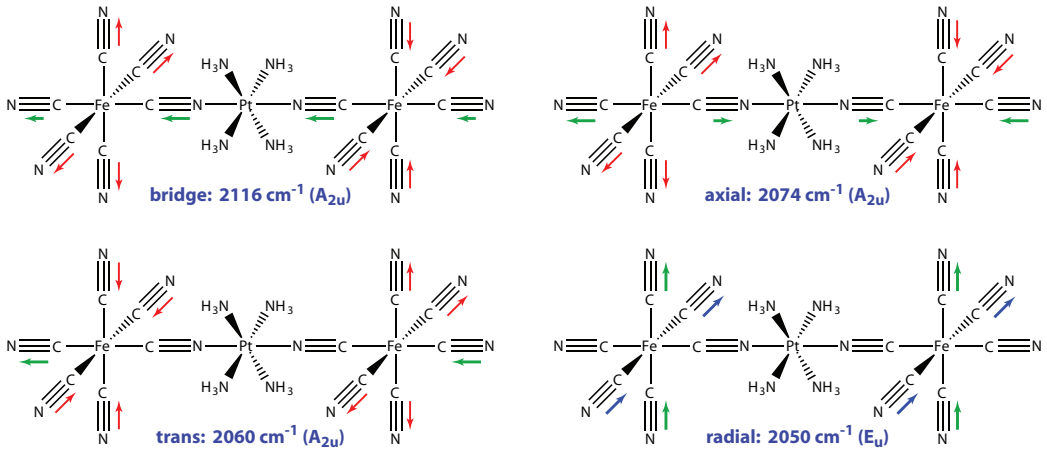

Figure 4A.2: A qualitative picture of the normal modes for the ν_{CN} vibrations ν_{radial}, ν_{trans}, ν_{axial}, and ν_{bridge}. Normal mode symmetries are based on the D_{4h} point group of the molecule. Red arrows represent symmetric displacements (not to scale).

4.A.3 Global and Target Analysis

Target model

The target model used to globally fit the transient IR data is shown in Figure 4A.3. The only changes from the chapter are in the labels corresponding to the rate constants. Many other target models were attempted to reproduce the data but were not as successful as this model, as is discussed below.

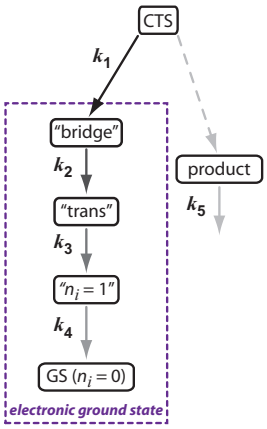

Figure 4A.3: Target model used for global analysis where $k_i = 1/\tau_i$.

The global analysis (GA) was performed on a total of 51 time traces (corresponding to 51 unique IR frequencies) from the raw data matrix over a time window of 0.16−50 ps. Data between 0−0.16 ps were excluded to ensure the resulting species-associated difference spectra (SADS) were not due to cross-phase modulation and/or solvent response (Section 4.A.5). Each of the 51 traces were fit to the equation[1,2]

$$\begin{aligned} f_{\mathrm{GA}}(t;\omega) = {} & A_1(\omega)\mathrm{ExpErf}\left[B, t_0, \tau_1, t\right] \cdots \\ & + A_2(\omega)\left(\mathrm{ExpErf}\left[B, t_0, \tau_2, t\right] - \mathrm{ExpErf}\left[B, t_0, \tau_1, t\right]\right) \cdots \\ & + A_3(\omega)\left(\mathrm{ExpErf}\left[B, t_0, \tau_3, t\right] - \mathrm{ExpErf}\left[B, t_0, \tau_2, t\right]\right) \cdots \\ & + A_4(\omega)\left(\mathrm{ExpErf}\left[B, t_0, \tau_4, t\right] - \mathrm{ExpErf}\left[B, t_0, \tau_3, t\right]\right) \cdots \\ & + A_5(\omega)\mathrm{ExpErf}\left[B, t_0, \tau_5 = 100\ \mu\mathrm{s}, t\right], \end{aligned} \tag{4A.1}$$

with ExpErf $[B, t_0, \tau_i, t]$ defined as

$$\begin{aligned}\text{ExpErf}\left[B, t_0, \tau_i, t\right] \equiv \exp &\left[\left(\frac{B}{4\sqrt{\ln(2)}\cdot\tau_i}\right)^2 - \frac{t-t_0}{\tau_i}\right]\cdots \\ &\times\frac{1}{2}\left(\text{erf}\left[\frac{t-t_0}{B}\cdot 2\sqrt{\ln(2)} - \frac{B}{4\sqrt{\ln(2)}\cdot\tau_i}\right]+1\right)\end{aligned} \tag{4A.2}$$

where erf is an error function. Note that Eqn. 4A.2 is the result of the convolution of an exponential decay with a Gaussian. In the above equations, A_i is the IR-frequency dependent amplitude of the i$^{\text{th}}$ exponential decay, B is the full-width at half-maximum (fwhm) of the Gaussian instrument response function ($B = \Delta t_{\text{IRF}} = 94$ fs), T_0 is time zero ($t_0 = 0$), and τ_i ($= 1/k_i$) is the time-constant of the i$^{\text{th}}$ exponential decay.

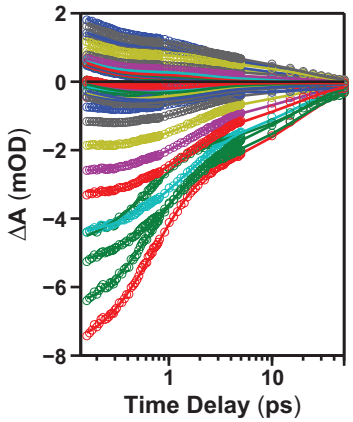

Figure 4A.4: Global fitting results for all fifty-one kinetic traces.

The only parameters that were fit locally were the amplitude terms $[A_i(\omega)]$ in Eqn. 4A.1. All other parameters were fit globally. Thus, only 5 time constants are used in the global fit. To minimize the number of parameters needed in the fitting routine, τ_5 was set to 100 μs (which is non-decaying from 0−50 ps) and τ_4 was set to the experimentally determined vibrational relaxation times for $Fe^{II}Pt^{IV}Fe^{II}$ in D_2O at room temperature from IR pump−probe experiments. Thus, each frequency is fit to an equation with 8 unknowns.

All fifty-one kinetic traces with their corresponding best fits from the global analysis are shown in Fig. 4A.4. Comparing the target model in Fig. 4A.3 with Eqn. 4A.1 one can see that the SADS for each species are simply $A_i(\omega)$, where $i = 1$ for CTS, $i = 2$ for "bridge," $i = 3$ for "trans," $i = 4$ for "$n_i = 1$," and $i = 5$ for product.

Results

Table 4A.1 shows the fitting results for the five kinetic traces shown in Figure 4.2b of the chapter. Recall that the global fit revealed the global parameters $\tau_1 = 110 \pm 10$ fs,

Table 4A.1: Global fitting results for five infrared probe frequencies. Amplitude columns (e.g., $A_{i=1}$) represent parameters that contribute to SADS for the CTS ($i = 1$), "bridge" ($i = 2$), "trans" ($i = 3$), "$n_i = 1$" ($i = 4$), and product ($i = 5$) species.

ω (cm^{-1})	τ_4 (ps)	$A_{i=1}$	$A_{i=2}$	$A_{i=3}$	$A_{i=4}$	$A_{i=5}$
1973	15	1.4	0.21	0.16	0.028	0
2031	19	3.1	1.2	1.8	0.83	0
2051	18	−7.4	−8.7	−3.9	−2.4	−0.21
2116	18	0.34	−0.66	−1.1	−0.27	−0.038
2136	18	0.67	−0.15	−0.36	−0.089	0

$\tau_2 = 630 \pm 50$ fs, and $\tau_3 = 1.3 \pm 0.1$ fs. Infrared pump−probe experiments in our group (see Chapter 3) have revealed the vibrational relaxation time constants (i.e., time constant for $n_i = 1 \rightarrow n_i = 0$), which are given in Table 4A.1 as τ_4.

Simulated kinetics

Using the target model shown in Fig. 4A.3 and the resulting rate constants extracted from the global analysis, it is possible to simulate the relative populations of each species. The

coupled rate equations from the target model are shown in Equation 4A.3.

$$\begin{aligned}
\dot{c}_1 &= -k_1(1-\Phi)c_1(t) - k_5\Phi c_1(t) \\
\dot{c}_2 &= k_1(1-\Phi)c_1(t) - k_2 c_2(t) \\
\dot{c}_3 &= k_2 c_2(t) - k_3 c_3(t) \\
\dot{c}_4 &= k_3 c_3(t) - k_4 c_4(t) \\
\dot{c}_5 &= k_4 c_4(t) \\
\dot{c}_6 &= k_5\Phi c_1(t) - k_6 c_6(t)
\end{aligned} \tag{4A.3}$$

Here, from top to bottom the equations represent the transient population of the CTS (c_1), "bridge" (c_2), "trans" (c_3), "$n_i = 1$" (c_4), GS (c_5), and product (c_6) species. The forward electron transfer (FET) quantum yield (Φ) is 0.01. It has been assumed that the FET rate (k_5) is equivalent to Δt_{IRF} (i.e., $k_5 = 1/0.094$ ps^{-1}), as this rate could not be measured with our time resolution as noted in the chapter. The solution to this system of coupled differential equations is illustrated graphically in Figure 4A.5. The population of the "trans" species is maximum at $t_{\mathrm{max}} = 1.01$ ps, whereas the population of the "bridge" species peaks at $t_{\mathrm{max}} = 0.23$ ps. Thus, if we consider only the primary contributions to the "bridge" and "trans" species (i.e., the ν_{bridge} and ν_{trans} modes, respectively) and assume that the ν_{bridge} and ν_{trans} modes are localized on the bridge and trans ligands, we can say that vibrational energy transfers from the bridge to the trans ligand in ~0.8 ps. The distance between the bridge and trans ligands (~0.5 nm) was calculated from the center of mass of the bridging ligand to the center of mass of the trans ligand obtained from the crystal structure.[3]

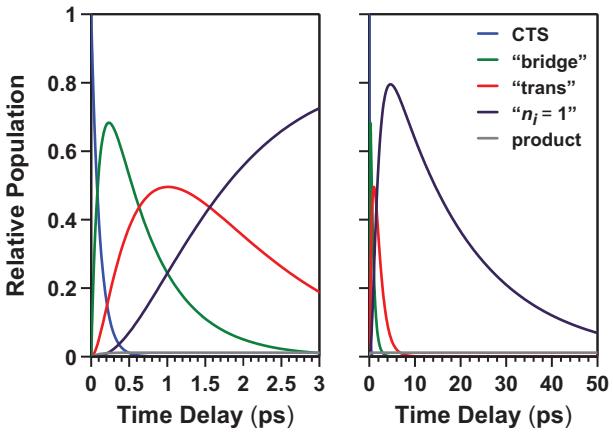

Figure 4A.5: Relative population of transient species as a function of pump−probe time delay (t_d) obtained from the solution of Eqn. 4A.3. Parameters used in the simulation (Eqn. 4A.3) are: $k_1 = 1/0.11$ ps^{-1}, $k_2 = 1/0.63$ ps^{-1}, $k_3 = 1/1.3$ ps^{-1}, $k_4 = 1/18$ ps^{-1}, $k_5 = 1/0.094$ ps^{-1}, $k_6 = 10^{-8}$ ps^{-1}, and $\Phi = 0.01$. Recovery of the GS (c_5) is omitted.

Alternative models attempted

Many target models were attempted before the final target model was found.

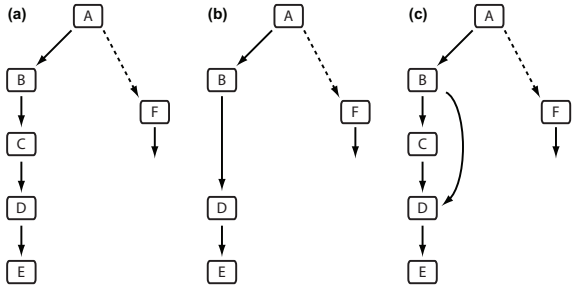

Figure 4A.6: Examples of attempted target models with generic labeling (A−F) representing a particular species in the target model. Model (a) is the model used in this chapter (compare Figure 4.3), model (b) failed to fit the rising component observed in the 2031 cm^{-1} region, and model (c) resulted in redundant parameters.

Given that we first use a target model to globally fit the transient data and then make assignments of each target species based on the generated SADS, the models were iterated based on the number of targets (i.e., boxes) and the connections between each target. Figures 4A.6b and 4A.6c illustrate two examples of alternate models tried.

4.A.4 Polarization-dependent SADS

We have obtained polarization-dependent SADS for $Fe^{II}Pt^{IV}Fe^{II}$ in D_2O by rotating the polarization of the pump pulse either parallel or perpendicular to the probe pulse. This allows us to calculate the SADS anisotropy, where $r_{\mathrm{SADS}} = (\mathrm{SADS}_{\parallel} - \mathrm{SADS}_{\perp})/(\mathrm{SADS}_{\parallel} + 2\mathrm{SADS}_{\perp})$. The anisotropy depends on the angle (θ_{ij}) between the electronic transition dipole moment and the vibrational dipole derivative vector by $r_{\mathrm{ij}}(\theta_{\mathrm{ij}}) = 0.2 \cdot (3\cos\theta_{\mathrm{ij}} - 1)$. When the transition dipoles are parallel (vibration parallel to MMCT axis) an anisotropy of 0.4 is achieved, whereas when the dipoles are perpendicular the anisotropy is -0.2 (vibration perpendicular to the MMCT axis). Figure 4A.7 clearly shows that there is polarization anisotropy in the SADS. It is most obvious in the case of the "trans" species, as the anisotropy approaches 0.4 in the peak regions we expect to see trans and axial modes, which are parallel to the MMCT axis.

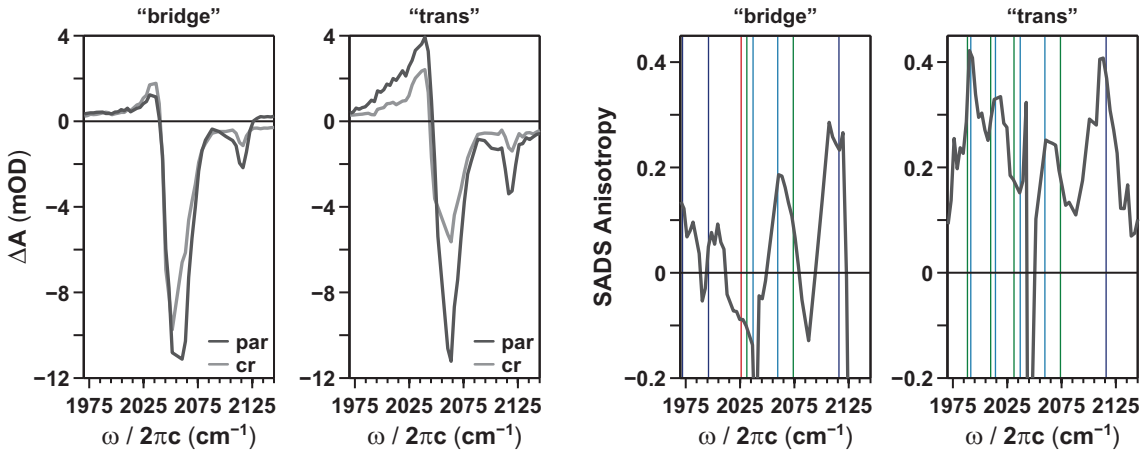

Figure 4A.7: The two left graphs show SADS obtained for the "bridge" and "trans" species with parallel (par) and crossed (cr) polarization conditions. The SADS anisotropy is plotted in the two graphs on the right. Vertical lines correspond to the ν_{radial} (red), ν_{trans} (cyan), ν_{axial} (green), and ν_{bridge} (blue) modes.

4.A.5 Neat Solvent (D_2O) Response

Transient infrared absorption data was globally fit to the target model starting at $t_{\mathrm{d}} = 160$ fs to ensure that cross-phase modulation artifacts and/or solvent response were not included

in the fit. Figure 4A.8 shows neat solvent response along with the $Fe^{II}Pt^{IV}Fe^{II}$ in D_2O response at $\omega = 1971$ cm^{-1} with a red dashed line defining the starting time of the fit. We could have chosen to fit from $t_d = 0$ by adding 2−3 "coherent artifacts." However, we believe that the addition of 2−3 more exponentials in the fit to include these artifacts would result in too many floating parameters and are confident that the results obtained here represent only the photochemistry involving $Fe^{II}Pt^{IV}Fe^{II}$. Solvent subtraction combined with global fitting from $t_d = 0$ was avoided to ensure that the resulting SADS do not contain artifacts created from the subtraction process.

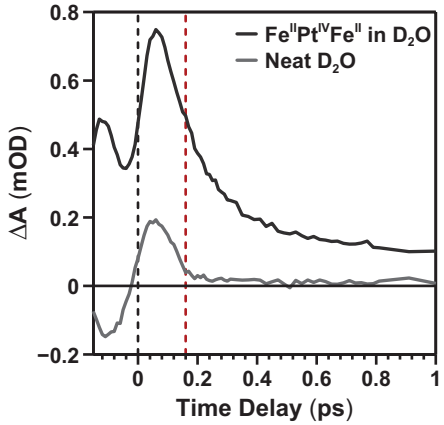

Figure 4A.8: Transient IR absorption data at $\omega = 1971$ cm^{-1} for $Fe^{II}Pt^{IV}Fe^{II}$ in D_2O (black line) and neat D_2O (gray line). Fitting of the data begins at $t_d = 160$ fs (dashed red line).

4.B Solvent Influence on BET and VER dynamics

Bocarsly and coworkers found that in $Ru^{II}Pt^{IV}Ru^{II}$ the back-electron transfer time scale changed from ∼480 fs in pure water to ∼1100 fs in a $\chi_{DMSO} = 0.05$ water/DMSO mixture. They also observed a change in vibrational relaxation times from 1.5 ps to 2.7 ps.[4] Differences were attributed to movement of the GS PES and therefore a change in driving force for BET. In an earlier study, Watson et al. observed "solvent-gated charge transfer" in $Fe^{II}Pt^{IV}Fe^{II}$ by changing the amount of DMSO in a DMSO/water mixture and measuring the UV/vis spectrum.[5] They found that at $\chi_{DMSO} > 0.123$ it is energetically favorable for the Pt^{IV} atom to oxidize the two Fe^{II} metal centers and therefore the complex dissociates

into $Pt^{II} + 2Fe^{III}$. The Fe^{II}/Fe^{III} redox couple changes because water is a better electron acceptor than DMSO. The increased electron accepting ability of water facilitates Fe−C π^* backbonding which makes it more difficult to oxidize iron. Adding small amounts of DMSO disrupts the water-cyanide interactions and makes the iron atoms more susceptible to oxidation.

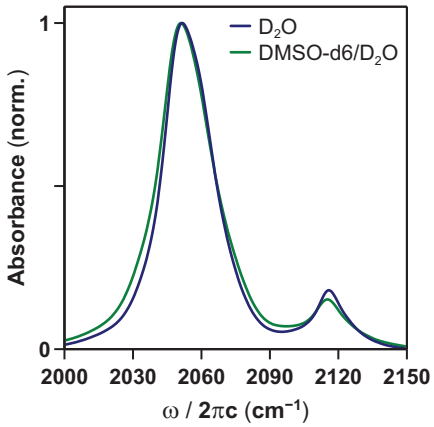

Figure 4B.1: Solvent-subtracted FTIR spectra of $Fe^{II}Pt^{IV}Fe^{II}$ in D_2O (blue) and a $\chi_{\text{DMSO-d6}} = 0.05$ mixture of DMSO-d6 and D_2O (green).

A study on the effect of DMSO on the back-electron transfer dynamics occurring in $Fe^{II}Pt^{IV}Fe^{II}$ is currently lacking. This is most likely due to the extremely fast BET rate in $Fe^{II}Pt^{IV}Fe^{II}$ making it difficult to separate the BET time scale from VER. Normalized FTIR spectra of $Fe^{II}Pt^{IV}Fe^{II}$ in both D_2O and a mixed-solvent containing a $\chi_{\text{DMSO-d6}} = 0.05$ mixture of DMSO-d6 and D_2O are presented in Figure 4B.1. The spectra are quite similar, though there are noticeable differences. The ν_{bridge} frequency shifts from 2116 cm^{-1} in D_2O to 2115 cm^{-1} in the mixed solvent where it is also slightly weaker. The large terminal ν_{CN} peak also shifts slightly with the main differences in the spectrum being at 2060 and 2076 cm^{-1}. These frequencies line up with the ν_{trans} and ν_{axial} modes, respectively. This suggests a slightly stronger ν_{trans} absorption in pure D_2O and weaker ν_{radial} and ν_{axial} absorptions, which would indicate a stronger interaction of pure D_2O with the ν_{trans} mode as one would expect.

We performed transient IR absorption spectroscopy on $Fe^{II}Pt^{IV}Fe^{II}$ in an 18.2% (v:v)

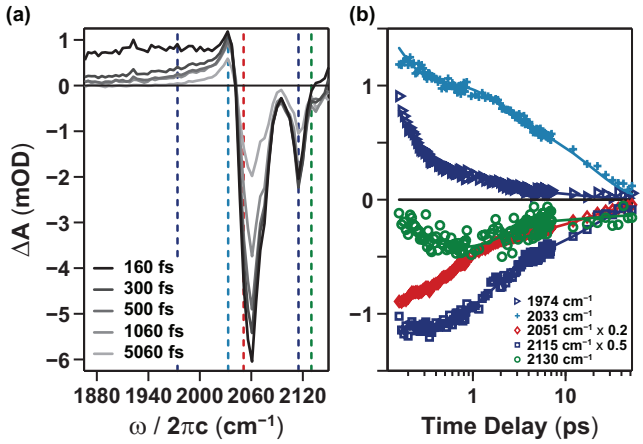

Figure 4B.2: Time-resolved IR absorption spectra and kinetics of $Fe^{II}Pt^{IV}Fe^{II}$ in a $\chi_{\text{DMSO-d6}} = 0.05$ DMSO-d6/D_2O mixture. (a) Time-resolved IR absorption spectra in the ν_{CN} region at five time delays (t_d) with pump and probe polarizations set to magic angle. The spectra consist of positive spectral features corresponding to transient photoproducts formed upon photoexcitation and negative features corresponding to bleaching of the electronic ground state. (b) Kinetics in the ν_{CN} region at five IR energies (dashed lines in (a)) from $t_d = 0.16-50$ ps on a logarithmic time axis. The solid lines are a global fit of the data to a target model. The timescales from the global fit are presented in Figure 4B.3a.

DMSO-d6/D_2O mixture ($\chi_{\text{DMSO-d6}} = 0.05$) with the same electronic pump energy of 1.07 μJ/pulse that was used in the pure D_2O case (see Chapter 4). It was very quickly observed that the photochemistry was different since we found much more photoproduct build-up on the sample cell windows due to the increased quantum yield of the second thermal FET step. The results of the experiment are presented in Figure 4B.2. These Figures can be compared directly with Figure 4.2 on page 93 to see the difference between pure D_2O and the mixed solvent. It is clear to see that the kinetics in the mixed-solvent case follow a very similar trend as in the pure D_2O case.

We quantified the difference in kinetics via global analysis on the data using the same target model obtained for pure D_2O shown in section 4.A.3. Our analysis reveals that the BET and subsequent vibrational energy relaxation dynamics do not change within the error of the analysis. However, there are differences in the SADS generated from the analysis as can be seen in Figure 4B.3. The biggest difference between the SADS in the two different

solvents (Figure 4B.3b and 4B.3c) is the amplitude of the bleach in the ν_{bridge} region of the spectrum. The larger amplitude is likely from the increased amount of product formed in the reaction leading to a larger signal from ferricyanide. The SADS of the CTS in the mixed-solvent case is much more flat in the $n_{\text{bridge}} > 6$ region, which could indicate a more significant population inversion in the ν_{bridge} mode when DMSO is present. A closer look at the low-energy transient absorption region presented in Figure 4B.3d highlights the similarities between the SADS of the "bridge," "trans," and "$n_i = 1$" species. The quantum yield of the second thermal FET step (i.e., product formation in the Figure) is ∼0.7% in D_2O and ∼1.4% in the DMSO-d6/D_2O mixture. This was estimated by taking the ratio of the product SADS to the total SADS amplitude in the terminal bleach region of the spectrum (which does not overlap with the ν_{CN} mode of ferricyanide). It is important to note that less points were fit in the mixed-solvent case due to less spectral resolution in the experiment (i.e., a different grating was used).

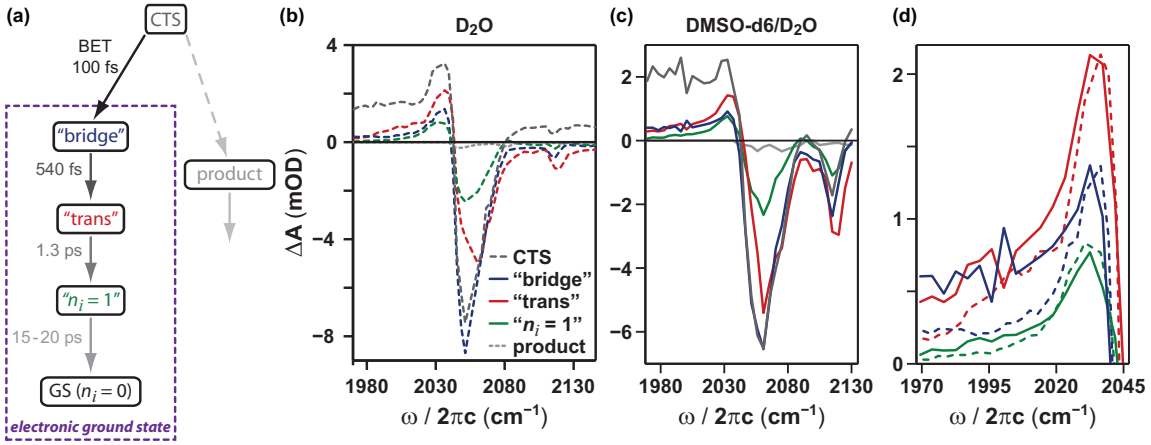

Figure 4B.3: (a) Target model with corresponding time constants extracted from the global fit. The dashed gray arrow represents FET (∼1.4%) to the non-decaying product species occurring within the instrument response. The purple dashed box encompasses the electronic GS. (b) SADS of each species with pure D_2O solvent. (c) SADS of each species with a $\chi_{\text{DMSO-d6}} = 0.05$ DMSO-d6/D_2O mixture as the solvent. (d) A closer look at the SADS associated with "bridge" (blue), "trans" (red), and "$n_i = 1$" (green) species. Dashed lines correspond to the D_2O SADS. Both the "bridge" and "trans" SADS for the DMSO-d6/D_2O solvent mixture have been scaled by a factor of 1.5 for comparison.

It is significant that there is no change (within error) to BET and VER dynamics in $Fe^{II}Pt^{IV}Fe^{II}$ with the addition of DMSO to the solvent. This highlights the role of the high-frequency ν_{CN} modes during relaxation of $Fe^{II}Pt^{IV}Fe^{II}$ in solution since changing the solvent does not change the kinetics. This strongly suggests that $Fe^{II}Pt^{IV}Fe^{II}$ and $Ru^{II}Pt^{IV}Ru^{II}$ behave differently during back-electron transfer. This work supports that electron transfer in $Fe^{II}Pt^{IV}Fe^{II}$ falls into the Marcus inverted region where multiple high-frequency intramolecular vibrational modes play a large role.

REFERENCES

[1] Van Stokkum, I. H. M.; Larsen, D. S.; Van Grondelle, R. *Biochim. Biophys. Acta - Bioenergetics* **2004**, *1657*, 82–104.

[2] van der Veen, R. M.; Cannizzo, A.; van Mourik, F.; Vlček, A.; Chergui, M. *J. Am. Chem. Soc.* **2011**, *133*, 305–315.

[3] Zhou, M.; Pfennig, B. W.; Steiger, J.; Vanengen, D.; Bocarsly, A. B. *Inorg. Chem.* **1990**, *29*, 2456–2460.

[4] Watson, D. F.; Tan, H.-S.; Schreiber, E.; Mordas, C.; Bocarsly, A. B. *J. Phys. Chem. A* **2004**, *108*, 3261–3267.

[5] Pfennig, B. W.; Bocarsly, A. B. *J. Phys. Chem.* **1992**, *96*, 226–233.

Chapter 5

COHERENT FIFTH-ORDER VISIBLE−INFRARED SPECTROSCOPIES: ULTRAFAST NON-EQUILIBRIUM VIBRATIONAL DYNAMICS IN SOLUTION

The work presented in this chapter has been published in the following paper:
Lynch, M.S.; Slenkamp, K.M.; Cheng, M.; Khalil, M. "Coherent Fifth-Order Visible−Infrared Spectroscopies: Ultrafast Non-Equilibrium Vibrational Dynamics in Solution," *J. Phys. Chem. A* **2012**, *116*, 7023−7032.

Obtaining a detailed description of photochemical reactions in solution requires measuring time-evolving structural dynamics of transient chemical species on ultrafast timescales. Time-resolved vibrational spectroscopies are sensitive probes of molecular structure and dynamics in solution. In this chapter, we develop doubly-resonant fifth-order nonlinear visible−infrared spectroscopies to probe non-equilibrium vibrational dynamics among coupled high-frequency vibrations during an ultrafast charge transfer process using a heterodyne detection scheme. The method enables the simultaneous collection of third- and fifth-order signals, which respectively measure vibrational dynamics occurring on electronic ground and excited states on a femtosecond timescale. Our data collection and analysis strategy allows transient dispersed vibrational echo (t-DVE) and dispersed pump−probe (t-DPP) spectra to be extracted as a function of electronic and vibrational population periods with high signal-to-noise (S/N $>$ 25). We discuss how the fifth-order experiments can measure (i) time-dependent anharmonic vibrational couplings, (ii) non-equilibrium frequency-frequency correlation functions, (iii) incoherent and coherent vibrational relaxation and transfer dynamics, and (iv) coherent vibrational and electronic (vibronic) coupling as a function of a photochemical reaction.

5.1 Introduction

Understanding and predicting ultrafast photochemical reactions in solution at the molecular level requires experimental probes capable of measuring non-equilibrium structural dynamics of reactive molecular and solvent species. Photochemical reactions in solution such as the primary photoisomerization event in vision, photodamage of DNA base pairs, and spin-flip transitions in molecular-based materials involve the synchronous movement of many inter- and intramolecular electronic and nuclear degrees of freedom.[1–3] These photochemical reactions span a range of timescales, but often the decisive period during which product distributions are determined occurs immediately after photoexcitation. Dynamics occurring during this crucial time period may involve multiple electronic and nuclear coordinates and are being intensely pursued by experimentalists and theorists alike. This is because creating a predictive model of a photochemical reaction in solution requires an understanding of conformational dynamics and timescales of non-equilibrium energy localization.[4]

There has been a concentrated experimental effort to develop nonlinear spectroscopies in the ultraviolet, visible and infrared regions of the electromagnetic spectrum to probe complex systems in solution in a multidimensional manner.[5–37] The goal of these experiments is to measure radiative and non-radiative energy flow among coupled inter- and intramolecular electronic and/or nuclear coordinates in the ground and excited electronic states of molecular and material systems. Simultaneously, the fields of ultrafast X-ray absorption and diffraction and electron diffraction techniques are rapidly moving towards measuring non-equilibrium time-evolving atomic structures during photochemical reactions.[38–46]

In this Chapter, we report on the development of heterodyne-detected doubly-resonant fifth-order nonlinear visible−infrared (vis−IR) echo spectroscopies to measure non-equilibrium vibrational dynamics among coupled vibrational modes during ultrafast photochemical reactions with high time resolution and signal-to-noise (S/N). The Chapter is organized as follows. In the remainder of Section 5.1 we qualitatively describe the detection strategy and the fifth-order response function measured by our experiments. Section 5.2 describes the vis−IR spectrometer and data collection methods used to simultaneously measure third- and fifth-order signals. Section 5.3 presents data analysis techniques, method validation,

and results on a cyano-bridged mixed-valence complex. Section 5.4 discusses the molecular insights which can be gained from this technique, compares the nonlinear spectroscopies developed in this Chapter to existing methods, and suggests further experimental opportunities.

The phase-sensitive fifth-order nonlinear signal field measured in our experiments is detected using spectral interferometry.[47] In this process, a low-amplitude signal field [$E_{\mathrm{sig}}(\omega)$] interferes with a time-delayed intense reference electric field of the same frequency [$E_{\mathrm{ref}}(\omega)$] in a spectrometer. The measured interferogram, $2E_{\mathrm{sig}}(\omega)E^{*}_{\mathrm{ref}}(\omega)\cos(\phi_{\mathrm{sig}}(\omega)-\phi_{\mathrm{ref}}(\omega)+\omega\tau_{\mathrm{ref}})$, is composed of spectral fringes whose period is proportional to the time delay (τ_{ref}) and phase between the two beams. The data is referred to as dispersed since the interferogram is detected in the frequency domain at the focal plane of a spectrograph. Careful mining of the so-called heterodyne-detected dispersed vibrational echo (HDVE) data allows the simultaneous extraction of transient IR dispersed pump−probe (t-DPP) and transient dispersed vibrational echo (t-DVE) spectra of a non-equilibrium distribution of species. Transient analogs of HDVE spectroscopy have recently been used to explore the dynamics of peptides and proteins in solution following a laser induced temperature-jump.[48,49] The word transient refers to an external stimulus shifting the system away from equilibrium, including a laser temperature jump,[50] photoinduced pH-jump,[51] or ultrafast photoexcitation,[52] the latter of which is the subject of this work. The nonlinear vis−IR spectroscopies developed here have been designed to simultaneously collect the third-order (i.e., equilibrium ground state, GS) and fifth-order (i.e., non-equilibrium excited state) signals at a sampling rate of 250 Hz. This enables a direct comparison of equilibrium versus non-equilibrium vibrational dynamics occurring on femtosecond to picosecond timescales.

The general pulse sequence used to collect fifth-order vis−IR data is shown in Figure 5.1. First, two interactions with a single visible pulse ($\mathbf{k}_{\mathrm{vis}}$) create a transient population on the electronic excited (or ground) state which evolves during the electronic population period τ_{vis}. A third-order nonlinear IR sequence follows, where the first IR pulse ($\mathbf{k}_1$) creates a vibrational coherence along τ_1, the second IR field ($\mathbf{k}_2$) generates a vibrational population along τ_2 (the vibrational waiting time), and the third IR pulse ($\mathbf{k}_3$) generates a second vibrational coherence along τ_3 from which the signal is detected at $t = \tau_{\mathrm{vis}} + \tau_1 + \tau_2 + \tau_3$. A

fourth independent IR local oscillator (LO) field that is delayed from the signal by a fixed τ_{LO} is mixed with the signal field for heterodyne detection.

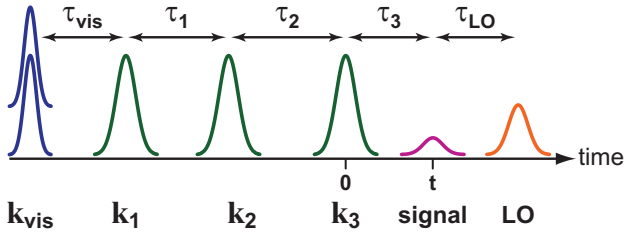

Figure 5.1: General pulse sequence for fifth-order nonlinear vis−IR spectroscopies highlighting the electronic population (τ_{vis}), vibrational coherence (τ_1), vibrational population (τ_2), and vibrational detection (τ_3) time periods. One visible beam (blue) and three IR beams (green) impinge on the sample to generate overlapping third- and fifth-order nonlinear signal fields (pink). An external LO (orange) is spatially overlapped with the signal fields and delayed from signal emission by τ_{LO}. Note that we define τ as the difference between maxima of the electric field envelopes. The field-matter interactions occur at the field maxima assuming impulsive excitation.

Many variants of the pulse sequence in Fig. 5.1 can be created by changing the time-ordering of the pulses. Each variation generates a different nonlinear signal with unique information content. In a t-DPP experiment, $\tau_1 = 0$ and τ_2 is scanned for fixed values of τ_{vis}. In t-DVE spectroscopy, τ_1 is scanned for fixed values of τ_{vis} and τ_2. The τ_3 time delay is not scanned since the experiments are performed in a time−frequency arrangement where the cosine Fourier transform along τ_3 is performed by a diffraction grating.

Data collected in these experiments aim to extract the fifth-order material response function, $\overleftrightarrow{\mathbf{R}}^5(\tau_3, \tau_2, \tau_1, \tau_{\mathrm{vis}})$. This fifth-order response function can be written as a six-point correlation function of the vibrational and electronic dipole operators by:

$$\begin{aligned}\overleftrightarrow{\mathbf{R}}^5(\tau_3, \tau_2, \tau_1, \tau_{\mathrm{vis}}) &= (i/\hbar)^5 \theta(\tau_3)\theta(\tau_2)\theta(\tau_1)\theta(\tau_{\mathrm{vis}}) \\ \times \langle\langle [[[[[\mathbf{M}(\tau_{\mathrm{vis}} + \tau_1 + \tau_2 + \tau_3), \mathbf{M}(\tau_{\mathrm{vis}} + \tau_1 + \tau_2)], \\ \mathbf{M}(\tau_{\mathrm{vis}} + \tau_1)], \mathbf{M}(\tau_{\mathrm{vis}})], \mathbf{K}(0)], \mathbf{K}(0)] \boldsymbol{\rho}_{00} \rangle\rangle,\end{aligned} \tag{5.1}$$

where θ is a Heaviside step function, $\mathbf{M}$ is the vibrational dipole operator with vibrational

transition dipole matrix elements $\mu^{n,n'} = \langle n|\mathbf{M}(\mathbf{Q})|n'\rangle$ over the local system vibrational coordinates $\mathbf{Q}$, $\mathbf{K}$ is the electronic dipole operator with matrix elements $\kappa^{g,e} = \langle g|\mathbf{K}(\mathbf{r};\mathbf{Q})|e\rangle$ over the electronic coordinates $\mathbf{r}$ at a particular local vibrational coordinate $\mathbf{Q}$, $\boldsymbol{\rho}_{00}$ is the initial reduced density matrix, and the trace denoted as $\langle\langle\cdots\rangle\rangle$ is over both electronic and vibrational state manifolds. In the above equation, τ_{i} represents the i^{th} experimental time-delay as defined in Figure 5.1. The response function in Equation 5.1 can be expanded into 64 terms since the first two visible interactions are indistinguishable. Twelve of the possible 64 correlation functions correspond to the phase matching geometry used in this experiment. Each term in the response is a product of the magnitudes of six interacting dipole matrix elements. Therefore, the difference in charge density induced by the resonant visible pump field must affect the vibrational modes in some way in order for a fifth-order signal to be present. For example, the visible pump could create (i) changes in the frequency, anharmonicity, or oscillator strength of the vibrational mode in the electronic excited state, (ii) transient photoproducts (e.g., photodissociation products) with vibrations within the bandwidth of the IR probe, or (iii) changes in the solvent environment leading to differing vibrational line shapes in the ground and electronic excited states.[53] Thus, the fifth-order response function as described above contains the molecular details of the coupling of electronic, nuclear, and solvent degrees of freedom as a function of a photochemical reaction.

Each unique contribution to the material response function can be visualized graphically with a double-sided Feynman diagram. Figure 5.2 depicts six of the possible twelve diagrams contributing to the fifth-order vis−IR signal under the phase matching conditions $\mathbf{k}_{\mathrm{sig}}^{(5)} = \mp\mathbf{k}_{\mathrm{vis}} \pm \mathbf{k}_{\mathrm{vis}} - \mathbf{k}_1 + \mathbf{k}_2 + \mathbf{k}_3$ for a simple model system consisting of one resonant excited electronic state and one resonant anharmonic vibrational mode. We note that when $\tau_{\mathrm{vis}} = \tau_1 = 0$ there are a total of 24 Feynman diagrams contributing to the fifth-order signal collected in this experiment. We stress that in general the number of possible diagrams changes as a function of τ_{vis}, since the number of accessible vibrational states changes as the photochemical reaction occurs. In our model, we assume that the optical field induces a vertical electronic transition which shifts population to the excited state ($n = 0$) or the ground state ($n' = 0$) under the Condon approximation such that the Franck-Condon factor ($F_{n,n'}$) between the two states is unity.

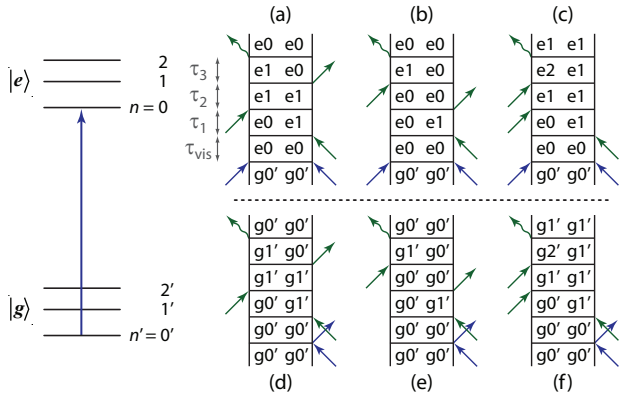

Figure 5.2: Double-sided Feynman diagrams contributing to the fifth-order signal in the phase matched direction $-\mathbf{k}_{\text{vis}}+\mathbf{k}_{\text{vis}}-\mathbf{k}_1+\mathbf{k}_2+\mathbf{k}_3$ for a model system containing one resonant electronic excited state and one resonant anharmonic vibrational mode as shown to the left. States are denoted as $|N,n\rangle$ where $N = g, e$ are the electronic states and $n'(n) = 0, 1, 2$ is the vibrational eigenstate in the electronic ground(excited) state, respectively. The three diagrams above the dashed line illustrate evolution on $|e\rangle$, whereas those below the dashed line correspond to evolution on $|g\rangle$.

Each Feynman diagram in Figure 5.2 represents a contribution to the nonlinear signal field and monitors the evolution of the density matrix following multiple interactions with external electric fields followed by the time-propagation between interactions. For example, diagram (a) begins with two interactions with the visible field populating the $|e0\rangle\langle e0|$ element of the density matrix which evolves during time delay τ_{vis}. This delay measures the lifetime of the electronic excited state. The first of three interactions with the mid-IR fields stimulates absorption on the bra side of the density matrix creating the vibrational coherence $|e0\rangle\langle e1|$ in the excited state which evolves during τ_1. The second mid-IR field is a ket-side interaction that induces absorption into an excited vibrational population in the electronic excited state $|e1\rangle\langle e1|$. Finally, the third IR field probes the coherence $|e1\rangle\langle e0|$ which evolves with an opposite phase with respect to the vibrational coherence in the τ_1 time period. The signal field is emitted in the phase-matched direction with frequency $\omega_{e1,e0} = \hbar^{-1}(E_{e1} - E_{e0})$. Signals arising from diagrams (a) and (d) are π out of phase due to differences in the nature of the second field-matter interaction. Monitoring frequencies $\omega_{e1,e0}$ and $\omega_{g1',g0'}$ as a function of τ_2 in a t-DPP experiment allows vibrational lifetimes in

the excited ($|e1\rangle\langle e1|$) and ground ($|g1'\rangle\langle g1'|$) electronic states to be compared directly. As stated above, the second optical interaction puts the density matrix in either an excited electronic or ground state population. Evolution of vibrational coherences in the optically-excited ground state can be very different than in the equilibrium ground electronic state since the local electric field surrounding the molecule has been altered by the two visible fields. The broad bandwidth of the ultrashort visible pulse can impulsively excite wavepackets of low-frequency modes in the ground (or excited) state, which would coherently oscillate during τ_{vis} and potentially couple to high-frequency modes probed by the IR fields. Experimentally measuring coherent motion of this nature requires excellent time resolution and high S/N, as the coherent oscillations would have low amplitude and decay rapidly.

5.2 Experimental Methods

5.2.1 Vis−IR spectrometer

The experiments are performed with the output of a commercial Spectra Physics Spitfire Pro 35F-XP regenerative amplifier operating at 1 kHz (800 nm, 35 fs, 3 W). The visible pump pulse (λ_{vis} = 400 nm) is generated by frequency doubling a portion of the 800 nm beam in a 0.1 mm thick β-barium borate (β-BBO) crystal. An acousto-optic programmable dispersive filter (Fastlite, Dazzler UV-250−400) temporally compresses the spectrally broad ($\Delta\lambda_{\text{fwhm}}$ = 8 nm = 500 cm^{-1}) pump pulse to ∼35 fs. The mid-IR pulses are generated via frequency conversion of the 800 nm pulses with a dual-pass optical parametric amplifier (OPA-800C, Newport) to generate near-IR signal and idler fields. The near-IR pulses are spatially and temporally overlapped in a 0.5 mm thick $AgGaS_2$ crystal for difference frequency mixing to generate tunable mid-IR pulses. For this experiment, the 80 fs mid-IR pulses are centered at ω_{MIR} = 2030 cm^{-1} (λ_{MIR} = 4.9 μm) and have a bandwidth of $\Delta\omega_{\text{fwhm}}$ = 270 cm^{-1}. The temporal width of the IR pulse at the sample is optimized by placing 3 mm of uncoated CaF_2 into the beam path compensate for group velocity dispersion mismatch.[54]

Figure 5.3 highlights the main features of the vis−IR interferometer. Approximately 3 μJ of mid-IR radiation is directed into a 5-beam interferometer in order to generate three

replica input pulses (0.5 μJ each), a tracer (T), and a local oscillator (LO) as described previously.[35] Each of the IR fields is sent through a gold-coated cube retroreflector and three of the beams (1, 2, T) are mounted to a computer-controlled translation stage (XMS50, Newport) for precise control of the relative timing of each input pulse.

The visible pulse with 1 μJ of energy (at the sample) passes through a computer-controlled delay stage (ILS150CC, Newport), a half-wave plate and polarizer combination, and a plano-convex lens ($f = 0.5$ m) before interacting with the sample. Along the way, the visible beam is directed into the mid-IR interferometer and reflected off a vertical retroreflector towards a 25 mm clear aperture hard-mounted hollow retroreflector (PLX Inc.). This retroreflector is attached to the same stage controlling IR beam 1 to ensure that τ_1 can be increased without changing τ_{vis}. A 25 g cylindrical aluminum counterweight is mounted opposite the 25 mm retroreflector to ensure mechanical stability of IR stage 1.

The three input IR beams are arranged in a boxcar geometry as shown in Figure 5.3. The visible beam passes through a 5 mm hole drilled through the center of the 90° off-axis parabolic mirror (PM1, Janos Technologies) which is used to focus the mid-IR beams onto the sample. The IR and visible beams are temporally and spatially overlapped at the sample with $1/e^2$ spot sizes at the focus of 150 μm and 200 μm, respectively. The cross-correlation time between the visible and IR fields as measured by differential transmission through a polished 250 μm Si wafer is 114 ± 8 fs. Both third- and fifth-order signals propagate in the same direction (pink solid line) and are overlapped with the LO (orange solid line) on a ZnSe beam splitter (Rocky Mountain Instrument Co.) for heterodyne detection. Reflected and transmitted beam combinations are vertically offset, focused into a monochromator (Triax 190, Horiba Jobin Yvon, 100 mm^{-1} grating) for spectral dispersion, and detected with a 2×64 mercury cadmium telluride (MCT) array detector (IR0144, Infrared Systems Development). Signals detected on the upper (+) and lower (−) stripes are π out of phase (i.e., $S_+^{(n)} = e^{i\pi} S_-^{(n)}$) due to phase shift on reflection at the beam splitter. Care is taken to ensure that the signal and LO are well overlapped spatially so that S_+ and S_- are equal on each of the MCT arrays.

We present t-HDVE data for two τ_{vis} points (120 and 5000 fs) where the IR coherence delay (τ_1) is scanned from −300 to 720 fs in 30 fs steps and the IR population delay (τ_2)

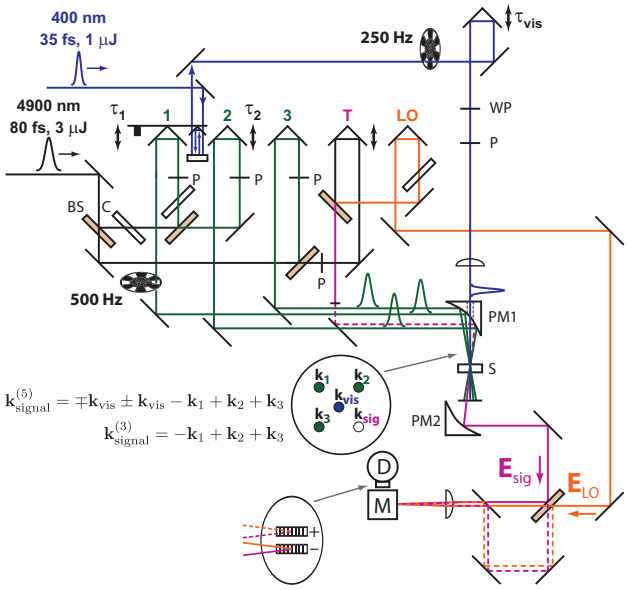

Figure 5.3: Simplified depiction of the six-beam vis−IR spectrometer. The phase matching geometry as viewed before the sample is shown in the circle in the center of the Figure. Balanced detection is illustrated at the bottom of the Figure, where two 64 channel linear MCT arrays vertically separated by 8.5 mm detect upper (+) and lower (−) signals that are π out of phase. Pulse energies and temporal widths shown correspond to values at the sample. IR stage 1 holds the small retroreflector which couples the τ_{vis} and τ_1 delays. Legend: BS, 50:50 ZnSe beam splitter; C, ZnSe compensation plate; WP, $\lambda/2$ plate; P, linear polarizer; PM1, parabolic mirror with 5 mm diameter hole; S, flowing sample solution; M, monochromator; D, 2×64 MCT array detector.

is scanned from 0 to 13 ps in unequal time steps. Each data point represents an average of 4000 laser shots and each τ_{vis} scan (i.e., entire scan at fixed τ_{vis}) was collected three times and averaged. Visible and infrared polarizations were set to parallel to maximize signal levels. The entire data set was collected in under 6 hours.

The model mixed-valence complex $Na_4[(NC)_5Fe^{II}-CN-Pt^{IV}(NH_3)_4-NC-Fe^{II}(CN)_5]$ (herein denoted as $Fe^{II}Pt^{IV}Fe^{II}$) was synthesized and purified following literature techniques and dissolved in D_2O to a final concentration of $\sim$8 mM.[55] A total sample volume of 10 mL was flowed through a sample cell housing two 1 mm CaF_2 windows separated with a custom-cut 50 μm Teflon® spacer so that fresh sample was irradiated at every shot. This arrangement results in optical densities (OD) of the sample in the visible and IR regions

of $OD_{400\ nm} = 0.082$, $OD_{4878\ nm}$ (ν_{trans}) = 0.23, and $OD_{4726\ nm}$ (ν_{bridge}) = 0.042. The sample cell was also translated in a raster pattern orthogonal to the pump axis to minimize heating effects and photoproduct accumulation. Using this detection method, we estimate difference signals as low as 10 μOD can be detected.

5.2.2 Extracting third- and fifth-order signals

As mentioned previously, the phase matching geometry used in this chapter results in the third- and fifth-order signals being spatially and temporally overlapped. These two signals are measured simultaneously at a sampling rate of 250 Hz by utilizing a double chopping scheme and balanced detection as described below.[56] The double chopping scheme is shown in Figure 5.4. The external LO is not modulated, the generated third-order IR field is modulated at 500 Hz via a chopper in the E_1 input arm, and the visible pump pulse is modulated at 250 Hz with a second chopper. The chopper in the IR arm is triggered with the second harmonic of the 250 Hz visible pump chopper, which in turn is locked to the fourth sub-harmonic of the 1 kHz pulse train. In this manner, the sequence of events is controlled by the 1 kHz repetition rate of the regenerative amplifier and single-shot data collection takes a minimum of ∼4 ms.

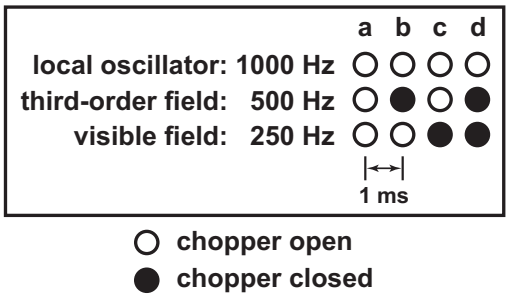

Figure 5.4: The double chopping scheme used to generate four signals (S_{a-d}) from four consecutive laser shots (a−d). The LO is not chopped, whereas the third-order field is chopped at 500 Hz (via $\mathbf{k}_1$) and the visible excitation field ($\mathbf{k}_{vis}$) is chopped at 250 Hz.

Defining a complex electric field in the frequency domain as $\mathbf{E}^{(n)}(\omega) = A^{(n)} \exp(i\phi(\omega))$, the four signals ($S_{a-d}$) generated with the chopping scheme in Fig. 5.4 as measured at the

focal plane of a spectrometer with a square-law detector can be expressed as:

$$\begin{aligned} S_{\mathrm{a}}(\omega_3;\tau_{\mathrm{vis}},\tau_1,\tau_2,\tau_{\mathrm{LO}}) &= |\mathbf{E}_{\mathrm{LO}}(\omega_3;\tau_{\mathrm{LO}})\exp(-i\omega_3\tau_{\mathrm{LO}})\cdots \\ &\quad + \mathbf{E}^{(3)}(\omega_3;\tau_1,\tau_2) + \mathbf{E}^{(5)}(\omega_3;\tau_{\mathrm{vis}},\tau_1,\tau_2)|^2 \\ &= A_{\mathrm{LO}}^2 + (A^{(3)})^2 + (A^{(5)})^2\cdots \\ &\quad + 2A^{(3)}A_{\mathrm{LO}}\cos[\Delta\phi_{3,\mathrm{LO}}(\omega_3;\tau_1,\tau_2)+\omega_3\tau_{\mathrm{LO}}]\cdots \\ &\quad + 2A^{(5)}A_{\mathrm{LO}}\cos[\Delta\phi_{5,\mathrm{LO}}(\omega_3;\tau_{\mathrm{vis}},\tau_1,\tau_2)+\omega_3\tau_{\mathrm{LO}}]\cdots \\ &\quad + 2A^{(3)}A^{(5)}\cos[\Delta\phi_{3,5}(\omega_3;\tau_{\mathrm{vis}},\tau_1,\tau_2)], \end{aligned} \tag{5.2}$$

$$S_{\mathrm{b}}(\omega_3;\tau_{\mathrm{LO}}) = |\mathbf{E}_{\mathrm{LO}}(\omega_3;\tau_{\mathrm{LO}})\exp(-i\omega_3\tau_{\mathrm{LO}})|^2 = A_{\mathrm{LO}}^2, \tag{5.3}$$

$$\begin{aligned} S_{\mathrm{c}}(\omega_3;\tau_1,\tau_2,\tau_{\mathrm{LO}}) &= |\mathbf{E}_{\mathrm{LO}}(\omega_3;\tau_{\mathrm{LO}})\exp(-i\omega_3\tau_{\mathrm{LO}}) + \mathbf{E}^{(3)}(\omega_3;\tau_1,\tau_2)|^2 \\ &= A_{\mathrm{LO}}^2 + (A^{(3)})^2 + 2A^{(3)}A_{\mathrm{LO}}\cos[\Delta\phi_{3,\mathrm{LO}}(\omega_3;\tau_1,\tau_2)+\omega_3\tau_{\mathrm{LO}}], \end{aligned} \tag{5.4}$$

$$S_{\mathrm{d}} = S_{\mathrm{b}}. \tag{5.5}$$

The spectral phase differences are defined as,

$$\Delta\phi_{3,\mathrm{LO}}(\omega_3;\tau_1,\tau_2) = \phi_3(\omega_3;\tau_1,\tau_2) - \phi_{\mathrm{LO}}(\omega_3), \tag{5.6}$$

$$\Delta\phi_{5,\mathrm{LO}}(\omega_3;\tau_{\mathrm{vis}},\tau_1,\tau_2) = \phi_5(\omega_3;\tau_{\mathrm{vis}},\tau_1,\tau_2) - \phi_{\mathrm{LO}}(\omega_3), \tag{5.7}$$

$$\Delta\phi_{3,5}(\omega_3;\tau_{\mathrm{vis}},\tau_1,\tau_2) = \phi_3(\omega_3;\tau_1,\tau_2) - \phi_5(\omega_3;\tau_{\mathrm{vis}},\tau_1,\tau_2), \tag{5.8}$$

The time dependence of each amplitude factor (A) has been omitted for ease of reading, though each follows the time dependence of the corresponding complex field ($\mathbf{E}$). Note that S_{b} and S_{d} are equivalent with this chopping scheme since the LO does not travel through the sample. If the LO was overlapped with the other beams at the sample, S_{b} would be equivalent to the vis−IR pump−probe response. Heterodyned third- and fifth-order signals

are isolated from $S_{\mathrm{a-d}}$ by

$$\begin{aligned} S^{(3)}(\omega_3;\tau_1,\tau_2,\tau_{\mathrm{LO}}) &= S_{\mathrm{c}} - S_{\mathrm{d}} \\ &= (A^{(3)})^2 + 2A^{(3)}A_{\mathrm{LO}}\cos[\Delta\phi_{3,\mathrm{LO}}(\omega_3;\tau_1,\tau_2) + \omega_3\tau_{\mathrm{LO}}], \end{aligned} \tag{5.9}$$

$$\begin{aligned} S^{(5)}(\omega_3;\tau_{\mathrm{vis}},\tau_1,\tau_2,\tau_{\mathrm{LO}}) &= S_{\mathrm{a}} - S_{\mathrm{c}} \\ &= (A^{(5)})^2 + 2A^{(5)}A_{\mathrm{LO}}\cos[\Delta\phi_{5,\mathrm{LO}}(\omega_3;\tau_{\mathrm{vis}},\tau_1,\tau_2) + \omega_3\tau_{\mathrm{LO}}]\cdots \\ &\quad + 2A^{(3)}A^{(5)}\cos[\Delta\phi_{3,5}(\omega_3;\tau_{\mathrm{vis}},\tau_1,\tau_2)]. \end{aligned} \tag{5.10}$$

Finally, signals on the upper (+) and lower (−) stripes of the 2×64 MCT array are out of phase, which allows the unambiguous detection of the third- and fifth-order signals via balanced detection:

$$\begin{aligned} S^{(3)}_{\pm}(\omega_3;\tau_1,\tau_2,\tau_{\mathrm{LO}}) &= (A^{(3)})^2 \pm 2A^{(3)}A_{\mathrm{LO}}\cos[\Delta\phi_{3,\mathrm{LO}}(\omega_3;\tau_1,\tau_2) + \omega_3\tau_{\mathrm{LO}}] \\ S^{(3)}_{\mathrm{bal}}(\omega_3;\tau_1,\tau_2,\tau_{\mathrm{LO}}) &= S^{(3)}_{+} - S^{(3)}_{-} = 4A^{(3)}A_{\mathrm{LO}}\cos[\Delta\phi_{3,\mathrm{LO}}(\omega_3;\tau_1,\tau_2) + \omega_3\tau_{\mathrm{LO}}], \end{aligned} \tag{5.11}$$

$$\begin{aligned} S^{(5)}_{\pm}(\omega_3;\tau_{\mathrm{vis}},\tau_1,\tau_2,\tau_{\mathrm{LO}}) &= (A^{(5)})^2 \pm 2A^{(5)}A_{\mathrm{LO}}\cos[\Delta\phi_{5,\mathrm{LO}}(\omega_3;\tau_{\mathrm{vis}},\tau_1,\tau_2) + \omega_3\tau_{\mathrm{LO}}] \\ S^{(5)}_{\mathrm{bal}}(\omega_3;\tau_{\mathrm{vis}},\tau_1,\tau_2,\tau_{\mathrm{LO}}) &= S^{(5)}_{+} - S^{(5)}_{-} = 4A^{(5)}A_{\mathrm{LO}}\cos[\Delta\phi_{5,\mathrm{LO}}(\omega_3;\tau_{\mathrm{vis}},\tau_1,\tau_2) + \omega_3\tau_{\mathrm{LO}}]. \end{aligned} \tag{5.12}$$

We collect the data given by Equations 5.9−5.12 with custom LabVIEW® software synchronized to the double-chopping scheme in order to perform the necessary subtractions on a shot-to-shot basis. The simultaneous detection of both equilibrium and non-equilibrium vibrational dynamics is a significant strength of this technique, as it allows for direct comparison of dynamics occurring on ground and excited electronic states. It also allows the phase of the fifth-order signal to be extracted by "phasing" the third-order signal to an independently determined DPP signal, as will be described and validated in the next section.

Visible and IR power-dependent studies have been performed in order to verify the fifth-order nature of the signal. The ground state DVE intensity as a function of incident IR power was found to be linear with respect to each of the IR beams ($\mathbf{k}_{1-3}$) by placing a 50:50 ZnSe beam splitter before the 5-beam mid-IR interferometer and measuring the DVE

intensity.[57] The vis−IR pump−probe signal scales linearly for visible pump powers ranging from 0.05−1 μJ, indicating that multiphoton absorption and higher-order effects can be ruled out.

5.3 Data Analysis and Results

5.3.1 Data analysis

Example raw third- and fifth-order HDVE spectral interferometric data (a single average) with no post processing is shown in Figure 5.5. We estimate the S/N of the third-order data to be greater than 60 and immediately note that even though the raw heterodyned fifth-order signal is ∼30 times smaller than the third-order signal ($\tau_{\mathrm{vis}} = 120$ fs) it still has S/N > 25 near the extrema. The spectral interferograms in Figure 5.5 show clear spectral oscillations with a frequency of 33 cm^{-1} corresponding to $\tau_{\mathrm{LO}} = -1000$ fs, which is held constant throughout the experiment. It is also apparent that the third- and fifth-order signals are π out of phase, indicating that one signal originates from the electronic ground state while the other is from an electronic excited state (i.e., non-equilibrium state).

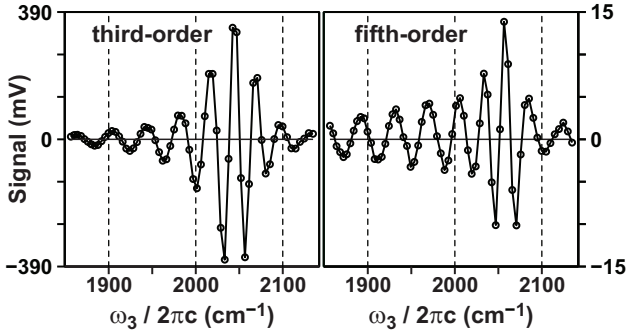

Figure 5.5: Raw third-order HDVE signal $S^{(3)}_{\mathrm{bal}}(\omega_3; \tau_1 = 0, \tau_2 = 200 \text{ fs}, \tau_{\mathrm{LO}} = -1000 \text{ fs})$ (left) and fifth-order t-HDVE signal $S^{(5)}_{\mathrm{bal}}(\omega_3; \tau_{\mathrm{vis}} = 120 \text{ fs}, \tau_1 = 0, \tau_2 = 200 \text{ fs}, \tau_{\mathrm{LO}} = -1000 \text{ fs})$ (right). These simultaneously-collected traces represent one average of the data set.

The advantages of heterodyne detection coupled with balance detection include signal amplification, noise reduction, and the ability to extract amplitude and phase information to construct the desired nonlinear signal. We use Fourier transform spectral interferometry

(FTSI) to extract the amplitude and phase of the electric field as detailed in Reference 48. In brief, spectra can be obtained by (i) taking the inverse Fourier transform (IFT) of the raw data in Fig. 5.5, (ii) multiplying the resulting time-domain signals by a window function ($W(\tau_3)$), and (iii) performing the forward Fourier transform into the frequency domain. The resultant complex signal, written as $\tilde{S}^{(3)}$ for the third-order response, is therefore calculated by

$$\begin{aligned}\tilde{S}^{(3)}(\omega_3;\tau_1,\tau_2,\tau_{\mathrm{LO}}) &= \mathrm{FT}\{W(\tau_3)\cdot\mathrm{IFT}[S^{(3)}_{\mathrm{bal}}(\omega_3;\tau_1,\tau_2,\tau_{\mathrm{LO}})]\}\\ &\propto A^{(3)}A_{\mathrm{LO}}\exp[i(\Delta\phi_{3,\mathrm{LO}}(\omega_3;\tau_1,\tau_2)+\omega_3\tau_{\mathrm{LO}})],\end{aligned} \tag{5.13}$$

where $S^{(3)}_{\mathrm{bal}}(\omega_3;\tau_1,\tau_2,\tau_{\mathrm{LO}})$ and $\Delta\phi_{3,\mathrm{LO}}(\omega_3;\tau_1,\tau_2)$ are given in Eqns. 5.11 and 5.6, respectively. A shifted Heaviside step function starting at $\tau_3 = 600$ fs was used for $W(\tau_3)$. We note that many temporal windows were tested and it was found that this window reproduced homodyne-detected DVE spectra with the greatest fidelity and maximum S/N. Third- and fifth-order DVE spectra, which are not phase sensitive, are calculated by the following equations:

$$S^{(3)}_{\mathrm{DVE}}(\omega_3;\tau_1,\tau_2) = \left|\tilde{S}^{(3)}(\omega_3;\tau_1,\tau_2)\right|^2 \propto \left(A^{(3)}A_{\mathrm{LO}}\right)^2, \tag{5.14}$$

$$S^{(5)}_{\text{t-DVE}}(\omega_3;\tau_{\mathrm{vis}},\tau_1,\tau_2) = \left|\tilde{S}^{(5)}(\omega_3;\tau_{\mathrm{vis}},\tau_1,\tau_2)\right|^2 \propto \left(A^{(5)}A_{\mathrm{LO}}\right)^2. \tag{5.15}$$

Note that Equations 5.14 and 5.15 represent the dispersed transient grating (DTG) response when $\tau_1 = 0$. The phase of the nonlinear signal field, which is calculated from the ratio of the imaginary and real components of $\tilde{S}^{(n)}$, is needed to construct DPP spectra. In practice, additional phase ambiguities corresponding to drift of the absolute timing of the LO are corrected with a phasing procedure that compares the HDVE-generated DPP spectra to "traditional" 2-beam DPP spectra collected for the same values of τ_2 immediately before starting the HDVE experiment. A constant phase factor given by $\exp(-i\phi)$ is adjusted to correct for timing between $\mathbf{k}_1$ and $\mathbf{k}_2$. Putting this together, the ground state DPP

spectrum is extracted from the HDVE data by using the relations below:

$$\begin{aligned}
\varphi^{(3)}(\omega_3;\tau_2,\tau_{\mathrm{LO}}) &= \tan^{-1}\left(\frac{\mathrm{Im}\left\{\tilde{S}^{(3)}(\omega_3;\tau_1=0,\tau_2,\tau_{\mathrm{LO}})\right\}}{\mathrm{Re}\left\{\tilde{S}^{(3)}(\omega_3;\tau_1=0,\tau_2,\tau_{\mathrm{LO}})\right\}}\right)\exp[-i(\omega_3\tau_{\mathrm{LO}}+\phi(\omega_3;\tau_2))],\\
S^{(3)}_{\mathrm{phs}}(\omega_3;\tau_2,\tau_{\mathrm{LO}}) &= \left|\tilde{S}^{(3)}(\omega_3;\tau_1=0,\tau_2,\tau_{\mathrm{LO}})\right|\cos[\varphi^{(3)}(\omega_3;\tau_2,\tau_{\mathrm{LO}})],\\
S^{(3)}_{\mathrm{DPP}}(\omega_3;\tau_2,\tau_{\mathrm{LO}}) &= a(\tau_2)\cdot\log_{10}\left(1+S^{(3)}_{\mathrm{phs}}(\omega_3;\tau_2,\tau_{\mathrm{LO}})\right),
\end{aligned} \tag{5.16}$$

In the above expressions, $\varphi^{(3)}(\omega_3;\tau_2,\tau_{\mathrm{LO}})$ is the corrected phase of the third-order signal, $\phi(\omega_3;\tau_2)$ is the constant phase factor correcting for drift, and $a(\tau_2)$ is a scaling parameter determined by comparing the absolute signal levels (in mOD) of the 2-beam DPP spectra to the signal levels (in arbitrary units) of the phased HDPP spectra ($S^{(3)}_{\mathrm{phs}}$). Not shown in Equation 5.16 is an unwrapping procedure used to extract the relative offset of the phase. Since the third- and fifth-order signals are collected simultaneously, both τ_{LO} and $\phi(\omega_3;\tau_2)$ are exactly the same for both signals. Thus the t-DPP signal can be written as,

$$\begin{aligned}
\varphi^{(5)}(\omega_3;\tau_{\mathrm{vis}},\tau_2,\tau_{\mathrm{LO}}) &= \tan^{-1}\left(\frac{\mathrm{Im}\left\{\tilde{S}^{(5)}(\omega_3;\tau_{\mathrm{vis}},\tau_1=0,\tau_2,\tau_{\mathrm{LO}})\right\}}{\mathrm{Re}\left\{\tilde{S}^{(5)}(\omega_3;\tau_{\mathrm{vis}},\tau_1=0,\tau_2,\tau_{\mathrm{LO}})\right\}}\right)\cdots\\
&\qquad\times\exp[-i(\omega_3\tau_{\mathrm{LO}}+\phi(\omega_3;\tau_2))],\\
S^{(5)}_{\mathrm{phs}}(\omega_3;\tau_{\mathrm{vis}},\tau_2,\tau_{\mathrm{LO}}) &= \left|\tilde{S}^{(5)}(\omega_3;\tau_{\mathrm{vis}},\tau_1=0,\tau_2,\tau_{\mathrm{LO}})\right|\cos[\varphi^{(5)}(\omega_3;\tau_{\mathrm{vis}},\tau_2,\tau_{\mathrm{LO}})],\\
S^{(5)}_{\mathrm{DPP}}(\omega_3;\tau_{\mathrm{vis}},\tau_2,\tau_{\mathrm{LO}}) &= a(\tau_2)\cdot\log_{10}\left(1+S^{(5)}_{\mathrm{phs}}(\omega_3;\tau_{\mathrm{vis}},\tau_2,\tau_{\mathrm{LO}})\right),
\end{aligned} \tag{5.17}$$

where the same scaling factor is used to scale the data given that the MCT array detector has good detection linearity. In summary, by comparing the extracted third-order signals to independently measured 2-beam DPP spectra, we are able to phase the fifth-order data to obtain t-DPP spectra as a function of the vibrational waiting time for fixed values of τ_{vis}.

5.3.2 Method validation

Jones et al. have previously validated third-order HDVE spectroscopy by phasing their data to obtain DPP spectra that reproduced an independently measured 2-beam DPP spectrum for one value of τ_2.[48] We offer further validation of the technique in Figure 5.6, where

it is shown that HDVE spectroscopy also reproduces vibrational relaxation and transfer dynamics occurring in the electronic ground state of $Fe^{II}Pt^{IV}Fe^{II}$. Coherent oscillations as a function of τ_2, which originate from superposition states involving multiple cyanide stretching vibrational modes, are clearly observed in both the traditional 2-beam DPP and the background-free HDVE-generated DPP traces.

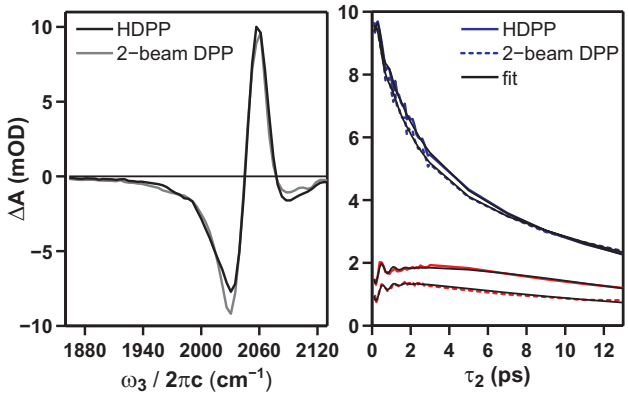

Figure 5.6: A comparison of HDPP and 2-beam DPP data taken of the electronic ground state of $Fe^{II}Pt^{IV}Fe^{II}$ as a function of ω_3 (left) for $\tau_2 = 200$ fs and τ_2 (right) for $\omega_3 = 2061$ cm^{-1} (blue, upper) and 2075 cm^{-1} (red, lower). Both of the time traces at $\omega_3 = 2075$ cm^{-1} show a coherent oscillation with a period of ~600 fs ($\omega_{osc} = 56$ cm^{-1}) and the same phase. Small differences in amplitude are from differences in the phase and amplitude of the LO field between the HDPP and 2-beam DPP techniques. Note that the lifetime of the vibrations is on the order of 15−20 ps which is why the signals have not reached zero by $\tau_2 = 13$ ps.

5.3.3 Results

We demonstrate ultrafast t-HDVE spectroscopy with the cyano-rich $Fe^{II}Pt^{IV}Fe^{II}$ molecule dissolved in D_2O, which we have recently studied using transient IR absorption spectroscopy.[58] The FTIR spectrum of the $Fe^{II}Pt^{IV}Fe^{II}$ complex dissolved in D_2O contains four high-frequency CN stretching (ν_{CN}) modes centered at 2050 cm^{-1} (ν_{radial}), 2060 cm^{-1} (ν_{trans}), 2074 cm^{-1} (ν_{axial}), and 2116 cm^{-1} (ν_{bridge}) that make up a multidimensional structural probe of photochemical dynamics occurring on ultrafast timescales. Metal-to-metal charge transfer excitation with a 400 nm photon shifts electron density from Fe^{II} to Pt^{IV}, from which rapid back-electron transfer (BET) occurs on a 110 fs timescale. Upon BET,

greater than 6 vibrational quanta of the ν_{bridge} mode (i.e., $n_{\text{bridge}} > 6$) are excited. This energy is transferred via intramolecular vibrational relaxation (IVR) into the $n_{\text{trans}} = 1 - 3$ (and $n_{\text{axial}} = 2 - 4$) states at a rate of ∼630 fs, from which each of the modes vibrationally cools in ∼1.3 ps and subsequently relaxes back to the ground state ($n = 0$) in $15 - 20$ ps. Fifth-order t-HDVE spectroscopies enable us to address the following questions: (i) how does vibrational energy relaxation (VER) and transfer occur within a non-equilibrium distribution of highly excited CN stretching modes at a particular τ_{vis}? (ii) How does coupling with the solvent change in the electronic excited state? (iii) How do coherent vibrational oscillations along τ_2 change as a function of τ_{vis}? Representative results for the t-DVE and t-DPP experiments are shown in Figure 5.7. Figure 5.7a shows two t-DVE surfaces plotted as a function of τ_1 and ω_3 for $\tau_2 = 200$ fs and $\tau_{\text{vis}} = 120$ and 5000 fs. The DVE trace is a maximum at ∼2061 cm^{-1} at early τ_{vis} and proceeds towards the GS equilibrium value of ∼2050 cm^{-1} as τ_{vis} increases to 5 ps. The peak shift, defined as the time at which the rephasing signal is a maximum for a particular value of ω_3, also appears to decrease as a function of τ_{vis} for fixed τ_2. Interestingly, we observe a peak shift in the $\omega_3 = 1950 - 2020$ cm^{-1} region indicating that an inhomogeneous distribution of excited-state species exists at early τ_{vis} and disappears once the population of those species approaches zero. Slices along $\tau_1 = 0$ shown in Fig. 5.7b illustrate that the shape of the t-DVE spectrum approaches that of the simultaneously-detected ground state as τ_{vis} increases.

Vibrational relaxation and transfer dynamics are evident from the t-DPP contour plots in Fig. 5.7c, where each signal is plotted as a function of the τ_2 and ω_3 variables at a fixed τ_{vis} delay. In these plots, negative features correspond to stimulated emission (e.g., $n = 1 \rightarrow 0$) whereas positive features represent stimulated absorption (e.g., $n = 2 \leftarrow 1$). At $\tau_{\text{vis}} = 120$ fs, when there is significant vibrational population in high-lying ν_{CN} levels ($n_{\text{bridge}} > 6$) such that a population inversion has been achieved, the infrared pump pulse stimulates emission down from the high-lying ν_{bridge} states into lower quanta of the ν_{CN} modes. This leads to the broad negative feature spanning frequencies lower than ∼2020 cm^{-1} growing in within the instrument response time and subsequently decaying at a rate of (300 fs)$^{-1}$. There is a corresponding rise at $\omega_3 = 2013$ cm^{-1} indicating that vibrational population from the highly excited ν_{bridge} mode is transferring via IVR into the ν_{trans} mode. These features are

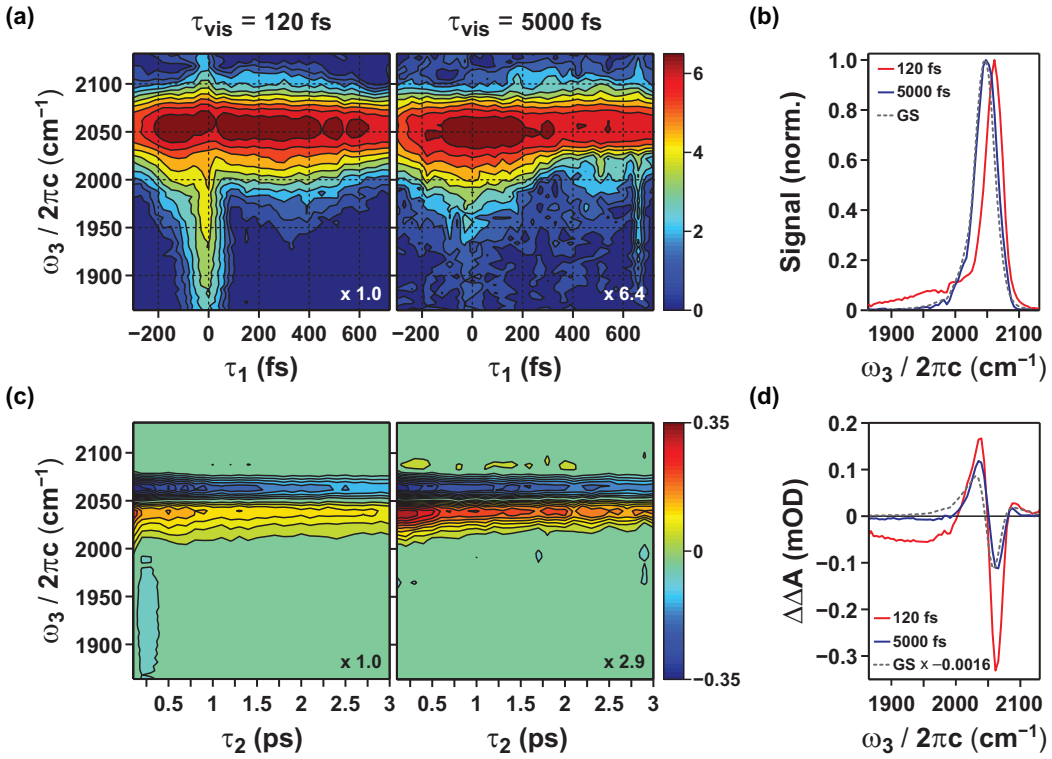

Figure 5.7: (a) Transient DVE surfaces at $\tau_{\text{vis}} = 120$ fs and 5000 fs for $\tau_1 = -300$ to 720 fs at $\tau_2 = 200$ fs. Contours are shown on an arcsinh color scale to enhance low-amplitude features. The 5000 fs data has been scaled to the maximum of the 120 fs data (see bottom right corner) so that the 10% contour lines drawn from zero to maximum can be compared directly. (b) Normalized vertical slices of the t-DVE surfaces from (a) at $\tau_1 = 0$ with the GS ($--$) shown for comparison. (c) Transient DPP surfaces (linear z-axis) at $\tau_{\text{vis}} = 120$ fs and 5000 fs from $\tau_2 = 0.1$ to 3 ps (recall $\tau_1 = 0$). The 5000 fs data has been scaled to the minimum value of the 120 fs data (see bottom right corner). Equal contours lines in 35 μOD intervals from -0.35 to 0.35 mOD (excluding the 0 mOD contour line for clarity). (d) Vertical slices of the t-DPP surfaces in (c) at $\tau_2 = 200$ fs. The GS is again plotted for comparison and has been multiplied by -1 and scaled to the bleach of the 5000 fs trace.

not present in the 5000 fs data since the vibrational population has reached the bottom of the potential energy surface. Slices along $\tau_2 = 200$ fs (Fig. 5.7d) show that the relative amplitude of the bleach at ~2061 cm^{-1} and transient absorption at ~2036 cm^{-1} change as a function of τ_{vis}. The additional phase information in the DPP technique helps address the reason for the spectral shift observed in the DVE traces (Fig. 5.7b) and highlights an advantage of collecting both signals simultaneously. It is also apparent that the transient

DPP bleach is shifted to higher energy by ∼5 cm^{-1}, implying that the ν_{CN} modes are slightly blue shifted in the non-equilibrium ground state. Detailed analysis and modeling of the data will be presented in a separate future publication. The results in Figure 5.7 illustrate the power of t-HDVE spectroscopy. The ability to vary three independent time variables (τ_{vis}, τ_1, and τ_2) allows a multi-coordinate view of many dynamical processes. This includes the role of high-frequency vibrations and energy flow amongst them, the degree of inhomogeneity in the transient photochemical species, the role of the solvent, and possible coherent effects as observed via changes in the modulation of t-DPP signals as a function of τ_2.

5.4 Discussion

5.4.1 Molecular insights

Transient HDVE spectroscopy is a versatile fifth-order technique that enables data from multiple nonlinear IR experiments to be simultaneously extracted for both equilibrium and non-equilibrium species with high S/N. We note that vibrational relaxation and transfer dynamics in electronically excited states are best extracted from phase-sensitive t-DPP spectra which scale linearly with concentration. The peak positions in t-DPP spectra measure how the frequency and anharmonicities of coupled vibrational modes change in the excited state. The time-dependent amplitudes of the various spectral features monitor the changes in the timescales and pathways for inter- and intramolecular vibrational and orientational relaxation following electronic excitation.

Transient DVE surfaces provide a window into how solvent interactions with high-frequency vibrational modes of excited-state species differ from those on the ground state. Monitoring the vibrational echo peak shift as a function of the vibrational waiting time enables the determination of frequency-frequency correlation functions (FFCFs) for both the ground and excited electronic states. A comparison of the two correlation functions is very meaningful, as linear response theory (LRT) assumes that the relaxation of a non-equilibrium disturbance is governed by the same laws as the fluctuations in the equilibrium (i.e., ground) state.[59,60] Therefore, in principle, t-DVE spectroscopy can be used as a direct

test of LRT for complex molecular systems in solution at room temperature. We note that the peak shift analysis is made challenging by small signal amplitudes and the presence of multiple coupled vibrational modes resulting in beats along τ_1.

Transient HDVE spectroscopy is capable of observing coherently coupled electronic and vibrational responses along multiple time periods. Coherent effects of the visible excitation on the nuclear modes can manifest themselves in the τ_2 dimension, where IR oscillatory features found at some IR frequencies (see Fig. 5.6) change as a function of τ_{vis}. We see these effects in the t-DPP spectra of $Fe^{II}Pt^{IV}Fe^{II}$ as noted previously. The coupling of low-frequency vibrational modes with high-frequency IR modes can be monitored during a t-DPP experiment. This can occur when the bandwidth of the visible pulse is sufficient to impulsively excite Raman modes in both the ground and electronically excited states. If the Raman modes are coupled to particular high-frequency IR modes, the time-dependent amplitude of peaks at that IR frequency would oscillate as a function of τ_{vis}.

A complete understanding of all the microscopic information contained in the experiments described in this Chapter will require a comparison with theoretical simulations of the role of high-frequency vibrations in ultrafast charge transfer processes. Several recent experimental studies have shown that linear response theories are not sufficient for the description of ultrafast photochemical reactions in solution.[61–67] We believe that these experiments represent an excellent means to test current theories of non-adiabatic charge transfer reactions in solution involving coupled high-frequency vibrations at room temperature.

5.4.2 Comparision with other techniques

The transient-HDVE experiments described in this Chapter belong to a class of ultrafast nonlinear IR spectroscopies designed to probe structural dynamics in solution following an external perturbation which shifts the molecular system far from equilibrium. These include transient 2D IR, homodyne-detected t-DVE, and t-DPP experiments performed in the traditional two-beam geometry.[68–75] In this section, t-HDVE spectroscopy will be compared to the above-mentioned methods.

The t-DPP signals obtained from t-HDVE spectroscopy are a projection of the t-2D

IR correlation spectrum along the ω_1 dimension using the projection-slice theorem. A significant advantage offered by t-DPP experiments, which can measure all the relevant vibrational phase and energy relaxation dynamics during τ_2, is data collection time and the ability to measure rephasing (R) and non-rephasing (NR) spectra simultaneously. Collecting 2D IR spectra in the so-called pump−probe geometry would eliminate this problem since R and NR generated simultaneously. However, the experiment would no longer be background free and balanced detection would not be possible since the probe IR beam acts as an internal LO.[76,77] An obvious advantage of 2D spectra is the ability to identify cross peaks, though isolating and interpreting these off-diagonal peaks becomes increasingly difficult with broad and overlapping spectra. This is the case with electronically-excited $Fe^{II}Pt^{IV}Fe^{II}$ in D_2O, as the broad negative feature for $\omega_3 < 2020$ cm^{-1} in Fig. 5.7d would lead to a very large peak in a t-2D IR spectrum that would obscure subtle features. The t-DVE experiments described here can measure the non-equilibrium FFCF of coupled vibrational modes by measuring the spectrally dispersed vibrational peak shift as a function of the photochemical reaction. In theory, this information is analogous to the analysis of the 2D line shapes from t-2D IR experiments. We note that the apparatus illustrated in Fig. 5.3 is capable of measuring transient absolute-value rephasing (R) 2D IR spectra. It is important to remember that the fifth-order spectra shown here do not simply represent difference spectra but offer a characterization of the amplitude and phase of only the fifth-order signal field.

For most molecular systems with relatively weak IR oscillators, homodyne detection of a fifth-order signal is not feasible due to extremely small signal levels. Even if a small signal was within the detection limit at early τ_2, poor S/N at larger τ_2 (and τ_{vis}) would make data analysis extremely challenging. Transient HDVE spectroscopy allows for signal amplification by mixing the fifth-order signal field with a reference field and performing balanced detection as described by Equations 5.11 and 5.12. This is crucial because it allows the measurement of only the signal of interest as the third- and fifth-order signal fields are spatially overlapped. It is worth noting that it is possible to change the phase of the signal arbitrarily with a pulse shaper, which has been demonstrated in both the optical and IR regimes of radiation.[18,24,78]

An advantage of measuring t-DPP experiments in a three-beam geometry is the capabil-

ity to independently control the polarization of each of the three IR beams. The measurement of non-standard tensor components of the fifth-order signal offers mode-selectivity for probing specific dynamical processes as a function of τ_2 and the removal of contributions from overlapping spectral features.[69] We plan to exploit this capability of our instrument in future studies.

Ultrafast transient IR spectroscopy is a commonly used spectroscopic technique to follow changes in the molecular vibrational spectrum following electronic excitation. A challenge in many vis−IR experiments is a difference in oscillator strength between electronic and vibrational transitions (i.e., $\kappa \gg \mu$). This results in an experimental tradeoff between sample concentration and visible excitation pump power. In a six-wave mixing vis−IR experiment, the signal is proportional to $|\kappa_{\mathrm{ge}}|^2|\mu_{\mathrm{ab}}||\mu_{\mathrm{bc}}||\mu_{\mathrm{cd}}||\mu_{\mathrm{da}}|$ where e and g are the electronic ground and excited states respectively and {a,b,c,d} are the vibrational states resonant with the IR excitation. For transient IR experiments, the signal is proportional to $|\kappa_{\mathrm{eg}}|^2|\mu_{\mathrm{ab}}|^2$. The fifth-order experiment allows for probing the effect of the electronic excitation on (i) both strong and weak IR absorbers as the signal is proportional to the product of four different transition dipole moment amplitudes such that cross terms involving the weak mode(s) can be observed (i.e., imagine a case where $|\mu_{\mathrm{bc}}| \approx |\mu_{\mathrm{cd}}| \approx |\mu_{\mathrm{da}}| \gg |\mu_{\mathrm{ab}}|$), (ii) vibrational phase and amplitude relaxation processes among coupled vibrational modes, and (iii) spectral diffusion among coupled vibrational modes. Fifth-order experiments with high time resolution can extract detailed information about the relevant electronic excited-state surfaces instead of solely measuring the kinetics of how vibrational population moves between the surfaces.

The pulse sequence in Fig. 5.1 is only one example of how the input pulses can be arranged to generate a fifth-order signal. For example, one could first vibrationally excite the molecule in the electronic ground state before inducing the electronic excitation by placing the visible pulse ($\mathbf{k}_{\mathrm{vis}}$) in Figure 5.1 between the second and third IR pulses ($\mathbf{k}_2$ and $\mathbf{k}_3$). This pulse sequence has been called either type II or triggered-exchange transient IR spectroscopy in the literature and has shown that vibrational excitation (i.e., "labeling") can have a significant impact on the resulting transient spectra.[26,68,74] Another interesting permutation of the pulse sequence in Fig. 5.1 involves separating the collinear visible pulses in time and scanning the time delay between them. In this case, electronic coherences must

couple to vibrational coherences along τ_1 and τ_3 for a signal to be present. Given that electronic coherences generally live on the order of a few IR field cycles, it is reasonable to imagine that strong coupling of the electronic and vibrational motion must be present to observe a signal.

It has been shown that several fifth-order coherent spectroscopies have been contaminated with cascading third-order signals.[79–84] In our case, such a contamination would result from a third-order vis−IR signal subsequently pumping a third-order IR−IR response. The use of double-chopping and balanced detection with an external LO allows any signals of the form $E^{(3)}E^{(3)}$ to be subtracted from our measured signal field. A concentration dependent study revealed a linear relationship between the measured fifth-order signal field, $|E^{(5)}E_{\mathrm{LO}}|$, and the sample concentration confirming that our measured signal is not contaminated. We note that at high sample concentrations reabsorption of the nonlinear fifth-order signal field leads to deviations from linearity. As mentioned at the end of Section 5.2, the fifth-order signal is linear as a function of visible pump power and in the power of each IR beam, as expected for a one-photon absorption process and single-IR-beam interactions, respectively.

5.5 Summary

We present the development of t-HDVE spectroscopy as a probe of non-equilibrium vibrational relaxation dynamics in complex molecular systems following photoexcitation. We perform proof-of-principle fifth-order t-DPP and t-DVE experiments on highly excited cyanide stretching vibrational modes in a trinuclear mixed-valence complex following ultrafast back electron transfer. The high time resolution of the technique presented in this study opens the door for measuring non-equilibrium vibrational and solvation dynamics before the product species equilibrate. Pathways not accessible by traditional 2D IR or transient 2D IR with low time resolution can be revealed, and the influence and magnitude of coupling between vibrational modes, solvent molecules, and electronic transitions can be explored. Detailed analysis of the data presented in this paper is the subject of a future publication.[85] The experiments described in this paper simultaneously measure multiple nonlinear IR signals on both ground and excited states on a femtosecond time scale. Small fifth-order signals are extracted with the use of both heterodyne and balanced detection, which allows both the

amplitude and phase of the signal field to be extracted with high S/N. Careful data analysis employing Fourier transform spectral interferometry generates t-DPP and t-DVE spectra, which have the combined ability to characterize the time-evolution of vibrational relaxation and anharmonic inter- and intramolecular vibrational couplings during an ultrafast photochemical reaction.

REFERENCES

[1] Polli, D.; Altoè, P.; Weingart, O.; Spillane, K. M.; Manzoni, C.; Brida, D.; Tomasello, G.; Orlandi, G.; Kukura, P.; Mathies, R. A.; Garavelli, M.; Cerullo, G. *Nature* **2010**, *467*, 440–443.

[2] Smeigh, A. L.; Creelman, M.; Mathies, R. A.; McCusker, J. K. *J. Am. Chem. Soc.* **2008**, *130*, 14105–14107.

[3] Middleton, C. T.; de La Harpe, K.; Su, C.; Law, Y. K.; Crespo-Hernández, C. E.; Kohler, B. *Annu. Rev. Phys. Chem.* **2009**, *60*, 217–239.

[4] Glowacki, D. R.; Rose, R. A.; Greaves, S. J.; Orr-Ewing, A. J.; Harvey, J. N. *Nat. Chem.* **2011**, *3*, 850–855.

[5] Tanimura, Y.; Mukamel, S. *J. Chem. Phys.* **1993**, *99*, 9496.

[6] Mukamel, S. *Annu. Rev. Phys. Chem.* **2000**, *51*, 691–729.

[7] Jonas, D. M. *Annu. Rev. Phys. Chem.* **2003**, *54*, 425–463.

[8] Cho, M. *PhysChemComm* **2002**, *5*, 40–58.

[9] Thielges, M. C.; Fayer, M. D. *Acc. Chem. Res.* **2012**, *45*, 1866–1874.

[10] Remorino, A.; Hochstrasser, R. M. *Acc. Chem. Res.* **2012**, *45*, 1896–1905.

[11] Hamm, P.; Savolainen, J. *J. Chem. Phys.* **2012**, *136*, 094516.

[12] Fayer, M. D. *Acc. Chem. Res.* **2012**, *45*, 3–14.

[13] West, B. A.; Womick, J. M.; Moran, A. M. *J. Chem. Phys.* **2011**, *135*, 114505.

[14] Lott, G. A.; Perdomo-Ortiz, A.; Utterback, J. K.; Widom, J. R.; Aspuru-Guzik, A.; Marcus, A. H. *Proc. Natl. Acad. Sci. U.S.A.* **2011**, *108*, 16521–16526.

[15] Collini, E.; Wong, C. Y.; Wilk, K. E.; Curmi, P. M. G.; Brumer, P.; Scholes, G. D. *Nature* **2010**, *463*, 644–647.

[16] Strasfeld, D. B.; Shim, S. H.; Zanni, M. T. *Adv. Chem. Phys.* **2009**, *141*, 1.

[17] Stone, K. W.; Turner, D. B.; Gundogdu, K.; Cundiff, S. T.; Nelson, K. A. *Acc. Chem. Res.* **2009**, *42*, 1452–1461.

[18] Shim, S.-H.; Zanni, M. T. *Phys. Chem. Chem. Phys.* **2009**, *11*, 748–761.

[19] Roberts, S. T.; Ramasesha, K.; Tokmakoff, A. *Acc. Chem. Res.* **2009**, *42*, 1239–1249.

[20] Ogilvie, J. P.; Kubarych, K. J. *Adv. At., Mol., Opt. Phys.* **2009**, *57*, 249.

[21] Garrett-Roe, S.; Hamm, P. *Acc. Chem. Res.* **2009**, *42*, 1412–1422.

[22] Bredenbeck, J.; Ghosh, A.; Nienhuys, H.-K.; Bonn, M. *Acc. Chem. Res.* **2009**, *42*, 1332–1342.

[23] Bakulin, A. A.; Liang, C.; La Cour Jansen, T.; Wiersma, D. A.; Bakker, H. J.; Pshenichnikov, M. S. *Acc. Chem. Res.* **2009**, *42*, 1229–1238.

[24] Myers, J. A.; Lewis, K. L. M.; Tekavec, P. F.; Ogilvie, J. P. *Opt. Expr.* **2008**, *16*, 17420–17428.

[25] Hamm, P.; Helbing, J.; Bredenbeck, J. *Annu. Rev. Phys. Chem.* **2008**, *59*, 291–317.

[26] Baiz, C. R.; Nee, M. J.; McCanne, R.; Kubarych, K. J. *Opt. Lett.* **2008**, *33*, 2533–2535.

[27] Zheng, J.; Kwak, K.; Fayer, M. D. *Acc. Chem. Res.* **2007**, *40*, 75–83.

[28] Moran, A. M.; Nome, R. A.; Scherer, N. F. *J. Chem. Phys.* **2007**, *127*, 184505/1.

[29] Kukura, P.; McCamant, D. W.; Mathies, R. A. *Annu. Rev. Phys. Chem.* **2007**, *58*, 461–488.

[30] Engel, G. S.; Calhoun, T. R.; Read, E. L.; Ahn, T. K.; Mančal, T.; Cheng, Y.-C.; Blankenship, R. E.; Fleming, G. R. *Nature* **2007**, *446*, 782–786.

[31] Li, X.; Zhang, T.; Borca, C.; Cundiff, S. *Phys. Rev. Lett.* **2006**, *96*, 057406/1.

[32] Cowan, M. L.; Bruner, B. D.; Huse, N.; Dwyer, J. R.; Chugh, B.; Nibbering, E. T. J.; Elsaesser, T.; Miller, R. J. D. *Nature* **2005**, *434*, 199–202.

[33] Brixner, T.; Stenger, J.; Vaswani, H. M.; Cho, M.; Blankenship, R. E.; Fleming, G. R. *Nature* **2005**, *434*, 625–628.

[34] Underwood, D.; Blank, D. A. *J. Phys. Chem. A* **2003**, *107*, 956–961.

[35] Khalil, M.; Demirdöven, N.; Tokmakoff, A. *J. Phys. Chem. A* **2003**, *107*, 5258–5279.

[36] Ge, N. H.; Hochstrasser, R. M. *PhysChemComm* **2002**, *5*, 17.

[37] Zanni, M. T.; Hochstrasser, R. M. *Curr. Opin. Struct. Biol.* **2001**, *11*, 516.

[38] Sciaini, G.; Miller, R. J. D. *Rep. Prog. Phys.* **2011**, *74*, 096101/1.

[39] Chergui, M. *Acta Crystallogr., Sect. A: Found. Crystallogr.* **2010**, *A66*, 229.

[40] Chen, L. X.; Zhang, X.; Lockard, J. V.; Stickrath, A. B.; Attenkofer, K.; Jennings, G.; Liu, D. J. *Acta Crystallogr., Sect. A: Found. Crystallogr.* **2010**, *A66*, 240.

[41] Bressler, C.; Chergui, M. *Annu. Rev. Phys. Chem.* **2010**, *61*, 263–282.

[42] Chergui, M.; Zewail, A. H. *ChemPhysChem* **2009**, *10*, 28.

[43] Ihee, H.; Rajagopal, S.; Srajer, V.; Pahl, R.; Anderson, S.; Schmidt, M.; Schotte, F.; Anfinrud, P. A.; Wulff, M.; Moffat, K. *Proc. Natl. Acad. Sci. U.S.A.* **2005**, *102*, 7145–7150.

[44] Chen, L. X. *Annu. Rev. Phys. Chem.* **2005**, *56*, 221–254.

[45] Schotte, F.; Soman, J.; Olson, J. S.; Wulff, M.; Anfinrud, P. A. *J. Struct. Biol.* **2004**, *147*, 235.

[46] Srinivasan, R.; Lobastov, V. A.; Ruan, C. Y.; Zewail, A. H. *Helv. Chim. Acta* **2003**, *86*, 1763.

[47] Lepetit, L.; Cheriaux, G.; Joffre, M. *J. Opt. Soc. Am. B* **1995**, *12*, 2467–2474.

[48] Jones, K. C.; Ganim, Z.; Tokmakoff, A. *J. Phys. Chem. A* **2009**, *113*, 14060–14066.

[49] Jones, K.; Ganim, Z.; Peng, C.; Tokmakoff, A. *J. Opt. Soc. Am. B* **2012**, *29*, 118–129.

[50] Gruebele, M.; Sabelko, J.; Ballew, R.; Ervin, J. *Acc. Chem. Res.* **1998**, *31*, 699.

[51] Gutman, M.; Huppert, D.; Pines, E. *J. Am. Chem. Soc.* **1981**, *103*, 3709.

[52] Anfinrud, P. A.; Han, C.; Lian, T.; Hochstrasser, R. M. *J. Phys. Chem.* **1990**, *94*, 1180.

[53] Cervetto, V.; Hamm, P.; Helbing, J. *J. Phys. Chem. B* **2008**, *112*, 8398–8405.

[54] Demirdöven, N.; Khalil, M.; Golonzka, O.; Tokmakoff, A. *Opt. Lett.* **2002**, *27*, 433–435.

[55] Wu, Y.; Cohran, C.; Bocarsly, A. B. *Inorg. Chim. Acta* **1994**, *226*, 251–258.

[56] Chung, H. S.; Khalil, M.; Smith, A. W.; Tokmakoff, A. *Rev. Sci. Instrum.* **2007**, *78*, 063101.

[57] Hamm, P.; Lim, M.; Asplund, M.; Hochstrasser, R. *Chem. Phys. Lett.* **1999**, *301*, 167–174.

[58] Lynch, M. S.; Van Kuiken, B. E.; Daifuku, S. L.; Khalil, M. *J. Phys. Chem. Lett.* **2011**, *2*, 2252–2257.

[59] Nitzan, A. *Chemical Dynamics in Condensed Phases*; Oxford University Press: New York, 2006.

[60] Bredenbeck, J.; Helbing, J.; Hamm, P. *Phys. Rev. Lett.* **2005**, *95*, 083201.

[61] Greaves, S. J.; Rose, R. A.; Oliver, T. A. A.; Glowacki, D. R.; Ashfold, M. N. R.; Harvey, J. N.; Clark, I. P.; Greetham, G. M.; Parker, A. W.; Towrie, M.; Orr-Ewing, A. J. *Science* **2011**, *331*, 1423–1426.

[62] Orr-Ewing, A. J.; Glowacki, D. R.; Greaves, S. J.; Rose, R. A. *J. Phys. Chem. Lett.* **2011**, *2*, 1139–1144.

[63] Rose, R. A.; Greaves, S. J.; Oliver, T. A. A.; Clark, I. P.; Greetham, G. M.; Parker, A. W.; Towrie, M.; Orr-Ewing, A. J. *J. Chem. Phys.* **2011**, *134*, 244503.

[64] Moskun, A.; Jailaubekov, A.; Bradforth, S.; Tao, G.; Stratt, R. *Science* **2006**, *311*, 1907–1911.

[65] Bragg, A. E.; Cavanagh, M. C.; Schwartz, B. J. *Science* **2008**, *321*, 1817–1822.

[66] Underwood, D. F.; Blank, D. A. *J. Phys. Chem. A* **2005**, *109*, 3295–3306.

[67] Stratt, R. M. *Science* **2008**, *321*, 1789–1790.

[68] Bredenbeck, J.; Helbing, J.; Hamm, P. *J. Am. Chem. Soc.* **2004**, *126*, 990–991.

[69] Bredenbeck, J.; Helbing, J.; Hamm, P. *J. Chem. Phys.* **2004**, *121*, 5943–5957.

[70] Baiz, C. R.; Kubarych, K. J. *J. Am. Chem. Soc.* **2010**, *132*, 12784–12785.

[71] Baiz, C. R.; McCanne, R.; Nee, M. J.; Kubarych, K. J. *J. Phys. Chem. A* **2009**, *113*, 8907–8916.

[72] Kania, R.; Stewart, A. I.; Clark, I. P.; Greetham, G. M.; Parker, A. W.; Towrie, M.; Hunt, N. T. *Phys. Chem. Chem. Phys.* **2010**, *12*, 1051.

[73] Cahoon, J. F.; Sawyer, K. R.; Schlegel, J. P.; Harris, C. B. *Science* **2008**, *319*, 1820–1823.

[74] Xiong, W.; Laaser, J. E.; Paoprasert, P.; Franking, R. A.; Hamers, R. J.; Gopalan, P.; Zanni, M. T. *J. Am. Chem. Soc.* **2009**, *131*, 18040–18041.

[75] Chung, H. S.; Ganim, Z.; Jones, K.; Tokmakoff, A. *Proc. Natl. Acad. Sci. U.S.A.* **2007**, *104*, 14237–14242.

[76] Faeder, S.; Jonas, D. M. *J. Phys. Chem. A* **1999**, *103*, 10489–10505.

[77] DeFlores, L. P.; Nicodemus, R. A.; Tokmakoff, A. *Opt. Lett.* **2007**, *32*, 2966–2968.

[78] Middleton, C. T.; Strasfeld, D. B.; Zanni, M. T. *Opt. Expr.* **2009**, *17*, 14526–14533.

[79] Blank, D.; Kaufman, L.; Fleming, G. *J. Chem. Phys.* **1999**, *111*, 3105–3114.

[80] Golonzka, O.; Demirdöven, N.; Khalil, M.; Tokmakoff, A. *J. Chem. Phys.* **2000**, *113*, 9893–9896.

[81] Kaufman, L.; Blank, D. A.; Fleming, G. *J. Chem. Phys.* **2001**, *114*, 2312–2331.

[82] Kubarych, K. J.; Milne, C. J.; Lin, S.; Astinov, V.; Miller, R. J. D. *J. Chem. Phys.* **2002**, *116*, 2016.

[83] Wilson, K. C.; Lyons, B.; Mehlenbacher, R.; Sabatini, R.; McCamant, D. W. *J. Chem. Phys.* **2009**, *131*, 214502.

[84] Mehlenbacher, R. D.; Lyons, B.; Wilson, K. C.; Du, Y.; McCamant, D. W. *J. Chem. Phys.* **2009**, *131*, 244512.

[85] Lynch, M. S.; Slenkamp, K. M.; Khalil, M. *J. Chem. Phys.* **2012**, *136*, 241101.

Chapter 6

PROBING NON-EQUILBRIUM VIBRATIONAL RELAXATION PATHWAYS OF HIGHLY EXCITED C≡N STRETCHING MODES FOLLOWING ULTRAFAST BACK-ELECTRON TRANSFER

The work presented in this chapter has been published in the following paper:
Lynch, M. S.; Slenkamp, K. M.; Khalil, M. "Communication: Probing non-equilbrium vibrational relaxation pathways of highly excited C≡N stretching modes following ultrafast back-electron transfer," *J. Chem. Phys.* **2012**, *136*, 241101.

Fifth-order nonlinear visible-infrared spectroscopy is used to probe coherent and incoherent vibrational energy relaxation dynamics of highly excited vibrational modes indirectly populated via ultrafast photoinduced back-electron transfer in a trinuclear cyano-bridged mixed-valence complex. The flow of excess energy deposited into four C≡N stretching (ν_{CN}) modes of the molecule is monitored by performing an IR pump−probe experiment as a function of the photochemical reaction (τ_{vis}). Our results provide experimental evidence that the nuclear motions of the molecule are both coherently and incoherently coupled to the electronic charge transfer process. We observe that intramolecular vibrational relaxation dynamics among the highly excited ν_{CN} modes change significantly en route to equilibrium. The experiment also measures a 7 cm^{-1} shift in the frequency of a ∼57 cm^{-1} oscillation reflecting a modulation of the coupling between the probed high-frequency ν_{CN} modes for $\tau_{vis} < 500$ fs.

Monitoring inter- and intramolecular vibrational energy flow in highly excited molecular and material systems is a necessary step for developing predictive models of chemical reactivity.[1–4] For example, measuring time-dependent vibrational energy flow within a molecule and into its surroundings during an ultrafast photochemical charge transfer reaction can identify specific nuclear motions which are coupled to the charge transfer process. This in turn opens up the possibility of optimizing the efficacy of charge transfer in molecular materials by manipulating the vibrational density of states within the ground and excited electronic states by chemical synthesis or coherent control with light.[5,6] Detailing vibrational energy flow in polyatomic molecules during ultrafast photoinduced chemical reactions in solution requires experimental tools that can measure coupled electronic and vibrational degrees of freedom with femtosecond time resolution.

Femtosecond third-order nonlinear infrared (IR) techniques such as two-dimensional (2D) IR spectroscopy have been extremely successful in measuring mode-specific inter- and intramolecular vibrational energy flow in ground electronic states for a range of molecular systems in solution.[7–12] Recently, transient two-dimensional infrared spectroscopy has been used to probe vibrational dynamics following electronic excitation in chemical, biological, and material systems.[13–20] Nonlinear IR probes are ideally suited to study energy transfer among coupled vibrational modes in ultra- fast charge transfer processes. Cyano-bridged transition metal mixed valence complexes serve as very interesting model systems for probing relaxation dynamics among highly excited vibrational modes populated in <200 fs by ultrafast back- electron transfer (BET).[21–24]

In this study, we use sub-120 fs transient heterodyne-detected dispersed vibrational echo (t-HDVE) spectroscopy to monitor inter- and intramolecular vibrational energy flow among a network of coupled cyanide stretching (ν_{CN}) vibrations following ultrafast metal-to-metal charge transfer (MMCT) in the trinuclear mixed valence compound $[(NC)_5Fe^{II}-CN-Pt^{IV}(NH_3)_4-NC-Fe^{II}(CN)_5]^{4-}$ (denoted as $Fe^{II}Pt^{IV}Fe^{II}$) dissolved in D_2O. The $Fe^{II}Pt^{IV}Fe^{II}$ molecule illustrated in Figure 6.1a contains four high-frequency ν_{CN} modes: ν_{radial} (2050 cm^{-1}), ν_{trans} (2060 cm^{-1}), ν_{axial} (2074 cm^{-1}), and ν_{bridge} (2116 cm^{-1}).[25] Three of the four modes lie along the long axis of the molecule and are orthogonal to the fourth degenerate ν_{radial} mode. The ultrafast photochemistry of this molecule has been studied by

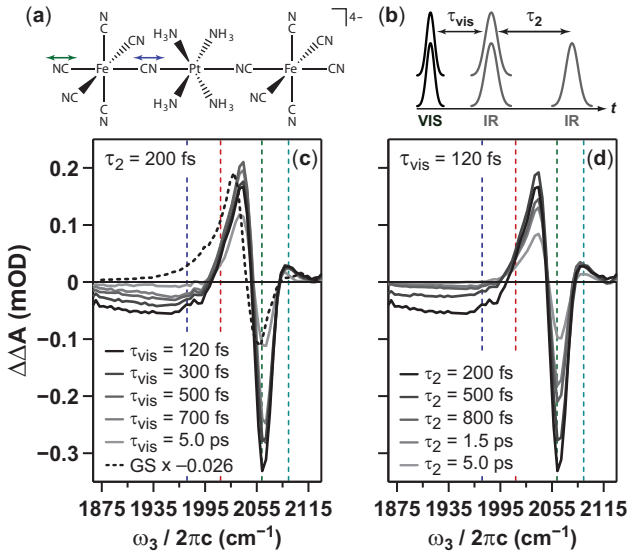

Figure 6.1: (a) Molecular structure of the $Fe^{II}Pt^{IV}Fe^{II}$ ion with arrows highlighting the ν_{bridge} (blue) and ν_{trans} (green) modes. (b) Transient DPP pulse sequence with one electronic population period (τ_{vis}) and one vibrational population period (τ_2). Transient DPP spectra for five values of τ_{vis} at τ_2= 200 fs (c) and five values of τ_2 at τ_{vis}= 120 fs (d). Dashed vertical lines are placed at 1974 cm^{-1} ($n_{\text{bridge}} > 6$; blue), 2013 cm^{-1} ($n_{\text{trans}} = 2 - 3$; red), 2061 cm^{-1} ($n_{\text{trans}} = 0$; green), and 2092 cm^{-1} ($n_{\text{bridge}} = 1$; cyan). The dashed black spectrum in (c) is a scaled third-order, 2-beam DPP spectrum of the GS at τ_2= 200 fs (the y axis for the GS spectrum is technically in units of ΔA).

our group and others using femtosecond transient IR and visible spectroscopies.[23,26] Our studies have shown that MMCT from Fe^{II} to Pt^{IV} induced with a 400 nm photon creates a short-lived $Fe^{III}Pt^{III}Fe^{II}$ (equivalently $Fe^{II}Pt^{III}Fe^{III}$) charge transfer state from which ultrafast BET occurs on a 110 fs time scale. Vibrational excitation of the ground electronic state following BET leads to different degrees of excitation in each of the four ν_{CN} modes. Energy is transferred between the highly excited ν_{CN} modes via intramolecular vibrational redistribution (IVR) and vibrational cooling (VC) to populate states with one quantum of vibrational energy ($n = 1$). Eventually, the coupled vibrational system relaxes to the ground state (GS) ($n = 0$) via intermolecular vibrational energy relaxation (VER) to surrounding solvent molecules. The goal of this study is to probe time-evolving IVR and VER pathways among coherently coupled vibrations with t-HDVE spectroscopy as the molecule

equilibrates in the ground electronic state following ultrafast BET.

The experimental technique utilizes the pulse sequence shown in Figure 6.1b. Three 80 fs IR pulses ($\mathbf{k}_{\mathrm{i}}$, where i = 1, 2, 3) are set up in the traditional boxcar geometry with a fourth 35 fs 400 nm pulse ($\mathbf{k}_{\mathrm{vis}}$) traveling down the center of the boxcar for charge transfer excitation. Third- and fifth-order IR signals are emitted in the background-free direction given by $-\mathbf{k}_1 + \mathbf{k}_2 + \mathbf{k}_3$. The time delay between the electronic excitation pulse and the first IR pulse (τ_{vis}) represents the electronic population period. Time delays between IR pulses follow labeling schemes used in third-order nonlinear IR spectroscopies where τ_1 is the vibrational coherence period, τ_2 is the vibrational population period (i.e., waiting time), and τ_3 is the detection period. An independent local oscillator field is mixed with the signal to perform spectral interferometry. The interferometric signal is spectrally dispersed (ω_3) with a spectrograph and measured with a 2×64 HgCdTe array detector. The fifth-order signal is carefully isolated with the combination of a double-chopping scheme and balanced detection as detailed previously.[25,27,28] In this experiment, we use the transient HDVE signals to construct transient dispersed pump−probe (t-DPP) spectra as a function of ω_3 for fixed values of τ_{vis} and τ_2 following the procedure outlined in Chapter 5. Transient DPP is a coherent multiple population period experiment with one population period reporting on the lifetime of the electronic excited state(s) (τ_{vis}) and the other tracking vibrational relaxation dynamics (τ_2) among coupled vibrational modes.

Transient DPP spectra along the electronic and vibrational population periods are shown in Figures 6.1c and 6.1d, respectively. We note that the black solid line representing $\mathbf{S}^{(5)}(\omega_3; \tau_{\mathrm{vis}} = 120$ fs, $\tau_2 = 200$ fs) is the same in both panels for comparison. Each of these spectra represents contributions from many overlapping vibrational features. Our previous work has identified four spectral regions of interest which are indicated with dashed vertical lines in Figures 6.1c and 6.1d.[23] They include: $n_{\mathrm{bridge}} > 6$ ($\omega_3 = 1974$ cm^{-1}), $n_{\mathrm{trans}} = 2 - 3$ ($\omega_3 = 2013$ cm^{-1}), $n_{\mathrm{bridge}} = 1$ ($\omega_3 = 2092$ cm^{-1}), and the GS represented here by $n_{\mathrm{trans}} = 0$ ($\omega_3 = 2061$ cm^{-1}). Following these vibrational states as a function of τ_{vis} and τ_2 provides a multidimensional probe of the molecular system as it relaxes to equilibrium.

The broad negative feature between 1870 and 2000 cm^{-1} in Figure 6.1c displays the IR pump−probe signal from high-lying vibrational levels ($n_{\mathrm{bridge}} > 6$) as a function of

τ_{vis}. The large positive peak in the 2000−2040 cm^{-1} region arises from absorption bands corresponding to $n_{trans} = 2(3) \leftarrow 1(2)$ and $n_{radial} = 2 \leftarrow 1$ transitions. The bleach peak located at ∼2060 cm contains contributions from the ν_{trans}, ν_{radial}, and ν_{axial} modes but is centered at the fundamental frequency of the ν_{trans} mode. A smaller absorption peak at ∼2090 cm^{-1} is the $n_{bridge} = 2 \leftarrow 1$ transition overlapped with multiple combination bands.[29] Finally, a very small bleach feature corresponding to $n_{bridge} = 1 \rightarrow 0$ is centered at 2116 cm^{-1}. A scaled 2-beam DPP spectrum of the GS is shown in Figure 16.1c for comparison, and we see that the bleach and transient absorption of the GS spectrum are shifted to lower energy by 6 and 9 cm^{-1}, respectively. We believe these frequencies are shifted in the fifth-order experiment since the ν_{trans} and ν_{axial} modes are more strongly coupled to the BET reaction and therefore have a larger transient population in the non-equilibrium ground state. In contrast, a third-order IR DPP experiment directly pumps the $n = 1$ states of all four ν_{CN} vibrations with a broad IR pump and will lead to a ground state bleach whose center frequency is dictated by the IR transition dipole strengths of individual ν_{CN} modes.[30]

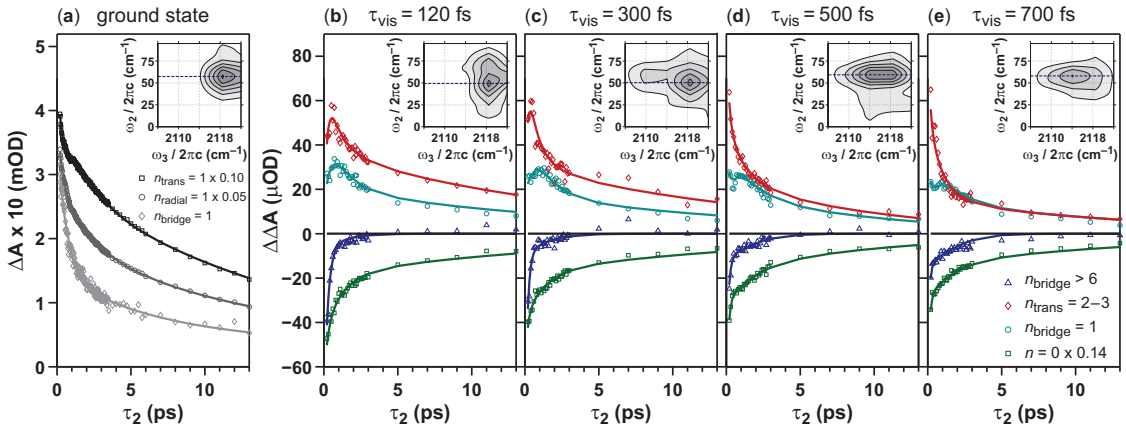

Figure 6.2: (a) Ground state vibrational relaxation dynamics. The $n_{bridge} = 1$ trace (2092 cm^{-1}, diamond) decays with two time scales, the $n_{trans} = 1$ trace (2037 cm^{-1}, square) contains a small rise, and the $n_{radial} = 1$ trace (2024 cm^{-1}, circle) does not rise. The inset shows a power spectrum of coherent beating along τ_2 observed in the ν_{bridge} region. (b)−(e) Non-equilibrium vibrational relaxation dynamics at four τ_{vis}. Labels correspond to $\omega_3 =$ 1974 cm^{-1} (blue triangles), 2013 cm^{-1} (red diamonds), 2061 cm^{-1} (green squares), and 2092 cm^{-1} (cyan circles). The solid lines represent fits to the data as described in the text.

Figure 6.2 contains kinetic traces along τ_2 for the IR frequencies highlighted in Figure 6.1. Ground state vibrational relaxation dynamics are presented in Fig. 6.2a. The dynamics of the $n = 1$ states for the ν_{bridge}, ν_{trans}, and ν_{radial} modes are shown since they represent IVR between the $n = 1$ manifold and VER from $n = 1 \rightarrow 0$. The $n_{\text{bridge}} = 1$ vibrational mode decays on two time scales: $T_{\text{IVR}} = 700 \pm 30$ fs and $T_{\text{VER}} = 17 \pm 2$ ps. The $n_{\text{trans}} = 1$ decays quickly on a 250 ± 20 fs time scale, begins to rise on a 780 ± 60 fs time scale (which is the same rate as the decay of $n_{\text{bridge}} = 1$), and subsequently decays with two time scales (1.7 ± 0.5 ps and 18.3 ± 0.5 ps). The $n_{\text{radial}} = 1$ trace decays with three time scales: 320 ± 30 fs, 2.4 ± 0.2 ps,and 20.1 ± 0.6 ps.The inset of Fig. 6.2a shows a power spectrum of coherent oscillations occurring along $\tau_2$in the ν_{bridge} region reporting on the $n_{\text{bridge}} = 1 \leftarrow 0$ transition. The 57 cm^{-1} low-frequency beat originates from a coherent coupling of the ν_{bridge} and ν_{trans} modes ($\Delta\omega = 56$ cm^{-1}), indicating that the modes along the long charge-transfer axis of the molecule are strongly coupled.

The remaining panels in Figures 6.2b−6.2e illustrate changes in coherent and incoherent vibrational relaxation dynamics as the BET reaction proceeds to equilibrium. General features of interest can be seen clearly in Fig. 6.2b where τ_{vis}= 120 fs: (i) the negative high-lying bridge feature ($n_{\text{bridge}} > 6$) decays very rapidly to zero, (ii) the $n_{\text{trans}} = 2 - 3$ region rises on a very fast time scale and subsequently decays with 12 time constants, (iii) the $n_{\text{bridge}} = 1$ region rises and sub- sequently decays more slowly than the $n_{\text{trans}} = 2 - 3$ feature, (iv) the bleach ($n_{\text{trans}} = 0$) slowly recovers on multiple time scales, and (v) the insets in each panel measure how the coupling between the ν_{bridge} and ν_{trans} modes is modulated by the BET reaction. It is clear from Figure 6.2 that vibrational dynamics change as the photochemical reaction time (τ_{vis}) increases. Most notably, the sharp rise feature in the $n_{\text{trans}} = 2 - 3$ trace is gone after $\tau_{\text{vis}} = 300$ fs. When $\tau_{\text{vis}} < 300$ fs, population in the $n_{\text{bridge}} > 6$ region is directly coupled to the $n_{\text{trans}} = 2-3$ state as shown in Figures 6.2b and 6.2c. However, as τ_{vis} becomes greater than 300 fs, there is already significant population in the $n_{\text{trans}} = 2 - 3$ state and therefore the dynamics of the two states are effectively decoupled. For these reasons, it was necessary to simultaneously fit the four kinetic traces at each τ_{vis} to two target models in order to extract time scales for the non-equilibrium IVR and VC dynamics. Detailed fitting results are given in Table 6A.1 of the appendix.[25]

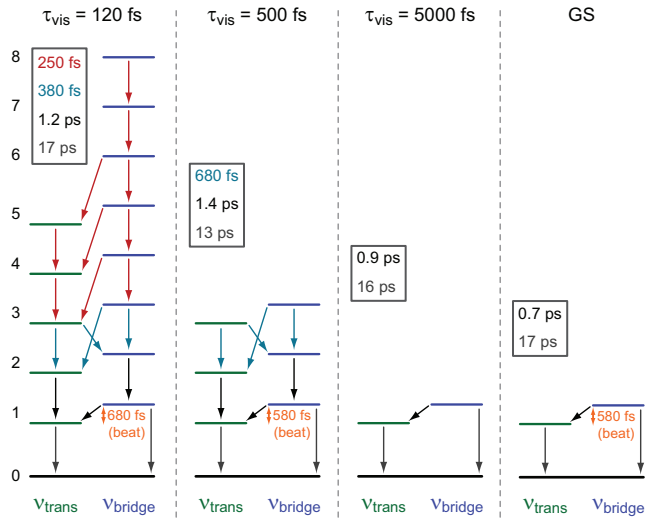

Figure 6.3: A schematic view of the non-equilibrium vibrational relaxation dynamics occurring in $Fe^{II}Pt^{IV}Fe^{II}$ upon BET. Vibrational quanta (n_i) are given on the left increasing from bottom to top with fitting parameters at each τ_{vis} shown within boxed legends. Downward arrows correspond to the transfer of vibrational population, whereas orange double-sided arrows represent coherent coupling of two modes oscillating at the given period. The signal-to-noise of the 5000 fs data prevented an accurate measurement of a beat frequency.

Modeling the t-DPP data unveiled four characteristic time constants associated with incoherent non-equilibrium vibrational relaxation dynamics in $Fe^{II}Pt^{IV}Fe^{II}$. The results are summarized in Figure 6.3 where populated vibrational levels and transitions between them are displayed as a function of τ_{vis}. Upon BET, population in the ν_{bridge} mode is inverted to $n_{bridge} > 6$ levels and subsequently transferred to lower-lying $n_{trans} = 2 - 3$ levels on a 250 ± 20 fs time scale (red arrows). When $\tau_{vis} < 300$ fs, this energy is quickly moved down to the $n = 1 - 2$ levels at a rate of $(380 \pm 80\ \text{fs})^{-1}$ as shown in cyan arrows. This rate increases to $(680 \pm 70\ \text{fs})^{-1}$ when $\tau_{vis} > 300$ fs indicating that the mechanism of vibrational relaxation from these levels changes as τ_{vis} increases. The third kinetic step, comparable to IVR in the GS, occurs on a 1.2 ± 0.1 ps time scale at $\tau_{vis} = 120$ fs and does not statistically change as a function of τ_{vis} (black arrows). The rate of the fourth kinetic step that reports on VER is $(17 \pm 3\ \text{ps})^{-1}$ is also constant with τ_{vis} within error (gray arrows) and consistent with ground state VER time scales.[23] These results show the decrease of the vibrational

lifetime with increasing quantum number for a particular mode at a specific τ_{vis} delay.

We also observe that as the reaction proceeds, the vibrational cooling rate from $n = 2-3$ levels decreases by a factor of $\sim$2 as shown by the cyan arrows in the first two panels of Figure 6.3. The above results imply that the vibrational population in a given mode and anharmonic couplings to other intra- and intermolecular modes is a function of τ_{vis} for the BET occurring in $Fe^{II}Pt^{IV}Fe^{II}$. The time-dependent anharmonic couplings affect both the number of available vibrational relaxation pathways and the rate of vibrational relaxation along each pathway by accessing different spectral densities at each τ_{vis} delay.

For the case of $Fe^{II}Pt^{IV}Fe^{II}$, the DPP signal at $\omega_3 = \omega_{\text{bridge}}$ is dominated by the response of the cross-peak between the bridge and the trans modes and displays a strong oscillation at 57 cm^{-1} in the GS, which is a signature of the coherent coupling between the ν_{bridge} and ν_{trans} modes as shown in the inset in Figure 6.2a.[31] The remaining insets in Figure 6.2 show how coherent coupling of the ν_{trans} mode with the ν_{bridge} mode changes as a function of τ_{vis}. The beat frequency downshifts to $\sim$50 cm^{-1} when $\tau_{\text{vis}} = 120$ fs and 300 fs and then back to its GS value of $\sim$57 cm^{-1} when $\tau_{\text{vis}} > 300$ fs. This interesting result strongly suggests that the ν_{bridge} mode is coherently coupled to the MMCT transition. We propose that the 7 cm^{-1} shift of the oscillation in the ν_{bridge} region arises from a coherently driven low-frequency Raman mode lying within the bandwidth of the visible pump pulse, which changes the nature of coupling between the high-frequency ν_{CN} modes. Our results would impose an upper limit of 500 fs on the dephasing time of low-frequency modes vibronically coupled to the MMCT transition in $Fe^{II}Pt^{IV}Fe^{II}$ as the frequency shift is negligible at $\tau_{\text{vis}} > 300$ fs. We note that impulsively excited low-frequency modes in the $70 - 600$ cm^{-1} region have been previously observed in femtosecond transient absorption experiments on prussian blue and dinuclear transition metal mixed valence compounds.[32–35]

The role of coupled electronic and nuclear motions in ultrafast photoinduced chemical reactions was brought to the forefront when vibrationally coherent photochemistry was observed in rhodopsin almost twenty years ago.[36] To explore how vibrational relaxation in high frequency vibrations affects ultrafast charge transfer processes, we performed fifth-order transient IR DPP spectroscopy at multiple time points during a photoinduced BET reaction in a trinuclear cyano-bridged mixed-valence complex. Our multidimensional exper-

iments reveal rich microscopic details on how coherent and incoherent vibrational relaxation pathways and dynamics are significantly altered as the coherently coupled ν_{CN} modes relax to equilibrium.

This work was supported by the Office of Basic Energy Sciences of the U.S. Department of Energy (DOE) (Grant No. DE-SC0002190). M.K. acknowledges support from the Camille and Henry Dreyfus New Faculty Award and the David and Lucille Packard Fellowship for Science and Engineering.

REFERENCES

[1] Gruebele, M.; Wolynes, P. G. *Acc. Chem. Res.* **2004**, *37*, 261–267.

[2] May, V.; Kühn, O.; Wiley, I. *Charge and Energy Transfer Dynamics in Molecular Systems*; Wiley VCH: Weinheim, 2011.

[3] Nesbitt, D.; Field, R. *J. Phys. Chem.* **1996**, *100*, 12735–12756.

[4] Glowacki, D. R.; Rose, R. A.; Greaves, S. J.; Orr-Ewing, A. J.; Harvey, J. N. *Nat. Chem.* **2011**, *3*, 850–855.

[5] Brüggemann, B.; Organero, J.; Pascher, T.; Pullerits, T.; Yartsev, A. *Phys. Rev. Lett.* **2006**, *97*, 208301.

[6] Grumstrup, E. M.; Johnson, J. C.; Damrauer, N. H. *Phys. Rev. Lett.* **2010**, *105*, 257403.

[7] Zheng, J.; Kwak, K.; Asbury, J.; Chen, X.; Piletic, I. *Science* **2005**, *309*, 1338.

[8] Khalil, M.; Demirdöven, N.; Tokmakoff, A. *J. Chem. Phys.* **2004**, *121*, 362–373.

[9] Bian, H.; Chen, H.; Li, J.; Wen, X.; Zheng, J. *J. Phys. Chem. A* **2011**, *115*, 11657–11664.

[10] Roberts, S. T.; Ramasesha, K.; Tokmakoff, A. *Acc. Chem. Res.* **2009**, *42*, 1239–1249.

[11] Kim, Y. S.; Hochstrasser, R. M. *Proc. Natl. Acad. Sci. U.S.A.* **2005**, *102*, 11185–11190.

[12] Rubtsov, I. V. *Acc. Chem. Res.* **2009**, *42*, 1385–1394.

[13] Hamm, P.; Helbing, J.; Bredenbeck, J. *Annu. Rev. Phys. Chem.* **2008**, *59*, 291–317.

[14] Bredenbeck, J.; Helbing, J.; Hamm, P. *J. Am. Chem. Soc.* **2004**, *126*, 990–991.

[15] Bredenbeck, J.; Helbing, J.; Hamm, P. *Phys. Rev. Lett.* **2005**, *95*, 083201.

[16] Baiz, C. R.; Kubarych, K. J. *J. Am. Chem. Soc.* **2010**, *132*, 12784–12785.

[17] Baiz, C. R.; McCanne, R.; Nee, M. J.; Kubarych, K. J. *J. Phys. Chem. A* **2009**, *113*, 8907–8916.

[18] Kania, R.; Stewart, A. I.; Clark, I. P.; Greetham, G. M.; Parker, A. W.; Towrie, M.; Hunt, N. T. *Phys. Chem. Chem. Phys.* **2010**, *12*, 1051.

[19] Xiong, W.; Laaser, J. E.; Paoprasert, P.; Franking, R. A.; Hamers, R. J.; Gopalan, P.; Zanni, M. T. *J. Am. Chem. Soc.* **2009**, *131*, 18040–18041.

[20] Cahoon, J. F.; Sawyer, K. R.; Schlegel, J. P.; Harris, C. B. *Science* **2008**, *319*, 1820–1823.

[21] Wang, C. F.; Mohney, B. K.; Akhremitchev, B. B.; Walker, G. C. *J. Phys. Chem. A* **2000**, *104*, 4314–4320.

[22] Tivansky, A. V.; Wang, C. F.; Walker, G. C. *J. Phys. Chem. A* **2003**, *107*, 9051–9058.

[23] Lynch, M. S.; Van Kuiken, B. E.; Daifuku, S. L.; Khalil, M. *J. Phys. Chem. Lett.* **2011**, *2*, 2252–2257.

[24] Doorn, S. K.; Dyer, R. B.; Stoutland, P. O.; Woodruff, W. H. *J. Am. Chem. Soc.* **1993**, *115*, 6398–6405.

[25] See appendix for steady-state spectra, details of the experimental setup, beat frequency measurements, and kinetic modeling.

[26] Watson, D. F.; Tan, H.-S.; Schreiber, E.; Mordas, C. J.; Bocarsly, A. B. *J. Phys. Chem. A* **2004**, *108*, 3261–3267.

[27] Jones, K. C.; Ganim, Z.; Tokmakoff, A. *J. Phys. Chem. A* **2009**, *113*, 14060–14066.

[28] Lynch, M. S.; Slenkamp, K. M.; Cheng, M.; Khalil, M. *J. Phys. Chem. A* **2012**, *116*, 7023–7032.

[29] 2D IR experiments on the ground state of $Fe^{II}Pt^{IV}Fe^{II}$ in Chapter 3 measured anharmonicities of 21, 23, 21, and 24 cm^{-1} for the radial, trans, axial, and bridging modes, respectively.

[30] We would expect the transient bleach to shift back to the GS frequency when $\tau_{vis} = 5$ ps. However, the bleach does not shift (see Fig. 6.1c) and therefore we conclude that the distribution of transient population in the $n = 1$ manifold is different for direct (IR) and indirect (UV/vis) excitation.

[31] Recall that the projection of a 2D IR spectrum onto the detection axis is equivalent to an IR DPP spectrum by the projection-slice theorem. In many cases, cross peak information is lost in the DPP spectrum due to large diag- onal peaks overwhelming smaller cross peaks. However, consider the case where a molecule has two vibrations

(ν_a and ν_b) with parallel transition dipole vectors where $|\mu_a| \gg |\mu_b|$. The DPP signal at $\omega_3 = \omega_b$ would be dominated by the cross-peak intensity as opposed to the diagonal peak (i.e., $|\mu_a|^2|\mu_b|^2 > |\mu_b|^4$) and the coherent coupling between the two modes would be observed as a beat with frequency $|\omega_a - \omega_b|$.

[32] Reid, P. J.; Silva, C.; Barbara, P.; Karki, L.; Hupp, J. *J. Phys. Chem.* **1995**, *99*, 2609–2616.

[33] Kambhampati, P.; Son, D. H.; Kee, T. W.; Barbara, P. F. *J. Phys. Chem. A* **2000**, *104*, 10637–10644.

[34] Son, D. H.; Kambhampati, P.; Kee, T. W.; Barbara, P. F. *J. Phys. Chem. A* **2002**, *106*, 4591–4597.

[35] Arnett, D. C.; Vohringer, P.; Scherer, N. F. *J. Am. Chem. Soc.* **1995**, *117*, 12262–12272.

[36] Wang, Q.; Schoenlein, R. W.; Peteanu, L. A.; Mathies, R. A.; Shank, C. V. *Science* **1994**, *266*, 422–424.

6.A Chapter 6 Supporting Information

6.A.1 Materials and Methods

The model complex $Na_4[(NC)_5Fe^{II}-CN-Pt^{IV}(NH_3)_4-NC-Fe^{II}(CN)_5]$ (i.e., $Fe^{II}Pt^{IV}Fe^{II}$) was synthesized according to literature procedures and subsequently purified.[1] Sample purity was verified with FTIR and UV/vis spectroscopy (see Figure 6A.1). Samples were prepared in D_2O to a concentration of ∼8 mM.

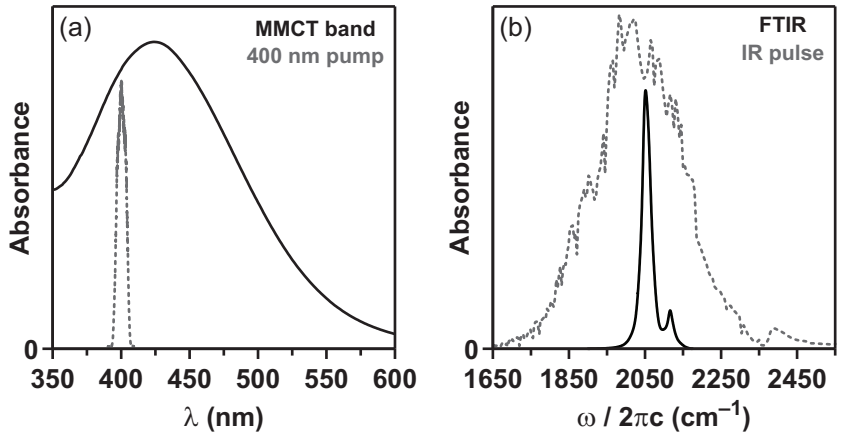

Figure 6A.1: Steady-state spectra of $Fe^{II}Pt^{IV}Fe^{II}$ in D_2O at room temperature with experimental visible and IR spectra overlaid. (a) UV/vis (−) and 400 nm pump spectra (−−). (b) FTIR (−) and IR pulse spectra (−−).

Complete experimental details and data analysis methods have been published elsewhere.[2] In brief, the experiments are performed with the output of a commercial Spectra Physics Spitfire Pro 35F-XP regenerative amplifier operating at 1 kHz (800 nm, 35 fs, 3 W). The visible pump pulse (λ_{vis} = 400 nm) is generated by frequency doubling a portion of the 800 nm beam in a 0.1 mm thick β-barium borate (β-BBO) crystal. An acousto-optic programmable dispersive filter (Fastlite, Dazzler UV-250−400) temporally compresses the spectrally broad ($\Delta\lambda_{fwhm}$ = 8 nm = 500 cm^{-1}; see Fig. 6A.1a) pump pulse to a final temporal width of ∼35 fs. The visible pulse energy at the sample was 1 μJ. The mid-IR pulses are generated via frequency conversion of the 800 nm pulses with an optical parametric amplifier (OPA), whereby ∼1 W of the amplified 800 nm beam is directed into a dual-pass

OPA (Newport, OPA-800C) to generate near-IR signal and idler pulses. Near-IR pulses are spatially and temporally overlapped in a 0.5 mm thick $AgGaS_2$ crystal for difference frequency mixing to generate tunable mid-IR pulses. For this experiment, the 80 fs mid-IR pulses were centered at $\omega_{\mathrm{MIR}} = 2030$ cm^{-1} with a bandwidth of $\Delta\omega_{\mathrm{MIR}} = 270$ cm^{-1} (see Fig. 6A.1b). The temporal width of the IR pulse at the sample is optimized by placing 3 mm of uncoated CaF_2 into the beam path to compensate for group velocity dispersion mismatch.[3] IR pulse energies at the sample were 0.5 μJ.

Data generated with this apparatus is a matrix including variables τ_{vis}, τ_2, and ω_3 (τ_1 = 0 for an IR DPP pump−probe measurement). We measured five values of τ_{vis} (120, 300, 500, 700, and 5000 fs), τ_2 was scanned from 0−13 ps in unequal time steps, and ω_3 ranged from 1870 cm^{-1} to 2130 cm^{-1} with ∼4 cm^{-1} spectral resolution. Kinetics along τ_{vis} were not fit since previous vis−IR pump−probe work in our group characterized dynamics occurring along this time variable.[4]

6.A.2 Coherent Oscillations along τ_2

Transient DPP traces as a function of τ_2 in the ν_{bridge} region are shown in Figure 6A.2 at five values of τ_{vis}, including a ground state (GS) trace that has been scaled. Power spectra shown in Figure 6.2 of the Chapter were generated as follows: (i) normalize trace, (ii) fit data from τ_2 = 0−2 ps to a biexponential (no offset) and subtract the fit from the data, (iii) interpolate the data (linear interpolation) to the smallest time step of 50 fs and delete the first two points (τ_2 = 0, 50 fs) to avoid erroneous frequencies from the subtraction, (iv) multiply the data by the Nuttal apodization filter function, and (v) take the magnitude-squared of the FFT of the resulting trace to afford the Fourier power spectrum.

6.A.3 Data Analysis and Kinetic Schemes

Kinetic traces shown in each panel of Figure 6.2 of the Chapter were simultaneously fit to one of two schemes depending on the value of τ_{vis}. The schemes illustrated in Fig. 6A.3 only differ in the first step of vibrational relaxation. We note that many other target models were created and fit to the data but were not as successful as the two schemes shown in

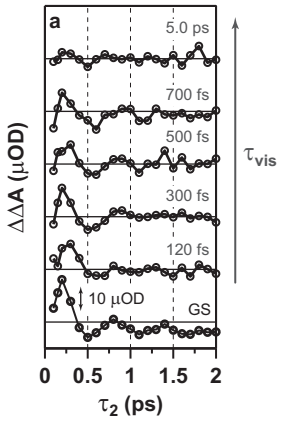

Figure 6A.2: Transient DPP signals in the ν_{bridge} mode region ($\omega_3 = 2114$ cm^{-1}), which oscillate as a function of τ_2. The GS spectrum has been scaled by a factor of -4, whereas the transient spectra follow the 10 μOD scale shown with the arrow. The trace at $\tau_{\text{vis}} = 5.0$ ps shows that the oscillations are within the noise.

Fig. 6A.3.

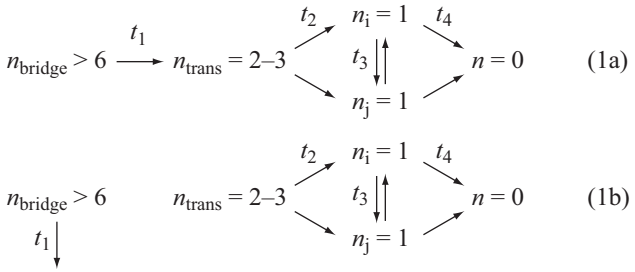

Figure 6A.3: Two schemes used to fit the non-equilibrium vibrational relaxation dynamics for $\tau_{\text{vis}} = 120$ and 300 fs (scheme 1a) and $\tau_{\text{vis}} = 500$, 700, and 5000 fs (scheme 1b). Here we define the time constant $t_{\text{i}} = 1/k_{\text{i}}$, where k_{i} is the first order rate of the i$^{\text{th}}$ process. In some cases multiple arrows are given for one time constant to point out that many pathways are possible; however, data was fit by following one pathway in the above schemes.

A total of four time traces (corresponding to 4 unique IR frequencies) from the raw data matrix were simultaneously fit from $\tau_2 = 0.1{-}13$ ps. Data between $\tau_2 = 0{-}0.1$ ps was excluded to ensure the resulting kinetic parameters were not due to cross-phase modulation and/or solvent response. Each set of four kinetic traces at a particular τ_{vis} was either fit to

scheme 1a (Eq. 6A.1) or 1b (Eq. 6A.2) with corresponding equations given by

$$\begin{aligned} f_{1a}(\tau_2;\omega_3) = {} & A_1(\omega_3)\mathrm{ExpErf}\left[B,t_0,t_1,\tau_2\right]\cdots \\ & + A_2(\omega_3)\left(\mathrm{ExpErf}\left[B,t_0,t_2,\tau_2\right]-\mathrm{ExpErf}\left[B,t_0,t_1,\tau_2\right]\right)\cdots \\ & + A_3(\omega_3)\left(\mathrm{ExpErf}\left[B,t_0,t_3,\tau_2\right]-\mathrm{ExpErf}\left[B,t_0,t_2,\tau_2\right]\right)\cdots \\ & + A_4(\omega_3)\left(\mathrm{ExpErf}\left[B,t_0,t_4,\tau_2\right]-\mathrm{ExpErf}\left[B,t_0,t_2,\tau_2\right]\right), \end{aligned} \tag{6A.1}$$

$$\begin{aligned} f_{1b}(\tau_2;\omega_3) = {} & A_1(\omega_3)\mathrm{ExpErf}\left[B,t_0,t_1,\tau_2\right]\cdots \\ & + A_2(\omega_3)\mathrm{ExpErf}\left[B,t_0,t_2,\tau_2\right]\cdots \\ & + A_3(\omega_3)\left(\mathrm{ExpErf}\left[B,t_0,t_3,\tau_2\right]-\mathrm{ExpErf}\left[B,t_0,t_2,\tau_2\right]\right)\cdots \\ & + A_4(\omega_3)\left(\mathrm{ExpErf}\left[B,t_0,t_4,\tau_2\right]-\mathrm{ExpErf}\left[B,t_0,t_2,\tau_2\right]\right), \end{aligned} \tag{6A.2}$$

where

$$\begin{aligned} \mathrm{ExpErf}\left[B,t_0,t_\mathrm{i},\tau_2\right] \equiv \exp & \left[\left(\frac{B}{4\sqrt{\ln(2)}\cdot t_\mathrm{i}}\right)^2-\frac{\tau_2-t_0}{t_\mathrm{i}}\right]\cdots \\ & \times\frac{1}{2}\left(\mathrm{erf}\left[\frac{\tau_2-t_0}{B}\cdot 2\sqrt{\ln(2)}-\frac{B}{4\sqrt{\ln(2)}\cdot t_\mathrm{i}}\right]+1\right). \end{aligned} \tag{6A.3}$$

Here, erf is an error function. Note that Eq. 6A.3 is the result of the convolution of an exponential decay with a Gaussian to account for the instrument response function (IRF). In the above equations, A_i is the IR-frequency dependent amplitude of the i^{th} exponential decay, B is the full-width at half-maximum (fwhm) of the Gaussian IRF ($B = \Delta t_{\mathrm{IRF}} = 114$ fs), t_0 is time zero ($t_0 = 0$), and τ_i ($= 1/k_\mathrm{i}$) is the time-constant of the i^{th} exponential decay.

The amplitude terms $A_\mathrm{i}(\omega_3)$ are fit locally whereas the time constants were fit globally. Thus, four time constants (t_{1-4}) are obtained from the global fit. We note that t_4 corresponds to the vibrational relaxation time constant commonly written as T_1. Complete fittings results are given in Table 6A.1.

Table 6A.1: Fitting parameters for the fits shown in Figure 6.2 following the labeling in the schemes. Error bars are reported at the 95% confidence level.

Parameter	$\tau_{\text{vis}} = 120$ fs	$\tau_{\text{vis}} = 300$ fs	$\tau_{\text{vis}} = 500$ fs	$\tau_{\text{vis}} = 700$ fs	$\tau_{\text{vis}} = 5$ ps
t_1[1]	0.25 ± 0.02	0.18 ± 0.03	0.19 ± 0.02	0.17 ± 0.04	0.2 ± 0.1
t_2	0.38 ± 0.08	0.42 ± 0.06	0.68 ± 0.07	0.69 ± 0.09	0.5 ± 0.2
t_3	1.2 ± 0.1	1.3 ± 0.1	1.38 ± 0.08	1.3 ± 0.1	0.9 ± 0.2
t_4	17 ± 3	17 ± 4	13 ± 2	15 ± 5	16 ± 6
$A_1(n_{\text{bridge}} > 6)$[2]	-0.8 ± 0.3	-0.8 ± 0.4	-0.6 ± 0.3	-0.5 ± 0.3	–
A_2	–	–	–	–	–
A_3	–	–	-0.3 ± 0.2	-0.5 ± 0.3	–
A_4	–	–	–	–	–
$A_1(n_{\text{trans}} = 2-3)$	–	–	0.3 ± 0.1	–	–
A_2	0.6 ± 0.4	0.6 ± 0.3	0.31 ± 0.06	0.5 ± 0.2	–
A_3	–	–	0.2 ± 0.1	–	–
A_4	0.20 ± 0.03	0.18 ± 0.03	0.14 ± 0.02	0.13 ± 0.05	0.08 ± 0.07
$A_1(n = 0)$	-0.4 ± 0.2	-0.4 ± 0.2	-0.4 ± 0.2	-0.3 ± 0.2	–
A_2	–	-0.3 ± 0.1	-0.19 ± 0.08	-0.26 ± 0.09	–
A_3	-0.2 ± 0.1	-0.16 ± 0.08	-0.3 ± 0.1	-0.3 ± 0.2	-0.4 ± 0.3
A_4	-0.12 ± 0.02	-0.13 ± 0.02	-0.12 ± 0.02	-0.15 ± 0.03	-0.16 ± 0.06
$A_1(n_{\text{bridge}} = 1)$	–	–	–	–	–
A_2	–	–	–	–	–
A_3	0.5 ± 0.3	0.5 ± 0.2	0.5 ± 0.2	0.4 ± 0.2	–
A_4	0.30 ± 0.05	0.22 ± 0.03	0.16 ± 0.04	0.16 ± 0.03	0.26 ± 0.04

[1] Time constants in ps. The first two time traces (left of vertical double bar) were fit with scheme 1a, whereas scheme 1b was used to fit the traces to the right of the double bar. [2] Amplitudes normalized such that $\sum_i |A_i(\tau_{\text{vis}}, \omega_3)| = 1$. Dashes (−) indicate a statistically insignificant contribution to the fit. In some cases (e.g., $n_{\text{bridge}} > 6$, $\tau_{\text{vis}} = 5000$ fs), the fit is within the noise of the data implying that within the 95% confidence interval the signal is zero.

REFERENCES

[1] Wu, Y.; Cohran, C.; Bocarsly, A. *Inorg. Chim. Acta* **1994**, *226*, 251–258.

[2] Lynch, M. S.; Slenkamp, K. M.; Cheng, M.; Khalil, M. *J. Phys. Chem. A* **2012**, *116*, 7023–7032.

[3] Demirdöven, N.; Khalil, M.; Golonzka, O.; Tokmakoff, A. *Opt. Lett.* **2002**, *27*, 433–435.

[4] Lynch, M. S.; Van Kuiken, B. E.; Daifuku, S. L.; Khalil, M. *J. Phys. Chem. Lett.* **2011**, *2*, 2252–2257.

Chapter 7

DEVELOPMENT OF FIFTH-ORDER FEMTOSECOND COHERENT INFRARED–RAMAN SPECTROSCOPY

7.1 Coupling IR and Raman Degrees of Freedom

Much like 2D IR spectroscopy, femtosecond stimulated Raman spectroscopy (FSRS) has seen remarkable growth over the past 10 years. FSRS was pioneered by the Mathies group in the mid 2000s.[1–3] Traditionally, FSRS is a tool used to measure time-evolving Raman spectra of electronically excited molecules created by an actinic pump in the UV/vis region of the spectrum. Using this approach, groups have studied many exciting problems such as molecular imaging, electron transfer dynamics, relaxation kinetics of Rhodopsin, and proton transfer dynamics in the green fluorescent protein (GFP).[4–15] FSRS is an unbelievably powerful tool given the simultaneous high time (<100 fs) and spectral (<10 cm^{-1}) resolution. This allows the user to extract detailed molecular information as a photochemical reaction is taking place. However, it is also desirable to obtain detailed molecular information about the ground electronic state by changing the nature of the actinic pump pulse.

The McCamant group has recently tried to add a second dimension to FSRS, where the actinic pulse is very short in time such that it can impulsively excite low-frequency Raman modes within the bandwidth of the actinic pump.[16,17] The effect of the impulsively driven Raman modes on high-frequency Raman modes is then determined with a stimulated Raman probe. In principle, this methodology enables the measurement of anharmonic couplings between low- and high-frequency vibrational modes. They chose acetonitrile as a model system, where the δ_{CCN} and and ν_{CC} modes at 379 and 920 cm^{-1} were impulsively excited with a 15 fs visible pulse and the ν_{CC}, ν_{CN} (2250 cm^{-1}), and ν_{CH} (2942 cm^{-1}) modes were probed with a 2000/20 fs Raman pump/probe combination. Unfortunately, the three-beam method was not able to uniquely select the desired fifth-oder signals of interest. Instead, the observed signals were due to cascading third-order Raman signals.

Non-coherent variations of this "IR−Raman" experiment have been performed by Dlott and coworkers, where they monitored the amplitude of anti-Stokes Raman features upon irradiation with a tunable mid-IR pulse.[18–28] In that work, specific vibrational modes in polyatomic liquids such as nitromethane or acetonitrile were excited with a spectrally narrow ($\sim$20 cm^{-1}) pulse with a time duration of $\sim$800 fs. The Raman spectrum of the vibrationally-excited molecule was then collected with a "traditional" Raman setup in the backscattering geometry. They exited the ν_{CH} mode at 3000 cm^{-1} and observed a 5 ps decay in the excess vibrational energy. They state that almost none of the energy transfers into the ν_{CN} mode; rather, about 50% of the energy goes into the δ_{CH} and the remainder goes into "doorway vibrations" consisting of highly excited low-frequency modes including the δ_{CCN} mode. Our group is currently developing a technique that combines ultrafast IR

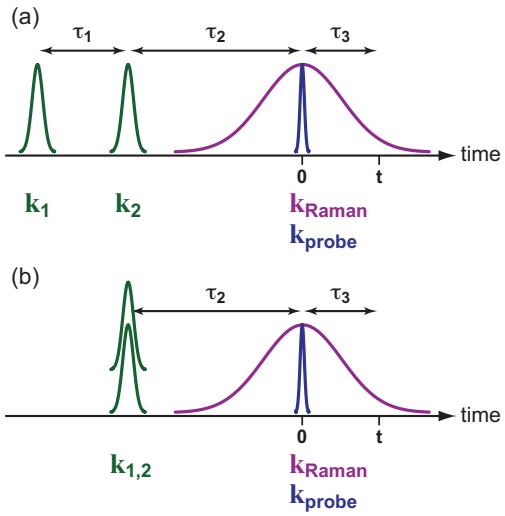

Figure 7.1: Pulse sequence for (a) 2D IR−FSRS and (b) IR−FSRS pump−probe spectroscopy. IR pulses in (a) are collinear.

spectroscopy with the FSRS technique in order to avoid signal cascades. It is essentially a "coherent version" of the experiments performed by Dlott and coworkers. The pulse sequences for 2D IR−FSRS and IR−FSRS pump−probe spectroscopies are presented in Figures 7.1a and 7.1b, respectively. Here, a resonant IR field directly populates a high-frequency IR-active mode and stimulated Raman spectra are collected as a function of the

vibrational population time τ_2.

For 2D IR−FSRS, two collinear IR pulses separated by the coherence time τ_1 are directed into the sample and τ_1 is scanned for fixed values of τ_2 just as in 2D IR spectroscopy. The very unique aspect of this technique is the ability to measure cross terms between an molecular dipole moment and a polarizability. When an IR mode is excited, how is the polarizability of the molecule changed? For example, consider a heme-containing protein with a marker CO ligand on the heme. If the ν_{CO} mode was excited, how would the porphyrin ring react? Additionally, how would the the low-frequency skeletal motions of the protein, which are highly interacting with the porphyrin ring, react to the IR excitation? Answers to these questions will greatly increase the existing knowledge of the relationship between structure, dynamics, and function. The goal of this project is to develop a spectroscopy that can probe inter- and intramolecular couplings across a large frequency window to further understand the role of coupled vibrations in charge transfer chemistry.

7.1.1 Model system candidates

Perhaps one of the most underrated aspects of spectroscopic method development is what model system(s) to start with. The chosen model compound needs to be (i) scientifically interesting, (ii) readily available to minimize synthesis/purification time, and (iii) highly soluble in common solvents. In addition, the molecule must have strong optical, infrared, and Raman absorptions in the spectral region of interest and be sufficiently "simple" so that preliminary data analysis and modeling is not overly complicated. Overlapping resonances complicate the issue and are therefore not desirable. For this chapter, consider the "available" regions of the spectrum to be from 385 to 405 nm in the UV/vis and 1900 to 2350 cm^{-1} (4.3−5.3 μm) in the IR.

Another thing to consider for techniques involving Raman scattering is that there are two approaches to Raman signals: resonant or non-resonant Raman spectroscopy. It is generally true that resonant Raman (RR) signals are significantly larger than non-resonant Raman signals. Within the RR group, one can be on-resonance, pre-resonance, or post-resonance. Each of these conditions can, and will, lead to different Raman spectra and are

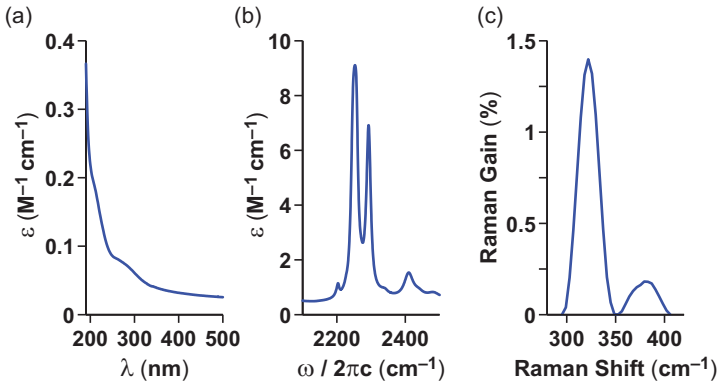

Figure 7.2: Ground state spectra for neat CH_3CN. (a) The UV/vis spectrum shows no resonant peaks between 200 to 500 nm. (b) The FTIR spectrum in the ν_{CN} region contains the ν_{CN} mode at 2253 cm^{-1} and the $\delta_{CH_3} + \nu_{CC}$ Fermi resonance at 2293 cm^{-1}. (c) The stimulated Raman spectrum is dominated by the CaF_2 window response ($\nu_{CaF} = 322$ cm^{-1}); however, a small peak corresponding to $\delta_{CCN} = 379$ cm^{-1} is present.

therefore important to consider.

The advantage of non-resonant systems is that the concentration of the scattering species is very high. Neat liquids are a perfect example, as they represent a very high concentration species. Neat liquids are also useful model systems since the resulting signal is anisotropic, which allows the spectroscopist to use polarization to enhance signals. An example of a neat liquid that would work well with the constraints of this chapter is acetonitrile (ACN, $H_3C{-}C{\equiv}N$) since it (i) does not absorb between 385−415 nm, (ii) has a ν_{CN} mode at 2253 cm^{-1}, and (iii) has a low-frequency Raman mode corresponding to $\delta_{CCN} = 379$ cm^{-1}. Ground state spectra of ACN demonstrating each of these facts are presented in Figure 7.2. In addition to the UV/vis (7.2a) and FTIR (7.2b) spectra, the low-frequency Raman gain spectrum collected in this work is given in Figure 7.2c. Note that the large peak at 322 cm^{-1} is from the two 1 mm CaF_2 windows holding ACN in the sample cell.

Systems that should lead to large Raman signals fall under the RR category. There are many good candidates for this work including sodium nitroprusside (Chapter 2), ferricyanide, metal−porphyrins, and solar cell dyes such as $Ru(dcbpy)_2(NCS)_2$ [RuN3, where dcbpy = cis-bis-(4,4-dicarboxy-2,2-bipyridine)]. Figure 7.3 shows the somewhat familiar ground state spectra of SNP in methanol. New, however, is the addition of the Raman gain

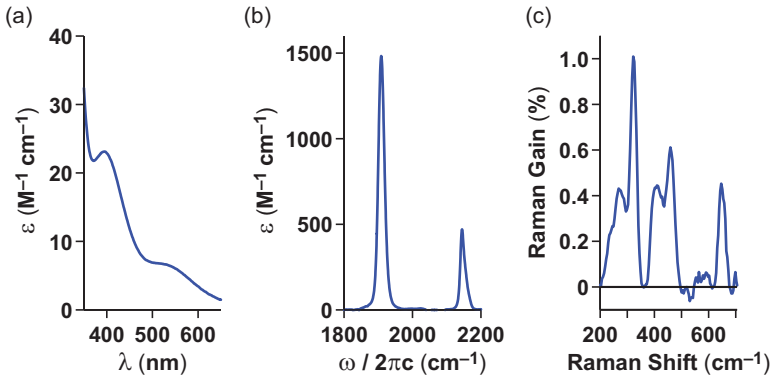

Figure 7.3: Ground state spectra for SNP in methanol. (a) The UV/vis spectrum shows a weak resonant electronic absorption at $\lambda_{max} = 394$ nm. (b) The two peaks in the FTIR spectrum correspond to $\nu_{NO} = 1909$ cm^{-1} and $\nu_{CN} = 2145$ cm^{-1}. (c) The stimulated Raman spectrum also contains window response, though ν_{FeC} and ν_{FeN} modes are present at approximately 450 and 650 cm^{-1}, respectively.

spectrum in 7.3c that shows the presence of low-frequency Raman modes including ν_{FeC} and ν_{FeN} modes.

It goes without saying that once the method has been characterized and established, more complicated systems can and should be explored. This might include systems such as proteins, nucleic acids, and functional enzymes.

7.2 Experimental Apparatus

7.2.1 The optical table

The pulse sequence in Figure 7.1a illustrates that three different frequencies of radiation are needed for this experiment. In general, this experiment requires (i) two collinear mid-IR pump fields, (ii) a high-energy narrow-band UV/vis Raman pump, and (iii) a low-energy broadband UV/vis Raman probe. The method of generation for each of these processes will be presented separately, at which point the characterization of the pulses will be shown and finally the data collection and analysis will be discussed. The optical layout for IR−Raman experiments is shown in Figure 7.4. The various pathways can be followed in detail below when each of the pulse generation techniques are described in more detail. Additional

parameters such as the EMCCD settings and the electronic triggering arrangement are included in the figure. The EMCCD operates in so-called "cropped mode" which enables collection of entire spectra at the 1 kHz repetition rate of the laser. The 1 kHz trigger from the timing delay generator (TDG) of the laser triggers the IR chopper (Newport, model 3501) that operates on the fourth subharmonic of 1 kHz (250 Hz). This 250 Hz signal then triggers the Raman-pump chopper which runs at the second harmonic of the 250 Hz trigger (500 Hz). These triggers are both directed into a National Instruments (NI) USB 6221 data acquisition (DAQ) board. In addition to those signals, both the 1 kHz trigger of the amplifier and the fire trigger from the EMCCD are sent into the DAQ board to time the LabVIEW program used for data collection. Figure legend: dashed gray boxes represent optics that are purged with clean, cry, CO_2-scrubbed air. Regen. Amp., regenerative amplifier; OPA, optical parametric amplifier; DFG, difference frequency generation; BS, 50/50 beamsplitter; β-BBO, β-barium borate (Type I); T, telescope; P, polarizer (calcite or brewster angle); WP or HWP, $\lambda/2$ plate; QWP, $\lambda/4$ plate; OAP, 90° off-axis parabolic mirror; Mono, monochromator; EMCCD, electronically multiplied charge-coupled device; TDG, timing delay generator.

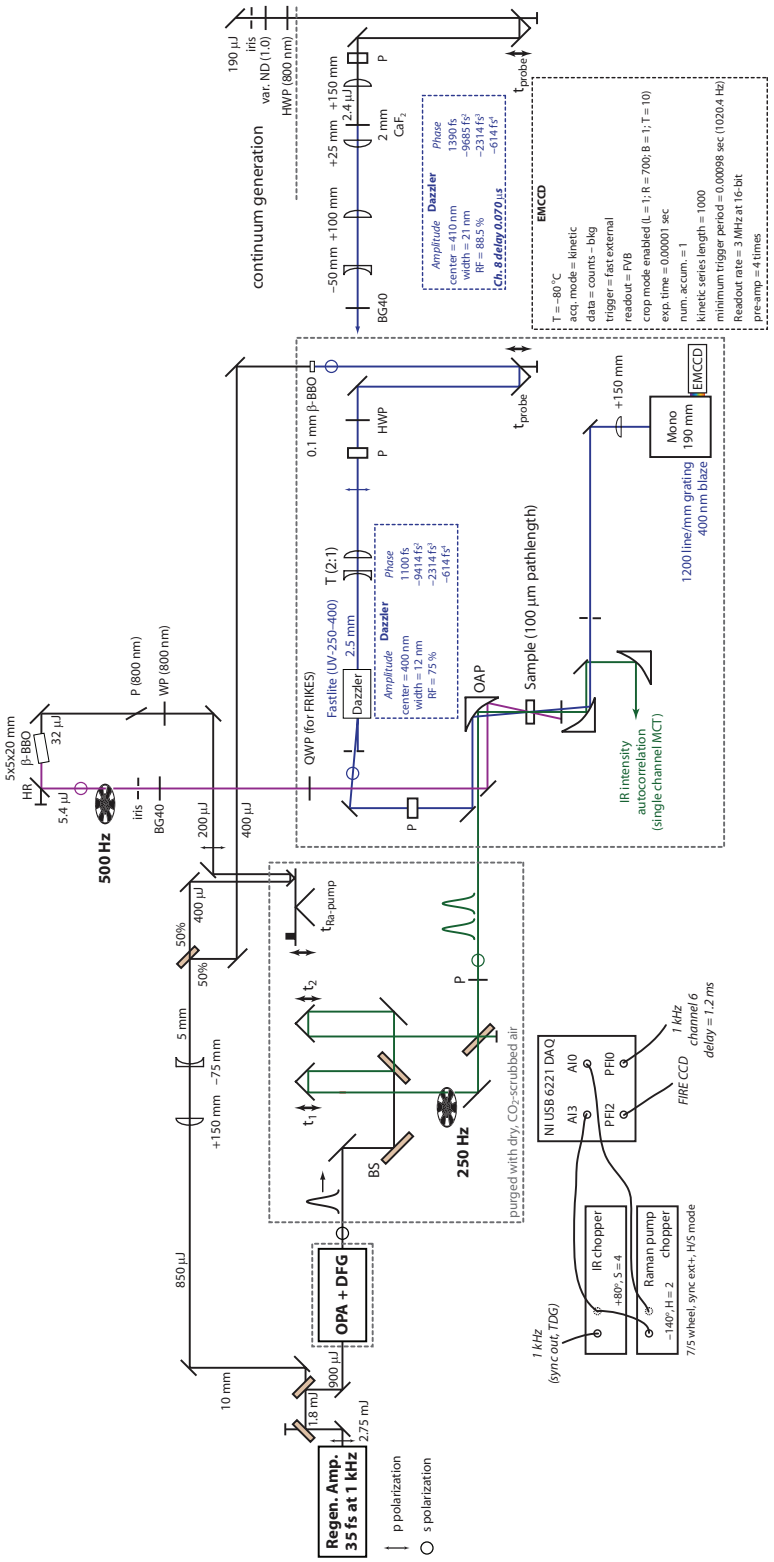

Figure 7.4: The optical layout for IR−Raman. See text for details and legend.

Collinear infrared pulse generation

The generation of the IR fields follows the exact same procedure used in the previous chapters. The difference arises once the mid-IR beam is split, as in this experiment only two duplicate pulses are required. The IR pulses are overlapped on an additional ZnSe beamsplitter in order for them to travel collinear into the sample. The off-axis parabolic (OAP) mirror used to focus all of the beams (IR, Raman pump and probe) is also different than used previously. Here, the OAP is a 1.5-inch protected-aluminum-coated optic with an effective focal length of 6.00 in (Newport, 50331AL). The IR pulse-pair is picked off after the sample in order to monitor the intensity of the beam and allow an interferometric autocorrelation to be collected simultaneously. IR energies at the sample are $\sim$0.5 μJ with a beam diameter of $\phi_{1/e^2} \approx 180$ μm. The IR spectrum was not centered on the ν_{CN} mode of ACN to avoid a large amount of CO_2 absorption; however, there was a significant amount of IR intensity at the ν_{CN} frequency.

Raman pump generation

The ideal Raman pump is a spectrally narrow ($\Delta\omega_{\mathrm{fwhm}} < 15$ cm^{-1}) pulse with a relatively large amount of energy (1$-$5 μJ/pulse). Of course, in the case of a RR experiment, the Raman pump would be centered on an electronic absorption; otherwise, it does not matter what the center frequency of the Raman pump is. There are three ways that people have successfully generated Raman pump pulses.[1,29] The easiest method is to filter the pulse with one or more narrow bandpass filters; however, these are hard to find in the UV, have a low damage threshold, are not very tunable, and do not achieve a very narrow Raman pump pulse. The more common approach is to use a spectral filter comprised of what is essentially a grating stretcher. Here, a broadband pulse is dispersed with a grating, collimated, a subsequently filtered with a narrow slit to select one frequency component or color. Once selected, the pulse is reconstructed by focusing the pulse onto a matched grating where angular dispersion and spatial chirp are corrected. This arrangement is also known as a zero-dispersion $4f$ pulse shaper and is used in many laboratories using pulse shapers. Tunability is achieved by moving the slit horizontally to change which color is

selected between the two gratings. McCamant et al. reported a 2.1 ps pulse from a 0.16 mm slit and a 8.7 ps pulse from a 0.02 mm slit for an input $\lambda = 780{-}820$ nm.

The less common approach is to use a long ($\sim$20 mm) β-BBO crystal to frequency double a broad 800 nm pulse. In this manner, phase matching is minimized and only a spectrally narrow portion of the 800 nm field can be doubled such that a very narrow pulse near $\lambda = 400$ nm is produced. The fwhm of the second harmonic (SH) pulse is be related to the group-delay mismatch between the fundamental frequency (FF) and the SH by $\Delta\nu_{\mathrm{SH}} = 0.886/\mathrm{GDM}$, where $\mathrm{GDM} = \delta L$ is the group delay mismatch with L representing the crystal length and $\delta = 1/\upsilon_{\mathrm{g,FF}} - 1/\upsilon_{\mathrm{g,SH}}$ is the group velocity (υ_{g}) mismatch between the FF and the SH.[29] Tunability is achieved by tuning the orthogonal angles of the crystal. Following the work of Pontecorvo et al., a $5 \times 5 \times 20$ mm β-BBO crystal (Type I, $\theta = 31.3°$, $\phi = 90°$, MgF_2-coated) was purchased from Altos Photonics for the $\lambda_{\mathrm{SH}} = 320{-}400$ nm range.[29] The input energy of the FF does change the output. It is generally best to keep $E_{\mathrm{FF}} < 50$ μJ/pulse. It is also important to keep the beam waist (w) small to avoid spatial walk-off ($w = 1 - 3$ mm); however, in practice it is a trade-off between w and the fluence (energy/area) of the beam. Unwanted generation processes occur at high fluence.

Raman probe generation

Traditionally the Raman probe is generated by continuum generation in a relatively thick ($l = 1{-}3$ mm) CaF_2 or sapphire window. A spectrally broad probe is desired so that many Raman peaks can be observed simultaneous over a large Raman shift range; however, one does not *have* to generate a continuum probe since frequency doubling a pulse with $\lambda_{\mathrm{FF}} = 800$ nm and $\Delta\lambda_{\mathrm{FF}} = 30$ nm in a 0.1 mm thick β-BBO crystal produces a field with $\lambda_{\mathrm{SH}} = 400$ nm and $\Delta\lambda_{\mathrm{SH}} = 8$ nm $= 500$ cm^{-1}. In this case, simply tuning the Raman probe according to the center of the Raman pump spectrum can afford a Raman spectrum ranging over $300{-}500$ cm^{-1} depending on the stability of the probe. This method is presented in Figure 7.4 inside the large gray box near the top of the page.

We also generated a continuum probe with two different methods for comparison. The first was achieved directly in the UV by focusing $\sim$1 μJ of $\lambda_{\mathrm{SH}} = 400$ nm light onto a

2 mm CaF_2 plate. The CaF_2 window was translated horizontally using an electronically controlled actuator to avoid photodamage. The resulting "white light" was collimated with a $f = 25$ mm lens and directed towards the UV-Dazzler^{TM} for amplitude shaping and temporal compression. An alternative way we generated a continuum in the UV was by focusing $\sim$2.4 μJ of $\lambda = 800$ nm light onto the same 2 mm CaF_2 window as shown on the very top of the layout in Figure 7.4. Collimation was achieved with a short focal length lens at which point the white-light was reduced in size by a factor of 2 because the Dazzler requires the input beam to be less than 3 mm in diameter. The probe was spectrally filtered with a BG40 filter before going through the Dazzler. The Dazzler itself acts as a spectral filter since it has a spectral range of 250$-$420 nm. Shaping was optimized by changing the collimation of the beam (slightly) using the $f = -50$ mm lens immediately before the Dazzler. The collimation of the beam significantly changes the minimum spectral width obtainable with the Dazzler, which has a shaping resolution of $\sim$0.2 nm. Prior to optimization, the output pulse could have a width of 1.0 nm or greater (amplitude settings: center = 400 nm, width = 0.3 nm, RF $< 10\%$). Shaping efficiency is also optimized by moving the Dazzler along the two axes orthogonal to the optical axis to optimize overlap of the optical beam with the RF pulse in the Dazzler crystal. The Dazzler is calibrated spectrally by rotating the Dazzler in the plane parallel to the optical table. The Dazzler settings are fairly straightforward to understand, as the input parameters are all in the frequency domain. Thus, the user can set the center frequency, the width of the pulse (according the a super Gaussian pulse shape), the relative RF power (0$-$100%), and the spectral phase parameters. The spectral phase parameters are group delay ($\partial\phi/\partial\omega$, fs), group delay dispersion ($\partial^2\phi/\partial\omega^2$, fs^2), third-order dispersion ($\partial^3\phi/\partial\omega^3$, fs^3), and fourth-order dispersion ($\partial^4\phi/\partial\omega^4$, fs^4). For our preliminary results, we used the "simple" β-BBO generation method was used to generate a relatively narrow Raman probe. This was chosen since the initial interest was in a few Raman modes in the low-frequency of the spectrum and therefore a very broad probe spectrum was not needed. Also, it was believed that avoiding the translating window would improve the stability of the probe, which is a very important parameter in FSRS.

IR−FSRS pulse characterization

Spectral and temporal pulse characterization is presented in Figure 7.5. The IR pump spectrum was collected on the HgCdTe array detector used in previous IR experiments, the Raman pump spectrum was measured with an Ocean Optics HR2000 compact spectrometer equipped with a 1200 line/mm grating, and the Raman probe spectrum was collected with an Electron Multiplication Charge-Coupled Device (EMCCD) array detector that will be described in the following section.

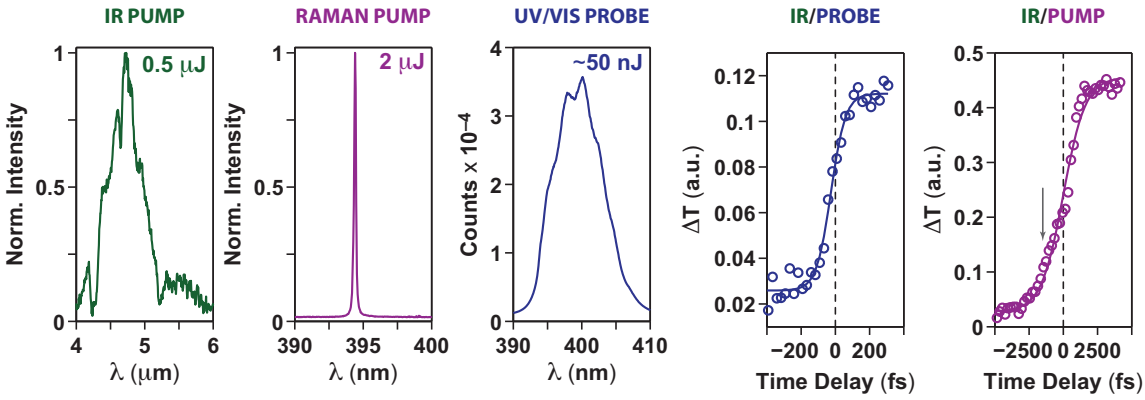

Figure 7.5: Pulse charactization in frequency (a−c) and time (d−e). (a) The IR pump spectrum with SNP in methanol for calibration: $\Delta\omega_{\text{fwhm}} \approx 300$ cm^{-1}, $\phi_{1/e^2} \approx 270$ μm. (b) The Raman pump spectrum: $\Delta\omega_{\text{fwhm}} \approx 12$ cm^{-1}, $\phi_{1/e^2} \approx 100$ μm. (c) The UV/vis probe spectrum: $\Delta\omega_{\text{fwhm}} \approx 550$ cm^{-1}, $\phi_{1/e^2} \approx 70$ μm. (d) IR/probe cross correlation in Si fit to a sigmoidal function: $\Delta t_{\text{cross}} = 130 \pm 30$ fs. (d) IR/pump cross correlation in Si fit to a sigmoidal function: $\Delta t_{\text{cross}} = 2.5 \pm 0.3$ ps. This time delay was fixed at -1 ps (grey arrow) for maximum Raman signal.

One advantage of having an IR pump is the ability to measure temporal cross-correlations between the IR pump and the Raman pump/probe. Cross-correlations were achieved in a polished 250 μm silicon wafer whereby the transmission of IR through the Si wafer is changed by the optical pulse. This results in a sigmoidal function as shown in Figure 7.5, where it is shown that the IR/probe correlation is ∼130 fs and the IR/pump correlation is ∼2.5 ps. In theory, the FSRS signal is maximized when the Raman probe precedes the Raman pump by approximately half of the Raman pump duration, which would be around 1 ps in this

experiment as shown by the grey arrow in the IR/pump cross correlation.

7.2.2 Detection, data collection, and analysis

Two data collection strategies exist for FSRS: (i) the "slow" method uses a dual photodiode array (DPDA) to collect signal and reference spectra and an electronic shutter to control the actinic pump to be on or off, (ii) the "fast" method uses a CCD to collect spectra at 1000 Hz and chops the actinic pump at 500 Hz to create subsequent "pump-on" and "pump-off" spectra collected in 2 ms. In case (i) the Raman gain is calculated by[1]

$$\text{Raman gain} = \frac{[(\text{probe} - \text{bkg})/(\text{ref} - \text{bkg})]_{\text{Raman pump on}}}{[(\text{probe} - \text{bkg})/(\text{ref} - \text{bkg})]_{\text{Raman pump off}}} \tag{7.1}$$

where "bkg" is the background DPDA response with all beams blocked and "ref" is the reference beam that does not hit the sample. Note that division is used so that the signal intensity does not depend on the probe intensity, as that will vary from day to day and experiment to experiment.

The more recent method (ii) relies on a fast CCD array detector that can detect high S/N, unsaturated single shot spectra at the common 1 kHz repetition rate of many commercial Ti:Sapphire lasers.[3] In order to collect photoelectrons generated when light is incident on the array, the total area of the CCD has to be cropped so that just a small area of the array is collected. This so-called "crop mode" greatly increases data collection time.

The EMCCD used in this chapter is model DU970P-UV made by Andor Technology. This camera contains a front-illuminated CCD with a UV coating affording a quantum efficiency of $10-50\%$ over $\lambda = 200-1000$ nm. The electron multiplication (EM) technology developed by Andor enables charge *from each pixel* to be multiplied on the sensor before it is read out, which provides single-photon sensitivity (not needed here in FSRS) with up to a 3 MHz readout rate. The array contains 1600×200 pixels that are 16×16 μm and cooled thermoelectrically down to -80 °C (193 K) to minimize dark current. No spacing between the pixels means that the total image area is 25.6×3.2 mm. Conveniently, the camera has dual output amplifiers making it so that one can use either "conventional mode"

or "electron multiplying mode" depending on the signal being measured. Common cropped areas used in this chapter are 400×20 pixels, which is more than enough area to collect the entire probe spectrum used here.

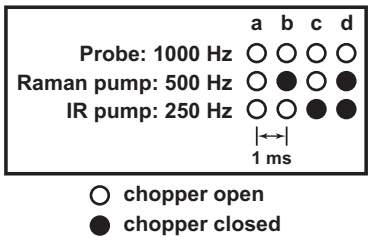

Figure 7.6: Double chopping scheme for IR−Raman spectroscopy. This method writes four signals ($S_{\mathrm{a-d}}$) in 4 ms (i.e., over 4 laser shots). Here, ∘ means chopper open (light hitting the sample) and • means chopper closed (beam blocked).

Collection of the probe spectrum at 1 kHz allows synched choppers to be placed in the IR pump and Raman pump arms to generate four unique signals in a total time of 4 ms in a similar manner as Chapter 5. This chopping sequence is illustrated in Figure 7.6. There are two approaches to generating ground- (GS) and IR-FSRS signals: subtraction or division. The subtraction technique given in Equation 7.2 generates four signals corresponding to IR−FSRS (S_{fifth}), IR−vis pump−probe (S_{third}), GS FSRS (S_{Raman}), and the probe spectrum (S_{probe}). As in Chapter 5, the ability to measure ground- and excited-state dynamics simultaneously is a real strength of this method since differences in the response can be very small. All signals are collected at the same time using custom LabVIEW$^{\mathrm{TM}}$ software.

$$\begin{aligned} S_{\mathrm{fifth}} &= S_{\mathrm{a}} - S_{\mathrm{b}} - S_{\mathrm{c}} + S_{\mathrm{d}} \\ S_{\mathrm{third}} &= S_{\mathrm{b}} - S_{\mathrm{d}} \\ S_{\mathrm{Raman}} &= S_{\mathrm{c}} - S_{\mathrm{d}} \\ S_{\mathrm{probe}} &= S_{\mathrm{d}}. \end{aligned} \tag{7.2}$$

In order to ensure that the Raman signals are normalized to daily probe fluctuations, one could also calculate Raman gain signals by

$$\begin{aligned} (\text{Raman Gain})_{\text{GS}} &= \frac{S_{\text{c}}}{S_{\text{d}}} \\ (\text{Raman Gain})_{\text{ES}} &= \frac{S_{\text{c}}}{S_{\text{d}}} - \frac{S_{\text{a}}}{S_{\text{b}}}. \end{aligned} \tag{7.3}$$

Results in this chapter will follow the collection strategy presented in Equation 7.2.

7.2.3 Femtosecond Raman-induced Kerr effect spectroscopy

Femtosecond Raman-induced Kerr effect spectroscopy or FRIKES was introduced by the Mathies group in 2008.[30] FRIKES is a variant of FSRS that uses a circularly polarized Raman pump pulse to avoid the need (in theory) of a Raman pump modulator (such as a shutter or a chopper). The Raman pump is converted from linear to circular polarization with a quarter-wave plate (QWP, $\lambda/4$) and the probe is left to be linearly polarized in the s direction ($\perp$ to table top). After the sample, the Raman probe is passed through an analyzer set in the p direction ($\parallel$ to table top). In this manner, with the Raman pump blocked there is zero signal on the array detector (the measurement is background free). When the Raman pump is on, induced anisotropic changes in the index of refraction of the sample rotate the polarization of the probe beam relative to the original s direction, which allows transmission of the signal through the analyzer. Note that this Raman-induced Kerr effect only occurs with the difference between $\lambda_{\text{Ra-pump}}$ and $\lambda_{\text{Ra-probe}}$ approach a Raman resonance in the system. The only signals that make it through the analyzer are therefore the Raman modes of interest so that a background free Raman spectrum is displayed on the EMCCD. The caveat, as eluded to earlier in this paragraph, is that the polarizability of the Raman mode has to be anisotropic. This is the case for neat liquids such as ACN.

7.3 Preliminary Results

The natural first goal of any Raman technique is to measure high quality Raman spectra of ground state species in solution. This allows the operator to determine optimal probe levels, Raman pump energies, Raman pump/probe time delay, and EMCCD settings. An example of the Raman spectrum of neat ACN is shown in Figure 7.7. Figure 7.7 demonstrates

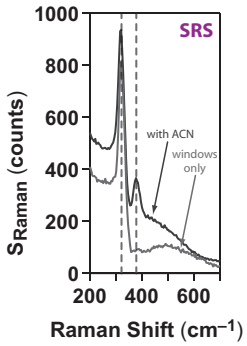

Figure 7.7: The stimulated Raman response (S_{Raman}) from neat ACN shown with and without ACN for comparison. Vertical dashed lines are at 322 and 379 cm^{-1}.

an early lesson learned, as the CaF_2 sample cell windows give a relatively large Raman response corresponding to $\nu_{\text{CaF}} = 322$ cm^{-1}. This is not a problem for Raman features greater than 350 cm^{-1}; however, it is important to not optimize laboratory parameters, such as the position of the sample cell, on the ν_{CaF} signal. The ACN peak corresponding to the low-frequency bend $\delta_{\text{CCN}} = 379$ cm^{-1} is clear, though quite a bit smaller than the CaF_2 resonance. Figure 7.8 shows the $S_{\text{third}}(\lambda_{\text{Ra-probe}}, \tau_2)$ and $S_{\text{fifth}}(\tilde{\nu}_{\text{Raman}}, \tau_2)$ responses in the FRIKES polarization geometry both with and without ACN between the sample cell windows, where the Raman shift is defined as $\tilde{\nu}_{\text{Raman}} = 10^7 \cdot (1/\lambda_{\text{Ra-pump}} - 1/\lambda_{\text{Ra-probe}})$ with $\tilde{\nu}_{\text{Raman}}$ in [cm^{-1}] and λ in [nm]. Figures 7.8a and 7.8b show the effect of IR excitation on the probe spectrum with and without ACN in the sample cell, respectively. Comparison of the signal with the probe spectrum in Figure 7.5 on page 173 shows that the IR excitation influences the entire spectrum as expected for the non-resonant response. Additionally, the signal in the ACN case appears to be absorptive (same signal phase) whereas in the case of the window response it is slightly dispersive (the phase changes along τ_2). Interestingly, the broad bandwidth of the IR pump pulse is able to coherently excite low-frequency modes in the molecule that can then be probed by the UV/vis pulse. This is seen quite clearly in Figure 7.8b, where the signal comes "in and out of the page" along τ_2 with a temporal period of 104 fs. This beat frequency corresponds to coherent excitation of the ν_{CaF} mode at 322 cm^{-1}. Though it's difficult to see in Figure 7.8a, the beat frequency does change

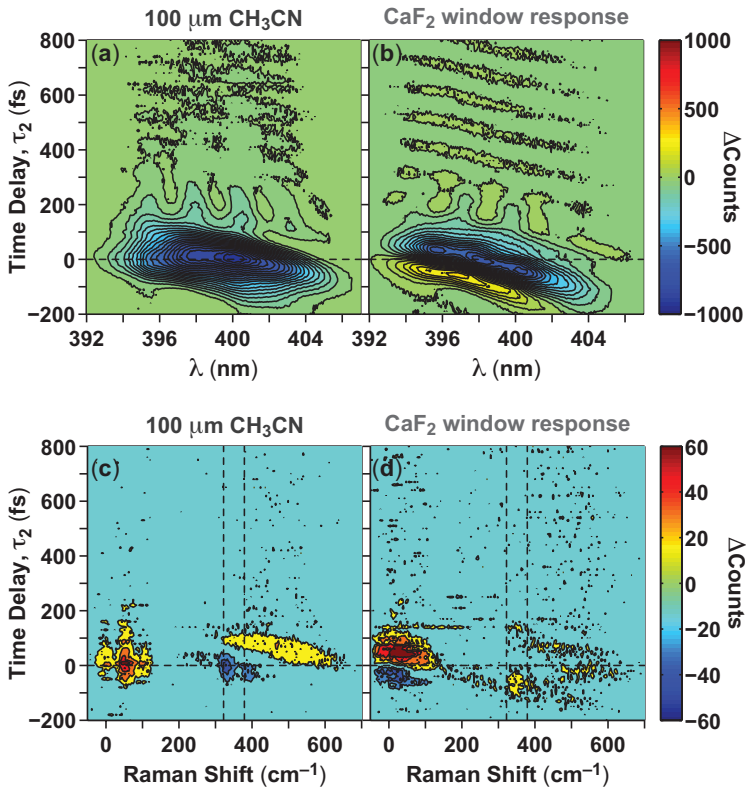

Figure 7.8: IR−vis (a−b) and IR−Raman (c−d) results. The z-axis (ΔCounts) is an absolute scale, where the maximum of the probe was ∼35000 counts (see Figure 7.5c), which gives the reader an idea of the signal levels observed here. Response with (a and c) and without (b and d) ACN are shown for comparison.

with the addition of ACN. The IR−FSRS response with and without ACN is compared in Figures 7.8c and 7.8d. Lines at $\tilde{\nu}_{\text{Raman}} = 322$ and 379 cm^{-1} are drawn on these figures to emphasize that bleaching of those features at $\tau_2 = 0$ is not present without ACN. A broad transient absorption also appears between $\tilde{\nu}_{\text{Raman}} = 300{-}600$ cm^{-1} and is only present for $\tau_2 = 0{-}200$ fs with ACN is present.

These results show that resonant IR excitation is affecting the low-frequency Raman modes of ACN, though the non-resonant nature of the Raman probe makes it difficult to assign specific transient absorption features. Slices of the IR−vis response are shown in Figure 7.9 in order to clearly see the signal levels and the temporal beats. Slices of the IR−FSRS response are shown in Figure 7.10. The data is clearly noisy, though the two

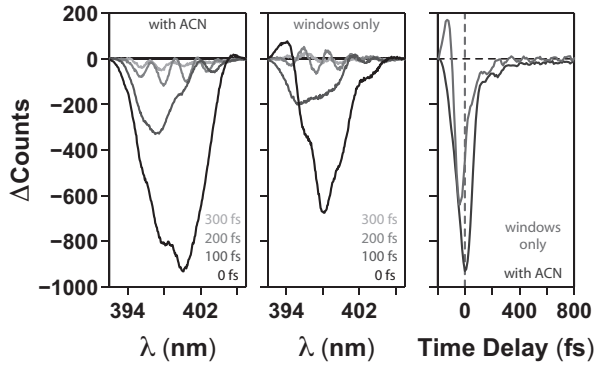

Figure 7.9: A closer look at the IR−vis response via slices along each axis.

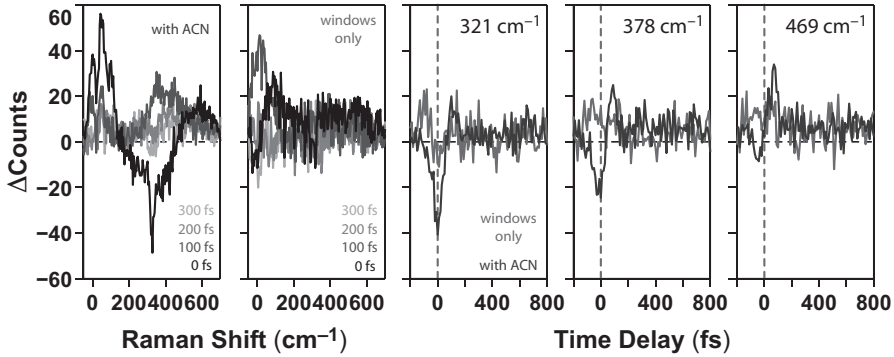

Figure 7.10: A closer look at the IR−Raman response via slices along each axis.

spectral Figures on the left clearly show a difference with and without ACN. The slices along τ_2 for the CaF_2 and ACN bleach features and the transient absorption help with the assignments drawn from the 2D contour plots.

7.4 Discussion and Outlook

The ultimate goal of this experiment is to directly measure cross terms between an IR dipole moment and the polarizability of a Raman mode. How does resonant IR excitation of a high-frequency IR-active mode affect the Raman spectrum of a molecule? Do new Raman features appear? Do line shapes change? Is it possible that an IR coherence affects the electronic coherences started in FSRS? The best way to answer this is with a full 2D

IR−FSRS measurement. The energy levels interrogated with such a technique are drawn

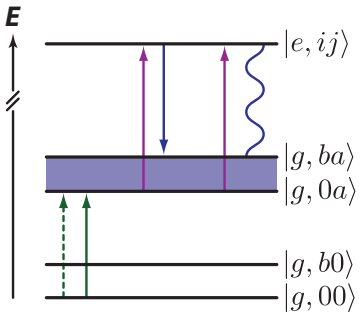

Figure 7.11: Energy-level diagram for coherent 2D IR−FSRS. The desired observable, the Raman shift of the excited-state molecule, is highlighed in purple.

in Figure 7.11. Here, ground (g) and excited (e) electronic states are coupled. First, an IR-active mode (a) is excited with a resonant IR field to generate a vibrational coherence along τ_1. A second IR interaction creates a vibrational population of state a in g, $|g, 0a\rangle$, that evolves along τ_2. Next, assuming the Raman-active mode b is anharmonically coupled to the a mode through some coupling constant X_{ab}, multiple interactions with the pump and probe result in stimulated Raman emission on top of the probe. Scanning τ_1 for fixed τ_2 results in a 2D data matrix $S(\tau_1, \tilde{\nu}_{\text{Raman}}; \tau_2)$. Fourier transformation along τ_1 results in a spectrum defined by $S(\omega_1, \tilde{\nu}_{\text{Raman}}; \tau_2)$.

$$\begin{aligned} E_{\text{signal}} &= E_{\text{e}} - E_{\text{g}} + (E_{\text{a,0}} + E_{\text{b,0}} - X_{\text{ab}}) - E_{\text{a,0}} \\ &= \hbar(\omega_{\text{Ra-pump}} + \omega_{\text{ab}} - \omega_{\text{IR}}) \\ \mathbf{k}^{(5)}_{\text{signal}} &= \pm\mathbf{k}_{\text{IR}} \mp \mathbf{k}_{\text{IR}} \pm \mathbf{k}_{\text{Raman}} \mp \mathbf{k}_{\text{Raman}} + \mathbf{k}_{\text{probe}} \end{aligned} \tag{7.4}$$

Energies associated with 2D IR−Raman spectroscopy are related in Equation 7.4 and a cartoon of what a 2D IR−Raman spectrum might look like is presented in Figure 7.12. In this cartoon, a 2100 cm^{-1} IR-active mode is coupled to 500 cm^{-1} Raman-active mode such that the Raman modes shifts by 50 cm^{-1} when the IR mode is excited. The line shapes of the peaks report on the cross-correlation between the IR- and Raman-active modes, a phenomenon that has not been experimentally observed. This correlation, if present, has many implications towards molecular dynamics in solution and the coordinates making up

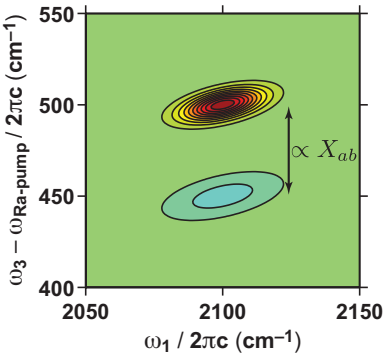

Figure 7.12: A cartoon of an IR−FSRS response. The IR pump frequency is plotted on the x-axis whereas the Raman shift is on the y-axis.

the potential energy surface. The separation of the peaks is related to (or equal to in this case) the coupling constant X_{ab}.

2D IR−FSRS is a very promising technique that has the ability to measure couplings between low- and high-frequency modes that have not been measured to date. We expect these measurements to be especially useful in the biochemistry community, as the impact high-frequency vibrations such as the CO stretch or the amide II vibration on the low-frequency modes of a protein is still not well-known.[31–33] The technique may also be able to help with the highly debated "wavelike energy transfer" through quantum coherence in photosynthetic systems first observed in 2007.[34–37] This effect was also observed in conjugated polymers by Scholes and coworkers.[38–40] Multidimensional IR−FSRS is a tool that can potentially bridge the gap between electronic and vibrational spectroscopies in a way that the coupling between electronic and nuclear degrees of freedom can be measured directly. The technique does not come without challenges, as spectroscopies involving vastly different laser frequencies are difficult due to the mismatch in absorption cross section at the two frequencies. Model systems will play a key role in measuring anharmonic couplings between low- and high-frequency modes.

REFERENCES

[1] McCamant, D. W.; Kukura, P.; Yoon, S.; Mathies, R. A. *Rev. Sci. Instrum.* **2004**, *75*, 4971.

[2] Kukura, P.; McCamant, D. W.; Mathies, R. A. *Annu. Rev. Phys. Chem.* **2007**, *58*, 461–488.

[3] Frontiera, R. R.; Mathies, R. A. *Laser & Photon. Rev.* **2011**, *5*, 102–113.

[4] Kukura, P. *Science* **2005**, *310*, 1006–1009.

[5] McCamant, D. W. *J. Phys. Chem. B* **2011**, *115*, 9299–9305.

[6] Dance, Z. E. X.; Ahrens, M. J.; Vega, A. M.; Ricks, A. B.; McCamant, D. W.; Ratner, M. A.; Wasielewski, M. R. *J. Am. Chem. Soc.* **2008**, *130*, 830–832.

[7] Kukura, P.; McCamant, D. W.; Davis, P. H.; Mathies, R. A. *Chem. Phys. Lett.* **2003**, *382*, 81–86.

[8] McCamant, D. W.; Kukura, P.; Mathies, R. A. *J. Phys. Chem. A* **2003**, *107*, 8208–8214.

[9] Rhinehart, J. M.; Mehlenbacher, R. D.; McCamant, D. *J. Phys. Chem. B* **2010**, *114*, 14646–14656.

[10] Frontiera, R. R.; Fang, C.; Dasgupta, J.; Mathies, R. A. *Phys. Chem. Chem. Phys.* **2012**, *14*, 405–414.

[11] Zhang, D.; Slipchenko, M. N.; Cheng, J.-X. *J. Phys. Chem. Lett.* **2011**, *2*, 1248–1253.

[12] Kovalenko, S. A.; Dobryakov, A. L.; Ernsting, N. P. *Rev. Sci. Instrum.* **2011**, *82*, 063102.

[13] Briand, J.; Léonard, J.; Haacke, S. *J. Opt.* **2010**, *12*, 084004.

[14] Fujisawa, T.; Creelman, M.; Mathies, R. A. *J. Phys. Chem. B* **2012**, *116*, 10453–10460.

[15] Plewicki, M.; Levis, R. *J. Opt. Soc. Am. B* **2008**, *25*, 1714–1719.

[16] Wilson, K. C.; Lyons, B.; Mehlenbacher, R.; Sabatini, R.; McCamant, D. W. *J. Chem. Phys.* **2009**, *131*, 214502.

[17] Mehlenbacher, R. D.; Lyons, B.; Wilson, K. C.; Du, Y.; McCamant, D. W. *J. Chem. Phys.* **2009**, *131*, 244512.

[18] Deak, J.; Iwaki, L.; Dlott, D. *J. Phys. Chem. A* **1998**, *102*, 8193–8201.

[19] Deàk, J. C.; Iwaki, L. K.; Dlott, D. D. *J. Phys. Chem. A* **1999**, *103*, 971–979.

[20] Iwaki, L.; Rhea, S.; Dlott, D. D. *J. Raman Spectrosc.* **2000**, *31*, 263–274.

[21] Iwaki, L. K.; Dlott, D. D. *J. Phys. Chem. A* **2000**, *104*, 9101–9112.

[22] Dlott, D. D. *Chem. Phys.* **2001**, *266*, 149–166.

[23] Iwaki, L.; Deak, J.; Rhea, S.; Dlott, D. *Pract. Spectrosc.* **2001**, *26*, 541–592.

[24] Shigeto, S.; Pang, Y.; Fang, Y.; Dlott, D. D. *J. Phys. Chem. B* **2008**, *112*, 232–241.

[25] Wang, Z.; Pakoulev, A.; Dlott, D. D. *Science* **2002**, *296*, 2201–2203.

[26] Seong, N.-H.; Fang, Y.; Dlott, D. D. *J. Phys. Chem. A* **2009**, *113*, 1445–1452.

[27] Shigeto, S.; Dlott, D. D. *Chem. Phys. Lett.* **2007**, *447*, 134–139.

[28] Wang, Z.; Pang, Y.; Dlott, D. *J. Phys. Chem. A* **2007**, *111*, 3196–3208.

[29] Pontecorvo, E.; Kapetanaki, S. M.; Badioli, M.; Brida, D.; Marangoni, M.; Cerullo, G.; Scopigno, T. *Opt. Expr.* **2011**, *19*, 1107–1112.

[30] Shim, S.; Mathies, R. A. *J. Raman Spectrosc.* **2008**, *39*, 1526–1530.

[31] Rosca, F.; Kumar, A. T. N.; Ionascu, D.; Ye, X.; Demidov, A. A.; Sjodin, T.; Wharton, D.; Barrick, D.; Sligar, S. G.; Yonetani, T.; Champion, P. M. *J. Phys. Chem. A* **2002**, *106*, 3540–3552.

[32] Hoersch, D.; Otto, H.; Cusanovich, M. A.; Heyn, M. P. *Phys. Chem. Chem. Phys.* **2009**, *11*, 5437–5444.

[33] Funkner, S.; Niehues, G.; Schmidt, D. A.; Heyden, M.; Schwaab, G.; Callahan, K. M.; Tobias, D. J.; Havenith, M. *J. Am. Chem. Soc.* **2012**, *134*, 1030–1035.

[34] Engel, G. S.; Calhoun, T. R.; Read, E. L.; Ahn, T. K.; Mančal, T.; Cheng, Y.-C.; Blankenship, R. E.; Fleming, G. R. *Nature* **2007**, *446*, 782–786.

[35] Lee, H.; Cheng, Y.-C.; Fleming, G. R. *Science* **2007**, *316*, 1462–1465.

[36] Scholes, G. D. *J. Phys. Chem. Lett.* **2010**, *1*, 2–8.

[37] Collini, E.; Wong, C. Y.; Wilk, K. E.; Curmi, P. M. G.; Brumer, P.; Scholes, G. D. *Nature* **2010**, *463*, 644–647.

[38] Collini, E.; Scholes, G. D. *Science* **2009**, *323*, 369–373.

[39] Scholes, G. D. *Nature* **2010**, *466*, 1047–1048.

[40] Turner, D. B.; Wilk, K. E.; Curmi, P. M. G.; Scholes, G. D. *J. Phys. Chem. Lett.* **2011**, *2*, 1904–1911.

Appendix A

MATLAB FILES

A.1 Global and target analysis

See section 4.A.3 on page 104 for details of the analysis. The analysis was broken up into three groups of 17 pixels (a, b, and c) leading to a total of 51 kinetic traces fit to the model. The m-file below, named glob_ta_mad2_a1.m, is for magic angle polarization conditions (hence the maa matrix name: magic angle for group a).

```
clear all
tic
global t2 B t0 y1 y2 y3 y4 y5 y6 y7 y8 y9 y10 y11 y12 y13 y14 y15 y16 y17

load t2a
load w3a
load maa

ran1=36:127;

t2=t2a(ran1);
w3=w3a;

y1=maa(1,ran1)';
y2=maa(6,ran1)';
y3=maa(9,ran1)';
y4=maa(12,ran1)';
y5=maa(16,ran1)';
y6=maa(19,ran1)';
```

```
y7=maa(21,ran1)';
y8=maa(24,ran1)';
y9=maa(28,ran1)';
y10=maa(30,ran1)';
y11=maa(37,ran1)';
y12=maa(44,ran1)';
y13=maa(45,ran1)';
y14=maa(46,ran1)';
y15=maa(47,ran1)';
y16=maa(48,ran1)';
y17=maa(49,ran1)';

B=0.094; % ps
t0=0.00;

tau1=0.12;
tau2=0.50;
tau3=1.40;

A1=1.4; % close to pixel 1
A2=0.3;
A3=0.2;
A4=0;
A5=0;

A6=1.5; % close to pixel 6
A7=0.3;
A8=0.2;
A9=0.0;
A10=0;
```

```
A11=1.4; % close to pixel 9
A12=0.2;
A13=0.5;
A14=0.1;
A15=0;

A16=1.5; % close to pixel 12
A17=0.3;
A18=0.7;
A19=0.1;
A20=0;

A21=1.5; % less than pixel 16
A22=0.4;
A23=0.9;
A24=0.2;
A25=0;

A26=2.2; % less than pixel 19
A27=0.8;
A28=1.2;
A29=0.6;
A30=0;

A31=3; % less than pixel 21
A32=1;
A33=2;
A34=1;
A35=0;
```

```
A36=0.9; % close to pixel 24
A37=-1;
A38=1;
A39=-0.2;
A40=-0.2;

A41=-5; % close to pixel 28
A42=-6;
A43=-5;
A44=-2;
A45=-0.1;

A46=-3; % close to pixel 30
A47=-4;
A48=-3;
A49=-1;
A50=-0.08;

A51=0.4; % close to pixel 37
A52=-0.3;
A53=-0.5;
A54=-0.05;
A55=-0.04;

A56=0.6; % close to pixel 44
A57=-0.3;
A58=-0.4;
A59=-0.1;
A60=-0.03;
```

```
A61=0.4; % close to pixel 45
A62=-0.5;
A63=-0.7;
A64=-0.2;
A65=-0.04;

A66=0.3; % close to pixel 46
A67=-0.7;
A68=-1;
A69=-0.3;
A70=-0.03;

A71=0.5; % close to pixel 47
A72=-0.4;
A73=-1;
A74=-0.2;
A75=-0.07;

A76=0.6; % close to pixel 48
A77=-0.2;
A78=-0.8;
A79=-0.1;
A80=-0.04;

A81=0.5; % close to pixel 49
A82=-0.1;
A83=-0.5;
A84=0;
A85=-0.04;
```

```
zerow=zeros(60,1);
zerot=zeros(length(t2),1);

w0=[ A1,tau1, A2,tau2, A3,tau3, A4, A5, A6, A7, A8, A9,A10,A11,A12,A13,...
    A14,A15,...
   A16,A17,A18,A19,A20,A21,A22,A23,A24,A25,A26,A27,A28,A29,A30,A31,A32,...
   A33,A34,A35,...
   A36,A37,A38,A39,A40,A41,A42,A43,A44,A45,A46,A47,A48,A49,A50,A51,A52,...
   A53,A54,A55,...
   A56,A57,A58,A59,A60,A61,A62,A63,A64,A65,A66,A67,A68,A69,A70,A71,A72,...
   A73,A74,A75,...
   A76,A77,A78,A79,A80,A81,A82,A83,A84,A85];
lb=[  0,0.05,  0,0.20,  0,1.00,  0,  0,  0,  0,  0,  0,  0,  0,  0,  0,  0,...
    0,  0,...
     0,  0,  0,  0,  0,  0,  0,  0,  0,  0,  0,  0,  0,  0,  0,  0,  0,  0,...
     0,  0,  0,...
   -20,-20,-20,-20,-20,-20,-20,-20,-20,-20,-20,-20,-20,-20,-20,-20,-20,...
   -20,-20,-20,...
   -20,-20,-20,-20,-20,-20,-20,-20,-20,-20,-20,-20,-20,-20,-20,-20,-20,...
   -20,-20,-20,...
   -20,-20,-20,-20,-20,-20,-20,-20,-20,-20];
ub=[+10,0.15,+10,1.50,+10,2.50,+10,+10,+10,+10,+10,+10,+10,+10,+10,+10,...
    +10,+10,...
   +10,+10,+10,+10,+10,+10,+10,+10,+10,+10,+10,+10,+10,+10,+10,+10,+10,+10,...
   +10,+10,+10,...
   +10,+10,+10,+10,+10,+10,+10,+10,+10,+10,+10,+10,+10,+10,+10,+10,+10,+10,...
   +10,+10,+10,...
   +10,+10,+10,+10,+10,+10,+10,+10,+10,+10,+10,+10,+10,+10,+10,+10,+10,+10,...
   +10,+10,+10,...
```

```
   +10,+10,+10,+10,+10,+10,+10,+10,+10,+10];
%%%%%%%%%%%%%%%%%%%%%%%%%%%%%
ub(8:5:88)=0;
w0(8:5:38)=0;
lb(8:5:38)=-0.0001; % Limit "A5" (tau_inf) to bleach traces
ub(8:5:38)=+0.0001;
lb(43:5:88)=-0.5;
ub(43:5:88)=0;
%%%%%%%%%%%%%%%%%%%%%%%%%%%%%
options=optimset('MaxFunEvals',1000000,'MaxIter',1000000,'TolX',1E-5);
[w,resnorm,residual,exitflag,output,lambda,jacobian]=...
    lsqnonlin(@globta_fxn_ma_a1,w0,lb,ub,options);
w=w';

yfit1a = w(1).*(exp((B./(2.*1.66511.*w(2))).^2-((t2-t0)./w(2))).*0.5.*...
    (erf((((t2-t0)./B).*1.66511)-(B./(2.*1.66511.*w(2))))+1));
yfit2a = w(3).*(exp((B./(2.*1.66511.*w(4))).^2-((t2-t0)./w(4))).*0.5.*...
    (erf((((t2-t0)./B).*1.66511)-(B./(2.*1.66511.*w(4))))+1) - exp((B./...
    (2.*1.66511.*w(2))).^2-((t2-t0)./w(2))).*0.5.*(erf((((t2-t0)./B).*...
    1.66511)-(B./(2.*1.66511.*w(2))))+1));
yfit3a = w(5).*(exp((B./(2.*1.66511.*w(6))).^2-((t2-t0)./w(6))).*0.5.*...
    (erf((((t2-t0)./B).*1.66511)-(B./(2.*1.66511.*w(6))))+1) - exp((B./...
    (2.*1.66511.*w(4))).^2-((t2-t0)./w(4))).*0.5.*(erf((((t2-t0)./B).*...
    1.66511)-(B./(2.*1.66511.*w(4))))+1));
yfit4a = w(7).*(exp((B./(2.*1.66511.*15)).^2-((t2-t0)./15)).*0.5.*...
    (erf((((t2-t0)./B).*1.66511)-(B./(2.*1.66511.*15)))+1) - exp((B./...
    (2.*1.66511.*w(6))).^2-((t2-t0)./w(6))).*0.5.*(erf((((t2-t0)./B).*...
    1.66511)-(B./(2.*1.66511.*w(6))))+1));
yfit5a = w(8).*(exp((B./(2.*1.66511.*1E8)).^2-((t2-t0)./1E8)).*0.5.*...
    (erf((((t2-t0)./B).*1.66511)-(B./(2.*1.66511.*1E8)))+1));
```

```
yfit11 = yfit1a+yfit2a+yfit3a+yfit4a+yfit5a;

yfit1b = w(9).*(exp((B./(2.*1.66511.*w(2))).^2-((t2-t0)./w(2))).*0.5.*...
    (erf((((t2-t0)./B).*1.66511)-(B./(2.*1.66511.*w(2))))+1));
yfit2b = w(10).*(exp((B./(2.*1.66511.*w(4))).^2-((t2-t0)./w(4))).*0.5.*...
    (erf((((t2-t0)./B).*1.66511)-(B./(2.*1.66511.*w(4))))+1) - exp((B./...
    (2.*1.66511.*w(2))).^2-((t2-t0)./w(2))).*0.5.*(erf((((t2-t0)./B).*...
    1.66511)-(B./(2.*1.66511.*w(2))))+1));
yfit3b = w(11).*(exp((B./(2.*1.66511.*w(6))).^2-((t2-t0)./w(6))).*0.5.*...
    (erf((((t2-t0)./B).*1.66511)-(B./(2.*1.66511.*w(6))))+1) - exp((B./...
    (2.*1.66511.*w(4))).^2-((t2-t0)./w(4))).*0.5.*(erf((((t2-t0)./B).*...
    1.66511)-(B./(2.*1.66511.*w(4))))+1));
yfit4b = w(12).*(exp((B./(2.*1.66511.*15)).^2-((t2-t0)./15)).*0.5.*...
    (erf((((t2-t0)./B).*1.66511)-(B./(2.*1.66511.*15)))+1) - exp((B./...
    (2.*1.66511.*w(6))).^2-((t2-t0)./w(6))).*0.5.*(erf((((t2-t0)./B).*...
    1.66511)-(B./(2.*1.66511.*w(6))))+1));
yfit5b = w(13).*(exp((B./(2.*1.66511.*1E8)).^2-((t2-t0)./1E8)).*0.5.*...
    (erf((((t2-t0)./B).*1.66511)-(B./(2.*1.66511.*1E8)))+1));
yfit22 = yfit1b+yfit2b+yfit3b+yfit4b+yfit5b;

yfit1c = w(14).*(exp((B./(2.*1.66511.*w(2))).^2-((t2-t0)./w(2))).*0.5.*...
    (erf((((t2-t0)./B).*1.66511)-(B./(2.*1.66511.*w(2))))+1));
yfit2c = w(15).*(exp((B./(2.*1.66511.*w(4))).^2-((t2-t0)./w(4))).*0.5.*...
    (erf((((t2-t0)./B).*1.66511)-(B./(2.*1.66511.*w(4))))+1) - exp((B./...
    (2.*1.66511.*w(2))).^2-((t2-t0)./w(2))).*0.5.*(erf((((t2-t0)./B).*...
    1.66511)-(B./(2.*1.66511.*w(2))))+1));
yfit3c = w(16).*(exp((B./(2.*1.66511.*w(6))).^2-((t2-t0)./w(6))).*0.5.*...
    (erf((((t2-t0)./B).*1.66511)-(B./(2.*1.66511.*w(6))))+1) - exp((B./...
    (2.*1.66511.*w(4))).^2-((t2-t0)./w(4))).*0.5.*(erf((((t2-t0)./B).*...
    1.66511)-(B./(2.*1.66511.*w(4))))+1));
```

```
yfit4c = w(17).*(exp((B./(2.*1.66511.*15)).^2-((t2-t0)./15)).*0.5.*...
    (erf((((t2-t0)./B).*1.66511)-(B./(2.*1.66511.*15)))+1) - exp((B./...
    (2.*1.66511.*w(6))).^2-((t2-t0)./w(6))).*0.5.*(erf((((t2-t0)./B).*...
    1.66511)-(B./(2.*1.66511.*w(6))))+1));
yfit5c = w(18).*(exp((B./(2.*1.66511.*1E8)).^2-((t2-t0)./1E8)).*0.5.*...
    (erf((((t2-t0)./B).*1.66511)-(B./(2.*1.66511.*1E8)))+1));
yfit33 = yfit1c+yfit2c+yfit3c+yfit4c+yfit5c;

yfit1d = w(19).*(exp((B./(2.*1.66511.*w(2))).^2-((t2-t0)./w(2))).*0.5.*...
    (erf((((t2-t0)./B).*1.66511)-(B./(2.*1.66511.*w(2))))+1));
yfit2d = w(20).*(exp((B./(2.*1.66511.*w(4))).^2-((t2-t0)./w(4))).*0.5.*...
    (erf((((t2-t0)./B).*1.66511)-(B./(2.*1.66511.*w(4))))+1) - exp((B./...
    (2.*1.66511.*w(2))).^2-((t2-t0)./w(2))).*0.5.*(erf((((t2-t0)./B).*...
    1.66511)-(B./(2.*1.66511.*w(2))))+1));
yfit3d = w(21).*(exp((B./(2.*1.66511.*w(6))).^2-((t2-t0)./w(6))).*0.5.*...
    (erf((((t2-t0)./B).*1.66511)-(B./(2.*1.66511.*w(6))))+1) - exp((B./...
    (2.*1.66511.*w(4))).^2-((t2-t0)./w(4))).*0.5.*(erf((((t2-t0)./B).*...
    1.66511)-(B./(2.*1.66511.*w(4))))+1));
yfit4d = w(22).*(exp((B./(2.*1.66511.*19)).^2-((t2-t0)./19)).*0.5.*...
    (erf((((t2-t0)./B).*1.66511)-(B./(2.*1.66511.*19)))+1) - exp((B./...
    (2.*1.66511.*w(6))).^2-((t2-t0)./w(6))).*0.5.*(erf((((t2-t0)./B).*...
    1.66511)-(B./(2.*1.66511.*w(6))))+1));
yfit5d = w(23).*(exp((B./(2.*1.66511.*1E8)).^2-((t2-t0)./1E8)).*0.5.*...
    (erf((((t2-t0)./B).*1.66511)-(B./(2.*1.66511.*1E8)))+1));
yfit44 = yfit1d+yfit2d+yfit3d+yfit4d+yfit5d;

yfit1e = w(24).*(exp((B./(2.*1.66511.*w(2))).^2-((t2-t0)./w(2))).*0.5.*...
    (erf((((t2-t0)./B).*1.66511)-(B./(2.*1.66511.*w(2))))+1));
yfit2e = w(25).*(exp((B./(2.*1.66511.*w(4))).^2-((t2-t0)./w(4))).*0.5.*...
    (erf((((t2-t0)./B).*1.66511)-(B./(2.*1.66511.*w(4))))+1) - exp((B./...
```

```
    (2.*1.66511.*w(2))).^2-((t2-t0)./w(2))).*0.5.*(erf((((t2-t0)./B).*...
    1.66511)-(B./(2.*1.66511.*w(2))))+1));
yfit3e = w(26).*(exp((B./(2.*1.66511.*w(6))).^2-((t2-t0)./w(6))).*0.5.*...
    (erf((((t2-t0)./B).*1.66511)-(B./(2.*1.66511.*w(6))))+1) - exp((B./...
    (2.*1.66511.*w(4))).^2-((t2-t0)./w(4))).*0.5.*(erf((((t2-t0)./B).*...
    1.66511)-(B./(2.*1.66511.*w(4))))+1));
yfit4e = w(27).*(exp((B./(2.*1.66511.*19)).^2-((t2-t0)./19)).*0.5.*...
    (erf((((t2-t0)./B).*1.66511)-(B./(2.*1.66511.*19)))+1) - exp((B./...
    (2.*1.66511.*w(6))).^2-((t2-t0)./w(6))).*0.5.*(erf((((t2-t0)./B).*...
    1.66511)-(B./(2.*1.66511.*w(6))))+1));
yfit5e = w(28).*(exp((B./(2.*1.66511.*1E8)).^2-((t2-t0)./1E8)).*0.5.*...
    (erf((((t2-t0)./B).*1.66511)-(B./(2.*1.66511.*1E8)))+1));
yfit55 = yfit1e+yfit2e+yfit3e+yfit4e+yfit5e;

yfit1f = w(29).*(exp((B./(2.*1.66511.*w(2))).^2-((t2-t0)./w(2))).*0.5.*...
    (erf((((t2-t0)./B).*1.66511)-(B./(2.*1.66511.*w(2))))+1));
yfit2f = w(30).*(exp((B./(2.*1.66511.*w(4))).^2-((t2-t0)./w(4))).*0.5.*...
    (erf((((t2-t0)./B).*1.66511)-(B./(2.*1.66511.*w(4))))+1) - exp((B./...
    (2.*1.66511.*w(2))).^2-((t2-t0)./w(2))).*0.5.*(erf((((t2-t0)./B).*...
    1.66511)-(B./(2.*1.66511.*w(2))))+1));
yfit3f = w(31).*(exp((B./(2.*1.66511.*w(6))).^2-((t2-t0)./w(6))).*0.5.*...
    (erf((((t2-t0)./B).*1.66511)-(B./(2.*1.66511.*w(6))))+1) - exp((B./...
    (2.*1.66511.*w(4))).^2-((t2-t0)./w(4))).*0.5.*(erf((((t2-t0)./B).*...
    1.66511)-(B./(2.*1.66511.*w(4))))+1));
yfit4f = w(32).*(exp((B./(2.*1.66511.*19)).^2-((t2-t0)./19)).*0.5.*...
    (erf((((t2-t0)./B).*1.66511)-(B./(2.*1.66511.*19)))+1) - exp((B./...
    (2.*1.66511.*w(6))).^2-((t2-t0)./w(6))).*0.5.*(erf((((t2-t0)./B).*...
    1.66511)-(B./(2.*1.66511.*w(6))))+1));
yfit5f = w(33).*(exp((B./(2.*1.66511.*1E8)).^2-((t2-t0)./1E8)).*0.5.*...
    (erf((((t2-t0)./B).*1.66511)-(B./(2.*1.66511.*1E8)))+1));
```

```
yfit66 = yfit1f+yfit2f+yfit3f+yfit4f+yfit5f;

yfit1g = w(34).*(exp((B./(2.*1.66511.*w(2))).^2-((t2-t0)./w(2))).*0.5.*...
    (erf((((t2-t0)./B).*1.66511)-(B./(2.*1.66511.*w(2))))+1));
yfit2g = w(35).*(exp((B./(2.*1.66511.*w(4))).^2-((t2-t0)./w(4))).*0.5.*...
    (erf((((t2-t0)./B).*1.66511)-(B./(2.*1.66511.*w(4))))+1) - exp((B./...
    (2.*1.66511.*w(2))).^2-((t2-t0)./w(2))).*0.5.*(erf((((t2-t0)./B).*...
    1.66511)-(B./(2.*1.66511.*w(2))))+1));
yfit3g = w(36).*(exp((B./(2.*1.66511.*w(6))).^2-((t2-t0)./w(6))).*0.5.*...
    (erf((((t2-t0)./B).*1.66511)-(B./(2.*1.66511.*w(6))))+1) - exp((B./...
    (2.*1.66511.*w(4))).^2-((t2-t0)./w(4))).*0.5.*(erf((((t2-t0)./B).*...
    1.66511)-(B./(2.*1.66511.*w(4))))+1));
yfit4g = w(37).*(exp((B./(2.*1.66511.*19)).^2-((t2-t0)./19)).*0.5.*...
    (erf((((t2-t0)./B).*1.66511)-(B./(2.*1.66511.*19)))+1) - exp((B./...
    (2.*1.66511.*w(6))).^2-((t2-t0)./w(6))).*0.5.*(erf((((t2-t0)./B).*...
    1.66511)-(B./(2.*1.66511.*w(6))))+1));
yfit5g = w(38).*(exp((B./(2.*1.66511.*1E8)).^2-((t2-t0)./1E8)).*0.5.*...
    (erf((((t2-t0)./B).*1.66511)-(B./(2.*1.66511.*1E8)))+1));
yfit77 = yfit1g+yfit2g+yfit3g+yfit4g+yfit5g;

yfit1h = w(39).*(exp((B./(2.*1.66511.*w(2))).^2-((t2-t0)./w(2))).*0.5.*...
    (erf((((t2-t0)./B).*1.66511)-(B./(2.*1.66511.*w(2))))+1));
yfit2h = w(40).*(exp((B./(2.*1.66511.*w(4))).^2-((t2-t0)./w(4))).*0.5.*...
    (erf((((t2-t0)./B).*1.66511)-(B./(2.*1.66511.*w(4))))+1) - exp((B./...
    (2.*1.66511.*w(2))).^2-((t2-t0)./w(2))).*0.5.*(erf((((t2-t0)./B).*...
    1.66511)-(B./(2.*1.66511.*w(2))))+1));
yfit3h = w(41).*(exp((B./(2.*1.66511.*w(6))).^2-((t2-t0)./w(6))).*0.5.*...
    (erf((((t2-t0)./B).*1.66511)-(B./(2.*1.66511.*w(6))))+1) - exp((B./...
    (2.*1.66511.*w(4))).^2-((t2-t0)./w(4))).*0.5.*(erf((((t2-t0)./B).*...
    1.66511)-(B./(2.*1.66511.*w(4))))+1));
```

```
yfit4h = w(42).*(exp((B./(2.*1.66511.*18)).^2-((t2-t0)./18)).*0.5.*...
    (erf((((t2-t0)./B).*1.66511)-(B./(2.*1.66511.*18)))+1) - exp((B./...
    (2.*1.66511.*w(6))).^2-((t2-t0)./w(6))).*0.5.*(erf((((t2-t0)./B).*...
    1.66511)-(B./(2.*1.66511.*w(6))))+1));
yfit5h = w(43).*(exp((B./(2.*1.66511.*1E8)).^2-((t2-t0)./1E8)).*0.5.*...
    (erf((((t2-t0)./B).*1.66511)-(B./(2.*1.66511.*1E8)))+1));
yfit88 = yfit1h+yfit2h+yfit3h+yfit4h+yfit5h;

yfit1i = w(44).*(exp((B./(2.*1.66511.*w(2))).^2-((t2-t0)./w(2))).*0.5.*...
    (erf((((t2-t0)./B).*1.66511)-(B./(2.*1.66511.*w(2))))+1));
yfit2i = w(45).*(exp((B./(2.*1.66511.*w(4))).^2-((t2-t0)./w(4))).*0.5.*...
    (erf((((t2-t0)./B).*1.66511)-(B./(2.*1.66511.*w(4))))+1) - exp((B./...
    (2.*1.66511.*w(2))).^2-((t2-t0)./w(2))).*0.5.*(erf((((t2-t0)./B).*...
    1.66511)-(B./(2.*1.66511.*w(2))))+1));
yfit3i = w(46).*(exp((B./(2.*1.66511.*w(6))).^2-((t2-t0)./w(6))).*0.5.*...
    (erf((((t2-t0)./B).*1.66511)-(B./(2.*1.66511.*w(6))))+1) - exp((B./...
    (2.*1.66511.*w(4))).^2-((t2-t0)./w(4))).*0.5.*(erf((((t2-t0)./B).*...
    1.66511)-(B./(2.*1.66511.*w(4))))+1));
yfit4i = w(47).*(exp((B./(2.*1.66511.*18)).^2-((t2-t0)./18)).*0.5.*...
    (erf((((t2-t0)./B).*1.66511)-(B./(2.*1.66511.*18)))+1) - exp((B./...
    (2.*1.66511.*w(6))).^2-((t2-t0)./w(6))).*0.5.*(erf((((t2-t0)./B).*...
    1.66511)-(B./(2.*1.66511.*w(6))))+1));
yfit5i = w(48).*(exp((B./(2.*1.66511.*1E8)).^2-((t2-t0)./1E8)).*0.5.*...
    (erf((((t2-t0)./B).*1.66511)-(B./(2.*1.66511.*1E8)))+1));
yfit99 = yfit1i+yfit2i+yfit3i+yfit4i+yfit5i;

yfit1j = w(49).*(exp((B./(2.*1.66511.*w(2))).^2-((t2-t0)./w(2))).*0.5.*...
    (erf((((t2-t0)./B).*1.66511)-(B./(2.*1.66511.*w(2))))+1));
yfit2j = w(50).*(exp((B./(2.*1.66511.*w(4))).^2-((t2-t0)./w(4))).*0.5.*...
    (erf((((t2-t0)./B).*1.66511)-(B./(2.*1.66511.*w(4))))+1) - exp((B./...
```

```
    (2.*1.66511.*w(2))).^2-((t2-t0)./w(2))).*0.5.*(erf((((t2-t0)./B).*...
    1.66511)-(B./(2.*1.66511.*w(2))))+1));
yfit3j = w(51).*(exp((B./(2.*1.66511.*w(6))).^2-((t2-t0)./w(6))).*0.5.*...
    (erf((((t2-t0)./B).*1.66511)-(B./(2.*1.66511.*w(6))))+1) - exp((B./...
    (2.*1.66511.*w(4))).^2-((t2-t0)./w(4))).*0.5.*(erf((((t2-t0)./B).*...
    1.66511)-(B./(2.*1.66511.*w(4))))+1));
yfit4j = w(52).*(exp((B./(2.*1.66511.*18)).^2-((t2-t0)./18)).*0.5.*...
    (erf((((t2-t0)./B).*1.66511)-(B./(2.*1.66511.*18)))+1) - exp((B./...
    (2.*1.66511.*w(6))).^2-((t2-t0)./w(6))).*0.5.*(erf((((t2-t0)./B).*...
    1.66511)-(B./(2.*1.66511.*w(6))))+1));
yfit5j = w(53).*(exp((B./(2.*1.66511.*1E8)).^2-((t2-t0)./1E8)).*0.5.*...
    (erf((((t2-t0)./B).*1.66511)-(B./(2.*1.66511.*1E8)))+1));
yfit1010 = yfit1j+yfit2j+yfit3j+yfit4j+yfit5j;

yfit1k = w(54).*(exp((B./(2.*1.66511.*w(2))).^2-((t2-t0)./w(2))).*0.5.*...
    (erf((((t2-t0)./B).*1.66511)-(B./(2.*1.66511.*w(2))))+1));
yfit2k = w(55).*(exp((B./(2.*1.66511.*w(4))).^2-((t2-t0)./w(4))).*0.5.*...
    (erf((((t2-t0)./B).*1.66511)-(B./(2.*1.66511.*w(4))))+1) - exp((B./...
    (2.*1.66511.*w(2))).^2-((t2-t0)./w(2))).*0.5.*(erf((((t2-t0)./B).*...
    1.66511)-(B./(2.*1.66511.*w(2))))+1));
yfit3k = w(56).*(exp((B./(2.*1.66511.*w(6))).^2-((t2-t0)./w(6))).*0.5.*...
    (erf((((t2-t0)./B).*1.66511)-(B./(2.*1.66511.*w(6))))+1) - exp((B./...
    (2.*1.66511.*w(4))).^2-((t2-t0)./w(4))).*0.5.*(erf((((t2-t0)./B).*...
    1.66511)-(B./(2.*1.66511.*w(4))))+1));
yfit4k = w(57).*(exp((B./(2.*1.66511.*18)).^2-((t2-t0)./18)).*0.5.*...
    (erf((((t2-t0)./B).*1.66511)-(B./(2.*1.66511.*18)))+1) - exp((B./...
    (2.*1.66511.*w(6))).^2-((t2-t0)./w(6))).*0.5.*(erf((((t2-t0)./B).*...
    1.66511)-(B./(2.*1.66511.*w(6))))+1));
yfit5k = w(58).*(exp((B./(2.*1.66511.*1E8)).^2-((t2-t0)./1E8)).*0.5.*...
    (erf((((t2-t0)./B).*1.66511)-(B./(2.*1.66511.*1E8)))+1));
```

```
yfit1111 = yfit1k+yfit2k+yfit3k+yfit4k+yfit5k;

yfit1l = w(59).*(exp((B./(2.*1.66511.*w(2))).^2-((t2-t0)./w(2))).*0.5.*...
    (erf((((t2-t0)./B).*1.66511)-(B./(2.*1.66511.*w(2))))+1));
yfit2l = w(60).*(exp((B./(2.*1.66511.*w(4))).^2-((t2-t0)./w(4))).*0.5.*...
    (erf((((t2-t0)./B).*1.66511)-(B./(2.*1.66511.*w(4))))+1) - exp((B./...
    (2.*1.66511.*w(2))).^2-((t2-t0)./w(2))).*0.5.*(erf((((t2-t0)./B).*...
    1.66511)-(B./(2.*1.66511.*w(2))))+1));
yfit3l = w(61).*(exp((B./(2.*1.66511.*w(6))).^2-((t2-t0)./w(6))).*0.5.*...
    (erf((((t2-t0)./B).*1.66511)-(B./(2.*1.66511.*w(6))))+1) - exp((B./...
    (2.*1.66511.*w(4))).^2-((t2-t0)./w(4))).*0.5.*(erf((((t2-t0)./B).*...
    1.66511)-(B./(2.*1.66511.*w(4))))+1));
yfit4l = w(62).*(exp((B./(2.*1.66511.*18)).^2-((t2-t0)./18)).*0.5.*...
    (erf((((t2-t0)./B).*1.66511)-(B./(2.*1.66511.*18)))+1) - exp((B./...
    (2.*1.66511.*w(6))).^2-((t2-t0)./w(6))).*0.5.*(erf((((t2-t0)./B).*...
    1.66511)-(B./(2.*1.66511.*w(6))))+1));
yfit5l = w(63).*(exp((B./(2.*1.66511.*1E8)).^2-((t2-t0)./1E8)).*0.5.*...
    (erf((((t2-t0)./B).*1.66511)-(B./(2.*1.66511.*1E8)))+1));
yfit1212 = yfit1l+yfit2l+yfit3l+yfit4l+yfit5l;

yfit1m = w(64).*(exp((B./(2.*1.66511.*w(2))).^2-((t2-t0)./w(2))).*0.5.*...
    (erf((((t2-t0)./B).*1.66511)-(B./(2.*1.66511.*w(2))))+1));
yfit2m = w(65).*(exp((B./(2.*1.66511.*w(4))).^2-((t2-t0)./w(4))).*0.5.*...
    (erf((((t2-t0)./B).*1.66511)-(B./(2.*1.66511.*w(4))))+1) - exp((B./...
    (2.*1.66511.*w(2))).^2-((t2-t0)./w(2))).*0.5.*(erf((((t2-t0)./B).*...
    1.66511)-(B./(2.*1.66511.*w(2))))+1));
yfit3m = w(66).*(exp((B./(2.*1.66511.*w(6))).^2-((t2-t0)./w(6))).*0.5.*...
    (erf((((t2-t0)./B).*1.66511)-(B./(2.*1.66511.*w(6))))+1) - exp((B./...
    (2.*1.66511.*w(4))).^2-((t2-t0)./w(4))).*0.5.*(erf((((t2-t0)./B).*...
    1.66511)-(B./(2.*1.66511.*w(4))))+1));
```

```
yfit4m = w(67).*(exp((B./(2.*1.66511.*18)).^2-((t2-t0)./18)).*0.5.*...
    (erf((((t2-t0)./B).*1.66511)-(B./(2.*1.66511.*18)))+1) - exp((B./...
    (2.*1.66511.*w(6))).^2-((t2-t0)./w(6))).*0.5.*(erf((((t2-t0)./B).*...
    1.66511)-(B./(2.*1.66511.*w(6))))+1));
yfit5m = w(68).*(exp((B./(2.*1.66511.*1E8)).^2-((t2-t0)./1E8)).*0.5.*...
    (erf((((t2-t0)./B).*1.66511)-(B./(2.*1.66511.*1E8)))+1));
yfit1313 = yfit1m+yfit2m+yfit3m+yfit4m+yfit5m;

yfit1n = w(69).*(exp((B./(2.*1.66511.*w(2))).^2-((t2-t0)./w(2))).*0.5.*...
    (erf((((t2-t0)./B).*1.66511)-(B./(2.*1.66511.*w(2))))+1));
yfit2n = w(70).*(exp((B./(2.*1.66511.*w(4))).^2-((t2-t0)./w(4))).*0.5.*...
    (erf((((t2-t0)./B).*1.66511)-(B./(2.*1.66511.*w(4))))+1) - exp((B./...
    (2.*1.66511.*w(2))).^2-((t2-t0)./w(2))).*0.5.*(erf((((t2-t0)./B).*...
    1.66511)-(B./(2.*1.66511.*w(2))))+1));
yfit3n = w(71).*(exp((B./(2.*1.66511.*w(6))).^2-((t2-t0)./w(6))).*0.5.*...
    (erf((((t2-t0)./B).*1.66511)-(B./(2.*1.66511.*w(6))))+1) - exp((B./...
    (2.*1.66511.*w(4))).^2-((t2-t0)./w(4))).*0.5.*(erf((((t2-t0)./B).*...
    1.66511)-(B./(2.*1.66511.*w(4))))+1));
yfit4n = w(72).*(exp((B./(2.*1.66511.*18)).^2-((t2-t0)./18)).*0.5.*...
    (erf((((t2-t0)./B).*1.66511)-(B./(2.*1.66511.*18)))+1) - exp((B./...
    (2.*1.66511.*w(6))).^2-((t2-t0)./w(6))).*0.5.*(erf((((t2-t0)./B).*...
    1.66511)-(B./(2.*1.66511.*w(6))))+1));
yfit5n = w(73).*(exp((B./(2.*1.66511.*1E8)).^2-((t2-t0)./1E8)).*0.5.*...
    (erf((((t2-t0)./B).*1.66511)-(B./(2.*1.66511.*1E8)))+1));
yfit1414 = yfit1n+yfit2n+yfit3n+yfit4n+yfit5n;

yfit1o = w(74).*(exp((B./(2.*1.66511.*w(2))).^2-((t2-t0)./w(2))).*0.5.*...
    (erf((((t2-t0)./B).*1.66511)-(B./(2.*1.66511.*w(2))))+1));
yfit2o = w(75).*(exp((B./(2.*1.66511.*w(4))).^2-((t2-t0)./w(4))).*0.5.*...
    (erf((((t2-t0)./B).*1.66511)-(B./(2.*1.66511.*w(4))))+1) - exp((B./...
```

```
    (2.*1.66511.*w(2))).^2-((t2-t0)./w(2))).*0.5.*(erf((((t2-t0)./B).*...
    1.66511)-(B./(2.*1.66511.*w(2))))+1));
yfit3o = w(76).*(exp((B./(2.*1.66511.*w(6))).^2-((t2-t0)./w(6))).*0.5.*...
    (erf((((t2-t0)./B).*1.66511)-(B./(2.*1.66511.*w(6))))+1) - exp((B./...
    (2.*1.66511.*w(4))).^2-((t2-t0)./w(4))).*0.5.*(erf((((t2-t0)./B).*...
    1.66511)-(B./(2.*1.66511.*w(4))))+1));
yfit4o = w(77).*(exp((B./(2.*1.66511.*18)).^2-((t2-t0)./18)).*0.5.*...
    (erf((((t2-t0)./B).*1.66511)-(B./(2.*1.66511.*18)))+1) - exp((B./...
    (2.*1.66511.*w(6))).^2-((t2-t0)./w(6))).*0.5.*(erf((((t2-t0)./B).*...
    1.66511)-(B./(2.*1.66511.*w(6))))+1));
yfit5o = w(78).*(exp((B./(2.*1.66511.*1E8)).^2-((t2-t0)./1E8)).*0.5.*...
    (erf((((t2-t0)./B).*1.66511)-(B./(2.*1.66511.*1E8)))+1));
yfit1515 = yfit1o+yfit2o+yfit3o+yfit4o+yfit5o;

yfit1p = w(79).*(exp((B./(2.*1.66511.*w(2))).^2-((t2-t0)./w(2))).*0.5.*...
    (erf((((t2-t0)./B).*1.66511)-(B./(2.*1.66511.*w(2))))+1));
yfit2p = w(80).*(exp((B./(2.*1.66511.*w(4))).^2-((t2-t0)./w(4))).*0.5.*...
    (erf((((t2-t0)./B).*1.66511)-(B./(2.*1.66511.*w(4))))+1) - exp((B./...
    (2.*1.66511.*w(2))).^2-((t2-t0)./w(2))).*0.5.*(erf((((t2-t0)./B).*...
    1.66511)-(B./(2.*1.66511.*w(2))))+1));
yfit3p = w(81).*(exp((B./(2.*1.66511.*w(6))).^2-((t2-t0)./w(6))).*0.5.*...
    (erf((((t2-t0)./B).*1.66511)-(B./(2.*1.66511.*w(6))))+1) - exp((B./...
    (2.*1.66511.*w(4))).^2-((t2-t0)./w(4))).*0.5.*(erf((((t2-t0)./B).*...
    1.66511)-(B./(2.*1.66511.*w(4))))+1));
yfit4p = w(82).*(exp((B./(2.*1.66511.*18)).^2-((t2-t0)./18)).*0.5.*...
    (erf((((t2-t0)./B).*1.66511)-(B./(2.*1.66511.*18)))+1) - exp((B./...
    (2.*1.66511.*w(6))).^2-((t2-t0)./w(6))).*0.5.*(erf((((t2-t0)./B).*...
    1.66511)-(B./(2.*1.66511.*w(6))))+1));
yfit5p = w(83).*(exp((B./(2.*1.66511.*1E8)).^2-((t2-t0)./1E8)).*0.5.*...
    (erf((((t2-t0)./B).*1.66511)-(B./(2.*1.66511.*1E8)))+1));
```

```
yfit1616 = yfit1p+yfit2p+yfit3p+yfit4p+yfit5p;

yfit1q = w(84).*(exp((B./(2.*1.66511.*w(2))).^2-((t2-t0)./w(2))).*0.5.*...
    (erf((((t2-t0)./B).*1.66511)-(B./(2.*1.66511.*w(2))))+1));
yfit2q = w(85).*(exp((B./(2.*1.66511.*w(4))).^2-((t2-t0)./w(4))).*0.5.*...
    (erf((((t2-t0)./B).*1.66511)-(B./(2.*1.66511.*w(4))))+1) - exp((B./...
    (2.*1.66511.*w(2))).^2-((t2-t0)./w(2))).*0.5.*(erf((((t2-t0)./B).*...
    1.66511)-(B./(2.*1.66511.*w(2))))+1));
yfit3q = w(86).*(exp((B./(2.*1.66511.*w(6))).^2-((t2-t0)./w(6))).*0.5.*...
    (erf((((t2-t0)./B).*1.66511)-(B./(2.*1.66511.*w(6))))+1) - exp((B./...
    (2.*1.66511.*w(4))).^2-((t2-t0)./w(4))).*0.5.*(erf((((t2-t0)./B).*...
    1.66511)-(B./(2.*1.66511.*w(4))))+1));
yfit4q = w(87).*(exp((B./(2.*1.66511.*18)).^2-((t2-t0)./18)).*0.5.*...
    (erf((((t2-t0)./B).*1.66511)-(B./(2.*1.66511.*18)))+1) - exp((B./...
    (2.*1.66511.*w(6))).^2-((t2-t0)./w(6))).*0.5.*(erf((((t2-t0)./B).*...
    1.66511)-(B./(2.*1.66511.*w(6))))+1));
yfit5q = w(88).*(exp((B./(2.*1.66511.*1E8)).^2-((t2-t0)./1E8)).*0.5.*...
    (erf((((t2-t0)./B).*1.66511)-(B./(2.*1.66511.*1E8)))+1));
yfit1717 = yfit1q+yfit2q+yfit3q+yfit4q+yfit5q;

figure
hold on
plot(t2,y1,'o',t2,y2,'o',t2,y3,'o',t2,y4,'o',t2,y5,'o',t2,y6,'o',t2,y7,'o')
plot(t2,y8,'o',t2,y9,'o',t2,y10,'o',t2,y11,'o',t2,y12,'o',t2,y13,'o',...
    t2,y14,'o')
plot(t2,y15,'o',t2,y16,'o',t2,y17,'o')
plot(t2,yfit11,t2,yfit22,t2,yfit33,t2,yfit44,t2,yfit55,t2,yfit66,t2,...
    yfit77,'linewidth',2)
plot(t2,yfit88,t2,yfit99,t2,yfit1010,t2,yfit1111,t2,yfit1212,...
    t2,yfit1313,t2,yfit1414,'linewidth',2)
```

```
plot(t2,yfit1515,t2,yfit1616,t2,yfit1717,t2,zerot,'k','linewidth',2)
xlim([0.12 50])
axis square
box on
set(gca,'xscale','log','tickdir','out','linewidth',2,'ticklength',...
    [0.03 0.01])
hold off

zt1=w(2);
zt2=w(4);
zt3=w(6);
zres=resnorm;
zresE=resnorm/17;

omegaf=[w3a(1) w3a(6) w3a(9) w3a(12) w3a(16) w3a(19) w3a(21) w3a(24)...
    w3a(28) w3a(30) w3a(37) w3a(44) w3a(45) w3a(46) w3a(47)...
    w3a(48) w3a(49)];
zerowf=zeros(length(omegaf),1);

spec1=zeros(length(omegaf),1);
spec2=zeros(length(omegaf),1);
spec3=zeros(length(omegaf),1);
spec4=zeros(length(omegaf),1);
spec5=zeros(length(omegaf),1);
spec1(1)=w(1);
spec1(2:end)=w(9:5:84);
spec2(1)=w(3);
spec2(2:end)=w(10:5:85);
spec3(1)=w(5);
spec3(2:end)=w(11:5:86);
```

```
spec4(1)=w(7);
spec4(2:end)=w(12:5:87);
spec5(1)=w(8);
spec5(2:end)=w(13:5:88);

figure
plot(omegaf,spec1,'-o',omegaf,spec2,'-o',omegaf,spec3,'-o',omegaf,spec4,...
    '-o',omegaf,spec5,'-o',omegaf,zerowf,'k','linewidth',2)
xlim([1965 2150])
legend('IS','bridge','trans','v=1','product','location','southwest')
legend boxoff
axis square

datmat21a=zeros(length(t2),17);
datmat21a(:,1)=y1;
datmat21a(:,2)=y2;
datmat21a(:,3)=y3;
datmat21a(:,4)=y4;
datmat21a(:,5)=y5;
datmat21a(:,6)=y6;
datmat21a(:,7)=y7;
datmat21a(:,8)=y8;
datmat21a(:,9)=y9;
datmat21a(:,10)=y10;
datmat21a(:,11)=y11;
datmat21a(:,12)=y12;
datmat21a(:,13)=y13;
datmat21a(:,14)=y14;
datmat21a(:,15)=y15;
datmat21a(:,16)=y16;
```

```
datmat21a(:,17)=y17;

fitmat21a=zeros(length(t2),17);
fitmat21a(:,1)=yfit11;
fitmat21a(:,2)=yfit22;
fitmat21a(:,3)=yfit33;
fitmat21a(:,4)=yfit44;
fitmat21a(:,5)=yfit55;
fitmat21a(:,6)=yfit66;
fitmat21a(:,7)=yfit77;
fitmat21a(:,8)=yfit88;
fitmat21a(:,9)=yfit99;
fitmat21a(:,10)=yfit1010;
fitmat21a(:,11)=yfit1111;
fitmat21a(:,12)=yfit1212;
fitmat21a(:,13)=yfit1313;
fitmat21a(:,14)=yfit1414;
fitmat21a(:,15)=yfit1515;
fitmat21a(:,16)=yfit1616;
fitmat21a(:,17)=yfit1717;

omegafa=omegaf;
wa=w;
zresEa=resnorm/17;

save wa wa
save omegafa omegafa
save t2 t2
save datmat21a datmat21a
save fitmat21a fitmat21a
```

```
save zresEa zresEa

toc % 12.4 minutes
```

The function file (globta_fxn_ma_a1.m) contains the following:

```
function fit = globta_fxn_ma_a1(w)

global t2 B t0 y1 y2 y3 y4 y5 y6 y7 y8 y9 y10 y11 y12 y13 y14 y15 y16 y17

fxn1a = w(1).*(exp((B./(2.*1.66511.*w(2))).^2-((t2-t0)./w(2))).*0.5.*...
    (erf((((t2-t0)./B).*1.66511)-(B./(2.*1.66511.*w(2))))+1));
fxn2a = w(3).*(exp((B./(2.*1.66511.*w(4))).^2-((t2-t0)./w(4))).*0.5.*...
    (erf((((t2-t0)./B).*1.66511)-(B./(2.*1.66511.*w(4))))+1) - exp((B./...
    (2.*1.66511.*w(2))).^2-((t2-t0)./w(2))).*0.5.*(erf((((t2-t0)./B).*...
    1.66511)-(B./(2.*1.66511.*w(2))))+1));
fxn3a = w(5).*(exp((B./(2.*1.66511.*w(6))).^2-((t2-t0)./w(6))).*0.5.*...
    (erf((((t2-t0)./B).*1.66511)-(B./(2.*1.66511.*w(6))))+1) - exp((B./...
    (2.*1.66511.*w(4))).^2-((t2-t0)./w(4))).*0.5.*(erf((((t2-t0)./B).*...
    1.66511)-(B./(2.*1.66511.*w(4))))+1));
fxn4a = w(7).*(exp((B./(2.*1.66511.*15)).^2-((t2-t0)./15)).*0.5.*...
    (erf((((t2-t0)./B).*1.66511)-(B./(2.*1.66511.*15)))+1) - exp((B./...
    (2.*1.66511.*w(6))).^2-((t2-t0)./w(6))).*0.5.*(erf((((t2-t0)./B).*...
    1.66511)-(B./(2.*1.66511.*w(6))))+1));
fxn5a = w(8).*(exp((B./(2.*1.66511.*1E8)).^2-((t2-t0)./1E8)).*0.5.*...
    (erf((((t2-t0)./B).*1.66511)-(B./(2.*1.66511.*1E8)))+1));
fxn11 = fxn1a+fxn2a+fxn3a+fxn4a+fxn5a;

fxn1b = w(9).*(exp((B./(2.*1.66511.*w(2))).^2-((t2-t0)./w(2))).*0.5.*...
    (erf((((t2-t0)./B).*1.66511)-(B./(2.*1.66511.*w(2))))+1));
fxn2b = w(10).*(exp((B./(2.*1.66511.*w(4))).^2-((t2-t0)./w(4))).*0.5.*...
```

```
    (erf((((t2-t0)./B).*1.66511)-(B./(2.*1.66511.*w(4))))+1) - exp((B./...
    (2.*1.66511.*w(2))).^2-((t2-t0)./w(2))).*0.5.*(erf((((t2-t0)./B).*...
    1.66511)-(B./(2.*1.66511.*w(2))))+1));
fxn3b = w(11).*(exp((B./(2.*1.66511.*w(6))).^2-((t2-t0)./w(6))).*0.5.*...
    (erf((((t2-t0)./B).*1.66511)-(B./(2.*1.66511.*w(6))))+1) - exp((B./...
    (2.*1.66511.*w(4))).^2-((t2-t0)./w(4))).*0.5.*(erf((((t2-t0)./B).*...
    1.66511)-(B./(2.*1.66511.*w(4))))+1));
fxn4b = w(12).*(exp((B./(2.*1.66511.*15)).^2-((t2-t0)./15)).*0.5.*...
    (erf((((t2-t0)./B).*1.66511)-(B./(2.*1.66511.*15)))+1) - exp((B./...
    (2.*1.66511.*w(6))).^2-((t2-t0)./w(6))).*0.5.*(erf((((t2-t0)./B).*...
    1.66511)-(B./(2.*1.66511.*w(6))))+1));
fxn5b = w(13).*(exp((B./(2.*1.66511.*1E8)).^2-((t2-t0)./1E8)).*0.5.*...
    (erf((((t2-t0)./B).*1.66511)-(B./(2.*1.66511.*1E8)))+1));
fxn22 = fxn1b+fxn2b+fxn3b+fxn4b+fxn5b;

fxn1c = w(14).*(exp((B./(2.*1.66511.*w(2))).^2-((t2-t0)./w(2))).*0.5.*...
    (erf((((t2-t0)./B).*1.66511)-(B./(2.*1.66511.*w(2))))+1));
fxn2c = w(15).*(exp((B./(2.*1.66511.*w(4))).^2-((t2-t0)./w(4))).*0.5.*...
    (erf((((t2-t0)./B).*1.66511)-(B./(2.*1.66511.*w(4))))+1) - exp((B./...
    (2.*1.66511.*w(2))).^2-((t2-t0)./w(2))).*0.5.*(erf((((t2-t0)./B).*...
    1.66511)-(B./(2.*1.66511.*w(2))))+1));
fxn3c = w(16).*(exp((B./(2.*1.66511.*w(6))).^2-((t2-t0)./w(6))).*0.5.*...
    (erf((((t2-t0)./B).*1.66511)-(B./(2.*1.66511.*w(6))))+1) - exp((B./...
    (2.*1.66511.*w(4))).^2-((t2-t0)./w(4))).*0.5.*(erf((((t2-t0)./B).*...
    1.66511)-(B./(2.*1.66511.*w(4))))+1));
fxn4c = w(17).*(exp((B./(2.*1.66511.*15)).^2-((t2-t0)./15)).*0.5.*...
    (erf((((t2-t0)./B).*1.66511)-(B./(2.*1.66511.*15)))+1) - exp((B./...
    (2.*1.66511.*w(6))).^2-((t2-t0)./w(6))).*0.5.*(erf((((t2-t0)./B).*...
    1.66511)-(B./(2.*1.66511.*w(6))))+1));
fxn5c = w(18).*(exp((B./(2.*1.66511.*1E8)).^2-((t2-t0)./1E8)).*0.5.*...
```

```
    (erf((((t2-t0)./B).*1.66511)-(B./(2.*1.66511.*1E8)))+1));
fxn33 = fxn1c+fxn2c+fxn3c+fxn4c+fxn5c;

fxn1d = w(19).*(exp((B./(2.*1.66511.*w(2))).^2-((t2-t0)./w(2))).*0.5.*...
    (erf((((t2-t0)./B).*1.66511)-(B./(2.*1.66511.*w(2))))+1));
fxn2d = w(20).*(exp((B./(2.*1.66511.*w(4))).^2-((t2-t0)./w(4))).*0.5.*...
    (erf((((t2-t0)./B).*1.66511)-(B./(2.*1.66511.*w(4))))+1) - exp((B./...
    (2.*1.66511.*w(2))).^2-((t2-t0)./w(2))).*0.5.*(erf((((t2-t0)./B).*...
    1.66511)-(B./(2.*1.66511.*w(2))))+1));
fxn3d = w(21).*(exp((B./(2.*1.66511.*w(6))).^2-((t2-t0)./w(6))).*0.5.*...
    (erf((((t2-t0)./B).*1.66511)-(B./(2.*1.66511.*w(6))))+1) - exp((B./...
    (2.*1.66511.*w(4))).^2-((t2-t0)./w(4))).*0.5.*(erf((((t2-t0)./B).*...
    1.66511)-(B./(2.*1.66511.*w(4))))+1));
fxn4d = w(22).*(exp((B./(2.*1.66511.*19)).^2-((t2-t0)./19)).*0.5.*...
    (erf((((t2-t0)./B).*1.66511)-(B./(2.*1.66511.*19)))+1) - exp((B./...
    (2.*1.66511.*w(6))).^2-((t2-t0)./w(6))).*0.5.*(erf((((t2-t0)./B).*...
    1.66511)-(B./(2.*1.66511.*w(6))))+1));
fxn5d = w(23).*(exp((B./(2.*1.66511.*1E8)).^2-((t2-t0)./1E8)).*0.5.*...
    (erf((((t2-t0)./B).*1.66511)-(B./(2.*1.66511.*1E8)))+1));
fxn44 = fxn1d+fxn2d+fxn3d+fxn4d+fxn5d;

fxn1e = w(24).*(exp((B./(2.*1.66511.*w(2))).^2-((t2-t0)./w(2))).*0.5.*...
    (erf((((t2-t0)./B).*1.66511)-(B./(2.*1.66511.*w(2))))+1));
fxn2e = w(25).*(exp((B./(2.*1.66511.*w(4))).^2-((t2-t0)./w(4))).*0.5.*...
    (erf((((t2-t0)./B).*1.66511)-(B./(2.*1.66511.*w(4))))+1) - exp((B./...
    (2.*1.66511.*w(2))).^2-((t2-t0)./w(2))).*0.5.*(erf((((t2-t0)./B).*...
    1.66511)-(B./(2.*1.66511.*w(2))))+1));
fxn3e = w(26).*(exp((B./(2.*1.66511.*w(6))).^2-((t2-t0)./w(6))).*0.5.*...
    (erf((((t2-t0)./B).*1.66511)-(B./(2.*1.66511.*w(6))))+1) - exp((B./...
    (2.*1.66511.*w(4))).^2-((t2-t0)./w(4))).*0.5.*(erf((((t2-t0)./B).*...
```

```
    1.66511)-(B./(2.*1.66511.*w(4))))+1));
fxn4e = w(27).*(exp((B./(2.*1.66511.*19)).^2-((t2-t0)./19)).*0.5.*...
    (erf((((t2-t0)./B).*1.66511)-(B./(2.*1.66511.*19)))+1) - exp((B./...
    (2.*1.66511.*w(6))).^2-((t2-t0)./w(6))).*0.5.*(erf((((t2-t0)./B).*...
    1.66511)-(B./(2.*1.66511.*w(6))))+1));
fxn5e = w(28).*(exp((B./(2.*1.66511.*1E8)).^2-((t2-t0)./1E8)).*0.5.*...
    (erf((((t2-t0)./B).*1.66511)-(B./(2.*1.66511.*1E8)))+1));
fxn55 = fxn1e+fxn2e+fxn3e+fxn4e+fxn5e;

fxn1f = w(29).*(exp((B./(2.*1.66511.*w(2))).^2-((t2-t0)./w(2))).*0.5.*...
    (erf((((t2-t0)./B).*1.66511)-(B./(2.*1.66511.*w(2))))+1));
fxn2f = w(30).*(exp((B./(2.*1.66511.*w(4))).^2-((t2-t0)./w(4))).*0.5.*...
    (erf((((t2-t0)./B).*1.66511)-(B./(2.*1.66511.*w(4))))+1) - exp((B./...
    (2.*1.66511.*w(2))).^2-((t2-t0)./w(2))).*0.5.*(erf((((t2-t0)./B).*...
    1.66511)-(B./(2.*1.66511.*w(2))))+1));
fxn3f = w(31).*(exp((B./(2.*1.66511.*w(6))).^2-((t2-t0)./w(6))).*0.5.*...
    (erf((((t2-t0)./B).*1.66511)-(B./(2.*1.66511.*w(6))))+1) - exp((B./...
    (2.*1.66511.*w(4))).^2-((t2-t0)./w(4))).*0.5.*(erf((((t2-t0)./B).*...
    1.66511)-(B./(2.*1.66511.*w(4))))+1));
fxn4f = w(32).*(exp((B./(2.*1.66511.*19)).^2-((t2-t0)./19)).*0.5.*...
    (erf((((t2-t0)./B).*1.66511)-(B./(2.*1.66511.*19)))+1) - exp((B./...
    (2.*1.66511.*w(6))).^2-((t2-t0)./w(6))).*0.5.*(erf((((t2-t0)./B).*...
    1.66511)-(B./(2.*1.66511.*w(6))))+1));
fxn5f = w(33).*(exp((B./(2.*1.66511.*1E8)).^2-((t2-t0)./1E8)).*0.5.*...
    (erf((((t2-t0)./B).*1.66511)-(B./(2.*1.66511.*1E8)))+1));
fxn66 = fxn1f+fxn2f+fxn3f+fxn4f+fxn5f;

fxn1g = w(34).*(exp((B./(2.*1.66511.*w(2))).^2-((t2-t0)./w(2))).*0.5.*...
    (erf((((t2-t0)./B).*1.66511)-(B./(2.*1.66511.*w(2))))+1));
fxn2g = w(35).*(exp((B./(2.*1.66511.*w(4))).^2-((t2-t0)./w(4))).*0.5.*...
```

```
    (erf((((t2-t0)./B).*1.66511)-(B./(2.*1.66511.*w(4))))+1) - exp((B./...
    (2.*1.66511.*w(2))).^2-((t2-t0)./w(2))).*0.5.*(erf((((t2-t0)./B).*...
    1.66511)-(B./(2.*1.66511.*w(2))))+1));
fxn3g = w(36).*(exp((B./(2.*1.66511.*w(6))).^2-((t2-t0)./w(6))).*0.5.*...
    (erf((((t2-t0)./B).*1.66511)-(B./(2.*1.66511.*w(6))))+1) - exp((B./...
    (2.*1.66511.*w(4))).^2-((t2-t0)./w(4))).*0.5.*(erf((((t2-t0)./B).*...
    1.66511)-(B./(2.*1.66511.*w(4))))+1));
fxn4g = w(37).*(exp((B./(2.*1.66511.*19)).^2-((t2-t0)./19)).*0.5.*...
    (erf((((t2-t0)./B).*1.66511)-(B./(2.*1.66511.*19)))+1) - exp((B./...
    (2.*1.66511.*w(6))).^2-((t2-t0)./w(6))).*0.5.*(erf((((t2-t0)./B).*...
    1.66511)-(B./(2.*1.66511.*w(6))))+1));
fxn5g = w(38).*(exp((B./(2.*1.66511.*1E8)).^2-((t2-t0)./1E8)).*0.5.*...
    (erf((((t2-t0)./B).*1.66511)-(B./(2.*1.66511.*1E8)))+1));
fxn77 = fxn1g+fxn2g+fxn3g+fxn4g+fxn5g;

fxn1h = w(39).*(exp((B./(2.*1.66511.*w(2))).^2-((t2-t0)./w(2))).*0.5.*...
    (erf((((t2-t0)./B).*1.66511)-(B./(2.*1.66511.*w(2))))+1));
fxn2h = w(40).*(exp((B./(2.*1.66511.*w(4))).^2-((t2-t0)./w(4))).*0.5.*...
    (erf((((t2-t0)./B).*1.66511)-(B./(2.*1.66511.*w(4))))+1) - exp((B./...
    (2.*1.66511.*w(2))).^2-((t2-t0)./w(2))).*0.5.*(erf((((t2-t0)./B).*...
    1.66511)-(B./(2.*1.66511.*w(2))))+1));
fxn3h = w(41).*(exp((B./(2.*1.66511.*w(6))).^2-((t2-t0)./w(6))).*0.5.*...
    (erf((((t2-t0)./B).*1.66511)-(B./(2.*1.66511.*w(6))))+1) - exp((B./...
    (2.*1.66511.*w(4))).^2-((t2-t0)./w(4))).*0.5.*(erf((((t2-t0)./B).*...
    1.66511)-(B./(2.*1.66511.*w(4))))+1));
fxn4h = w(42).*(exp((B./(2.*1.66511.*18)).^2-((t2-t0)./18)).*0.5.*...
    (erf((((t2-t0)./B).*1.66511)-(B./(2.*1.66511.*18)))+1) - exp((B./...
    (2.*1.66511.*w(6))).^2-((t2-t0)./w(6))).*0.5.*(erf((((t2-t0)./B).*...
    1.66511)-(B./(2.*1.66511.*w(6))))+1));
fxn5h = w(43).*(exp((B./(2.*1.66511.*1E8)).^2-((t2-t0)./1E8)).*0.5.*...
```

```
    (erf((((t2-t0)./B).*1.66511)-(B./(2.*1.66511.*1E8)))+1));
fxn88 = fxn1h+fxn2h+fxn3h+fxn4h+fxn5h;

fxn1i = w(44).*(exp((B./(2.*1.66511.*w(2))).^2-((t2-t0)./w(2))).*0.5.*...
    (erf((((t2-t0)./B).*1.66511)-(B./(2.*1.66511.*w(2))))+1));
fxn2i = w(45).*(exp((B./(2.*1.66511.*w(4))).^2-((t2-t0)./w(4))).*0.5.*...
    (erf((((t2-t0)./B).*1.66511)-(B./(2.*1.66511.*w(4))))+1) - exp((B./...
    (2.*1.66511.*w(2))).^2-((t2-t0)./w(2))).*0.5.*(erf((((t2-t0)./B).*...
    1.66511)-(B./(2.*1.66511.*w(2))))+1));
fxn3i = w(46).*(exp((B./(2.*1.66511.*w(6))).^2-((t2-t0)./w(6))).*0.5.*...
    (erf((((t2-t0)./B).*1.66511)-(B./(2.*1.66511.*w(6))))+1) - exp((B./...
    (2.*1.66511.*w(4))).^2-((t2-t0)./w(4))).*0.5.*(erf((((t2-t0)./B).*...
    1.66511)-(B./(2.*1.66511.*w(4))))+1));
fxn4i = w(47).*(exp((B./(2.*1.66511.*18)).^2-((t2-t0)./18)).*0.5.*...
    (erf((((t2-t0)./B).*1.66511)-(B./(2.*1.66511.*18)))+1) - exp((B./...
    (2.*1.66511.*w(6))).^2-((t2-t0)./w(6))).*0.5.*(erf((((t2-t0)./B).*...
    1.66511)-(B./(2.*1.66511.*w(6))))+1));
fxn5i = w(48).*(exp((B./(2.*1.66511.*1E8)).^2-((t2-t0)./1E8)).*0.5.*...
    (erf((((t2-t0)./B).*1.66511)-(B./(2.*1.66511.*1E8)))+1));
fxn99 = fxn1i+fxn2i+fxn3i+fxn4i+fxn5i;

fxn1j = w(49).*(exp((B./(2.*1.66511.*w(2))).^2-((t2-t0)./w(2))).*0.5.*...
    (erf((((t2-t0)./B).*1.66511)-(B./(2.*1.66511.*w(2))))+1));
fxn2j = w(50).*(exp((B./(2.*1.66511.*w(4))).^2-((t2-t0)./w(4))).*0.5.*...
    (erf((((t2-t0)./B).*1.66511)-(B./(2.*1.66511.*w(4))))+1) - exp((B./...
    (2.*1.66511.*w(2))).^2-((t2-t0)./w(2))).*0.5.*(erf((((t2-t0)./B).*...
    1.66511)-(B./(2.*1.66511.*w(2))))+1));
fxn3j = w(51).*(exp((B./(2.*1.66511.*w(6))).^2-((t2-t0)./w(6))).*0.5.*...
    (erf((((t2-t0)./B).*1.66511)-(B./(2.*1.66511.*w(6))))+1) - exp((B./...
    (2.*1.66511.*w(4))).^2-((t2-t0)./w(4))).*0.5.*(erf((((t2-t0)./B).*...
```

```
    1.66511)-(B./(2.*1.66511.*w(4))))+1));
fxn4j = w(52).*(exp((B./(2.*1.66511.*18)).^2-((t2-t0)./18)).*0.5.*...
    (erf((((t2-t0)./B).*1.66511)-(B./(2.*1.66511.*18)))+1) - exp((B./...
    (2.*1.66511.*w(6))).^2-((t2-t0)./w(6))).*0.5.*(erf((((t2-t0)./B).*...
    1.66511)-(B./(2.*1.66511.*w(6))))+1));
fxn5j = w(53).*(exp((B./(2.*1.66511.*1E8)).^2-((t2-t0)./1E8)).*0.5.*...
    (erf((((t2-t0)./B).*1.66511)-(B./(2.*1.66511.*1E8)))+1));
fxn1010 = fxn1j+fxn2j+fxn3j+fxn4j+fxn5j;

fxn1k = w(54).*(exp((B./(2.*1.66511.*w(2))).^2-((t2-t0)./w(2))).*0.5.*...
    (erf((((t2-t0)./B).*1.66511)-(B./(2.*1.66511.*w(2))))+1));
fxn2k = w(55).*(exp((B./(2.*1.66511.*w(4))).^2-((t2-t0)./w(4))).*0.5.*...
    (erf((((t2-t0)./B).*1.66511)-(B./(2.*1.66511.*w(4))))+1) - exp((B./...
    (2.*1.66511.*w(2))).^2-((t2-t0)./w(2))).*0.5.*(erf((((t2-t0)./B).*...
    1.66511)-(B./(2.*1.66511.*w(2))))+1));
fxn3k = w(56).*(exp((B./(2.*1.66511.*w(6))).^2-((t2-t0)./w(6))).*0.5.*...
    (erf((((t2-t0)./B).*1.66511)-(B./(2.*1.66511.*w(6))))+1) - exp((B./...
    (2.*1.66511.*w(4))).^2-((t2-t0)./w(4))).*0.5.*(erf((((t2-t0)./B).*...
    1.66511)-(B./(2.*1.66511.*w(4))))+1));
fxn4k = w(57).*(exp((B./(2.*1.66511.*18)).^2-((t2-t0)./18)).*0.5.*...
    (erf((((t2-t0)./B).*1.66511)-(B./(2.*1.66511.*18)))+1) - exp((B./...
    (2.*1.66511.*w(6))).^2-((t2-t0)./w(6))).*0.5.*(erf((((t2-t0)./B).*...
    1.66511)-(B./(2.*1.66511.*w(6))))+1));
fxn5k = w(58).*(exp((B./(2.*1.66511.*1E8)).^2-((t2-t0)./1E8)).*0.5.*...
    (erf((((t2-t0)./B).*1.66511)-(B./(2.*1.66511.*1E8)))+1));
fxn1111 = fxn1k+fxn2k+fxn3k+fxn4k+fxn5k;

fxn1l = w(59).*(exp((B./(2.*1.66511.*w(2))).^2-((t2-t0)./w(2))).*0.5.*...
    (erf((((t2-t0)./B).*1.66511)-(B./(2.*1.66511.*w(2))))+1));
fxn2l = w(60).*(exp((B./(2.*1.66511.*w(4))).^2-((t2-t0)./w(4))).*0.5.*...
```

```
    (erf((((t2-t0)./B).*1.66511)-(B./(2.*1.66511.*w(4))))+1) - exp((B./...
    (2.*1.66511.*w(2))).^2-((t2-t0)./w(2))).*0.5.*(erf((((t2-t0)./B).*...
    1.66511)-(B./(2.*1.66511.*w(2))))+1));
fxn3l = w(61).*(exp((B./(2.*1.66511.*w(6))).^2-((t2-t0)./w(6))).*0.5.*...
    (erf((((t2-t0)./B).*1.66511)-(B./(2.*1.66511.*w(6))))+1) - exp((B./...
    (2.*1.66511.*w(4))).^2-((t2-t0)./w(4))).*0.5.*(erf((((t2-t0)./B).*...
    1.66511)-(B./(2.*1.66511.*w(4))))+1));
fxn4l = w(62).*(exp((B./(2.*1.66511.*18)).^2-((t2-t0)./18)).*0.5.*...
    (erf((((t2-t0)./B).*1.66511)-(B./(2.*1.66511.*18)))+1) - exp((B./...
    (2.*1.66511.*w(6))).^2-((t2-t0)./w(6))).*0.5.*(erf((((t2-t0)./B).*...
    1.66511)-(B./(2.*1.66511.*w(6))))+1));
fxn5l = w(63).*(exp((B./(2.*1.66511.*1E8)).^2-((t2-t0)./1E8)).*0.5.*...
    (erf((((t2-t0)./B).*1.66511)-(B./(2.*1.66511.*1E8)))+1));
fxn1212 = fxn1l+fxn2l+fxn3l+fxn4l+fxn5l;

fxn1m = w(64).*(exp((B./(2.*1.66511.*w(2))).^2-((t2-t0)./w(2))).*0.5.*...
    (erf((((t2-t0)./B).*1.66511)-(B./(2.*1.66511.*w(2))))+1));
fxn2m = w(65).*(exp((B./(2.*1.66511.*w(4))).^2-((t2-t0)./w(4))).*0.5.*...
    (erf((((t2-t0)./B).*1.66511)-(B./(2.*1.66511.*w(4))))+1) - exp((B./...
    (2.*1.66511.*w(2))).^2-((t2-t0)./w(2))).*0.5.*(erf((((t2-t0)./B).*...
    1.66511)-(B./(2.*1.66511.*w(2))))+1));
fxn3m = w(66).*(exp((B./(2.*1.66511.*w(6))).^2-((t2-t0)./w(6))).*0.5.*...
    (erf((((t2-t0)./B).*1.66511)-(B./(2.*1.66511.*w(6))))+1) - exp((B./...
    (2.*1.66511.*w(4))).^2-((t2-t0)./w(4))).*0.5.*(erf((((t2-t0)./B).*...
    1.66511)-(B./(2.*1.66511.*w(4))))+1));
fxn4m = w(67).*(exp((B./(2.*1.66511.*18)).^2-((t2-t0)./18)).*0.5.*...
    (erf((((t2-t0)./B).*1.66511)-(B./(2.*1.66511.*18)))+1) - exp((B./...
    (2.*1.66511.*w(6))).^2-((t2-t0)./w(6))).*0.5.*(erf((((t2-t0)./B).*...
    1.66511)-(B./(2.*1.66511.*w(6))))+1));
fxn5m = w(68).*(exp((B./(2.*1.66511.*1E8)).^2-((t2-t0)./1E8)).*0.5.*...
```

```
    (erf((((t2-t0)./B).*1.66511)-(B./(2.*1.66511.*1E8)))+1));
fxn1313 = fxn1m+fxn2m+fxn3m+fxn4m+fxn5m;

fxn1n = w(69).*(exp((B./(2.*1.66511.*w(2))).^2-((t2-t0)./w(2))).*0.5.*...
    (erf((((t2-t0)./B).*1.66511)-(B./(2.*1.66511.*w(2))))+1));
fxn2n = w(70).*(exp((B./(2.*1.66511.*w(4))).^2-((t2-t0)./w(4))).*0.5.*...
    (erf((((t2-t0)./B).*1.66511)-(B./(2.*1.66511.*w(4))))+1) - exp((B./...
    (2.*1.66511.*w(2))).^2-((t2-t0)./w(2))).*0.5.*(erf((((t2-t0)./B).*...
    1.66511)-(B./(2.*1.66511.*w(2))))+1));
fxn3n = w(71).*(exp((B./(2.*1.66511.*w(6))).^2-((t2-t0)./w(6))).*0.5.*...
    (erf((((t2-t0)./B).*1.66511)-(B./(2.*1.66511.*w(6))))+1) - exp((B./...
    (2.*1.66511.*w(4))).^2-((t2-t0)./w(4))).*0.5.*(erf((((t2-t0)./B).*...
    1.66511)-(B./(2.*1.66511.*w(4))))+1));
fxn4n = w(72).*(exp((B./(2.*1.66511.*18)).^2-((t2-t0)./18)).*0.5.*...
    (erf((((t2-t0)./B).*1.66511)-(B./(2.*1.66511.*18)))+1) - exp((B./...
    (2.*1.66511.*w(6))).^2-((t2-t0)./w(6))).*0.5.*(erf((((t2-t0)./B).*...
    1.66511)-(B./(2.*1.66511.*w(6))))+1));
fxn5n = w(73).*(exp((B./(2.*1.66511.*1E8)).^2-((t2-t0)./1E8)).*0.5.*...
    (erf((((t2-t0)./B).*1.66511)-(B./(2.*1.66511.*1E8)))+1));
fxn1414 = fxn1n+fxn2n+fxn3n+fxn4n+fxn5n;

fxn1o = w(74).*(exp((B./(2.*1.66511.*w(2))).^2-((t2-t0)./w(2))).*0.5.*...
    (erf((((t2-t0)./B).*1.66511)-(B./(2.*1.66511.*w(2))))+1));
fxn2o = w(75).*(exp((B./(2.*1.66511.*w(4))).^2-((t2-t0)./w(4))).*0.5.*...
    (erf((((t2-t0)./B).*1.66511)-(B./(2.*1.66511.*w(4))))+1) - exp((B./...
    (2.*1.66511.*w(2))).^2-((t2-t0)./w(2))).*0.5.*(erf((((t2-t0)./B).*...
    1.66511)-(B./(2.*1.66511.*w(2))))+1));
fxn3o = w(76).*(exp((B./(2.*1.66511.*w(6))).^2-((t2-t0)./w(6))).*0.5.*...
    (erf((((t2-t0)./B).*1.66511)-(B./(2.*1.66511.*w(6))))+1) - exp((B./...
    (2.*1.66511.*w(4))).^2-((t2-t0)./w(4))).*0.5.*(erf((((t2-t0)./B).*...
```

```
    1.66511)-(B./(2.*1.66511.*w(4))))+1));
fxn4o = w(77).*(exp((B./(2.*1.66511.*18)).^2-((t2-t0)./18)).*0.5.*...
    (erf((((t2-t0)./B).*1.66511)-(B./(2.*1.66511.*18)))+1) - exp((B./...
    (2.*1.66511.*w(6))).^2-((t2-t0)./w(6))).*0.5.*(erf((((t2-t0)./B).*...
    1.66511)-(B./(2.*1.66511.*w(6))))+1));
fxn5o = w(78).*(exp((B./(2.*1.66511.*1E8)).^2-((t2-t0)./1E8)).*0.5.*...
    (erf((((t2-t0)./B).*1.66511)-(B./(2.*1.66511.*1E8)))+1));
fxn1515 = fxn1o+fxn2o+fxn3o+fxn4o+fxn5o;

fxn1p = w(79).*(exp((B./(2.*1.66511.*w(2))).^2-((t2-t0)./w(2))).*0.5.*...
    (erf((((t2-t0)./B).*1.66511)-(B./(2.*1.66511.*w(2))))+1));
fxn2p = w(80).*(exp((B./(2.*1.66511.*w(4))).^2-((t2-t0)./w(4))).*0.5.*...
    (erf((((t2-t0)./B).*1.66511)-(B./(2.*1.66511.*w(4))))+1) - exp((B./...
    (2.*1.66511.*w(2))).^2-((t2-t0)./w(2))).*0.5.*(erf((((t2-t0)./B).*...
    1.66511)-(B./(2.*1.66511.*w(2))))+1));
fxn3p = w(81).*(exp((B./(2.*1.66511.*w(6))).^2-((t2-t0)./w(6))).*0.5.*...
    (erf((((t2-t0)./B).*1.66511)-(B./(2.*1.66511.*w(6))))+1) - exp((B./...
    (2.*1.66511.*w(4))).^2-((t2-t0)./w(4))).*0.5.*(erf((((t2-t0)./B).*...
    1.66511)-(B./(2.*1.66511.*w(4))))+1));
fxn4p = w(82).*(exp((B./(2.*1.66511.*18)).^2-((t2-t0)./18)).*0.5.*...
    (erf((((t2-t0)./B).*1.66511)-(B./(2.*1.66511.*18)))+1) - exp((B./...
    (2.*1.66511.*w(6))).^2-((t2-t0)./w(6))).*0.5.*(erf((((t2-t0)./B).*...
    1.66511)-(B./(2.*1.66511.*w(6))))+1));
fxn5p = w(83).*(exp((B./(2.*1.66511.*1E8)).^2-((t2-t0)./1E8)).*0.5.*...
    (erf((((t2-t0)./B).*1.66511)-(B./(2.*1.66511.*1E8)))+1));
fxn1616 = fxn1p+fxn2p+fxn3p+fxn4p+fxn5p;

fxn1q = w(84).*(exp((B./(2.*1.66511.*w(2))).^2-((t2-t0)./w(2))).*0.5.*...
    (erf((((t2-t0)./B).*1.66511)-(B./(2.*1.66511.*w(2))))+1));
fxn2q = w(85).*(exp((B./(2.*1.66511.*w(4))).^2-((t2-t0)./w(4))).*0.5.*...
```

```
    (erf((((t2-t0)./B).*1.66511)-(B./(2.*1.66511.*w(4))))+1) - exp((B./...
    (2.*1.66511.*w(2))).^2-((t2-t0)./w(2))).*0.5.*(erf((((t2-t0)./B).*...
    1.66511)-(B./(2.*1.66511.*w(2))))+1));
fxn3q = w(86).*(exp((B./(2.*1.66511.*w(6))).^2-((t2-t0)./w(6))).*0.5.*...
    (erf((((t2-t0)./B).*1.66511)-(B./(2.*1.66511.*w(6))))+1) - exp((B./...
    (2.*1.66511.*w(4))).^2-((t2-t0)./w(4))).*0.5.*(erf((((t2-t0)./B).*...
    1.66511)-(B./(2.*1.66511.*w(4))))+1));
fxn4q = w(87).*(exp((B./(2.*1.66511.*18)).^2-((t2-t0)./18)).*0.5.*...
    (erf((((t2-t0)./B).*1.66511)-(B./(2.*1.66511.*18)))+1) - exp((B./...
    (2.*1.66511.*w(6))).^2-((t2-t0)./w(6))).*0.5.*(erf((((t2-t0)./B).*...
    1.66511)-(B./(2.*1.66511.*w(6))))+1));
fxn5q = w(88).*(exp((B./(2.*1.66511.*1E8)).^2-((t2-t0)./1E8)).*0.5.*...
    (erf((((t2-t0)./B).*1.66511)-(B./(2.*1.66511.*1E8)))+1));
fxn1717 = fxn1q+fxn2q+fxn3q+fxn4q+fxn5q;

fit = abs(fxn11-y1) + abs(fxn22-y2) + abs(fxn33-y3) + abs(fxn44-y4)...
    + abs(fxn55-y5) + abs(fxn66-y6) + abs(fxn77-y7) + abs(fxn88-y8)...
    + abs(fxn99-y9) + abs(fxn1010-y10) + abs(fxn1111-y11) +...
    abs(fxn1212-y12) + abs(fxn1313-y13) + abs(fxn1414-y14) +...
    abs(fxn1515-y15) + abs(fxn1616-y16) + abs(fxn1717-y17);
```

The results for the three groups are then combined and plotted with the following m-file (figures_21_ma.m). This represents iteration 21 of the analysis.

```
clear all

load t2
load w3a
load datmat21a
load fitmat21a
load omegafa
```

```
load datmat21b
load fitmat21b
load omegafb
load datmat21c
load fitmat21c
load omegafc
load wa
load wb
load wc
load zresEa
load zresEb
load zresEc

B=0.094;
t0=0;
zerowfa=zeros(length(omegafa),1);
zerowfb=zeros(length(omegafb),1);
zerowfc=zeros(length(omegafc),1);
zerow=zeros(60,1);
zerot=zeros(length(t2),1);
tau1a=wa(2);
tau2a=wa(4);
tau3a=wa(6);
tau1b=wb(2);
tau2b=wb(4);
tau3b=wb(6);
tau1c=wc(2);
tau2c=wc(4);
tau3c=wc(6);
```

```
tau1mean=(wa(2)+wb(2)+wc(2))./3;
tau1sd=std([wa(2) wb(2) wc(2)]); % tau1 = 110 fs

tau2mean=(wa(4)+wb(4)+wc(4))./3;
tau2sd=std([wa(4) wb(4) wc(4)]); % tau2 = 630 fs

tau3mean=(wa(6)+wb(6)+wc(6))./3;
tau3sd=std([wa(6) wb(6) wc(6)]); % tau3 = 1.31 ps



figure
hold on
plot(t2,datmat21a,'o')
plot(t2,fitmat21a,t2,zerot,'k','linewidth',2)
axis([0.12 max(t2) -8 2.5])
set(gca,'xscale','log','tickdir','out','linewidth',2,'ticklength',...
    [0.03 0.01])
axis square
box on
hold off

figure
hold on
plot(t2,datmat21b(:,15:17),'o')
plot(t2,fitmat21b(:,15:17),t2,zerot,'k','linewidth',2)
axis([0.12 max(t2) -9 2.5])
set(gca,'xscale','log','tickdir','out','linewidth',2,'ticklength',...
    [0.03 0.01])
axis square
box on
```

```
hold off

figure
hold on
plot(t2,datmat21c,'o')
plot(t2,fitmat21c,t2,zerot,'k','linewidth',2)
axis([0.12 max(t2) -9 2.5])
set(gca,'xscale','log','tickdir','out','linewidth',2,'ticklength',...
    [0.03 0.01])
axis square
box on
hold off

omegatot=zeros(51,1);
omegatot(1)=omegafa(1); % made from wa, wb and wc
omegatot(2)=omegafb(1);
omegatot(3)=omegafc(1);
omegatot(4)=omegafb(2);
omegatot(5)=omegafc(2);
omegatot(6)=omegafa(2);
omegatot(7)=omegafb(3);
omegatot(8)=omegafc(3);
omegatot(9)=omegafa(3);
omegatot(10)=omegafb(4);
omegatot(11)=omegafc(4);
omegatot(12)=omegafa(4);
omegatot(13)=omegafc(5);
omegatot(14)=omegafb(5);
omegatot(15)=omegafc(6);
omegatot(16)=omegafa(5);
```

```
omegatot(17)=omegafc(7);
omegatot(18)=omegafb(6);
omegatot(19)=omegafa(6);
omegatot(20)=omegafb(7);
omegatot(21)=omegafa(7);
omegatot(22)=omegafc(8);
omegatot(23)=omegafb(8);
omegatot(24)=omegafa(8);
omegatot(25)=omegafb(9);
omegatot(26)=omegafc(9);
omegatot(27)=omegafb(10);
omegatot(28)=omegafa(9);
omegatot(29)=omegafb(11);
omegatot(30)=omegafa(10);
omegatot(31)=omegafb(12);
omegatot(32)=omegafb(13);
omegatot(33)=omegafb(14);
omegatot(34)=omegafb(15);
omegatot(35)=omegafc(10);
omegatot(36)=omegafa(11);
omegatot(37)=omegafc(11);
omegatot(38)=omegafc(12);
omegatot(39)=omegafc(13);
omegatot(40)=omegafa(12);
omegatot(41)=omegafa(13);
omegatot(42)=omegafa(14);
omegatot(43)=omegafa(15);
omegatot(44)=omegafa(16);
omegatot(45)=omegafa(17);
omegatot(46)=omegafb(16);
```

```
omegatot(47)=omegafb(17);
omegatot(48)=omegafc(14);
omegatot(49)=omegafc(15);
omegatot(50)=omegafc(16);
omegatot(51)=omegafc(17);

spec1a=zeros(length(omegafa),1);
spec2a=zeros(length(omegafa),1);
spec3a=zeros(length(omegafa),1);
spec4a=zeros(length(omegafa),1);
spec5a=zeros(length(omegafa),1);
spec1a(1)=wa(1);
spec1a(2:end)=wa(9:5:84);
spec2a(1)=wa(3);
spec2a(2:end)=wa(10:5:85);
spec3a(1)=wa(5);
spec3a(2:end)=wa(11:5:86);
spec4a(1)=wa(7);
spec4a(2:end)=wa(12:5:87);
spec5a(1)=wa(8);
spec5a(2:end)=wa(13:5:88);

spec1b=zeros(length(omegafb),1);
spec2b=zeros(length(omegafb),1);
spec3b=zeros(length(omegafb),1);
spec4b=zeros(length(omegafb),1);
spec5b=zeros(length(omegafb),1);
spec1b(1)=wb(1);
spec1b(2:end)=wb(9:5:84);
spec2b(1)=wb(3);
```

```
spec2b(2:end)=wb(10:5:85);
spec3b(1)=wb(5);
spec3b(2:end)=wb(11:5:86);
spec4b(1)=wb(7);
spec4b(2:end)=wb(12:5:87);
spec5b(1)=wb(8);
spec5b(2:end)=wb(13:5:88);

spec1c=zeros(length(omegafc),1);
spec2c=zeros(length(omegafc),1);
spec3c=zeros(length(omegafc),1);
spec4c=zeros(length(omegafc),1);
spec5c=zeros(length(omegafc),1);
spec1c(1)=wc(1);
spec1c(2:end)=wc(9:5:84);
spec2c(1)=wc(3);
spec2c(2:end)=wc(10:5:85);
spec3c(1)=wc(5);
spec3c(2:end)=wc(11:5:86);
spec4c(1)=wc(7);
spec4c(2:end)=wc(12:5:87);
spec5c(1)=wc(8);
spec5c(2:end)=wc(13:5:88);

spec1=zeros(51,1);
spec1(1)=spec1a(1);
spec1(2)=spec1b(1);
spec1(3)=spec1c(1);
spec1(4)=spec1b(2);
spec1(5)=spec1c(2);
```

```
spec1(6)=spec1a(2);
spec1(7)=spec1b(3);
spec1(8)=spec1c(3);
spec1(9)=spec1a(3);
spec1(10)=spec1b(4);
spec1(11)=spec1c(4);
spec1(12)=spec1a(4);
spec1(13)=spec1c(5);
spec1(14)=spec1b(5);
spec1(15)=spec1c(6);
spec1(16)=spec1a(5);
spec1(17)=spec1c(7);
spec1(18)=spec1b(6);
spec1(19)=spec1a(6);
spec1(20)=spec1b(7);
spec1(21)=spec1a(7);
spec1(22)=spec1c(8);
spec1(23)=spec1b(8);
spec1(24)=spec1a(8);
spec1(25)=spec1b(9);
spec1(26)=spec1c(9);
spec1(27)=spec1b(10);
spec1(28)=spec1a(9);
spec1(29)=spec1b(11);
spec1(30)=spec1a(10);
spec1(31)=spec1b(12);
spec1(32)=spec1b(13);
spec1(33)=spec1b(14);
spec1(34)=spec1b(15);
spec1(35)=spec1c(10);
```

```
spec1(36)=spec1a(11);
spec1(37)=spec1c(11);
spec1(38)=spec1c(12);
spec1(39)=spec1c(13);
spec1(40)=spec1a(12);
spec1(41)=spec1a(13);
spec1(42)=spec1a(14);
spec1(43)=spec1a(15);
spec1(44)=spec1a(16);
spec1(45)=spec1a(17);
spec1(46)=spec1b(16);
spec1(47)=spec1b(17);
spec1(48)=spec1c(14);
spec1(49)=spec1c(15);
spec1(50)=spec1c(16);
spec1(51)=spec1c(17);

spec2=zeros(51,1);
spec2(1)=spec2a(1);
spec2(2)=spec2b(1);
spec2(3)=spec2c(1);
spec2(4)=spec2b(2);
spec2(5)=spec2c(2);
spec2(6)=spec2a(2);
spec2(7)=spec2b(3);
spec2(8)=spec2c(3);
spec2(9)=spec2a(3);
spec2(10)=spec2b(4);
spec2(11)=spec2c(4);
spec2(12)=spec2a(4);
```

```
spec2(13)=spec2c(5);
spec2(14)=spec2b(5);
spec2(15)=spec2c(6);
spec2(16)=spec2a(5);
spec2(17)=spec2c(7);
spec2(18)=spec2b(6);
spec2(19)=spec2a(6);
spec2(20)=spec2b(7);
spec2(21)=spec2a(7);
spec2(22)=spec2c(8);
spec2(23)=spec2b(8);
spec2(24)=spec2a(8);
spec2(25)=spec2b(9);
spec2(26)=spec2c(9);
spec2(27)=spec2b(10);
spec2(28)=spec2a(9);
spec2(29)=spec2b(11);
spec2(30)=spec2a(10);
spec2(31)=spec2b(12);
spec2(32)=spec2b(13);
spec2(33)=spec2b(14);
spec2(34)=spec2b(15);
spec2(35)=spec2c(10);
spec2(36)=spec2a(11);
spec2(37)=spec2c(11);
spec2(38)=spec2c(12);
spec2(39)=spec2c(13);
spec2(40)=spec2a(12);
spec2(41)=spec2a(13);
spec2(42)=spec2a(14);
```

```
spec2(43)=spec2a(15);
spec2(44)=spec2a(16);
spec2(45)=spec2a(17);
spec2(46)=spec2b(16);
spec2(47)=spec2b(17);
spec2(48)=spec2c(14);
spec2(49)=spec2c(15);
spec2(50)=spec2c(16);
spec2(51)=spec2c(17);

spec3=zeros(51,1);
spec3(1)=spec3a(1);
spec3(2)=spec3b(1);
spec3(3)=spec3c(1);
spec3(4)=spec3b(2);
spec3(5)=spec3c(2);
spec3(6)=spec3a(2);
spec3(7)=spec3b(3);
spec3(8)=spec3c(3);
spec3(9)=spec3a(3);
spec3(10)=spec3b(4);
spec3(11)=spec3c(4);
spec3(12)=spec3a(4);
spec3(13)=spec3c(5);
spec3(14)=spec3b(5);
spec3(15)=spec3c(6);
spec3(16)=spec3a(5);
spec3(17)=spec3c(7);
spec3(18)=spec3b(6);
spec3(19)=spec3a(6);
```

```
spec3(20)=spec3b(7);
spec3(21)=spec3a(7);
spec3(22)=spec3c(8);
spec3(23)=spec3b(8);
spec3(24)=spec3a(8);
spec3(25)=spec3b(9);
spec3(26)=spec3c(9);
spec3(27)=spec3b(10);
spec3(28)=spec3a(9);
spec3(29)=spec3b(11);
spec3(30)=spec3a(10);
spec3(31)=spec3b(12);
spec3(32)=spec3b(13);
spec3(33)=spec3b(14);
spec3(34)=spec3b(15);
spec3(35)=spec3c(10);
spec3(36)=spec3a(11);
spec3(37)=spec3c(11);
spec3(38)=spec3c(12);
spec3(39)=spec3c(13);
spec3(40)=spec3a(12);
spec3(41)=spec3a(13);
spec3(42)=spec3a(14);
spec3(43)=spec3a(15);
spec3(44)=spec3a(16);
spec3(45)=spec3a(17);
spec3(46)=spec3b(16);
spec3(47)=spec3b(17);
spec3(48)=spec3c(14);
spec3(49)=spec3c(15);
```

```
spec3(50)=spec3c(16);
spec3(51)=spec3c(17);

spec4=zeros(51,1);
spec4(1)=spec4a(1);
spec4(2)=spec4b(1);
spec4(3)=spec4c(1);
spec4(4)=spec4b(2);
spec4(5)=spec4c(2);
spec4(6)=spec4a(2);
spec4(7)=spec4b(3);
spec4(8)=spec4c(3);
spec4(9)=spec4a(3);
spec4(10)=spec4b(4);
spec4(11)=spec4c(4);
spec4(12)=spec4a(4);
spec4(13)=spec4c(5);
spec4(14)=spec4b(5);
spec4(15)=spec4c(6);
spec4(16)=spec4a(5);
spec4(17)=spec4c(7);
spec4(18)=spec4b(6);
spec4(19)=spec4a(6);
spec4(20)=spec4b(7);
spec4(21)=spec4a(7);
spec4(22)=spec4c(8);
spec4(23)=spec4b(8);
spec4(24)=spec4a(8);
spec4(25)=spec4b(9);
spec4(26)=spec4c(9);
```

```
spec4(27)=spec4b(10);
spec4(28)=spec4a(9);
spec4(29)=spec4b(11);
spec4(30)=spec4a(10);
spec4(31)=spec4b(12);
spec4(32)=spec4b(13);
spec4(33)=spec4b(14);
spec4(34)=spec4b(15);
spec4(35)=spec4c(10);
spec4(36)=spec4a(11);
spec4(37)=spec4c(11);
spec4(38)=spec4c(12);
spec4(39)=spec4c(13);
spec4(40)=spec4a(12);
spec4(41)=spec4a(13);
spec4(42)=spec4a(14);
spec4(43)=spec4a(15);
spec4(44)=spec4a(16);
spec4(45)=spec4a(17);
spec4(46)=spec4b(16);
spec4(47)=spec4b(17);
spec4(48)=spec4c(14);
spec4(49)=spec4c(15);
spec4(50)=spec4c(16);
spec4(51)=spec4c(17);

spec5=zeros(51,1);
spec5(1)=spec5a(1);
spec5(2)=spec5b(1);
spec5(3)=spec5c(1);
```

```
spec5(4)=spec5b(2);
spec5(5)=spec5c(2);
spec5(6)=spec5a(2);
spec5(7)=spec5b(3);
spec5(8)=spec5c(3);
spec5(9)=spec5a(3);
spec5(10)=spec5b(4);
spec5(11)=spec5c(4);
spec5(12)=spec5a(4);
spec5(13)=spec5c(5);
spec5(14)=spec5b(5);
spec5(15)=spec5c(6);
spec5(16)=spec5a(5);
spec5(17)=spec5c(7);
spec5(18)=spec5b(6);
spec5(19)=spec5a(6);
spec5(20)=spec5b(7);
spec5(21)=spec5a(7);
spec5(22)=spec5c(8);
spec5(23)=spec5b(8);
spec5(24)=spec5a(8);
spec5(25)=spec5b(9);
spec5(26)=spec5c(9);
spec5(27)=spec5b(10);
spec5(28)=spec5a(9);
spec5(29)=spec5b(11);
spec5(30)=spec5a(10);
spec5(31)=spec5b(12);
spec5(32)=spec5b(13);
spec5(33)=spec5b(14);
```

```
spec5(34)=spec5b(15);
spec5(35)=spec5c(10);
spec5(36)=spec5a(11);
spec5(37)=spec5c(11);
spec5(38)=spec5c(12);
spec5(39)=spec5c(13);
spec5(40)=spec5a(12);
spec5(41)=spec5a(13);
spec5(42)=spec5a(14);
spec5(43)=spec5a(15);
spec5(44)=spec5a(16);
spec5(45)=spec5a(17);
spec5(46)=spec5b(16);
spec5(47)=spec5b(17);
spec5(48)=spec5c(14);
spec5(49)=spec5c(15);
spec5(50)=spec5c(16);
spec5(51)=spec5c(17);

zerowtot=zeros(51,1);

%%%%%%%%%%%%%%%%%%%%  SADS FIGS  %%%%%%%%%%%%%%%%%%%%


%%%%%%%%%%%% "new" assignments %%%%%%%%%%%%
Delt_br=24;
x10=[2116 2116]; % bridge (1)
x11=[2116-1*Delt_br 2116-1*Delt_br];
x12=[2116-2*Delt_br 2116-2*Delt_br];
x13=[2116-3*Delt_br 2116-3*Delt_br];
```

```
x14=[2116-4*Delt_br 2116-4*Delt_br];
x15=[2116-5*Delt_br 2116-5*Delt_br];
x16=[2116-6*Delt_br 2116-6*Delt_br];
y1=[-12 12];

Delt_ax=21.4;
x20=[2074 2074]; % axial (2)
x21=[2074-1*Delt_ax 2074-1*Delt_ax];
x22=[2074-2*Delt_ax 2074-2*Delt_ax];
x23=[2074-3*Delt_ax 2074-3*Delt_ax];
x24=[2074-4*Delt_ax 2074-4*Delt_ax];
x25=[2074-5*Delt_ax 2074-5*Delt_ax];

Delt_tr=22.7;
x30=[2059.6 2059.6]; % trans (3)
x31=[2059.6-1*Delt_tr 2059.6-1*Delt_tr];
x32=[2059.6-2*Delt_tr 2059.6-2*Delt_tr];
x33=[2059.6-3*Delt_tr 2059.6-3*Delt_tr];
x34=[2059.6-4*Delt_tr 2059.6-4*Delt_tr];
x35=[2059.6-5*Delt_tr 2059.6-5*Delt_tr];

Delt_ra=21;
x40=[2049.8 2049.8]; % radial (4)
x41=[2049.8-1*Delt_ra 2049.8-1*Delt_ra];
x42=[2049.8-2*Delt_ra 2049.8-2*Delt_ra];
x43=[2049.8-3*Delt_ra 2049.8-3*Delt_ra];
x44=[2049.8-4*Delt_ra 2049.8-4*Delt_ra];
x45=[2049.8-5*Delt_ra 2049.8-5*Delt_ra];

%%%%%%%%%%%%%%%%%%%%%%%% for figure 4 %%%%%%%%%%%%%%%%%%%
```

```
figure
hold on
plot(omegatot,(spec1),'-','color',[0 0 0.5],'linewidth',3)
plot(omegatot,(spec2),'-','color',[0 0.5 0],'linewidth',3)
plot(omegatot,(spec3),'-b','linewidth',3)
plot(omegatot,(spec4),'-r','linewidth',3)
plot(omegatot,(spec5),'-c','linewidth',3)
plot(omegatot,zerowtot,'k','linewidth',2)
xlim([1970 2140])
set(gca,'linewidth',2,'tickdir','out','ticklength',[0.03 0.01],...
    'fontname','arial','fontweight','b'...
    ,'fontsize',20,'ytick',-12:4:4,'xtick',1980:40:2140)
box on
set(gca,'plotboxaspectratio',[1 1.3 1])
% legend('IS','bridge','trans','v=1','Product','location','southwest')
hold off

figure
hold on
plot(omegatot,(spec2),'-','color',[0 0.5 0],'linewidth',3)
plot(omegatot,(spec3),'-b','linewidth',3)
plot(omegatot,(spec4),'-r','linewidth',3)
plot(omegatot,zerowtot,'k','linewidth',2)
axis([1970 2046 0 3])
set(gca,'linewidth',2,'tickdir','out','ticklength',[0.03 0.01],...
    'fontname','arial','fontweight','b'...
    ,'fontsize',20,'ytick',0:0.5:2)
box on
set(gca,'plotboxaspectratio',[1 1.6 1])
```

```
legend('bridge','trans','v=1','location','northwest')
hold off

figure % "bridge"
hold on
plot(x14,y1,':b',x15,y1,':b',x16,y1,':b','linewidth',2)
plot(x22,y1,':',x23,y1,':',x24,y1,':',x25,y1,':','color',[1 140/255 0],...
    'linewidth',2)
plot(omegatot,(spec2),'-','color',[0 0.5 0],'linewidth',3)
axis([1970 2046 0 2.5])
set(gca,'linewidth',2,'tickdir','out','ticklength',[0.03 0.01],...
    'fontname','arial','fontweight','b'...
    ,'fontsize',20,'ytick',0:0.5:2)
box on
set(gca,'plotboxaspectratio',[1 1.6 1])
hold off

figure % "trans"
hold on
plot(x31,y1,':g',x32,y1,':g',x33,y1,':g',x34,y1,':g',x35,y1,':g',...
    'linewidth',2)
plot(x22,y1,':',x23,y1,':',x24,y1,':',x25,y1,':','color',[1 140/255 0],...
    'linewidth',2)
plot(omegatot,(spec3),'-b','linewidth',3)
axis([1970 2046 0 2.5])
set(gca,'linewidth',2,'tickdir','out','ticklength',[0.03 0.01],...
    'fontname','arial','fontweight','b'...
    ,'fontsize',20,'ytick',0:0.5:2)
box on
set(gca,'plotboxaspectratio',[1 1.6 1])
```

```
hold off

figure % "v = 1"
hold on
plot(x31,y1,':g','linewidth',2)
plot(x21,y1,':','color',[1 140/255 0],'linewidth',2)
plot(x41,y1,':c','linewidth',2)
plot(omegatot,(spec4),'-r','linewidth',3)
axis([1970 2046 0 2.5])
set(gca,'linewidth',2,'tickdir','out','ticklength',[0.03 0.01],...
    'fontname','arial','fontweight','b'...
    ,'fontsize',20,'ytick',0:0.5:2)
box on
set(gca,'plotboxaspectratio',[1 1.6 1])
hold off

ISma=spec1;
BRma=spec2;
TRma=spec3;
V1ma=spec4;
PRma=spec5;

save ISma ISma
save BRma BRma
save TRma TRma
save V1ma V1ma
save PRma PRma
save omegatot omegatot
```